

Society of Automotive Engineers  
of China (SAE-China)  
International Federation  
of Automotive Engineering Societies (FISITA)  
*Editors*

# Proceedings of the FISITA 2012 World Automotive Congress

Volume 11: Advanced Vehicle  
Manufacturing Technology



# Lecture Notes in Electrical Engineering

Volume 199

For further volumes:  
<http://www.springer.com/series/7818>

Society of Automotive Engineers of China  
(SAE-China) · International Federation of  
Automotive Engineering Societies (FISITA)  
Editors

# Proceedings of the FISITA 2012 World Automotive Congress

Volume 11: Advanced Vehicle  
Manufacturing Technology



 Springer

The Springer logo, which is a stylized black chess knight (horse) facing left, positioned to the left of the word 'Springer' in a black, serif font.

*Editors*  
SAE-China  
Beijing  
People's Republic of China

FISITA  
London  
UK

ISSN 1876-1100  
ISBN 978-3-642-33746-8  
DOI 10.1007/978-3-642-33747-5  
Springer Heidelberg New York Dordrecht London

ISSN 1876-1119 (electronic)  
ISBN 978-3-642-33747-5 (eBook)

Library of Congress Control Number: 2012948289

© Springer-Verlag Berlin Heidelberg 2013

This work is subject to copyright. All rights are reserved by the Publisher, whether the whole or part of the material is concerned, specifically the rights of translation, reprinting, reuse of illustrations, recitation, broadcasting, reproduction on microfilms or in any other physical way, and transmission or information storage and retrieval, electronic adaptation, computer software, or by similar or dissimilar methodology now known or hereafter developed. Exempted from this legal reservation are brief excerpts in connection with reviews or scholarly analysis or material supplied specifically for the purpose of being entered and executed on a computer system, for exclusive use by the purchaser of the work. Duplication of this publication or parts thereof is permitted only under the provisions of the Copyright Law of the Publisher's location, in its current version, and permission for use must always be obtained from Springer. Permissions for use may be obtained through RightsLink at the Copyright Clearance Center. Violations are liable to prosecution under the respective Copyright Law.

The use of general descriptive names, registered names, trademarks, service marks, etc. in this publication does not imply, even in the absence of a specific statement, that such names are exempt from the relevant protective laws and regulations and therefore free for general use.

While the advice and information in this book are believed to be true and accurate at the date of publication, neither the authors nor the editors nor the publisher can accept any legal responsibility for any errors or omissions that may be made. The publisher makes no warranty, express or implied, with respect to the material contained herein.

Printed on acid-free paper

Springer is part of Springer Science+Business Media ([www.springer.com](http://www.springer.com))



# Contents

## **Part I Applications of Aluminum, Magnesium and Zinc Alloys, Composites**

<b>Forming Simulation of Automotive Part in Woven Composite Material</b> . . . . .	3
F2012-H01-001	
Q. Q. Chen, C. T. Xu, P. Boisse, A. Saouab and C. H. Park	
<b>A New Equation of Load Curve of Critical Wrinkles Variable Blank Holder Force in the Warm Deep-Drawing of Twin-Roll Cast Mg Sheets</b> . . . . .	11
F2012-H01-002	
Zhimin Liu, Shuming Xing, Peiwei Bao, Lingyun Zhao, Desen Yang, Shuping He, Lijun Chen, Yuangang Deng and Xiangju Yuan	
<b>Single-Composition Hemming Sealant Application for an Aluminium Alloy Hood</b> . . . . .	23
F2012-H01-003	
Yong Fan, Jun Shan, Yu Chen, Xianming He, Jingzhen Wu and Thomas Dave	
<b>Ballistic Resistance of Aluminium Foam by Ogive-Nosed and Conical-Nosed Projectiles Impact</b> . . . . .	33
F2012-H01-005	
Yonggang Bao and Nianmei Zhang	
<b>Re-Engineering Functionality by Optimizing Hybrid Parts Design</b> . . .	41
F2012- H01-006	
Dan Leuciuc and Stefan Tabacu	

## **Part II Advanced Body Manufacturing Technology**

**New Joint Structure Design of Extended Van Body . . . . . 59**

F2012-H02-003

Yingchun Bu

**High Temperature Oxidation Resistance and Mechanical Properties  
of Uncoated Ultrahigh-Strength Steel 22MnB5 . . . . . 67**

F2012-H02-007

Zaiqi Yao, Fangwu Ma, Qiang Liu, Fuquan Zhao, Fangfang Li,  
Jianping Lin, Xiaona Wang and Wei Song

**Systematic Optimization of Concurrent Design of Product  
and Locating Strategy by Datum Flow Chain . . . . . 79**

F2012-H02-008

Shan Jun and Cao Jun

## **Part III Welding, Joining and Fastening**

**Laser Remote Process Technology on Automotive Manufacture . . . . . 89**

F2012-H04-002

Johannes Buehrle, Martin Bea and Ruediger Brockmann

**Characteristic Analysis of the Gas-Powder Stream  
for Laser Cladding . . . . . 99**

F2012-H04-005

Weihong Liu, Binshi Xu, Shiyun Dong and Shixing Yan

## **Part IV Stamping Technology**

**Hot V-Bend Formability of Galvannealed Boron Steel  
for Hot Stamping . . . . . 111**

F2012-H06-004

Masahiro Nakata, Koji Akioka, Masaru Takahashi, Hiroshi Takebayashi,  
Kazuhito Imai, Toru Takayama and Nobusato Kojima

**Research on Holding Pressure and Cooling Process During  
Hot Forming of Ultra-High Strength Steel 22MnB5 . . . . . 123**

F2012-H06-005

Xiaona Wang, Fangwu Ma, Qiang Liu and Fuquan Zhao

**Research on Heavy-Duty Truck Axle Housing Hydroforming . . . . . 133**

F2012-H06-008

Weicheng Zhu, Chenglin Xu, Yucheng Zhang, Zhuang Fu, Shibao Liu,  
Guansheng Wang, Haiping Li, Wencheng Li,  
Hanying Li and Baoyang Song

**Part V Paints, Polymers and Coatings**

**Weight Reduction and Paint-Less of Plastic Parts  
of Automobile by Polypropylene/Elastomer Blends . . . . . 145**

F2012-H07-002

Hiroaki Nagashima and Kayo Kikuchi

**Physical Properties of TPO Airbag Cover Using DFSS  
(Design for Six Sigma) Concept . . . . . 159**

F2012-H07-004

Woojeong Oh, Hyeondon Kim, Yong Chun, Eungsoo Kim,  
Jeongmoo Lee and Kidae Choi

**Building Analysis Methodology of an Integrally Female  
Vacumm Forming and Injection Compression Moulding . . . . . 171**

F2012-H07-005

Jo Hyunkwon, Yang Heeseung, Lee Hyunchul, Jang Ickgeun,  
Park Eunjung and Lee Siwook

**Effect of Artificial Environment Test on Performance  
of Automotive Coating. . . . . 179**

F2012-H07-009

Naxin Wang, Tao Wu, Dazheng Liao, Shu Zhang and Ran Zhao

**Part VI Exterior Body Panels**

**A Prediction Approach for Oil Canning of Sheet Metal  
Forming Based on Strain Gradient . . . . . 191**

F2012-H08-003

Kangkang Yan, Xinyu Wang, Zhongxiao Wang, Yu Zhang and Ping Hu

**Part VII Advanced Process Management**

**A New Connection Solution for Hybrid Vehicle . . . . . 205**  
F2012-H09-002  
Julian Zhou

**Part VIII Other**

**Development of UTS 980 MPa Grade Steel Tube with Excellent  
Formability for Automotive Body Parts . . . . . 213**  
F2012-H10-003  
Masatoshi Aratani, Yasuhide Ishiguro, Yuji Hashimoto,  
Shunsuke Toyoda, Hideto Kimura, Osamu Sonobe and Makio Gunji

**Research on Solutions of Cloud Manufacturing  
in Automotive Industry . . . . . 225**  
F2012-H10-004  
Zhongxiao Jin

**Manufacturing Technology of Passenger Car Rear Axle Drive . . . . . 235**  
F2012-H10-006  
Dongni Li, Zhaodan Yuan, Zhiyong Gao, Guorui Zhao,  
Yongshun Jiang, Hongbiao Gao and Tao Li

**Part I**  
**Applications of Aluminum, Magnesium**  
**and Zinc Alloys, Composites**

# Forming Simulation of Automotive Part in Woven Composite Material

Q. Q. Chen, C. T. Xu, P. Boisse, A. Saouab and C. H. Park

**Abstract** In the present work, a thermo-visco-elastic model for forming simulation of woven thermoplastic composites has been proposed considering the effect of temperature and the influence of strain rate. This model is implanted into a new membrane finite element, which can consider not only the strain in fibre direction but also the shear caused by the relative movement of weft and warp during the deformation of woven composite material. The simulations of bias-test have been performed to validate this method. Finally, the forming process of an automotive part in woven composite material is simulated with this method.

**Keywords** Woven composite · Thermoforming process · Finite element · Simulation

## 1 Introduction

Woven composites are becoming popular in industries due to their excellent advantages. Accordingly, the development of numerical tool for simulating the forming process of this kind of material becomes more and more important [1, 2].

---

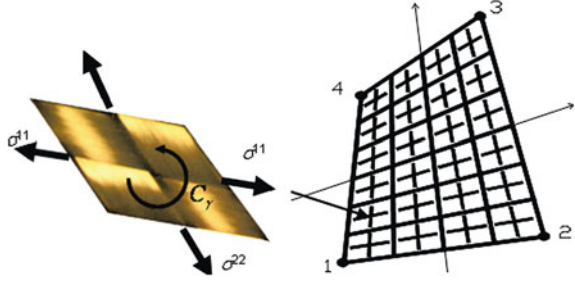
F2012-H01-001

---

Q. Q. Chen (✉) · C. T. Xu  
Changan Auto Global R&D Center, Chongqing 401120, China  
e-mail: sunqiemail@163.com

P. Boisse  
Laboratoire de Mécanique des Contacts et des Structures, UMR 5159, CNRS, INSA Lyon,  
18-20 rue des Sciences F69621 Villeurbanne, France

A. Saouab · C. H. Park  
Laboratoire Ondes et Milieux Complexes, FRE 3102, CNRS, University of Le Havre,  
53 rue Prony F76600 Le Havre, France

**Fig.1** Element in this model

For modelling the performing of woven composite, two different approaches exist: the geometrical approach and the finite element approach. The models based on the geometrical approach are called fishnet algorithms [3, 4]. An alternative to these geometrical methods is the use of finite element approaches, most of which are obtained by homogenizing the mechanical behaviour of the underlying meso-structure and considering the woven as an anisotropic continuum [5, 6]. Other authors have proposed the semi-discrete element methods [7, 8]. All those models have been proved to be efficient and fast in the suitable cases, especially for the simulation of woven composite with thermosetting resin; however we note that the calculation of woven thermoplastic composite is still questionable with those models. Instead, a thermo-visco-elastic model for forming simulation of woven thermoplastic composites based on a new finite element method has been proposed in present work. The element of this model is considered to be consisted by the weft and the warp of woven (Fig. 1).

This model considers the behavior of woven and the behavior of resin respectively, and the strain energy of material is calculated in the field of large strain kinematics. For woven, the strain energy is assumed to be composed by the strain energy caused by tension of yarns and the strain energy caused by the relative movement between the yarns; for resin, a thermo-visco model is used to calculate the strain energy considering the influence of processing temperature and the strain rate.

## 2 Specify Dynamic Equation

We use the explicit dynamic approach in the current work. The dynamic equation in a set of degree of freedom can be written as:

$$\mathbf{M}\ddot{\mathbf{u}} + \mathbf{F}^{\text{int}} = \mathbf{F}^{\text{ext}} \quad (1)$$

where  $\mathbf{u}$  is the degree of freedom,  $\mathbf{M}$  is the mass matrix,  $\mathbf{F}^{\text{int}}$  is the internal force vector and  $\mathbf{F}^{\text{ext}}$  is the applied load vector. The internal force vector can be obtained from the strain energy  $G_{\text{int}}$ :

$$\mathbf{F}^{\text{int}} = \frac{\partial G_{\text{int}}}{\partial u} \quad (2)$$

In the case of woven composite material, the woven is combined tightly with the resin. Hence we can consider that the textile reinforcement has the same displacement as the resin. Then, the strain energy of composite can be obtained by the sum of the strain energy of resin and woven:

$$\int g_l dV = \int g_r dV_r + \int g_f dV_f \quad (3)$$

where  $g_l^e$ ,  $g_r^e$  and  $g_f^e$  are strain energy of composite, resin and woven, respectively. Assuming that  $v_r$  and  $v_f$  are the resin volume fraction and the fiber volume fraction, then Eq. (3) becomes:

$$G_l = v_r G_r + v_f G_f \quad (4)$$

With Eq. (2), we obtain the internal force vector of composite by using the internal force vector of resin  $\mathbf{F}_r^{\text{int}}$  and the internal force vector of woven  $\mathbf{F}_f^{\text{int}}$ :

$$\mathbf{F}_l^{\text{int}} = v_r \mathbf{F}_r^{\text{int}} + v_f \mathbf{F}_f^{\text{int}} \quad (5)$$

## 2.1 The Internal Force of Woven

To obtain the internal force vector of woven, it is considered that the yarn has only the tensile stiffness in the fiber direction and the mechanisms of bending is ignored. Then the internal force vector can be written as:

$$F_f^{\text{int}} = \sum \left( \frac{\partial \varepsilon_{11}^f}{\partial u} \sigma_{11}^f L_1 S_1 + \frac{\partial \varepsilon_{22}^f}{\partial u} \sigma_{22}^f L_2 S_2 + C_\gamma \frac{\partial \gamma}{\partial u} \right) \quad (6)$$

Where  $L_i$  is the fiber's length,  $S_i$  is the section area of yarn,  $\sigma_{ii}^f$  and  $\varepsilon_{ii}^f$  are the tensile stress and strain.  $C_\gamma$  is the shear torque obtained from the experiment,  $\gamma$  is the shear strain. The tensile strain can be obtained by:

$$\varepsilon_{ii}^f = \frac{dX^T E_{ii}^f dX}{2dL_i^2} \quad (7)$$

If the yarns initial direction is:

$$\bar{k}_i = r_{i1} \bar{e}_1 + r_{i2} \bar{e}_2 \quad (8)$$

Then Eq. (7) can be developed as:



$$\begin{aligned} \varepsilon_{ii}^f = & (2 \cdot \bar{e}_1 \cdot \bar{u}_{,1} + \bar{u}_{,1} \cdot \bar{u}_{,1})r_{i1}^2 + (2 \cdot \bar{e}_2 \cdot \bar{u}_{,2} + \bar{u}_{,2} \cdot \bar{u}_{,2})r_{i2}^2 \\ & + 2(\bar{e}_1 \cdot \bar{u}_{,2} + \bar{e}_2 \cdot \bar{u}_{,1} + \bar{u}_{,2} \cdot \bar{u}_{,1})r_{i1}r_{i2} = [B_{ii}^f]\{\bar{u}\} \end{aligned} \quad (9)$$

Where  $[B_{ii}^f]$  can be calculated as:

$$[B_{ii}^f] = \frac{1}{L_i} \langle \bar{X}_{,1} \cdot N_{,1}(\varsigma, \eta)r_{i1}^2 + \bar{X}_{,2} \cdot N_{,2}(\varsigma, \eta)r_{i2}^2 + (\bar{X}_{,1} \cdot N_{,2}(\varsigma, \eta) + \bar{X}_{,2} \cdot N_{,1}(\varsigma, \eta))r_{i1} \rangle \quad (10)$$

$N$  in Eq. (10) is the shape function. With Hook's law, the stress of yarn can be obtained by:

$$\sigma_{ii}^f = E_{ii}^f [B_{ii}^f] \{\bar{u}\} \quad (11)$$

where  $E_{ii}^f$  is the tensile modulus of fiber. The shear strain of woven can be considered as the change of angle between the yarns of woven, which can be specified as:

$$\gamma = [B_\gamma] \{\bar{u}\} \quad (12)$$

Where  $[B_\gamma]$  can be written as:

$$\begin{aligned} [B_\gamma] = & \frac{1}{\|\bar{k}_1\| \|\bar{k}_2\|} (N_{,1}(\varsigma, \eta)r_{\alpha 1} + N_{,2}(\varsigma, \eta)r_{\alpha 2}) \cdot \bar{k}_1 \\ & + \frac{1}{\|\bar{k}_1\| \|\bar{k}_2\|} (N_{,1}(\varsigma, \eta)r_{\beta 1} + N_{,2}(\varsigma, \eta)r_{\beta 2}) \cdot \bar{k}_2 \end{aligned} \quad (13)$$

## 2.2 The Internal Force of Resin

To calculate the internal force vector of resin, we define the related covariant vectors by:

$$\vec{g}_1 = \left\langle \frac{\partial N}{\partial \xi} \right\rangle \{\vec{x}\}, \quad \vec{g}_2 = \left\langle \frac{\partial N}{\partial \eta} \right\rangle \{\vec{x}\} \quad (14)$$

The corresponding contra-variant vectors are obtained by  $\delta$  (Dirac delta function):

$$\vec{g}_\alpha \cdot \vec{g}^\beta = \delta_\alpha^\beta \quad (15)$$

Then the natural membrane Green strain of resin  $\varepsilon_{ij}^r$  can be written as:

$$\varepsilon_{ij}^r = \varepsilon_{ij}^r(\mathbf{U}) = (\vec{g}_i \cdot \mathbf{U}_j + \vec{g}_j \cdot \mathbf{U}_i)/2 \quad (16)$$

where  $i, j = \zeta, \eta$ . Then the stress of resin  $\sigma_{ij}^{viscous}$  can be calculated by:

$$\sigma_{ij}^{viscous} = 2\mu\dot{\epsilon}_{ij} - \frac{2}{3}\mu\dot{\epsilon}_{kk}\delta_{ij} \quad (17)$$

where  $i, j = \zeta, \eta, z$ ,  $\mu$  is the viscosity of resin.  $\epsilon_{ij}^m$  can be expressed as:

$$\epsilon^r = [B^r]\{\bar{u}\} \quad (18)$$

Where  $[B^r]$  can be written as:

$$[B_r^m] = \begin{bmatrix} \frac{dN_1}{d\zeta}g_{11} & \frac{dN_1}{d\zeta}g_{12} & \frac{dN_1}{d\zeta}g_{13} & \dots & \frac{dN_4}{d\zeta}g_{11} & \frac{dN_4}{d\zeta}g_{12} & \frac{dN_4}{d\zeta}g_{13} & 0 \dots 0 \\ \frac{dN_1}{d\eta}g_{21} & \frac{dN_1}{d\eta}g_{22} & \frac{dN_1}{d\eta}g_{23} & \dots & \frac{dN_4}{d\eta}g_{21} & \frac{dN_4}{d\eta}g_{22} & \frac{dN_4}{d\eta}g_{23} & 0 \dots 0 \\ \frac{dN_1}{d\eta}g_{11} + \frac{dN_1}{d\zeta}g_{21} & \frac{dN_1}{d\eta}g_{12} + \frac{dN_1}{d\zeta}g_{22} & \frac{dN_1}{d\eta}g_{13} + \frac{dN_1}{d\zeta}g_{23} & \dots & \frac{dN_4}{d\eta}g_{11} + \frac{dN_4}{d\zeta}g_{21} & \frac{dN_4}{d\eta}g_{12} + \frac{dN_4}{d\zeta}g_{22} & \frac{dN_4}{d\eta}g_{13} + \frac{dN_4}{d\zeta}g_{23} & 0 \dots 0 \end{bmatrix} \quad (19)$$

Then, the internal force of resin can be written as:

$$\mathbf{F}_r^{\text{int}} = \{\bar{u}\}^T [B^r]^T \mathbf{D} [B_r^r] \quad (20)$$

Where  $\mathbf{D}$  is can be written as:

$$\mathbf{D} = \begin{bmatrix} \frac{4\mu}{3} & -\frac{2\mu}{3} & 0 \\ -\frac{2\mu}{3} & \frac{4\mu}{3} & 0 \\ 0 & 0 & 2\mu \end{bmatrix} \quad (21)$$

### 3 Validation and Forming Simulation

In this section, firstly we will show the validation of this model. To validate this model, the experiments of bias extension test were conducted and the numeric results obtained by our model are compared with the experimental result. Secondly, we will show the forming simulation of an automotive part.

#### 3.1 Validation

The experiments of bias extension test are performed with the woven composite material composed of carbon woven fabrics and Polyphenylene Sulfide (PPS) resin. Specimens are cut from laminates in a rectangular form with dimensions of a length three times greater than a width:  $210 \times 70$  mm. In this work, the warp and weft tows in the specimen are orientated initially at  $\pm 45^\circ$  to the direction of the applied tensile load. Tests are conducted at temperatures  $295^\circ\text{C}$  (processing temperature of resin), and at constant actuator displacement rates  $5$  mm/min which

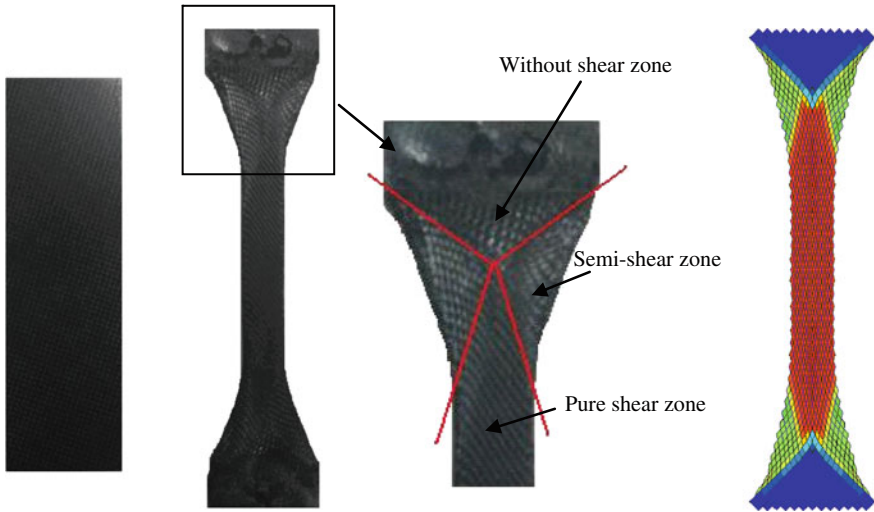


**Fig. 2** Specimen of bias extension test. **a** Specimen before deformation. **b** Specimen after deformation. **c** Simulation result

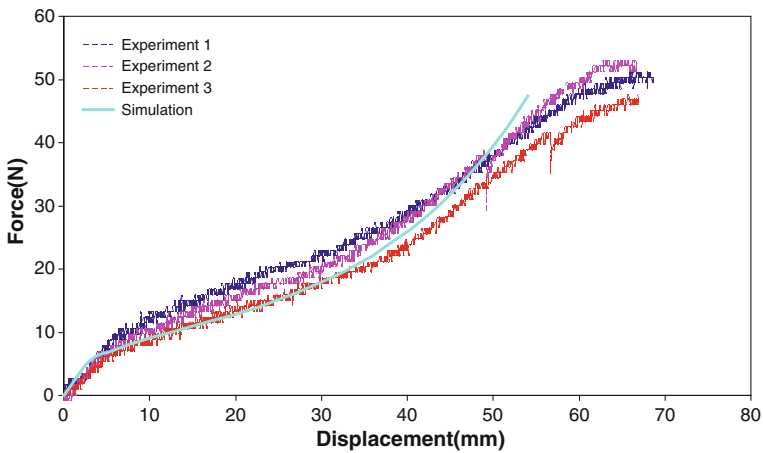


**Fig. 3** Experimental and simulation results of tensile force against displacement at tensile speed 5 mm/min (Carbon/PPS)

consistent with the shear rates in sheet-forming processes. During this test, the central area is sheared whereas four others areas are half-sheared and the clamping areas are not sheared Fig. 2.

The tensile force against displacement is shown in Fig. 3. We note that the simulation result gives good agreement to the experimental results.

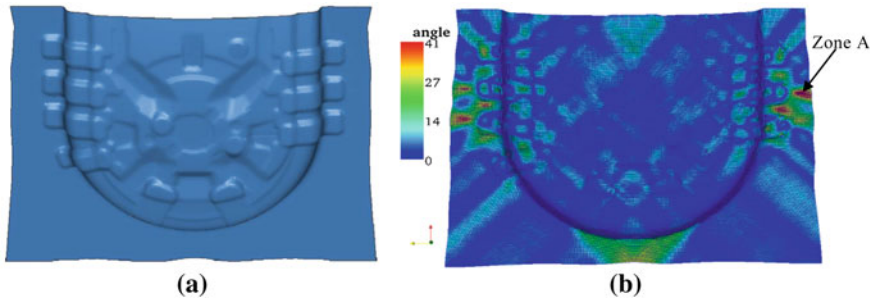


**Fig. 4** Simulation result of boot floor forming. **a** Final form. **b** Change of angle between yarns

### 3.2 Forming Simulation

A woven composite boot floor forming process is simulated by this model. The simulation is performed at temperatures 295 °C, with the punch speed 20 mm/s and the woven's yarn are oriented at  $+45^{\circ}/-45^{\circ}$  compared to the mould. We interest in the final form of the boot floor and the change of angles between the yarns, which are shown in Fig. 4. We note that the maximal change of angle between yarns appears at the zone A, with the value  $41^{\circ}$ .

## 4 Conclusion

In the current work, we proposed a model for the woven composite forming simulation. This thermo-visco-elastic model can describe both the woven's behaviour and the resin's behaviour. Compared with others, this model considers the influence of temperature and the influence of the strain rate to the material's behaviour. This advantage increases the precision of the simulation result. The bias extension tests were performed to validate this model. The good agreement of the comparison between the experimental results and the simulation result shows the efficient of this model. Finally, the simulation results of boot floor forming are shown in this paper, with which we can observe the maximal change of angle between yarns is  $41^{\circ}$ .

## References

1. Boisse P, Borr M, Buet K, Cherouat A (1997) Finite element simulation of textile composite forming including the biaxial fabric behaviour. *Compos B* 28(4):453–464
2. Shuler SF, Advani SG (1996) Transverse squeeze flow of concentrated aligned fibers in viscous fluids. *J Non-Newton Fluid Mech* 65(1):47–74

3. McGuinness GB, ÓBrádaigh CM (1998) Characterization of thermoplastic composite melts in rhombus-shear: the picture-frame experiment. *Compos A* 29(1–2):115–132
4. Milani AS, Nemes JA, Abeyaratne RC, Holzapfel GA (2007) A method for the approximation of non-uniform fiber misalignment in textile composites using picture frame test. *Compos A* 38(6):1493–1501
5. Zener C, Peng X, Cao J (2005) A continuum mechanics-based nonorthogonal constitutive model for woven composite fabrics. *Compos A* 36:859–874
6. Yu WR, Pourboghra F (2002) Non-orthogonal constitutive equation for woven fabric reinforced thermoplastic composites. *Compos A* 33:1095–1105
7. Boisse P, Borr M, Buet K, Cherouat A (1997) Finite element simulations of textile composite forming including the biaxial fabric behaviour. *Compos B* 28:453–464
8. Hamila N, Boisse P (2008) Simulations of textile composite reinforcement draping using a new semi-discrete three node finite element. *Compos B* 39:999–1010

# A New Equation of Load Curve of Critical Wrinkles Variable Blank Holder Force in the Warm Deep-Drawing of Twin-Roll Cast Mg Sheets

Zhimin Liu, Shuming Xing, Peiwei Bao, Lingyun Zhao, Desen Yang, Shuping He, Lijun Chen, Yuangang Deng and Xiangju Yuan

**Abstract** A new equation of load curve of critical wrinkles variable blank holder force (VBHF) during the warm deep-drawing of twin-roll cast Mg sheets was derived, which based on correlative energy conservation theorem. Experiments of limited drawing ratio (LDR) suggested that calculated load curve of minimum wrinkles using the new formulas fit to the tested data very well. The LDR was improved from 1.75 to 1.92 by using a new three segments way of load VBHF applied in the warm deep-drawing, at the forming temperature of 523 K and punch velocity of 45 mm/min. Finally, the VBHF warm deep-drawing process is also simulated by the finite element method, and a new technique of variable punch velocity (VPV) is applied in the simulation. The simulation indicated that the VPV technology can improve the LDR from 1.86 to 2.26 and gain the whole cylinder part, at the forming temperature of 523 K, when the punch velocity varied gradually from 30 to 5 mm/s.

**Keywords** Magnesium alloy · Twin-roll cast · Blank holder force · Warm deep-drawing · Limit drawing ratio

---

F2012-H01-002

---

Z. Liu (✉) · L. Zhao · D. Yang · S. He · L. Chen · Y. Deng · X. Yuan  
Institute of Stamping Design, Department of Process, Changan Automobile Co., Ltd,  
401120 Chongqing, China  
e-mail: 007liuzhimin@163.com

S. Xing · P. Bao  
School of Mechanical, Electronic and Control Engineering, Beijing Jiaotong University,  
100044 Beijing, China  
e-mail: shumixing1962@126.com

## 1 Introduction

As the lightest structural material, magnesium alloys have high potential application in automobile body manufacture [1–3]. However, the poor formability at room temperature make the stamping part of the magnesium alloy sheet must be formed at high temperature [4, 5]. The stamping technique of variable blank holder force (VBHF) was the effective way to improve the formability of sheet, forming precision and surface quality [6, 7]. In recent years, how to implement the VBHF technology has become one of the research emphases in the field of sheet metal forming [8, 9]. Generally, the load curve of minimum wrinkles were usually calculated by the equation of blank holder force (BHF) based on the Fields-Backofen model. Nevertheless, magnesium alloys usually generated easily the conspicuous dynamic recrystallization during high temperature deformation, which resulted in the sharp soften phenomena. So the equation of BHF based on the Fields-Backofen model can not fit to the deep-drawing of magnesium sheets.

Therefore, the aim of the present investigation is to propose a VBHF engineering equation of the curve of minimum wrinkles suit for the magnesium alloy sheet, optimize and control the BHF during the process of deep-drawing. In this research, based on the plastic theory and consulting correlative energy conservation theorem, a new theoretical mathematic models of BHF had been established during the process of deep drawing, which including the factors of the characteristics of magnesium alloy material at the high temperature and the structure of stamping dies. Experiments of limited drawing ratio (LDR) at warm temperature are performed to validate the new equation of variable BHF. Finally, the VBHF technology is discussed by the numerical approach.

## 2 Equation Derivation

According to the correlative energy conversation theorem, the released energy of single ripple  $U_\theta$  can be described as follows [10, 11]:

$$U_\theta = U_w + U_Q \quad (1)$$

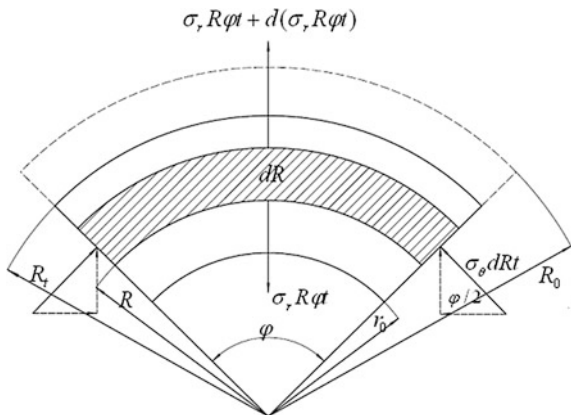
where  $U_w$  is the required bending work, and  $U_Q$  is the wasting work of the BHF.

The external force act on the differential bulk of the sheet during arbitrary stage of deep-drawing is illustrated in Fig. 1. Where the radius of flange  $R_0$  change to  $R_r$ ,  $\varphi$  is the central angle of arbitrary arc,  $dR$  is the width of fan-shaped bulk,  $t$  is the thickness,  $\sigma_\theta$  is tangent stress,  $\sigma_r$  is radial stress.

When the external force acted on the differential bulk is on balance, the radial force can be described as follows:

$$\sigma_r R \varphi t + d(\sigma_r R \varphi t) - \sigma_r R \varphi t + 2\sigma_\theta dR t \sin \frac{\varphi}{2} = 0 \quad (2)$$

**Fig. 1** The differential bulk of the sheet



When the angle  $\phi$  is wee, variable the thickness can be ignored, i.e.  $dt = 0$ , Eq. (2) can be written as:

$$d\sigma_r = -(\sigma_r + \sigma_\theta) \frac{dR}{R} \tag{3}$$

The surface ripple of the flange can be shown in Fig. 2, and the mathematical model of the wrinkle can be described as:

$$y = \frac{y_0}{2} \left( 1 - \cos 2\pi \frac{\phi}{\phi_0} \right) \left( \frac{R - r}{R_t - r} \right)^{1/2} \tag{4}$$

where  $R_t$  is the external radius of flange,  $r$  is the internal radius of flange,  $R$  is the radius of arbitrary point in the flange,  $\phi_0$  is the central angle,  $\phi$  is the central angle of arbitrary arc,  $y_0$  is the maximum flexibility of single ripple,  $y$  is the flexibility of arbitrary point in the flange.

As our former research about characteristics of twin-roll cast  $Mg$  sheets [12, 13], the dislocation glide is dominant deformation mechanisms at high temperature and lower strain rate, i.e.  $Z < Z_0$ . So the equation of stress–strain curve can be written as [13]:

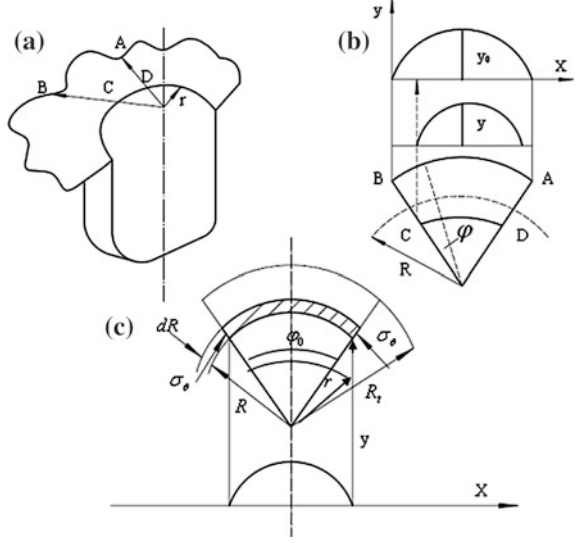
$$\begin{aligned} \sigma_i &= K_1 \cdot [\sigma_{ss}^*{}^2 + (\sigma_0^2 - \sigma_{ss}^*{}^2) \cdot \exp(-\Omega \varepsilon_i)]^{0.5} + K_2 \cdot \exp(\varepsilon_i / \varepsilon_0) \\ &= K_1 \cdot [A + B \exp(-\Omega \varepsilon_i)]^{0.5} + K_2 \cdot \exp(\varepsilon_i / \varepsilon_0) \end{aligned} \tag{5}$$

where  $\Omega$  is a constant reflecting dislocation annihilation and rearrangement,  $\sigma_0$  is the initial stress, and  $\sigma_{ss}^*$  is the saturation stress.

Since the flange is in the stage of plane stress, according to the Eqs. (3) and (5), the radial stress  $\sigma_r$  can be derived as:



**Fig. 2** The surface ripple of the flange



$$\sigma_r = -K_1 \int \left\{ A + B \exp \left[ -\frac{\Omega R_t}{R} \left( 1 - \frac{R_t}{R_0} \right) \right] \right\}^{0.5} \cdot \frac{dR}{R} - K_2 \int \exp \left[ \frac{R_t}{\varepsilon_0 R} \left( 1 - \frac{R_t}{R_0} \right) \right] \cdot \frac{dR}{R} \quad (6)$$

Similarly, the tangent stress  $\sigma_\theta$  can be given as follows:

$$\sigma_\theta = K_1 \left[ A + B \exp \left( -\frac{M}{R} \right) \right]^{0.5} + K_2 \exp \left( \frac{N}{R} \right) + K_1 \int \left[ A + B \exp \left( -\frac{M}{R} \right) \right]^{0.5} \cdot \frac{dR}{R} + K_2 \int \exp \left( \frac{N}{R} \right) \cdot \frac{dR}{R} = \left\{ K_1 \left[ A + B \exp \left( -\frac{M}{R} \right) \right]^{0.5} + K_1 \sigma_d \right\} + \left\{ K_2 \exp \left( \frac{N}{R} \right) + K_2 \sigma_{sem} \right\} \quad (7)$$

where assume  $M = \Omega R_t \left( 1 - \frac{R_t}{R_0} \right)$ ,  $N = \frac{R_t}{\varepsilon_0} \left( 1 - \frac{R_t}{R_0} \right)$ ,  $\sigma_{sem} = \int \exp \left( \frac{N}{R} \right) \cdot \frac{dR}{R}$ ,

$\sigma_d = \int \left[ A + B \exp \left( -\frac{M}{R} \right) \right]^{0.5} \cdot \frac{dR}{R}$ .

Based on the mathematical of the wrinkle [10], according to Eq. (7) the energy  $U_\theta$  can be expressed as:

$$U_\theta = \int_r^R \sigma_\theta S' t dR = \frac{1}{2} \int_r^{R_t} \int_0^{\phi_0} \frac{\pi^2 y_0^2}{\phi_0^2} \frac{1}{R} \frac{R-r}{R_t-r} \sin^2 \frac{2\pi\phi}{\phi_0} \cdot \left\{ K_1 \left[ A + B \exp \left( -\frac{M}{R} \right) \right]^{0.5} + K_1 \sigma_d + K_2 \exp \left( \frac{N}{R} \right) + K_2 \sigma_{sem} \right\} t d\phi dR \quad (8)$$

Likewise, in stage of the plane stress the required bending work  $U_w$  can be derived as:

$$\begin{aligned}
 U_w &= \int_r^{R_t} \int_0^l \frac{1}{2} D \left( \frac{d^2 y}{dx^2} \right)^2 dldx = \int_r^{R_t} \int_0^l \frac{1}{2} \frac{d\sigma_i}{d\varepsilon_0} \left( \frac{d^2 y}{dx^2} \right)^2 dldx \\
 &= \frac{\pi^4 y_0^2 t^3}{6\phi_0^4 (R_t - r)} \int_r^{R_t} \int_0^{\phi_0} \frac{R - r}{R^3} \cos^2 \left( \frac{2\pi\phi}{\phi_0} \right) \cdot \left[ -\frac{B\Omega K_1 \exp\left(-\frac{M}{R}\right)}{2\sqrt{A + B \exp\left(-\frac{M}{R}\right)}} + \frac{K_2}{\varepsilon_0} \exp\left(\frac{N}{R}\right) \right] d\phi dR
 \end{aligned} \quad (9)$$

The blank holder force  $Q$  can be given by [10]:

$$Q = \frac{2\pi}{y_0 \phi_0} (U_\theta - U_w) = \frac{2\pi}{y_0} \left( \frac{U_\theta}{\phi_0} - \frac{U_w}{\phi_0} \right) \quad (10)$$

where  $\phi_0$  is the central angle of arbitrary ripple,  $y_0$  is the maximum flexibility at the location of  $R = R_t$  on the flange.

Substituting Eqs. (8)–(9) into Eq. (10), and the differential coefficient equation of blank holder force  $Q$  can be written as:

$$\frac{\partial Q}{\partial \phi_0} = \frac{\pi^2 y_0^2 t^3 V}{4(R_t - r)} \cdot \frac{1}{\phi_0^2} + \left[ \frac{\pi^4 y_0^2 t^3}{24(R_t - r)} \left( \frac{2K_2}{\varepsilon_0} D_{sem} - B\Omega K_1 D_d \right) \right] \cdot \frac{1}{\phi_0^4} \quad (11)$$

where

$$\begin{aligned}
 V &\approx 2K_1 \sqrt{A}(r + M) \left[ \exp\left(-\frac{M}{R_t}\right) - \exp\left(-\frac{M}{r}\right) \right] + 2K_2 (R_t - r) \\
 &\quad - \frac{3}{4} K_2 N^2 \left( \frac{1}{R_t} - \frac{1}{r} \right) - \left( \frac{1}{R_t^2} - \frac{1}{r^2} \right) \left( \frac{K_2 N^3}{12} + \frac{K_2 r N^2}{8} \right) - \left( \frac{1}{R_t^3} - \frac{1}{r^3} \right) \left( \frac{K_2 r N^3}{27} \right) \\
 &\quad + K_2 \ln\left(\frac{r}{R_t}\right) \cdot (r \ln N - 2N - r) + \frac{2K_1 \sqrt{A}}{M} \left[ R_t \exp\left(-\frac{M}{R_t}\right) - r \exp\left(-\frac{M}{r}\right) \right] \\
 &\quad + \frac{2rK_1 \sqrt{A}}{M} \cdot \left[ R_t \exp\left(-\frac{M}{R_t}\right) - r \exp\left(-\frac{M}{r}\right) + \frac{R_t}{M} \exp\left(-\frac{M}{R_t}\right) - \frac{r}{M} \exp\left(-\frac{M}{r}\right) \right] \\
 &\quad + K_2 \left[ R_t \ln\left(\frac{N}{R_t}\right) - r \ln\left(\frac{N}{r}\right) \right] + \frac{K_2 r}{2} (\ln^2 R_t - \ln^2 r) \\
 D_d &\approx \frac{2\sqrt{A + B \exp\left(-\frac{M}{R_t}\right)}}{MB} \cdot \left( \frac{r}{R_t} - \frac{2r}{M} - 1 \right) - \frac{2\sqrt{A + B \exp\left(-\frac{M}{r}\right)}}{MB} \cdot \frac{2r}{M}
 \end{aligned}$$

$$D_{sem} = \frac{r}{N} \left[ \frac{1}{R_t} \exp\left(\frac{N}{R_t}\right) - \frac{1}{r} \exp\left(\frac{N}{r}\right) \right] - \frac{1}{N} \left[ \exp\left(\frac{N}{R_t}\right) - \exp\left(\frac{N}{r}\right) \right],$$

Then assumed the Eq. (11) equal to zero, i.e.  $\frac{\partial Q}{\partial \phi_0} = 0$ , the central angle  $\phi_0$  can be expressed in the form:

$$\phi_0 = \sqrt{\frac{\frac{\pi^4 y_0^2 t^3}{12(R_t-r)} \left( \frac{2K_2}{\varepsilon_0} D_{sem} - B\Omega K_1 D_d \right)}{\frac{\pi^2 y_0^2 t}{4(R_t-r)} V}} = \pi t \sqrt{\frac{1}{3V} \left( \frac{2K_2}{\varepsilon_0} D_{sem} - B\Omega K_1 D_d \right)} \quad (12)$$

Substituting Eq. (12) into (10), the variable BHF engineering equation of the curve of minimum ripple can be described as:

$$Q = \frac{3\pi}{4} \cdot \frac{y_0}{t(R_t-r)} \cdot \frac{\varepsilon_0 V^2}{2K_2 D_{sem} - B\Omega K_1 \varepsilon_0 D_d} \quad (13)$$

The Eq. (13) can be applied only on the given condition where the Zener-Hollomon parameter ( $Z$ ) is less than the critical value  $Z_0$  ( $Z < 1.54E11$ ), and the dominant mechanism of TRC-Mg is slip.

When the Zener-Hollomon parameter ( $Z$ ) is higher than the critical value  $Z_0$  ( $Z > 1.54E11$ ), consulting mechanism of the twinning, the equation of stress-strain curve can be described as follows [13]:

$$\sigma_i = K_1 X_T \sigma_{twin} + (1 - X_T) K_1 \cdot [A + B \exp(-\Omega \varepsilon_i)]^{0.5} + K_2 \cdot \exp(\varepsilon_i / \varepsilon_0) \quad (14)$$

where  $\sigma_{twin}$  is stress of twinning,  $X_T$  is the fraction of grains that have twinned,  $\exp(\varepsilon_i / \varepsilon_0)$  is a breakage ratio function.

Since three types of mechanisms of the twinning, dislocation slip and semi-solid slip exist in the TRC magnesium sheet, the released energy of tangent stress  $U_\theta$  can be written as:

$$U_\theta = [U_\theta]_{twin} + [U_\theta]_{slip} + [U_\theta]_{sem} \quad (15)$$

Similarly, in term of above derivation based on the mechanism of dislocation slip, the energy of tangent stress  $[U_\theta]_{twin}$  can be given by:

$$\begin{aligned} [U_\theta]_{twin} &= \frac{r X_T b K_1 \pi^2 y_0^2 t \left(1 - \frac{R_t}{R_0}\right)^n}{4n(R_t-r)\phi_0} \left\{ \frac{1}{n} \left[ \left(\frac{R_t}{r}\right)^n - 1 \right] - \ln\left(\frac{R_t}{r}\right) \right\} + \\ &\frac{a K_1 X_T \pi^2 y_0^2 t}{4n(R_t-r)\phi_0} \left[ (R_t-r) + R_t \ln R_t - r \ln r - (R_t-r) - \frac{r}{2} (\ln^2 R_t - \ln^2 r) \right] = K_\theta \cdot \frac{1}{\phi_0} \end{aligned} \quad (16)$$

The summation energy of  $[U_\theta]_{slip}$  and  $[U_\theta]_{sem}$  can be described as:

$$[U_\theta]_{slip} + [U_\theta]_{sem} = \frac{\pi^2 y_0^2 t V'}{4(R_t-r)\phi_0} \quad (17)$$

where

$$\begin{aligned}
V' \approx & 2K_1(1 - X_T)\sqrt{A}(r + M) \left[ \exp\left(-\frac{M}{R_t}\right) - \exp\left(-\frac{M}{r}\right) \right] + 2K_2(R_t - r) \\
& - \frac{3}{4}K_2N^2 \left( \frac{1}{R_t} - \frac{1}{r} \right) - \left( \frac{1}{R_t^2} - \frac{1}{r^2} \right) \left( \frac{K_2N^3}{12} + \frac{K_2rN^2}{8} \right) - \left( \frac{1}{R_t^3} - \frac{1}{r^3} \right) \left( \frac{K_2rN^3}{27} \right) \\
& + K_2 \ln\left(\frac{r}{R_t}\right) \cdot (r \ln N - 2N - r) \\
& + \frac{2K_1(1 - X_T)\sqrt{A}}{M} \left[ R_t \exp\left(-\frac{M}{R_t}\right) - r \exp\left(-\frac{M}{r}\right) \right] + \frac{2rK_1(1 - X_T)\sqrt{A}}{M} \\
& \cdot \left[ R_t \exp\left(-\frac{M}{R_t}\right) - r \exp\left(-\frac{M}{r}\right) + \frac{R_t}{M} \exp\left(-\frac{M}{R_t}\right) - \frac{r}{M} \exp\left(-\frac{M}{r}\right) \right] \\
& + K_2 \left[ R_t \ln\left(\frac{N}{R_t}\right) - r \ln\left(\frac{N}{r}\right) \right] + \frac{K_2r}{2} (\ln^2 R_t - \ln^2 r)
\end{aligned}$$

In the same way, the required bending work  $[U_w]_{nwin}$  can be written as:

$$\begin{aligned}
[U_w]_{nwin} &= \frac{X_T b K_1 n t^3 \pi^4 y_0^2 \left(1 - \frac{R_t}{R_0}\right)^{n-1}}{12 R_t (R_t - r) \phi_0^3} \left\{ \frac{1}{n} \left[ \left(\frac{R_t}{r}\right)^n - 1 \right] - \frac{r}{(1+n)R_t} \left[ \left(\frac{R_t}{r}\right)^{n+1} - 1 \right] \right\} \\
&= K_{w1} \cdot \frac{1}{\phi_0^3}
\end{aligned} \tag{18}$$

The summation bending work of  $[U_w]_{slip}$  and  $[U_w]_{sem}$  can be written as:

$$\begin{aligned}
[U_w]_{slip} + [U_w]_{sem} &= \left\{ \frac{\pi^4 y_0^2 t^3}{24(R_t - r)} \left[ \frac{2K_2}{\varepsilon_0} D_{sem} - (1 - X_T) B \Omega K_1 D_d \right] \right\} \cdot \frac{1}{\phi_0^3} \\
&= K_{w2} \cdot \frac{1}{\phi_0^3}
\end{aligned} \tag{19}$$

So the variable BHF engineering equation of the curve of minimum wrinkles can be expressed as:

$$Q = \frac{\pi}{y_0} \left[ \frac{48k_\theta^2 (R_t - r)^2 + 24k_\theta (R_t - r) \pi^2 y_0^2 t V' + 3(\pi^2 y_0^2 t V')^2}{32(k_{w1} + k_{w2})(R_t - r)^2} \right] \tag{20}$$

In general, the variable BHF engineering equation of the curve of minimum wrinkles based on Fields-Backofen is given as [10, 11]:

$$Q = 1.5K \frac{y_0}{t} \cdot \frac{\pi r^2}{4} \cdot \frac{1}{n^3} (1 - \rho)^{1+n} \cdot \frac{\frac{\rho}{m} \left\{ \frac{1}{n} \left[ \left(\frac{\rho}{m}\right)^n - 1 \right] - \ln \frac{\rho}{m} \right\}^2}{\left(\frac{\rho}{m} - 1\right) \left\{ \frac{1}{n} \left[ \left(\frac{\rho}{m}\right)^n - 1 \right] - \frac{1}{1+n} \left[ \left(\frac{\rho}{m}\right)^n - \frac{\rho}{m} \right] \right\}} \tag{21}$$

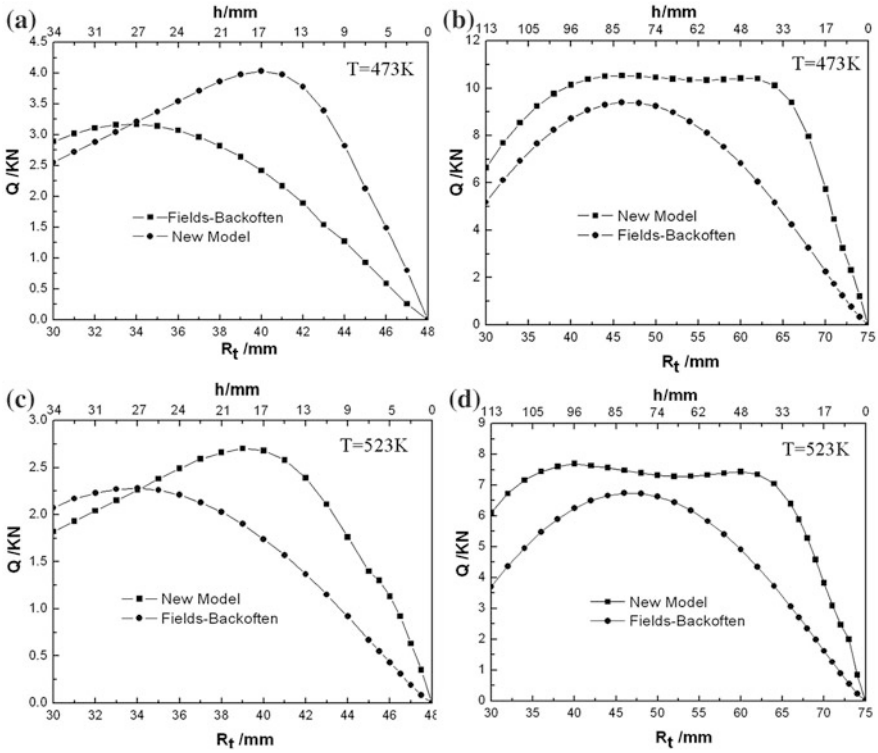


Fig. 3 The curves of minimum wrinkles BHF calculated by using two models

where  $K$  is the strength-hardening coefficient,  $n$  is the strain-hardening exponent,  $t$  is the sheet thickness,  $\rho = R_t/R_0$  denotes the deep drawing phase and  $m = r/R_0$  expresses the deep drawing ratio.

### 3 Application of the New Equation

The load curves of the minimum wrinkles VBHF of two magnesium sheets during the warm deep-drawing test were calculated, which based on the new model and Fields-Backofen respectively. Where the specimens are 3.3 mm thick, and the diameters are 96 and 150 mm respectively. The description of load curves of critical wrinkle in Fig. 3 illustrates that the peak of VBHF of the 96 mm diameter specimen calculated by using the new equation appears on the metaphase, but the peak of VBHF gained by using the Fields-Backofen occurs on the initial stage, when the temperature is less than 523 K. It can be clearly seen that the peak of VBHF of the 150 mm diameter gained by the new model have a platform, which corresponds to the influence between dynamic recrystallization and strain hardening during the warm deep-drawing.

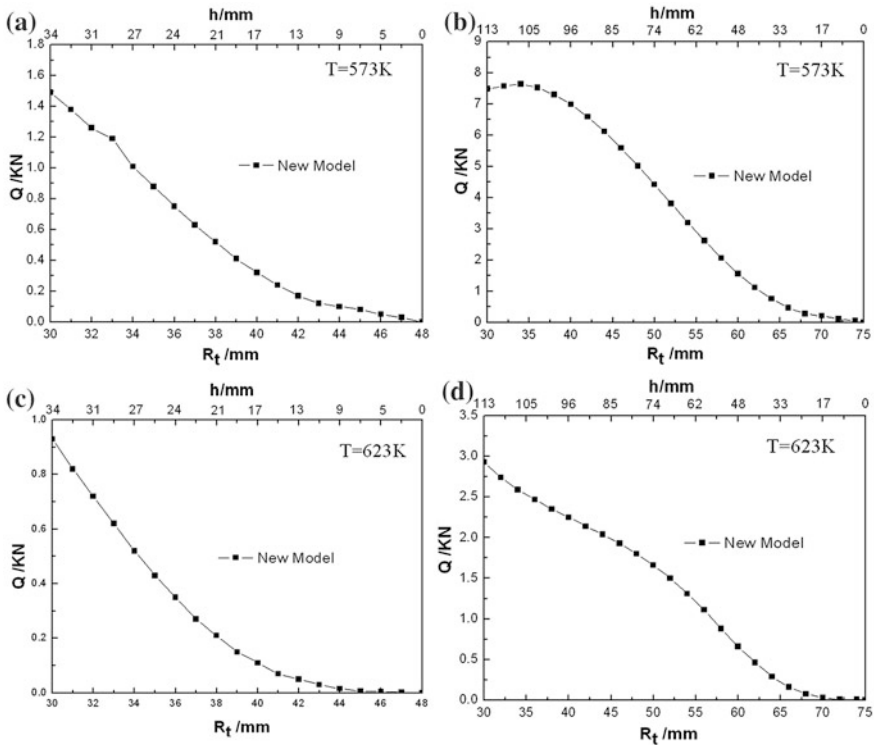


Fig. 4 The curves of minimum wrinkles BHF calculated by the new model

When the temperature is higher than 573 K, the load curves of the VBHF based on the new model were shown in Fig. 4, it can be seen that severe soften phenomena occur because of dynamic recrystallization. In addition, for the prominent dynamic recrystallization, the strength-hardening coefficient  $K$  and the strain-hardening exponent  $n$  can not be measured through hot tensile testing, which means the Fields-Backofen is not fit to the hot-stamping of magnesium alloy sheets.

In contrast, the peak values of VBHF were calculated and tested, as shown in Table 1. The different peak values of specimens during the warm deep-drawing testing reveal that the peak values calculated by using the new model fit to the experiment data very well, and the new model was more accurate than the Fields-Backofen model.

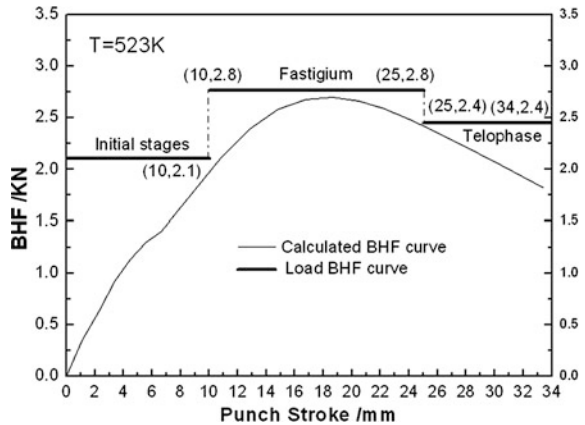
## 4 Numerical Studies of VBHF and Experiments

According to the theorem of VBHF in deep drawing, the designed load curve of critical wrinkles variable blank holder force should be similar to the calculated load curve. However, it is difficult to assure the blank holder force simultaneously

**Table 1** Peak value of VBHF calculated by two models

Types of model	Diameter of sheet R/mm	Peak value	Peak value	Peak value	Peak value
		Q(T = 473 K)/KN	Q(T = 523 K)/KN	Q(T = 573 K)/KN	Q(T = 623 K)/KN
Fields-backofen model	48	3.07	2.28	—	—
	75	9.4	6.74	—	—
The new model	48	4.03	2.7	1.49	0.93
	75	10.39	7.7	7.3	2.93
Testing data	48	3.96	2.97	1.98	—
	75	9.9	7.92	6.93	—

**Fig. 5** Punch load and calculated BHF curve by new model



change with the punch motion for the common equipment. So the three segments way of load VBHF was proposed during the warm deep-drawing according to the practical working-condition, as shown in Fig. 5. It is evident that the loading BHF have been optimize three stages, which are initial stages, fastigium and telophase. Comparison with the warm deep drawing experiments aided by the three segments way of VBHF and constant BHF, the results indicated that the limit drawing ratio (LDR) was improved from 1.75 to 1.92, when the forming temperature is 523 K and punch velocity is 45 mm/min.

The results of numerical simulation FLD revealed that LDR of constant BHF is 1.73, as shown in the Fig. 6a, and the LDR of the three segments way of VBHF can reach 1.86, as shown in Fig. 6b. Where the forming temperature is 532 K and the punch velocity is 30 mm/s.

Generally, magnesium alloys formability increase with decrease strain-rates. However, the lower strain-rates affect the efficiency of manufacture. So according to the practical working-efficiency, a new deep-drawing process through the approach of variable punch velocity (VPV) applied in the numerical simulation with using three segment way of VBHF, as described in Fig. 7. Where the forming temperature is 532 K and the punch velocity varies from 5 to 30 mm/s. It can be seen obviously that the LDR has been increased from 1.86 to 2.26, and gained the whole cylinder part. The new technique of VBHF combined VPV can be named

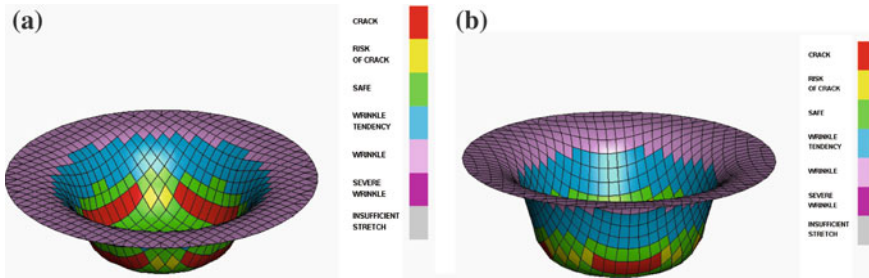


Fig. 6 Comparison of LDR with constant BHF and VBHF. a BHF, b VBHF

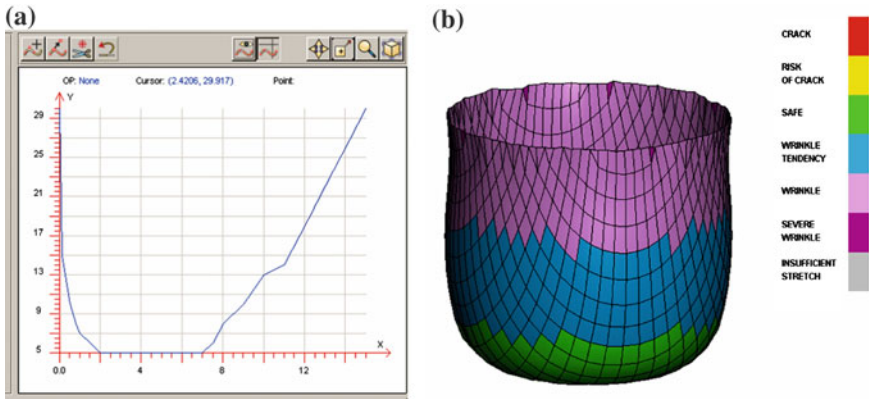


Fig. 7 The FLD of three segments way of VBHF combined VPV. a VPV. b FLD

servo-flexible stamping, which utilized to implement the VBHF simultaneously with VPV and stepwise motion.

Recently, several press builders developed metal forming presses that utilize the mechanical servo-drive technology. The mechanical servo-drive press offers the flexibility of a hydraulic press (infinite slide speed and position control, availability of press force at any slide position) with the speed accuracy and reliability of a mechanical press [14]. The new servo-drive presses can satisfy the requirement of implement VBHF simultaneously with VPV and stepwise motion of the servo-flexible stamping. So it can be predicted that the new servo-flexible stamping will become a new potential stamping process in the future.

### 5 Conclusions

Based on the plastic theory and correlative energy conservation theorem, a new theoretical mathematic model of VBHF had been established during the warm deep-drawing of TRC magnesium sheet. The results of experiments suggested that



the calculated load curve of minimum wrinkles VBHF using the new equation fit to the tested data very well. Furthermore, the warm deep-drawing results revealed that the LDR of cylinder parts was improved from 1.75 to 1.92 by the three segments way of loading VBHF, at the forming temperature of 523 K and punch velocity of 45 mm/min.

The numerical simulations indicated that the LDR can be improved observably from 1.86 to 2.26, and gained the whole cylinder part, by the new servo-flexible stamping technology that the three segments way of loading VBHF combined VPV.

## References

1. Stanford N, Barnett M (2008) Effect of composition on the texture and deformation behaviour of wrought Mg alloys. *Scripta Mater* 58(3):179–182
2. Jiang J, Godfrey A, Liu W et al (2008) Identification and analysis of twinning variants during compression of a Mg-Al-Zn alloy. *Scripta Mater* 58:122–125
3. Wu L, Jain A, Brown DW et al (2008) Twinning-detwinning behavior during the strain-controlled low-cycle fatigue testing of a wrought magnesium alloy, ZK60A. *Acta Mater* 56(4):688–695
4. Chen FK, Huang TB, Chang CK (2003) Deep drawing of square cups with magnesium alloy AZ31 sheets. *Int J Mach Tools Manuf* 43(15):1553–1559
5. Zhang SH, Zhang K, Xu YC et al (2007) Deep-drawing of magnesium alloy sheets at warm temperatures. *J Mater Process Technol* 185(1–3):147–151
6. Doege E, Sommer N (1987) Blank-holder pressure and blank-holder layout in deep drawing of thin sheet metal. *Adv Technol Plast* 11:1305–1314
7. Yoshihara S, Manabe K, Nishimura H (2005) Effect of blank holder force control in deep-drawing process of magnesium alloy sheet. *J Mater Process Technol* 170(3):579–585
8. Doege E, Elend LE (2001) Design and application of pliable blank holder systems for the optimization of process conditions in sheet metal forming. *J Mater Process Technol* 111:182–187
9. Sheng ZQ, Jirathearanat S, Altan T (2004) Adaptive FEM simulation for prediction of variable blank holder force in conical cup drawing. *Int J Mach Tools Manuf* 44:487–494
10. Liang B, Hu S (1987) The plasticity theory of sheet forming. Mechanics Industry Press, Beijing (in Chinese)
11. Chang Qun-Feng, Li Da-Yong, Peng Ying-Hong (2007) Experimental and numerical study of warm deep drawing of AZ31 magnesium alloy sheet. *Int J Mach Tools Manuf* 47:436–443
12. Liu Z, Xing S, Bao P-W (2010) Characteristics of hot tensile deformation and microstructure evolution of twin-roll cast AZ31B magnesium alloys. *Trans Nonferr Met Soc China* 20:776–782
13. Liu Zhimin, Xingy Shuming, Bao Peiwei (2010) A new analytical model for the flow stress of twin-roll casting magnesium sheet at elevated temperatures. *J Mater Sci Technol* 26(5):461–466
14. Osakada K, Mori K, Altan T (2011) Mechanical servo press technology for metal forming. *CIRP Ann-Manuf Technol* 60:651–672

# Single-Composition Hemming Sealant Application for an Aluminium Alloy Hood

Yong Fan, Jun Shan, Yu Chen, Xianming He, Jingzhen Wu  
and Thomas Dave

**Abstract** Normal process is to use a two-composition hemming sealant for an aluminum alloy hood. The hemmed hood assembly then needs to be cured using high-frequency curing equipment. The curing process can help to solve quality problems such as, hood distortion and mismatch between inner/outer parts during the manufacturing process. The equipment required for the application of two-composition sealant and high-frequency curing is very complex and expensive. The sealant application process is also very difficult. In order to reduce cost, investment and area footprint requirement, we needed to develop a single-composition hemming sealant for a new and future product. After investigations and trials using a two-composition hem sealer we were able to establish the technical and performance requirements of a two-composition sealant. Using the same process we established the performance of a single-composition sealant by undertaking trials offline with the same parts. From these results and working closely with a sealant manufacturer, a project was undertaken to develop a single-composition hemming sealant for use on aluminium alloy hoods that meets the technical and performance requirements of the two composition material. For overcoming any possible mismatch between the inner/outer parts of the product, we requested the new sealant included glass beading. After finishing further trials using the new sealant material, we commenced testing on aluminium hoods for our new product. The function tests included bench test, GTR test and on road test. The test also included quality checks for hood surface distortion, panel mismatch between inner and outer panels and part dimension. The aluminum alloy hood is hemmed by using a press machine and hem die, this type of hemming process can

---

F2012-H01-003

---

Y. Fan (✉) · J. Shan · Y. Chen · X. He · J. Wu · T. Dave  
SAIC Motor Passenger Vehicle Co, Shanghai, China  
e-mail: wujingzhen@saicmotor.com

assure that the glass beading can be forced into the surface of aluminium alloy. The result of our experiments indicates that the single-composition sealant can meet the requirements of vehicle function and manufacturing process. We decided to commence using the new single-composition sealant for all aluminium alloy parts on our new and future products. This negated the need the expensive curing equipment and process. This technology has been in use on our product for more than 6 months. We have gained several benefits and experience from using this new technology. (1) Reduced equipment investment, circa 3512900 RMB. (2) Cost per car reduction of circa 10 RMB per vehicle. (3) Equipment failure ratio and running cost have been reduced considerably. (4) Environmental benefits. The curing process emits fumes into the atmosphere. Finally we have a quality product at a reduced cost, this is very important due to the high level of competition in our business.

**Keywords** Hood · Hem · Sealant · Aluminium alloy

## 1 Introduce of Background

SAIC and PATAC together developed a new car basing the GM glabal E platform. This new car is called BP31 in SAIC. In the process of development, we analysed in detail the sealants of carbody. Some sealants are designed by PATAC, some sealants are changed by SAIC. It is very important that we changed the hemming sealant for the aluminium hood. We developed the single-composition sealant to replace the two-composition sealant that is confirmed by engineering and design. The shortcomings of two-composition are badness process, big investment etc. we associate with sealant supplier to developed a single-composition for our new car. We gained successes in that point.

## 2 The Development of the Hemming Sealant

According to the technical and performance requirements of a two-composition sealant, we established the performance of a single-composition sealant by undertaking trials offline. From these results a sealant supplier was requested to develop a single-composition hemming sealant for use on aluminum alloy hoods that meets the technical and performance requirements. The sealant supplier has developed the single-composition in a short time. We arranged some tests to confirm the new product.

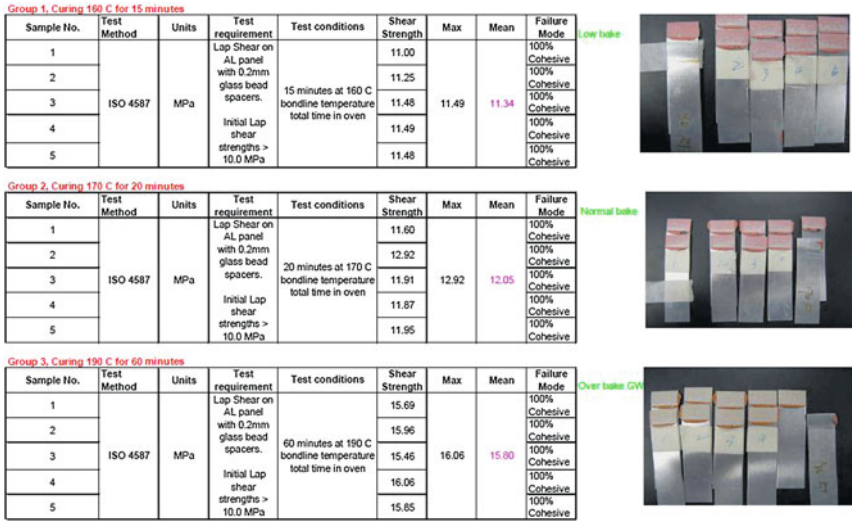


Fig. 1 The results of lap shear test

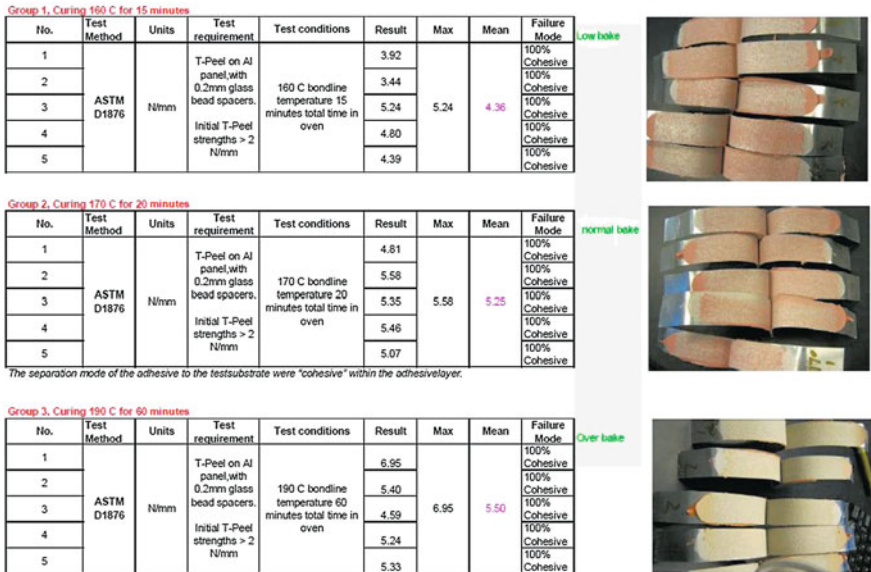


Fig. 2 The results of T-peel test

**Fig. 3** The results of bead structure test



### ***2.1 Lap Shear Test***

Test condition, Oven setting is 160°, 170° and 190° respectively. Timing started when the samples had been in the oven after 2 min for temperature ramp up. Conditioning after curing 23° and 50 % relative humidity for 24 h. Testing speed: Lap shear 10 mm/min. The results were shown in Fig. 1.

### ***2.2 T-peel Test***

Test condition, Oven setting is 160°, 170° and 190° respectively. Start timing when samples in oven after 2 min for temperature ramping up. Conditioning after curing at 23° and 50 % relative humidity for 24 h. Testing speed: T-peel speed 10 mm/min. The results were as shown in Fig. 2.

### ***2.3 Bead Structure Test***

The bead structure was tested in three states: low bake, normal bake, over bake.

**Table 1** The results of test summaries in the condition of low bake

Group 1, low bake. Curing 160 °C for 15 min					
Items	Testings	Specification	Units	Mean result	Conclusion
1	Lap shear (Initial)	>10.0	MPa	11.34	Pass
2	T-peel (Initial)	>2	N/mm	4.36	Pass
3	Bead structure	Be evaluate by SAIC	N/A	Pass	Pass
4	3 mm Bond gap versus Lap shear strength testing	Be evaluate by SAIC	MPa	6.02	Pass
5	3 mm Bond gap versus T-peel Shear Strength testing	Be evaluate by SAIC	N/mm	3.91	Pass
6	4 mm Bond gap versus Lap shear strength testing	Be evaluate by SAIC	MPa	5.07	Pass
7	4 mm Bond gap versus T-peel strength testing	Be evaluate by SAIC	N/mm	4.58	Pass
8	Lap shear (Cold test)	>7.5	MPa	15.50	Pass
9	T-Peel (cold test)	>1.5	N/mm	6.95	Pass
10	Lap shear (Hot test, Test at 80 °C)	>7.5	MPa	15.49	Pass
11	Lap shear (Hot test, after 24 h recovery)	>7.5	MPa	15.54	Pass
12	Lap shear (Humidity test)	>7.5	MPa	12.78	Pass
13	Lap shear (Salt spray tests, immediate)	>7.5	MPa	12.47	Pass
14	Lap shear (Salt spray test, after 24 h recovery)	>7.5	MPa	12.78	Pass
15	Lap shear (5 Rd VDA test)	>7.5	MPa	13.83	Pass
16	Lap shear (7 Rd VDA test)	>7.5	MPa	12.91	Pass
17	Lap shear (10 Rd VDA test)	>7.5	MPa	12.05	Pass
18	Lap shear (Water test, immediate)	>7.5	MPa	12.60	Pass
19	Lap shear (Water test, after 24 h recovery)	>7.5	MPa	13.54	Pass

The process meets all the technical requirements. The results were as shown in Fig. 3.

## 2.4 Test Summaries

The important tests for any sealant are, Lap-shear test, T-peel test and bead structure test. Results are described above. The results of other tests carried out are shown in the test summaries below. See Tables 1, 2 and 3. According to the results above, we have jointly developed a hemming sealant suitable for use on

**Table 2** The results of test summaries in the condition of normal bake

Group 2, normal bake. Curing 170 °C for 20 min					
Items	Testings	Specification	Units	Mean result	Conclusion
1	Lap shear (Initial)	>10.0	MPa	12.05	Pass
2	T-peel (Initial)	>2	N/mm	5.25	Pass
3	Bead structure	be evaluate by SAIC	N/A	Pass	Pass
4	Lap shear (Cold test)	>7.5	MPa	15.01	Pass
5	T-peel (Cold test)	>1.5	N/mm	7.10	Pass
6	Lap shear(Hot test, test at 80 °C)	>7.5	MPa	15.97	Pass
7	Lap shear (Hot test, after 24 h recovery)	>7.5	MPa	17.21	Pass
8	Lap shear (Humidity test)	>7.5	MPa	13.06	Pass
9	Lap shear (Salt spray tests, immediate)	>7.5	MPa	12.39	Pass
10	Lap shear (Salt spray tests, after 24 h recovery)	>7.5	MPa	13.86	Pass
11	Lap shear (5 Rd VDA test)	>7.5	MPa	12.50	Pass
12	Lap shear (7 Rd VDA test)	>7.5	MPa	12.89	Pass
13	Lap shear (10 Rd VDA test)	>7.5	MPa	11.63	Pass
14	Lap shear (Water test, immediate)	>7.5	MPa	12.76	Pass
15	Lap shear (Water test, after 24 h recovery)	>7.5	MPa	13.85	Pass

aluminium hoods and one that meets all the process and technical requirements. After the material tests were completed, the engineering designed department undertook their own function tests. The function tests included bench test, GTR test and on road test. All the function tests were passed, meeting the product requirements.

### 3 The Dimension Variety Test

For investigating the dimension variation after curing, we compared the hood dimension between the two conditions (two-composite and single composite material). Both before curing and after curing. The results are comparable and meet the product quality and technical requirements. See the Figs. 4, 5 and 6.

The flush dimension variability shows mostly below 0.55 mm, the maximum tolerance specified is 0.83 mm. The gap dimension variability is mostly below 0.5 mm, the maximum tolerance is 0.52 mm.

According to the test results above, the gap and dimension variability are below 1.0 mm. This meets the product quality and process requirements. The results

**Table 3** The results of test summaries in the condition of over bake

Group 3, over bake. Curing 190 °C for 60 min					
Items	Testings	Specification	Units	Mean result	Conclusion
1	Lap shear (Initial)	>10.0	MPa	15.80	Pass
2	T-peel (Initial)	>2	N/mm	5.50	Pass
3	Bead structure	Be evaluate by SAIC	N/A	Pass	Pass
4	3 mm Bond gap versus lap shear strength testing	Be evaluate by SAIC	MPa	7.01	Pass
5	3 mm Bond gap versus T-peel shear strength testing	Be evaluate by SAIC	N/mm	6.90	Pass
6	4 mm Bond gap versus lap shear strength testing	Be evaluate by SAIC	MPa	5.10	Pass
7	4 mm Bond gap versus T-peel strength testing	Be evaluate by SAIC	N/mm	6.09	Pass
8	Lap Shear (Cold test)	>7.5	MPa	19.43	Pass
9	T-peel (cold test)	>1.5	N/mm	7.65	Pass
10	Lap shear (Hot test, test at 80 °C)	>7.5	MPa	16.16	Pass
11	Lap shear (Hot test, after 24 h recovery)	>7.5	MPa	19.19	Pass
12	Lap shear (Humidity test)	>7.5	MPa	17.06	Pass
13	Lap shear (Salt spray tests, immediate)	>7.5	MPa	17.08	Pass
14	Lap shear (Salt spray test, after 24 h recovery)	>7.5	MPa	17.26	Pass
15	Lap shear (5Rd VDA test)	>7.5	MPa	16.71	Pass
16	Lap shear (7Rd VDA test)	>7.5	MPa	14.83	Pass
17	Lap shear (10 Rd VDA test)	>7.5	MPa	13.73	Pass
18	Lap shear (Water test, immediate)	>7.5	MPa	15.42	Pass
19	Lap shear (Water test, after 24 h recovery)	>7.5	MPa	16.39	Pass

show that the glass beads in the sealant can make the hood dimension stable, and help to overcome the panel mismatch between the inner and outer panels of the product.

## 4 Investment Analysis

Because we were able to cancel the curing station and using a single composite material were able to use a manual process to apply the hem sealer, the project investment is greatly reduced. See the Figs. 7 and 8 and Table 4:



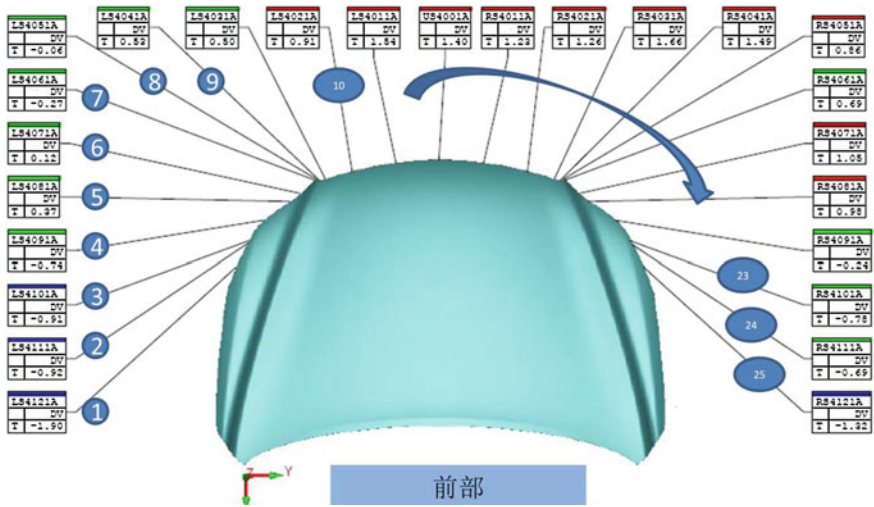


Fig. 4 The measurement points of aluminium alloy hood

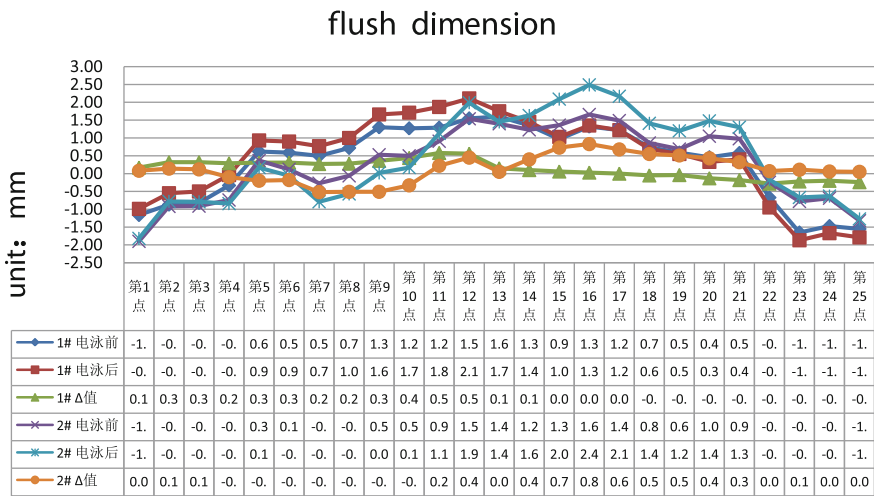


Fig. 5 Dimension variability

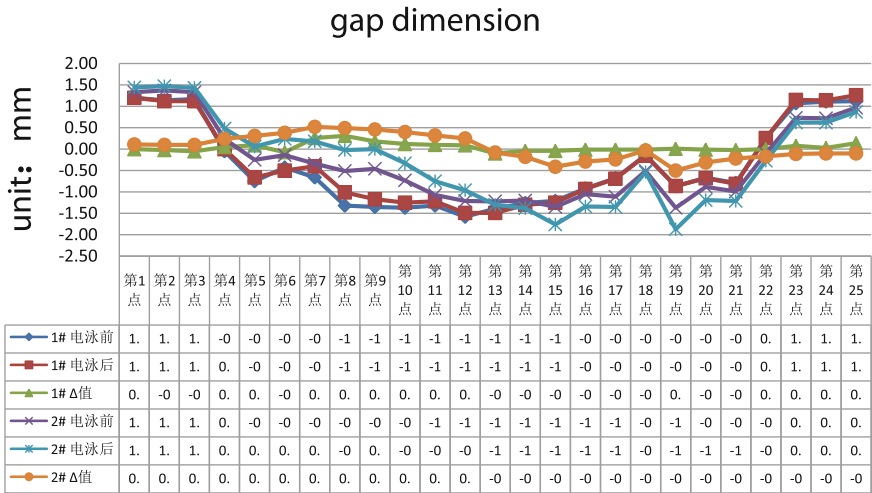


Fig. 6 Gap dimension variability

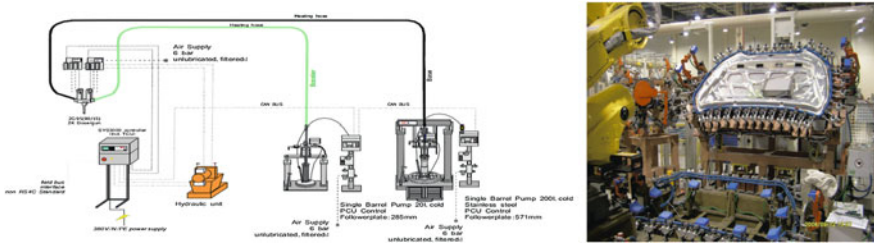


Fig. 7 The equipments required for a two-composition sealant

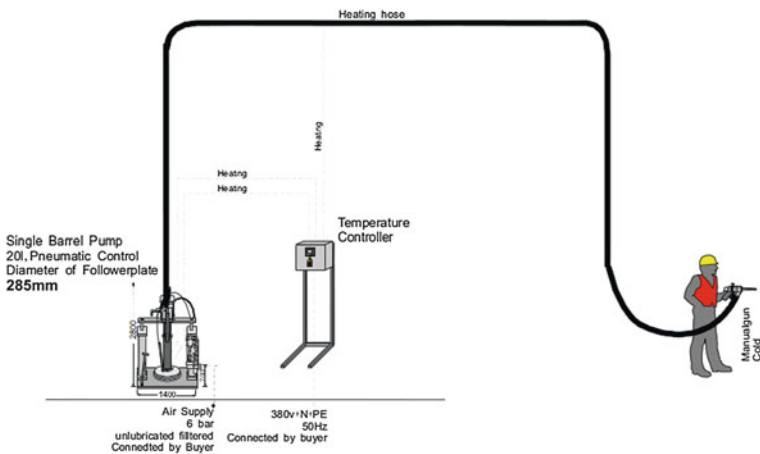


Fig. 8 The equipment required for a single-composition sealant

**Table 4** Investment comparison list of the two processes

	Investment (yan)	Peripheral equipments (yan)	Summation (yuan)	Sealing quality
Single-composition handwork	Sealing equipments (141,200)	0	141,200	Good
Tow-composition sealant automatic application (with curing)	sealing + curing + jig (2,764,100)	robots + buffer (1,100,000)	3,864,100	Good
Save investment			3,512,900	

## 5 Conclusion

Single-composition sealant has now taken the place of the original specified two-composition sealant for hemming of aluminium alloy products in our business. It makes the sealing application process easy, efficient and at reduced cost.

The glass beads are mixed with the single-composition material, beads are forced into the surface of aluminum alloy plate, which in turn eliminates the affect of any mismatch of inner and outer parts.

This sealing technology cancels the curing process after hemming, Reducing investment.

This technology can be considered for different or difficult hemming applications in the future, for example around the rear wheel arch on the body. The single-composition sealant has only been developed and tested for aluminium alloy material in this study.

# Ballistic Resistance of Aluminium Foam by Ogive-Nosed and Conical-Nosed Projectiles Impact

Yonggang Bao and Nianmei Zhang

**Abstract** The paper investigates oblique penetration and perforation of low density aluminium foam with ogive-nosed and conical-nosed projectiles. Based on dynamic spherical cavity-expansion approximation, the simplified analytical penetration model has been reformulated to calculate ballistic penetration resistance of aluminium foam. In oblique penetration and perforation process, the axial and lateral force, and rotative moment of the projectile can be calculated accurately; the variation of velocity, deceleration and energy dissipation can be obtained. Ballistic trajectory and attitude of the projectile are the more important parameters to describe its motion state; ballistic trajectories of the nose and rear depict the effects of angle of incidence, angle of attack and initial strike velocity. This paper provides an analytical method which can obtain accurate and fast calculations of oblique penetration and perforation.

**Keywords** Oblique perforation • Oblique penetration • Ogive-nosed projectile • Conical-nosed projectile • Low density aluminium foam

---

F2012-H01-005

---

Y. Bao (✉)

Automotive Engineering Research Institute, Beijing Automotive Group Co., Ltd,  
Beijing 100021, China

e-mail: baoyonggang@beijing-atc.com.cn

N. Zhang

College of Physical Sciences, Graduate University of Chinese Academy of Science,  
Beijing 100049, China

e-mail: nianmeizhang@yahoo.com

## 1 Introduction

Aluminium foams offer a unique combination of properties such as low density, high stiffness, strength and energy absorption that can be tailored through design of the microstructure. The unique properties of foams promise a variety of applications in vehicle design ranging from light-weight construction, impact energy absorption to various types of acoustic damping and thermal insulation [1].

The investigations of light shelter against small projectiles are very important to vehicle. So we select aluminium foam plates as simple shield.

In oblique penetration process, contact condition between the projectile and target material is very complex and changes with time. For the normal perforation and penetration, the force state on projectile surface can be regarded as almost axially symmetric [2, 3]. The normal impact analysis model can be reduced to one-dimensional model in the direction of penetrator axis. The normal ballistic trajectory is nearly a straight line and the transverse vibration can be omitted. But for the oblique perforation and penetration, the projectiles bear asymmetric loading, in the theoretical analysis, which can be reduced to two-dimensional analysis model in most of the cases. The asymmetric loading produces moment of rotation which causes projectile to rotating.

Force loading on projectile surface is affected by the shape, motion state of projectile and physical properties of target materials, so this paper establishes motion equations of oblique penetration and perforation by ogive-nosed and conical-nosed projectiles. The target material is used low density aluminium foam  $300 \text{ kg/m}^3$ . The projectiles were launched with striking velocities  $100 \text{ m/s}$ , angle of penetrator axis is  $60^\circ$  and angle of attack in the region  $-50$  to  $20^\circ$ . We obtain the detailed ballistic trajectory and many more parameters in the total penetration process. At last, we discuss the mechanisms of oblique penetration of low density aluminium foams.

## 2 Analytical Model

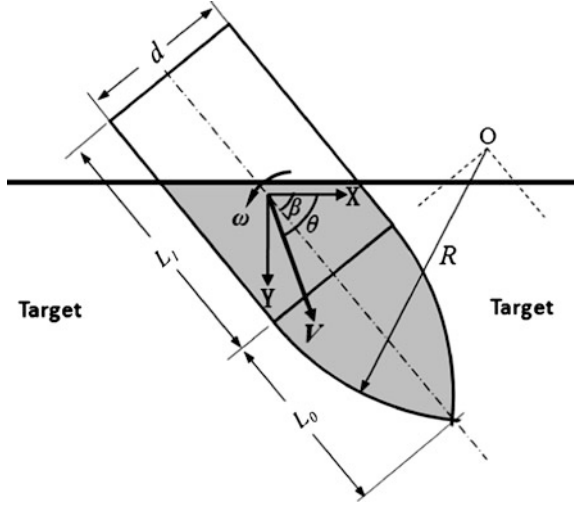
### 2.1 Ogive-Nosed Projectile Model

The shape of ogive-nosed projectile can be described by three independent parameters as shown in Fig. 1:  $R$ ,  $d$  and  $L_1$  are the circle radius of arc, outer diameter and length of shank, respectively.

Angle of attack  $\delta$  is defined as the angle between velocity attitude and penetrator axis:

$$\delta = \theta - \beta \quad (1)$$

**Fig. 1** Ogive-nosed projectile



where,  $\theta$ ,  $\beta$  and  $\delta$  are the angle of incidence, angle of penetrator axis and angle of attack, respectively. Clockwise rotation of the three parameters is positive.

The normal velocity of arbitrary point on the ogive-nosed surface can be obtained, as shown in Fig. 1:

$$V_{n,k} = V \cos \delta \cos \theta + (-1)^{k-1} \left( V \sin \delta \sin \theta + V_{\omega} \cos \frac{\theta - \theta_0}{2} \right) \cos \gamma \quad (2)$$

where,  $\gamma$  is the included angle between the outward normal of meridian plane and the plane of incidence,  $\gamma = -\frac{\pi}{2} \sim \frac{\pi}{2}$ .

The normal pressure on the surface of projectile is obtained by dynamic cavity expansion approximation,  $\sigma_n = A + B\rho V_n^2$ , where  $A$  is the quasi-static radial stress required to open the spherical cavity which can be defined by yield limit,  $B\rho V_n^2$  is the dynamic term and  $\rho$  is the target density which depend only on the material properties of Aluminium foam.

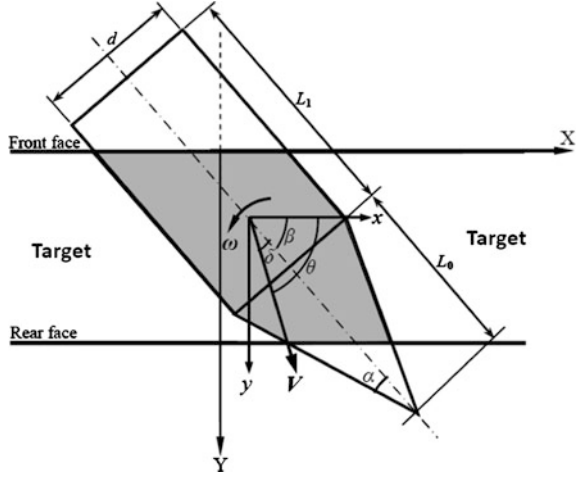
Base on the fundamental assumptions and mechanics analysis hereinbefore, the accurate motion equations (3a–3f) of the projectile can be derived as follows by use of Newton’s law.

$$\frac{dV}{dt} = -\frac{1}{m} F_{\tau} \quad (3a)$$

$$\frac{d\theta}{dt} = -\frac{1}{mV} F_d \quad (3b)$$

$$\frac{d\omega}{dt} = \frac{1}{I} M_d \quad (3c)$$

**Fig. 2** Conical-nosed projectile



$$\frac{d\beta}{dt} = -\omega \tag{3d}$$

$$\frac{dX}{dt} = V \cos \theta \tag{3e}$$

$$\frac{dY}{dt} = V \sin \theta \tag{3f}$$

where,  $(X, Y)$  is the coordinate of projectile nose,  $V, \theta, \omega$  indicate the velocity, angle of incidence and angular velocity of the penetrator, respectively.  $F_v, F_d, M_d$  are two resultant forces which parallel and perpendicular to axial direction, and moment of rotation, respectively.

### 2.2 Conical-Nosed Projectile Model

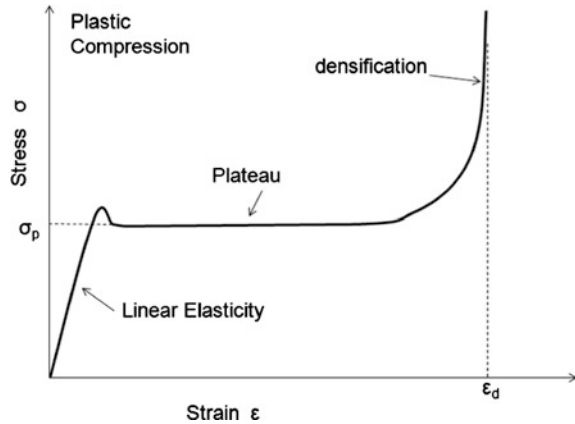
Geometric parameters of conical-nosed projectiles are shown in Fig. 2. The shank diameter is set to be  $d$ , half-cone angle is  $\alpha$ , length of the shank is  $L_1$ , respectively.

Force loading analysis of Conical-nosed projectile is the same as ogive-nosed projectile.

### 2.3 Mechanical Property of Aluminium Foam

Low density aluminium foam shows a stable plateau stress on the stress–strain curve where stress keeps almost constant with varying strain, as shown in Fig. 3.

**Fig. 3** Static compressive stress–strain response



This physical property makes aluminium foam to have the higher capacity of absorbing energy.

The density of aluminium foam is  $300 \text{ kg/m}^3$ , mechanical properties as follows: compressive modulus  $1.0 \text{ GPa}$ , compressive strength  $3.0 \text{ MPa}$ , and shear strength  $1.0 \text{ MPa}$ .

## 2.4 Calculational Method

The motion differential equations (3a–3f) are solved by using the fourth-order Runge–Kutta method. The ballistic trajectory and the other parameters described motion state can be obtained in total perforation process.

## 3 Results

### 3.1 Results of Ogive-Nosed Projectile

Eight ballistic trajectories (two correlative lines are a pair-bound trajectory) under the same impact velocity  $100 \text{ m/s}$ , the effects of angle of attack on ballistic trajectories which display in Fig. 4. When angle of attack in a small range ( $|\delta| < 30^\circ$ ), the trajectories of the nose and rear are in a straight line in the total penetration process. In this condition, the dissymmetric force account for a very small effect for trajectories. Along with  $|\delta|$  is increasing more than  $30^\circ$ , the ballistic trajectories of the nose and rear have significant deviation.

For low density aluminium foams, ballistic trajectories are different from their matrix material. Low density lead to great changes for strength, macrostructure which is the main cause of this phenomenon [4].



**Fig. 4** Ballistic trajectories under different initial strike angles

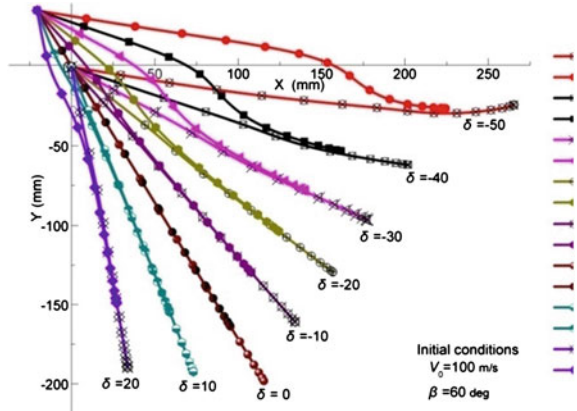


**Fig. 5** Variation of angular velocity under initial angle of attack

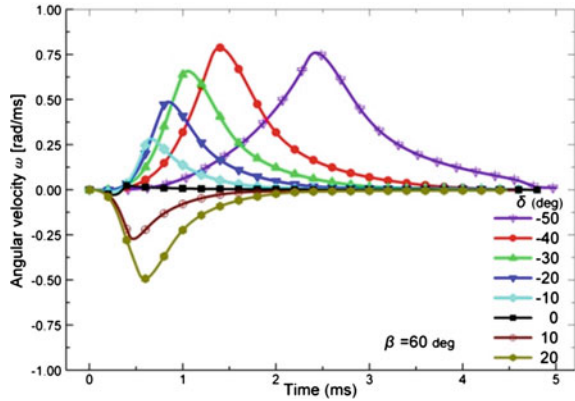
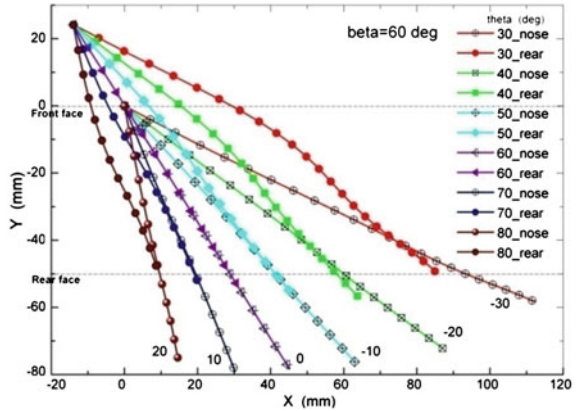


Figure 5 shows the variations of projectile angular velocity (or rotational velocity) under different initial angles of attack. Angle of attack  $\delta$  is an important factor for angular velocity. For the curve of  $\delta = 0^\circ$ , the angular velocity is not obvious in the total penetrating process. When  $|\delta| > 0^\circ$ , angular velocity will appear a maximum or minimum value in the initial stage. In Fig. 5, the maximum or minimum value is increasing or decreasing with the change of  $\delta$ . With the increasing of  $|\delta|$ , the contact state acts on one part of the penetrator surface and the dissymmetric force is very obvious.

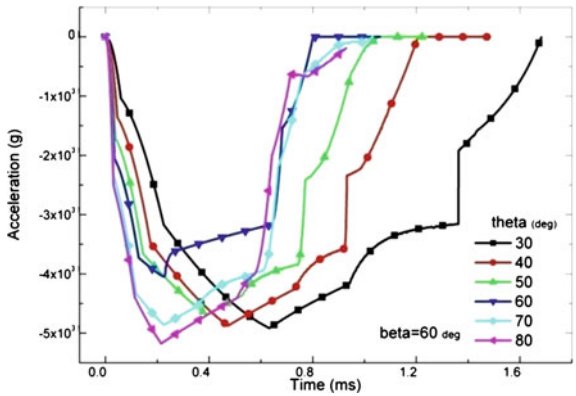
### 3.2 Results of Conical-Nosed Projectile

Six ballistic trajectories under the same impact velocity 100 m/s, the effects of angle of attack on ballistic trajectories which are displayed in Fig. 6. When the initial strike condition is velocity attitude and penetrator axis in a straight line

**Fig. 6** Ballistic trajectories under different initial strike angle



**Fig. 7** Decelerations under different angle of attack



( $\delta = 0^\circ$ ), ballistic trajectory is a straight line, dissymmetric force account for a very small effect for the projectile. When velocity attitude and penetrator axis are out of line which means the absolute value of angle of attack is greater than zero, the trajectories of cone-nose and rear of the projectile are out of line at the incipient stage; when the projectile is about to perforate the aluminium foam layer, the trajectories of cone-nose and rear tend to a line progressively. Angle of attack is the most important factor which affects ballistic trajectories.

Figure 7 shows the variations of projectiles deceleration with time. These has a uniform discipline from the six deceleration lines: the deceleration remained at high level in the total perforation process, the deceleration reach to the maximum value sharply and it can maintain steady at higher value until the projectile perforated aluminium foam, then the deceleration decreases to zero quickly. The normal pressure on the surface of projectile is obtained by the dynamic cavity expansion approximation,  $\sigma_n = A + B\rho V_n^2$ , where  $A$  is the quasi-static radial stress required to open the cylindrical cavity,  $B\rho V_n^2$  is the dynamic term ( $\rho$  is the target density). As seen from Fig. 7,  $A$  is the important part which is much larger than

dynamic term, which is why the deceleration can maintain steady at higher value in almost the total perforation process. This is the more important characteristic for aluminium foam which is different from their matrix material.

## 4 Conclusions

The following conclusions offer some guidelines for light shelter design of vehicle:

1. When angle of attack in a small range ( $|\delta| < 30^\circ$ ), the trajectories of projectiles in a straight line, lateral loading on projectile is not obvious. The major cause is low density aluminium foams lead to lower stiffness and strength than aluminium alloy.
2. Lateral loading caused by angle of attack and impact angle, which is the primary factor to causing angular acceleration and rotational velocity. In initial impact, lateral loading is very faint for both conical-nosed and ogive-nosed projectiles.
3. The quasi-static radial stress required to open the cylindrical cavity which is much important than the dynamic term.

## References

1. Banhart J (2005) Aluminium foams for lighter vehicles. *Int J Veh Des* 37(2–3):114–125
2. Bao YG, Zhang NM et al (2011) Theoretical approach in predicting perforation of aluminum alloy foam target against different ogive-nosed projectile. *Appl Mech Mater* 44–47:3060–3066
3. Bao YG, Zhang NM et al (2011) Perforation of cone-nose projectile to bi-layered aluminum alloy foam target. *Appl Mech Mater* 52–54:436–441
4. Gibson LJ, Ashby MF (1999) *Cellular solids: structure and properties*. Cambridge University Press, Cambridge

# Re-Engineering Functionality by Optimizing Hybrid Parts Design

Dan Leuciuc and Stefan Tabacu

**Abstract** Hybrid parts are defined by the combination of different materials and/or manufacturing technologies. Several examples can identify the usage of hybrid concepts: adding metal inserts to plastic parts (therefore making the parts provide increased strength and resistance); adding soft type material to hard plastic (squeak and rattle avoidance, meet seal-off requirements); replacement of steel with aluminium and magnesium based alloys; replacement of metal components with composite counterparts. Further improvements are possible by upgrading from 2 k type concepts to 3–4 k hybrids and replacing multiple component assemblies with a single hybrid structure that may consist of plastic, (heavy/light) metal, composites, foam/textures. Present paper presents (i) a general concept that is being used to define new, innovative solutions addressing functionality required for components, and (ii) presents an actual example of a part that was redesigned and optimized, achieving increased performance, lower cost, and reduce weight.

**Keywords** Hybrid concepts · Functional optimization · Weight reduction · Replace steel with light alloys

---

F2012- H01-006

---

D. Leuciuc (✉) · S. Tabacu  
ALSECA Engineering SA, Tunari, Romania  
e-mail: stefan.tabacu@upit.ro

S. Tabacu  
Faculty of Mechanics and Technology, University of Pitesti, Arges, Romania

# 1 Introduction

Mobility industry is at a crossing. The worldwide crisis from 2008 not only lasted longer than anyone anticipated but it also inducted some fundamental changes to the global markets; the automotive industry (and the consequent way cars are being designed, manufactured and distributed) is an integral part of the reshaped global environment.

In addition to this (rather challenging) geopolitical context there is a constant push for the automotive industry to reduce (tailgate) emissions, overall carbon footprint (from production throughout the lifetime of the vehicle), while preserving performance and actually increase the number of (mostly electronic) added features.

The overall result is rather simple to reach: vehicles need to provide increased safety and overall performance and comply with environmental friendly legislation—all that in an overall context of volatile raw materials and tougher than ever competition.

There is an undivided attention geared towards improving ALL the components that together are used to build the vehicle; from large subassemblies all the way down to little components there is a constant push to reach solutions that provide same if not improved functionality for an overall lower weight. Metal-to-plastic conversions, the usage of light alloys, composite material usage, all these solutions are being contemplated for usage in every single area of the vehicle [1–4]. The traditional design (and the way parts used to be developed) is being questioned with Original Equipment Manufacturers (OEM's) looking for alternatives that comply with these ever more challenging requirements. In the end, given the tougher and tougher competition and the overall context just described, both from an OEM as well as their supply base perspective, only the players that first of all understand and consequently commit to meet or exceed these mandatory performance criteria will survive.

With the above mentioned in mind the conclusion is rather simple: for the automotive industry (OEM and supply base) it is mandatory to be able to come up with increased performance and innovative solutions that can help provide differentiating features and performance at best value for landed cost. This is the new normal, the new evaluation criteria in place that performance is being assessed against.

Due to the challenges afore-mentioned the entire automotive business is constantly being reshaped based on an ever changing and challenging environment.

Having understood the exact needs one can move towards the next step—actual product development. Detailed matrices, correlated and based on cross-references with previous work and detailed market benchmarking, quantify needs and requirements. One of the most valuable capabilities at this point is represented by the advanced product manufacturability know-how. Rather than rely on a procedure where design is developed and further down the road relate it with actual manufacturing realities, we point to manufacturability at the initial design

development. This approach allows for better overall product definition, through a simplified, cost-effective process. Not only the manufacturing process is properly addressed (starting with the early design stage) but also the ultimate final product reaches exceptional value through this demonstrated paradigm-shifting methodology.

Once the design is completed the validation is performed extensively in the virtual space, by means of advanced simulation software usage. This (numerical simulation) is done for both actual product validation as well as the manufacturing process. At the point of entering physical testing the product is advanced validated therefore the overall real life testing is not only time-condensed but also of lower cost.

An integral part of such an innovative product design alternative is represented by the usage of hybrid concepts. The mix of materials and/or processes allows for reaching increased functionality while reducing overall weight and product cost. Results are incrementally rewarding the upfront effort investment.

## 2 Engineering Process Overview

In order to survive on the market today one needs to follow one of the following approaches:

- Master the globally-based, commodity-type business. Simple plastic parts (injection molded; most of them with no secondary operation or added components); fasteners, even simple metallic components fall in this category. Raw material prices are well known and controlled by the final client (OEM's); the manufacturing infrastructure (definition and operating cost) are also of common knowledge. Therefore competitors are differentiating themselves by means of economies of scale, mass production high-yield efficiency. Operational margins are thin; low cost Asian-based competitors are shipping product around the world and have been successful in shutting down competition from Europe and especially North America;
- Being capable of re-engineering functionality by complete system definition change. Applying new concepts and components based on alternative technologies, companies that rely on innovation are capable of making a difference against competitors. Rather than be content to compete in a mature market (as described above), these competitors rely on engineering know-how to essentially generate new market segments based on different rules. Customers (the OEM's), based on such suppliers having validated expertise, would trust them to develop alternative design solutions and associated technologies. Such emerging sectors allow players to rake in a larger operating margin (sustaining the R&D work) and the recognition of development associated cost.

Integration of the working principle is presented in Fig. 1.



Fig. 1 Working principle

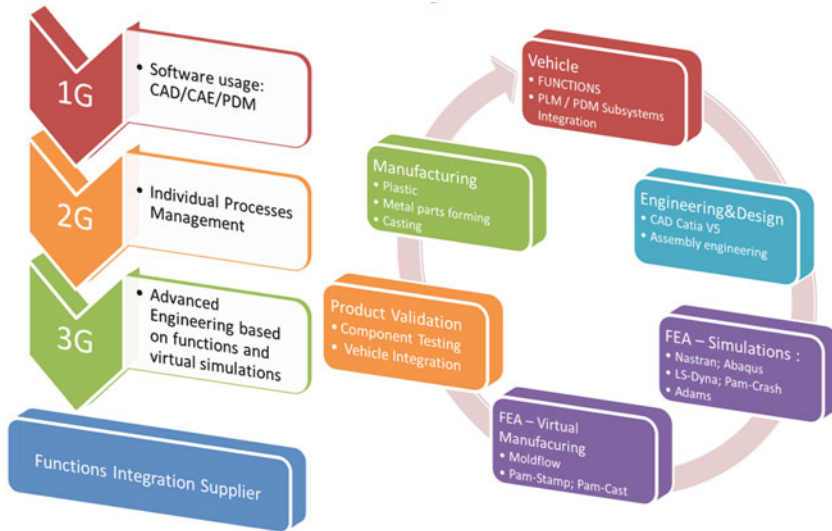


Fig. 2 Engineering process

The advanced, validated engineering process is presented in Fig. 2. Extensive virtual simulations are expected to optimize various solutions; in addition the comprehensive and wide-based approach is going to assure best-in-class results.

Having established the project foundation the next question is how to reach the desired results. It is evidently easier said than done and given the tremendous pressure and the challenging environment the natural question that is posed pertains to how can one identify the opportunities and deliver against them.

Based on in-depth market analysis the solution identifies hybrid part design. Hybrid parts are defined by a combination of different materials and technologies used to manufacture an assembly (that usually replaces assemblies consisting of “traditional” parts that would be made out of a single material/single manufacturing process) [5]. Several examples can further identify the usage of hybrid concepts: adding metal inserts to plastic parts (therefore making the parts provide increased strength and resistance); adding soft type material to a hard plastic one (avoid squeak and rattle [6], provide sealing); add multiple component foam to plastic or metal parts (seal-off performance); add soundproofing padding to metal or plastic parts (acoustic performance), partial/total hard plastic replacement with non-woven material (lower weight, better soundproofing) while maintaining some of the part made out of hard plastic; use of bio materials [7, 8]; partial replacement of steel made components with light alloys based on aluminium and magnesium, partial replacement of metal components with composite material made counter-parts [9] .

The hybrid parts are based on the usage of the materials provided in Table 1 (for convenience we have also added basic manufacturing processes and strength/weaknesses for each of them)

In order to be able to propose alternative solutions (i.e. the hybrid design) effectively one needs to be able to take the above mentioned materials and associated manufacturing technologies and apply them to the required functionality in the vehicle. That is the point where the validated experience of the parties involved in the project comes to play, as you need to tailor the technologies to the specific needs, basically defining a concept that can be validated to comply with the entire specification details.

In summary, in order to identify applications of hybrid design based the following steps should be performed:

- (i) Understand the functionality that is required for the (sub)systems;
- (ii) Seek for alternative innovative design to replace “traditional” design;
- (iii) Relate the opportunities with desired performance;
- (iv) Correlate the potential opportunities with manufacturing capabilities;
- (v) Define a product concept that meets performance and manufacture criteria;
- (vi) Validate solution through virtual and physical test;
- (vii) Launch the actual product manufacturing.

The actual areas of the vehicles that we focus on are:

- Plastic parts/assemblies that lack performance (example molded wheel-liners that do not provide soundproofing and also have poor impact resistance; quarter/door panels that are heavy and do not provide soundproofing performance);
- Overmolded parts that have high optimization potential (metal inserts that are over-engineered, replacement of steel inserts with light alloys) [9, 10];
- Paradigm-shifting by means of multiple material solutions (soundproofing non-woven for reduced weight and soundproofing, plastic overmolding for shape complexity, light alloy inserts for strength and dimensionally controlled



**Table 1** Material, manufacturing process and process performances

Name	Description	Manufacturing process	Strength	Weaknesses
Plastic	Various grades of oil based components (PP/PE, POM, PA...)	Injection molding of granules in custom tools	Low cost, one step process Shape/form freedom	Low strength, especially at high temperature Low dimensional stability Poor soundproofing performance Heavy part due to density Requires anti-rust treatment
Steel	Various grades of steel	Turning, casting or stamping	Low cost for high volume Good dimensional performance	Higher price, complex manufacturing process Multistep process, used as stand alone requires multiple attachment points Shape limitations Requires surface treatment to assure proper bonding
Light alloys	Various alloys based on Al and Mg	(High pressure) casting, thixomolding, turning, hot stamping	Low weight Good dimensional performance	
Non-woven padding	Oil based and/or vegetal based textures	Forming	Very good sound-proofing performance Low weight	
Multi-component foam	PUR based sealants	Foam-in-place technology based on multiple component mix	Good sealing property at low density product	

attachment points). Examples of parts would pertain to consoles, interior garnish, quarter panels;

- Thermoformed panels made out of thin wall sheets that are covered with soundproofing non-woven padding.

### 3 Manufacturing Technologies

The hybrid parts are, as previously mentioned, parts or assemblies that rely on multiple materials and multiple manufacturing technologies. Our focus, based on the experience that was gained in several projects and in-production implementation, relies on plastic injection molding as a core expertise. Multiple material components and insert-molding have been for years used by our team; in addition injection molding allows for non-woven material inserts. Most importantly, injection molding can be ultimately the liaison between different materials and technologies, the way a complex assembly can effectively and efficiently be put together. As result the main and first technology that is being considered is injection molding, with its derivatives (multi-material, over-molding); 2, 3 and even 4 k material/processes are based on injection molding. In order to achieve this end result the following manufacturing infrastructure is being considered:

- “Regular” injection molding by means of a one-barrel machine. No matter the actual machine type (horizontal vs. vertical, electrical vs. hydraulic vs. hybrid) the process basically consists of resin pellets that are melted down and pushed in a custom shaped cavity build in a metallic tool. Using metal inserts requires special part design (that would allow consistent insert positioning in the tool); in certain conditions vertical press is to be considered to achieve reliable results, with the note that this is possible only for small size presses;
- Multiple shot machines: would have a second (parallel or perpendicular) barrel added to the main one, therefore allowing for 2 k shots. Most of the application would relate to soft edge overmolded on hard plastic, soft plastic overmolded on hard core, resulting in a piece that is both strong (due to main substrate) and soft (overmolding). The increased price in machine and tooling assures a faster, more consistent cycle. The most complex overmolding machines would allow for three or even four different substrates to be molded (ex. different color materials for rear stop lights).

Depending on the application certain machine customization may be required: extended platen to compensate for the insert areas; smaller than average barrel size (again for compensating part of the final assembly being non-injection molded). Such considerations should be taken into account depending on the actual project details and the design particularities in discussion.

The second technology that we would like to refer to is thermoforming. Due to certain unchallenged advantages of the parts made through a thermoforming process this technology sees more and more usage (and consequently being able to replace injection molded or other type of processes):

- Ability to work thinner wall thickness than injection molding (with consequent weight reduction);
- Ability to form a multitude of different materials (plastic made sheets, non-woven textile based materials);
- If combined with textured type surface of the tools it can provide the so called class A surface appearance.

As a support of the main manufacturing processes above mentioned (injection molding and thermoforming) one should also rely on:

- Stamping of sheet metals;
- Turning/CNC cutting;
- (High) pressure casting;
- Thixomolding of Mg alloys [11];
- Hot temperature forming of Mg alloys.

## 4 Case Study

As mentioned above a multidisciplinary team was set and put to usage in order for hybrid approach to be used at new concept designs. Results are short of spectacular and clients have been positively providing feedback for the options that resulted by using such new/innovative approach. In this paper our intent is to provide but only one complete example of such work, and several design alternatives that were reached.

One of our customers uses a fixation lever for the rear bench attachment and engagement in the vehicle environment. The back seat fixation lever is analysed in order to improve the current design while maintaining functionality and interface with mating parts.

Numerical simulation, design analysis and experiments were some of the necessary steps performed in order to achieve the proposed goal.

The first step consisted in the development and validation of a numerical model according to ECE 11 requirements as the main objective was to review the design proposal regarding the structural response of the lever—striker rear seat assembly.

In Fig. 3a the testing environment is presents while Fig. 3b displays the required acceleration history during the event.

Figure 4 presents the numerical model used for the analysis (as a frame during the simulation showing the interaction between the moving rigid blocks and the metallic frame of the back seat).

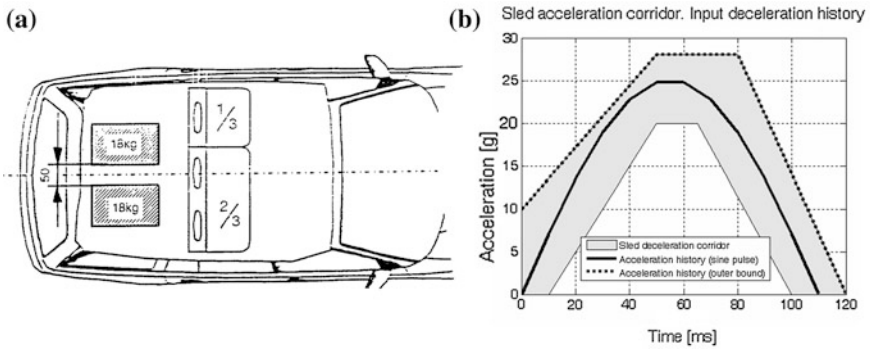


**Fig. 3** Experimental requirements; **a** positions of test blocks before test of rear seat-backs; **b** sled deceleration corridor

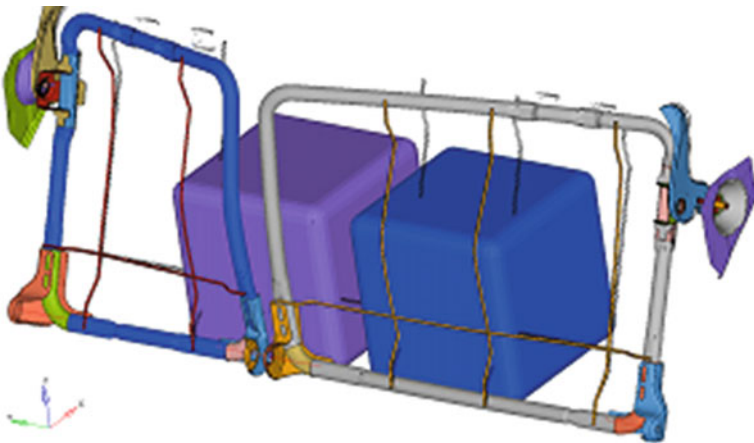


**Fig. 4** Computational model of the rear seats assembly

Results obtained from the numerical analysis were processed (according to SAE J211 standard) in order to identify the force history and the peak value (Fig. 5).

At this point a design update of the metallic insert was performed. The current design was evaluated for a mass reduction and the potential ultimate performance increase of a magnesium material change.

Figure 6 displays the existing and the proposed solution of the insert.

The thickness of the magnesium insert was set in order to match the performances of a simple testing equipment used to validate the preliminary proposed design. Figure 7a presents the simple testing equipment. Load is applied by a screw having inserted a load cell between one end and the part.

The numerical model allowed for an evaluation of the maximum force that may be applied before the part fails. Figure 7b displays the measured forces during the experiment. The green line plots the load evaluated by numerical analysis. The red

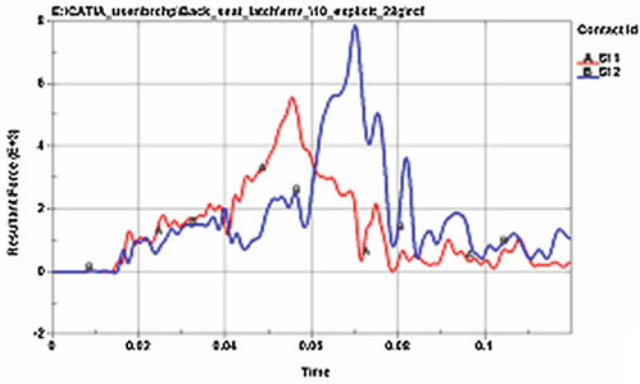


Fig. 5 Calculated contact force: red line right side; blue line left side

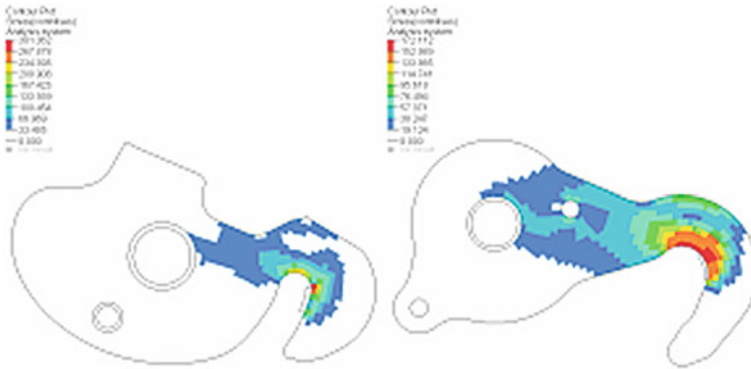


Fig. 6 Current versus redesigned shape of the insert

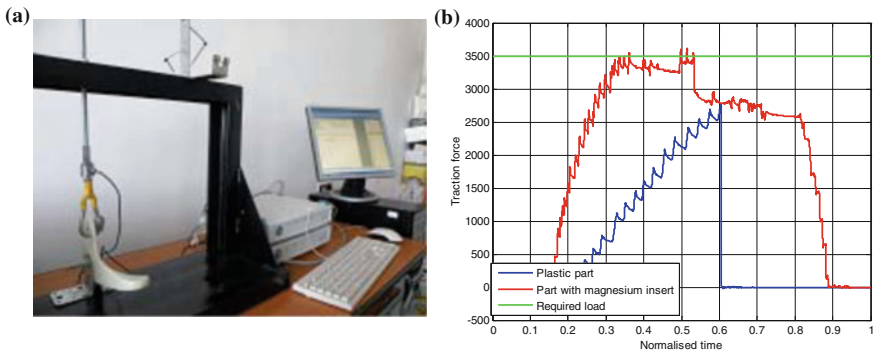


Fig. 7 Experiments: a equipment; b results



		Failure load	
		2800 N	<b>NOK</b> <b>Part separation</b>
<b>Thermoplastics only (no metal insert)</b>			
		3500 N	<b>OK</b> <b>Crack without part separation</b>
<b>Part with magnesium insert</b>			

Fig. 8 Tested parts

line plot the results for the part with magnesium insert while the blue line plots the measured load for the part without any metallic insert.

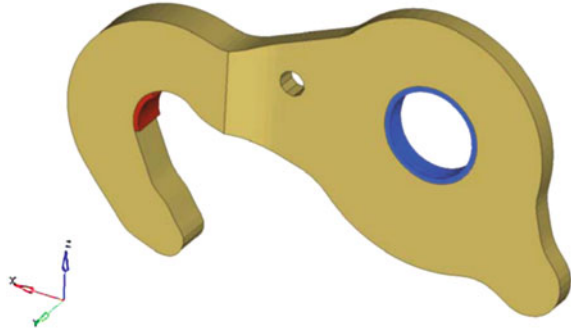
The parts after the experiment are presented in Fig. 8.

The experiment provided additional entry data for the design of the final insert made of magnesium. Although initial optimized design was already compliant with the requirements, per the additional request of the customer a further, second stage, design optimization was performed, one that increased the strength performance of the optimized design. The ultimate solution was represented by a local reinforcement of the magnesium made insert, see design presented in Fig. 9.

The ultimate part optimization and performance increase was subject to complying with performance criteria that the initial, current-in-production design, did not meet. It pertains to achieving whatever balance state of the component mounted in vehicle position, state that allows for radical safety performance improvement.

The present study provides a comparison between two different lever designs: (i) current production part and (ii) optimized design proposed. The optimized part is completely interchangeable with the existing in-production design, having the overall same footprint, attachment points, and functional areas. The difference is

**Fig. 9** Metallic insert—magnesium. Final configuration



represented by a reduced weight insert, which provides both significant weight reduction as well as lower component cost; last but not least the optimized design achieves whatever balance state.

Figure 10a represents a general view of the proposed (optimized) geometry, highlighting inertia properties obtained from CATIA V5 software.

As per details revealed in Fig. 11a, gravity centre coordinates for optimized geometry are obtained using following equations:

$$\begin{aligned} x_{COG} &= \frac{x_{COG\_plastic} \cdot m_{plastic} + x_{COG\_metal} \cdot m_{metal}}{m_{plastic} + m_{metal}} \\ z_{COG} &= \frac{z_{COG\_plastic} \cdot m_{plastic} + z_{COG\_metal} \cdot m_{metal}}{m_{plastic} + m_{metal}} \end{aligned} \quad (1)$$

where components masses are:  $m_{plastic} = 0.104$  kg and  $m_{metal} = 0.097$  kg.

Relative to the rotation centre the gravity centre for the optimized geometry has the following coordinates:

$$x_{COG} = 18.55 \text{ mm}$$

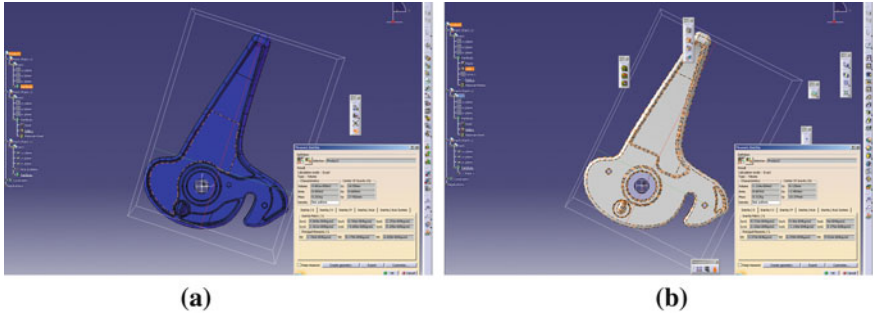
$$z_{COG} = 17.502 \text{ mm}$$

Figure 11a highlights the force acting on the striker component in the absence of moment applied by the retention spring (for the optimized geometry):

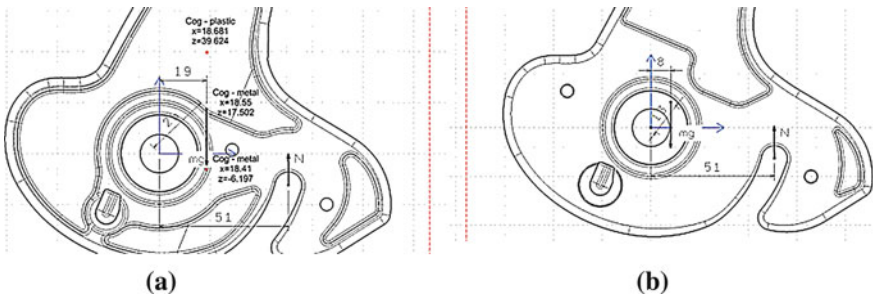
$$N \cdot 51 = m \cdot g \cdot 19 \Rightarrow N = \frac{0.201 \cdot 9.81 \cdot 19}{51} = 0.73 \text{ [N]} \quad (2)$$

Figure 10b shows a general view of the current in-production geometry and the measured inertia properties as resulted from CATIA software.

Figure 11b shows in-production geometry details related to applied force acting on Striker.



**Fig. 10** Mass and inertia: **a** optimised design; **b** current design



**Fig. 11** Identification of the COG: **a** optimised design; **b** current design

Gravity centre coordinates relative to the rotation centre are:

$$x_{COG} = 8.125 \text{ mm}$$

$$z_{COG} = 10.374 \text{ mm}$$

where component masses is:  $m_{plastic} = 0.103 \text{ kg}$  and  $m_{metal} = 0.209 \text{ kg}$ .

The force acting on striker absent the moment applied by the retention spring is:

$$N \cdot 51 = m \cdot g \cdot 19 \Rightarrow N = \frac{0.312 \cdot 9.81 \cdot 8}{51} = 0.48 \text{ [N]} \quad (3)$$

In the nominal position (the mounting set-up) the centre of gravity is located between rotation axis and the mounting axis (Striker). As result the lever rests on the mating part (reaction  $N \neq 0$ ). A potential state of whatever balance could be achieved only if the centre of gravity is located on the vertical rotation axis below the centre of rotation.

Furthermore, the Lever separation from the bearing surface as result of the coil spring torque was investigated.

Inertia moment relative to the rotation axis is calculated with the following formula:



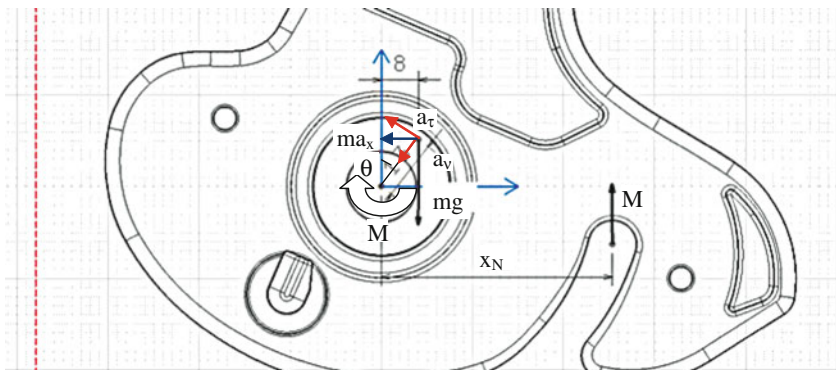


**Fig. 12** Applied forces

$$J_y^0 = J_y + m \cdot r^2 \quad (4)$$

$$r_{cg-0}^2 = x_{cg}^2 + z_{cg}^2 \quad (5)$$

Reaction applied on the Lever, determined as result of the action of the moment generated by the coil spring, is:

$$\begin{aligned} N \cdot x_N - M - m \cdot g \cdot x_{cg} &= 0 \\ N &= \frac{M + m \cdot g \cdot x_{cg}}{x_N} \end{aligned} \quad (6)$$

The movement of the lever, considered in transitory state acting as result of a force  $F_x$  applied in the centre of gravity, is determined with the formula:

$$J_y^0 \cdot \varepsilon = -M + F_x \cdot z_{cg} - m \cdot g \cdot x_{cg} + N \cdot x_N \quad (7)$$

Inertia force (acceleration that acts in the part centre of gravity) is (Fig. 12):

$$\begin{aligned} F_x &= m \cdot a_x \\ a_x &= a_r \cdot \cos \theta + a_v \cdot \sin \theta \\ a_x &= r_{cg-0} \cdot \ddot{\theta} \cdot \cos \theta + r_{cg-0} \cdot \dot{\theta}^2 \cdot \sin \theta \end{aligned} \quad (8)$$

As result the problem in discussion can be summarized as follows:

$$J_y^0 \cdot \ddot{\theta} = -M + m \cdot \left( r_{cg-0} \cdot \ddot{\theta} \cdot \cos \theta + r_{cg-0} \cdot \dot{\theta}^2 \cdot \sin \theta \right) \cdot z_{cg} - m \cdot g \cdot x_{cg} + N \cdot x_N \quad (9)$$

This problem can be solved by means of numerical methods (Runge–Kutta).

In order to solve this equation we need to start considering the following initial conditions:

**Table 2** Required acceleration to unlock the part

$M$ (Nm)	$a_x$ (m/s <sup>2</sup> ) Original design	$a_x$ (m/s <sup>2</sup> ) Optimized design
0.5	1.63	2.7
1	3.29	5.12
2.5	7.9	12.7
5	15.9	25.11
10	32.1	49.83

**Table 3** Solution comparison

Design description	Weight performance	Cost performance	Notes
Current in production	1 (set as reference)	1 (set as reference)	Does not comply with imposed state of balance/ECE 11
Optimized insert in steel material	−57 %	−70 %	Complies with imposed state of balance/ECE 11
Optimized insert in Mg material	−80 %	−40 %	Complies with imposed state of balance/ECE 11

$$\begin{cases} \theta = 0 \text{ rad} \\ \dot{\theta} \text{ rad/s} \end{cases} \text{ for } t_i = 0 \text{ s.} \tag{10}$$

Solving the problem can be done by means of MATLAB software. The following solving sequence is proposed:

- Reaction at the bearing surface is determined based on a torque applied as result of certain coil spring rigidity.
- The value determined as discussed is introduced in equation [11].
- Initial conditions are determined and solved, such that calculated acceleration [12] to generate the part separation from the bearing surface. A dynamic reaction  $N$  is calculated, this value needs to be null (0).

Results obtained are centralized in Table 2. The results depend on the applied torque generated by the coil spring.

The overall comparison of different solutions (starting with the current, in-production design and running through different optimized proposals) is presented in Table 3.

## 5 Conclusion

Vehicles need to provide increased safety and overall performance and comply with environmental friendly legislation—all that in an overall context of volatile raw materials market and tougher than ever competition. Metal-to-plastic conversions, the usage of light alloys and composite materials, all these solutions are

being contemplated for potential application in every single area of the vehicle. Once the design is completed the validation is performed extensively in the virtual space, by means of advanced simulation software usage. This (numerical simulation) is done for both actual product validation as well as the manufacturing process.

A case study was presented as it provides information about the proposed steps for product engineering and re-engineering.

Metallic inserts replacements and design optimisation for better impact response were investigated and presented as a general conclusion. Final result provided significant performance improvement (functionality, lower weight), obtained also at a lower overall component cost.

## References

1. Cui X, Wang S, Hu SJ (2008) A method for optimal design of automotive body assembly using multi-material construction. *Mater Des* 29:381–387
2. Gibson RF (2010) A review of recent research on mechanics of multifunctional composite materials and structures. *Compos Struct* 92:2793–2810
3. Hufenbach W, Böhm R, Thieme M, Winkler A, Mäder E, Rausch J, Schade M (2011) Polypropylene/glass fibre 3D-textile reinforced composites for automotive applications. *Mater Des* 32:1468–1476
4. Perry N, Bernard A, Laroche F, Pompidou S (2012) Improving design for recycling—application to composites. *CIRP Ann Manuf Technol* 61:151–154
5. Sayer M, Bektas NB, Sayman O (2010) An experimental investigation on the impact behavior of hybrid composite plates. *Compos Struct* 92:1256–1262
6. Zhang J, Chaisombat K, He S, Wang CH (2012) Hybrid composite laminates reinforced with glass/carbon woven fabrics for lightweight load bearing structures. *Mater Des* 36:75–80
7. Abu Talib AR, Ali A, Badie MA, Lah NAC, Golestaneh AF (2010) Developing a hybrid, carbon/glass fiber-reinforced, epoxy composite automotive drive shaft. *Mater Des* 31:514–521
8. Davoodi MM, Sapuan SM, Ahmad D, Aidi A, Khalina A, Jonoobi M (2011) Concept selection of car bumper beam with developed hybrid bio-composite material. *Mater Des* 32:4857–4865
9. Sokolova OA, Carradň A, Palkowski H (2011) Metal–polymer–metal sandwiches with local metal reinforcements: a study on formability by deep drawing and bending. *Compos Struct* 94:1–7
10. Tan CY, Akil HM (2012) Impact response of fiber metal laminate sandwich composite structure with polypropylene honeycomb core. *Compos Part B* 43:1433–1438
11. Ozdemir I, Muecklich S, Podlesak H, Wielage B (2011) Thixoforming of AA 2017 aluminum alloy composites. *J Mater Process Technol* 211:1260–1267
12. Hufenbach W, Langkamp A, Adam F, Krahl M, Hornig A, Zschoyge M, Modler KH (2011) An integral design and manufacturing concept for crash resistant textile and long-fibre reinforced polypropylene structural components. *Procedia Eng* 10:2086–2091

**Part II**  
**Advanced Body Manufacturing**  
**Technology**

# New Joint Structure Design of Extended Van Body

Yingchun Bu

**Abstract** To meet the demand of market, all home automobile manufacture companies are try to develop extended and widened vehicles, based on the standard light vans, to expand space for transportation. Taking HIACE SY6480 as basic model, our company developed the extended vans, to expand the market. This article explain mainly the structure design logic of the extended body of HIACE product, and according to the special requirement for the extended body and the technological features of large lining parts, design a new joint structure and suitable production technology for making it: 1. Design a single-side spot-weld plus liquid structure glue method for the extended fender plate. 2. At the butt joint of front and rear side fender plates, design a method of stiffened plate structure plus liquid structure glue. 3. Adopt a coped structure for front and rear side fenders. All these are new joint structures and production techniques that ensure the firmness of the front and rear joint of side fenders, the strength and rigidity of the body structure, and the smoothness of the body surface. As this kind of body structure is a creative design in China, the national patent office has approved the “New joint structure of extended van body” as a national utility model patent, and obtained patent right. This time the new structure design is to conduct a new extended reform of the van body, under the condition that do not change the modeling but continue to use the original model. So there are lot of constrain conditions, no large alternations to the origin model is allowed. Nevertheless, the new structure is still an effective means in optimizing the existence structure. In automobile body structure design, the design logic can only

---

F2012-H02-003

---

Y. Bu (✉)

Brilliance Automobile Engineering Research Institute, Shenyang, China  
e-mail: yingchun.bu@brilliance-auto.com

be realized when it connected with the techniques as pressing, welding, painting and others, to get a good combined result.

**Keywords** Extended body · Structural design · Joint process · Vehicle quality

The vehicle body of light vans is composed of a series of complex space curved surfaces. It is a kind of transportation means not only, but a handiwork as well. As a handicraft work, the van body should have features of smoothness, beautiful modeling, and fairing surfaces; while as transportation means the body have various carrying space to meet various demands. At present, to meet the demand of market, all domestic automobile manufacturing works are try the best to develop vehicles with extended and widened body, based on the standard model of light vans, in order to expand the carrying space.

The body of light vans is composed mainly of left and right fenders, door assembly, front panel assembly, roof panel, chassis frame, floor, etc. The extended body needs to extend mainly the side fender, roof panel, frame and the floor, thus to enlarge the longitudinal size of the body. The extended side fender is the most important part in all the metal panel parts, as it has special position in the body. It should have smooth outline contours, and enough stiffness at the same time, so the design of extended body structure may affect directly the surface quality, outline dimension, strength and rigidity of the body [1].

## 1 Extended Side Fender Structure and Technological Analysis

In production process of large batch production of light vans, the side fender is commonly made of one steel sheet, pressed by moulds to form a whole side fender. But due to limitations of many factors, such as size of the work table of the press equipment, the influence of the mass of the mould to the lifting equipment, the extended side fender of light van body could usually not been made as a whole panel. Most manufacturing works make the side fender by jointing of three or two side panels to form the final side fender, to overcome all these unfavorable factors [2].

According to the market demands, based on the standard model, a extended model with right-hand steering wheel should be developed, for exporting. The length of bare body of standard model is 4826 mm, which should be extended to 5156 mm, 330 mm longer; one row of passenger seats is added, making the total seats to 14; as shown in Fig. 1 (where 1 rear port of side fender; 2 front port of side fender; 3 front panel; 4 roof panel).

After extending, the side fender of the body is extended from 3427 mm of the standard model to 3757 mm. Due to the limitation of pressing equipments, the side fender is divided into two sections, front and rear.

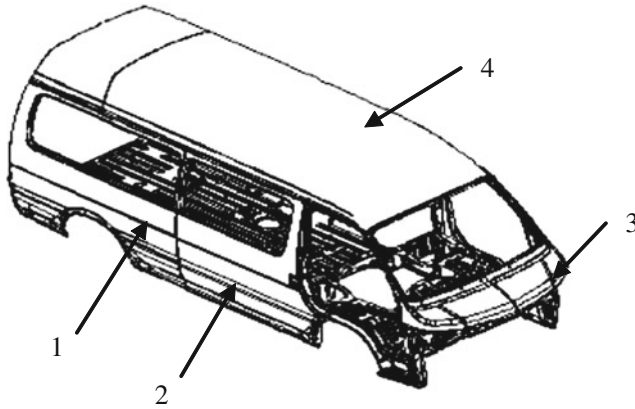


Fig. 1 Extended Body

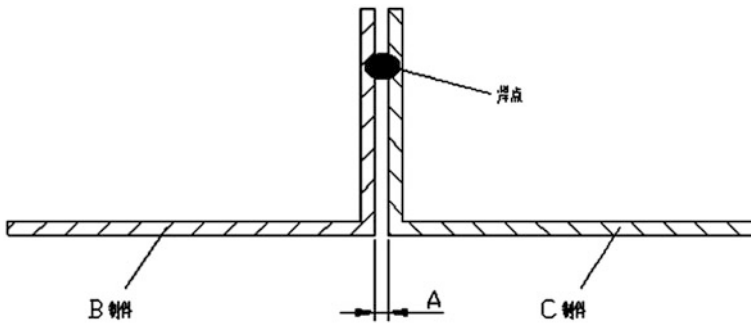


Fig. 2 Butt spot-welding

At present, the structure and technology of home models of extended body adopt commonly butt spot-weld method or argon arc soldering method, with features as following:

### 1.1 For Butt Spot-Welding

Owing to the manufacturing tolerance of the pressed parts and the positioning tolerance of the fixtures, gaps A or interfere may usually appear between part B and C in butt spot-welding (Fig. 2), thus the part B and part C could not be located with positioning pins, the result is that every side fender, jointed of B and C, will have their own length, different with all others, that will also influence mounting size of body accessories and the overall length of the vehicle. Besides, in welding

**Table 1** Comparison of relevant parameters

	Length of side fender (mm)	Material thickness (mm)	Drawing depth of product (mm)
HIACE	3757	0.8	168
XXX model	2945	0.9	177
D-value	612	-0.10	-9.00

it is difficult to ensure the surface of B and the surface of C falling into the same plane, thus damage the smoothness of the outside surface of the side fender [3].

## 1.2 For Argon Arc Soldering

Before soldering, all parts have to be carefully processed and cleaned, get rid of all greasy dirt and oxidation film, and ensure the mounting clearance; after soldering, it needs to ground the weld beads, making them transit smoothly with the surfaces of front and rear side fenders. The height of HIACE side fender is 1538 mm, to ground such a long weld bead will be a hard work for the worker, usually one man can only conduct ten sets in one shift. On the other hand, as the thickness of the part is only 0.8 mm, after welding and cooling uneven area will appear around the weld seam. This kind of defect could not be repaired; it may only be compensated with putty smearing process when the assembly is transferred to the painting workshop. But this technique is a backward one, the coating is easy to be stripped, the working efficiency is not high as it is a kind of manual work, and finally the outline quality of the vehicle could not be ensured [4].

Both above processes could not meet the requirement of modern production and high quality products, so we should develop a technique for large batch production, to achieve good outline quality, right overall size, high working efficiency, and low labor strength.

Before, the left side fender structure of the XXX van model is made of two butted side fenders, front and rear, the welding process for them is the single-side spot-weld plus shock absorb glue. That method is imported from Japan, with good practice.

The overall size, thickness of outer plate, and the drawing depth of side fender parts are quite different to the XXX model, as in Table 1.

It is clear the length of side fender is 612 mm larger than XXX model's, the thickness is 0.1 mm less than that, and the drawing depth is 9 mm less, therefore the plastic deformation of HIACE is less than that of XXX model, and both the stiffness and strength are less than XXX model. In production of HIACE standard model, as the side fender is relatively larger, and with flat shape and less plastic deformation, the central portion always have larger and shallow depressions. Now the length of extended model is 330 mm longer than that of the standard model, if there is no enough plastic deformation, the rigidity of extended side fender, composed by welding of the front and rear portions, will be further small than that of the standard model.



## **2 Structure Design and Technological Analysis of the Extended Side Fender**

Under the condition that the original modeling has to be followed and no alteration is allowed, the body design has to be able to ensure the joint of front and rear portion keep firm, and the rigidity of the side fender stronger [5].

### ***2.1 Ensure Firm Joint of Front and Rear Portion of the Side Fender***

In running of the vehicle, if the stiffness of the extended side fender is not good, vibration may be easily produced. Under the working of force in Y direction, the amplitude of vibration of front and rear portion may not be the same, that may result in the cracking of weld seam at that point; and the painting coat may be cracked or even strip-off, to damage the outline quality and the quality of the vehicle.

To ensure the firmness of the joint, according to the features of HIACE body, and referring to the structure of XXX model, we develop the joint technique of single-side spot welding plus liquid glue. In the XXX model, the technique used is single-side spot welding plus shock absorbing glue, where the glue works only for shock absorbing, no effect to the joint of the front and rear fender part; Here, the liquid structure glue may reduce the dent deformation produced by the welding, thus to improve the joint strength of the front and rear portion, to improve the serviceability of the steel plate, remove the stress concentration, and then improve greatly the crash safety and service life of the side fender. Besides, add double row weld spot at the butt joint of the middle and lower portion, thus to improve the joint performance of the front and rear side fenders.

The enlarged view in Fig. 3 show mainly the position and the form of the weld spot for front and rear side fenders.

### ***2.2 Ensure the Structure Strength of the Body***

From A–A section in Fig. 4, it can be seen there are reinforced plate and bracing piece been used to reinforce the butt joint of the front and rear side fender. Place the reinforced plate at the middle portion of the extended fender, weld the plate to the windowsill of the extended fender at the butt position, and bond the inner surface of the side fender with liquid structure glue, making the front and rear portion of the fender to form an integer part, thus to ensure they have enough strength and rigidity; For the third study of the fender, apply expansion glue under the window of the fender, which will expand after heating to firmly attached to the inner surface of the fender, to support the contour of the fender, and then reduce the vibration in running (see Fig. 4) [6].

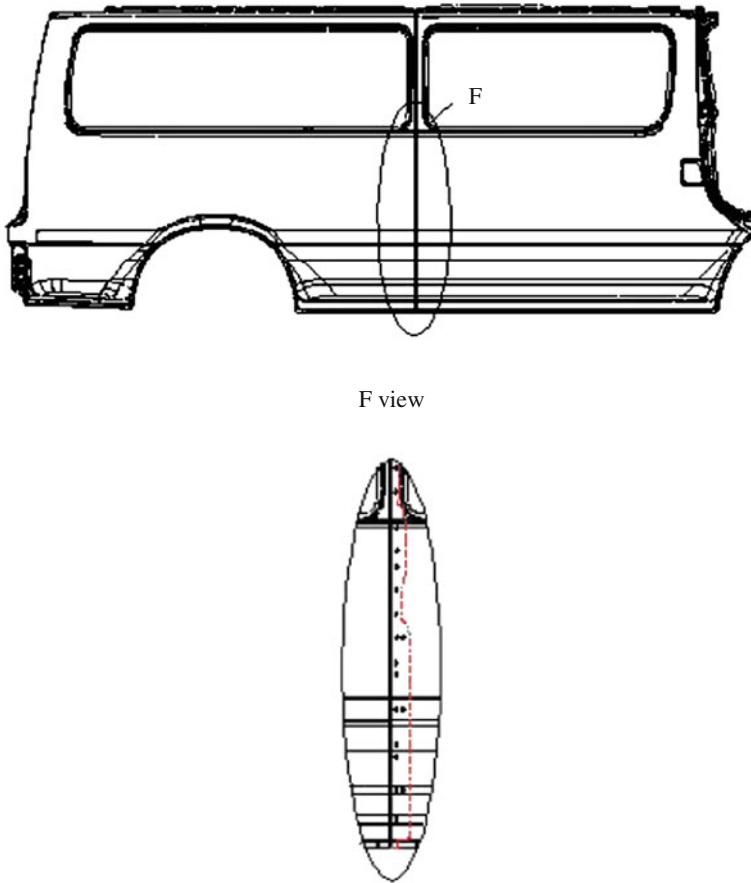


Fig. 3 The Position and The Form of The Weld Spot for Front and Rear Side

### ***2.3 Ensure the Outward Appearance and Improve Production Efficiency***

Adopting this butt joint structure, the main positioning of the front part of the fender in welding is at the frame of the driver's door, where for the rear part is at the rear back lamp, thus it may compensate the processing tolerance of the pressed parts, ensure the overall size of the welded rear side fender, and then ensure the overall dimension of vehicle, avoiding the defect that the front and rear portion are not in same plane due to spot welding, and finally ensuring the smoothness of the outer surfaces of the front and rear side fenders.

Above three designs make the joint of front and rear portion of the side fender keep firm, without tendency of relative vibration, ensuring no crack and/or strip-off on the painting coat. They make the vehicle always be an integer body in running,

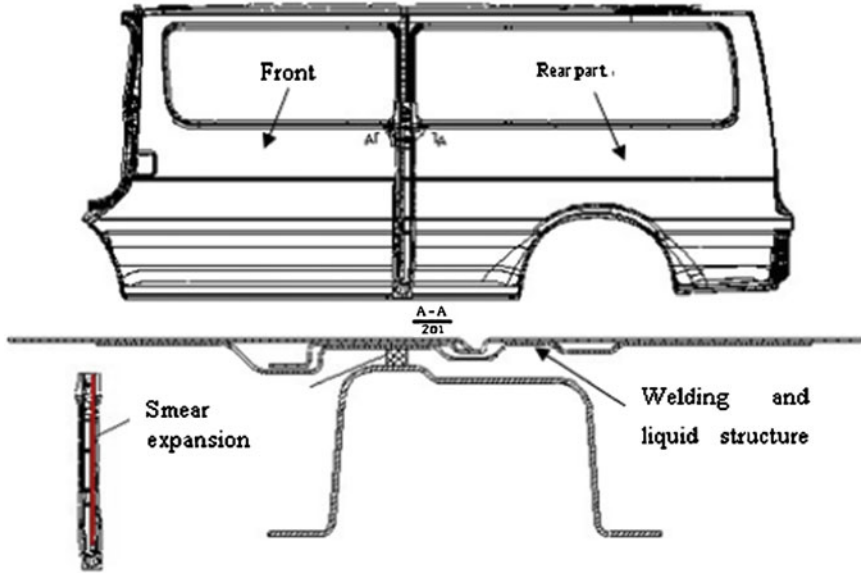


Fig. 4 Body Structure

make the vehicle undergoes the 60000 km road test (15000 km intensified road test), meet thoroughly the technical requirement.

The left-hand extended van takes the same structure for its extended side fender, thus the quality and production efficiency of that model vans are also improved greatly.

This kind of joint structure of van body is firstly bring designed, so the national patent office has approved the “New joint structure of extended van body” as a national utility model.

## References

1. Ling N (1997) Automobile design. Mach Ind Press, Beijing
2. Li S (1982) Pressing technology. Mach Ind Press, Beijing
3. Yang W (1996) Automobile assembly-welding technology and fixture design. Inst Technol press, Beijing
4. Shen H (2004) Welding technology and tactics. Mach Ind Press, Beijing
5. Song X (2006) Automobile body manufacturing technology. Inst Technol press, Beijing
6. Lin Z (2005) Automobile body manufacturing quality control technology. Mach Ind Press, Beijing

# High Temperature Oxidation Resistance and Mechanical Properties of Uncoated Ultrahigh-Strength Steel 22MnB5

Zaiqi Yao, Fangwu Ma, Qiang Liu, Fuquan Zhao, Fangfang Li, Jianping Lin, Xiaona Wang and Wei Song

**Abstract** High temperature oxidation resistance, flow stress curves and forming limit diagram (FLD) of the uncoated hot stamping steel sheet 22MnB5 were investigated in this paper. Compared with the specimens heated at 850 and 950 °C, the specimens austenitized at 900 °C have better surface quality, but oxidation layer without exfoliated still exists. In the temperature range of 500–900 °C with the strain rates of 0.45, 0.10 and 0.015 s<sup>-1</sup>, the isothermal flow stress of 22MnB5 with austenite microstructure satisfied the classical Inoue Katsuro constitutive equation:  $\sigma = K\epsilon^n \dot{\epsilon}^m$ . The least squares curve fitting results show that constitutive equation satisfied  $\sigma = K \exp(\beta/T) \epsilon^{n(T, \dot{\epsilon})} \dot{\epsilon}^{m(T)}$  during the nono-isothermal deformation. Based on the parameters obtained by tensile tests, the bulging processing was simulated and analyzed using ABAQUS software. The results of simulation date and tests date about failure mode and FLD of specimen are consistent, so the creditability and rationality of simulation method are verified.

**Keywords** Hot stamping · 22MnB5 · High temperature oxidation resistance · Forming curve · UHSS

---

F2012-H02-007

---

Z. Yao (✉) · F. Ma · Q. Liu · F. Zhao · X. Wang · W. Song  
Geely Automobile Research Institute Co., Ltd, Linhai, China  
e-mail: yaozaiqi@gmail.com

F. Li · J. Lin  
College of Mechanical Engineering, Tongji University, Shanghai, China

## 1 Introduction

In recent years, to meet the overall requirements of automotive lightweight and crash safety, hot stamping technique is widely applied in the automotive industries [1, 2]. Hot stamping is a non-isothermal forming process for sheet metals: firstly, the as-delivered boron steel with ferritic-pearlitic microstructure austenitizing at the elevated temperature, and then the component with fine-grained martensite formed through hot stamping and subsequent quenching in water cooled die. The tensile strength of steel after hot stamping may be improved to 250 % of initial value, and percentage elongation still remained about 7–10 %. The hot stamped parts applied in the automotive industry are mainly body-in-white components, like A-pillar inner, B-pillar inner, bumper reinforcement, roof rail and tunnel etc. (see Fig. 1).

22MnB5 is one of the most typical hot stamping boron steels. This steel has acceptable hardenability and produces martensitic microstructure after proper hot stamping processing. The ultimate tensile strength after hot stamping is increased to about 1500 MPa. The 22MnB5 with Al–Si coating has excellent oxidation resistance at about 900 °C [3]. However, to reduce production cost, oxidation prevention of the uncoated sheet has been further investigated at high temperature recently [4].

Flow stresses and forming limits of sheets are the important index for their formability at elevated temperatures. The effect of forming temperature on stress–strain curves of boron steel was investigated and their typical constitutive equations have been reviewed [5–11].

Generally, the relationship between the flow stress of 22MnB5 steel and  $\varepsilon$ ,  $\dot{\varepsilon}$ ,  $T$  is described by the following equations [6]:

$$\sigma = \sigma(\varepsilon, \dot{\varepsilon}, T) \quad (1)$$

Until now, there are some errors between the fitted value for several constitutive equations and measured value of the hot stamped steel sheet. Therefore, simulation analyzed date of hot stamping processing have poor precision based on the parameters obtained by constitutive equations.

In this paper, high temperature oxidation resistance of 22MnB5 steel sheet was evaluated at different austenitizing temperatures firstly. Base on experiments about the flow stresses and isothermal forming limits of the 22MnB5 at different temperatures, typical constitutive equations were derived using interpolation method. As analogical method, the flow stresses were derived at different temperatures, which offer effective input for hot stamping simulation. Compared with stamping experiment dates, the FLD and bulging fracture modes were simulated and analyzed using ABAQUS software.

**Fig. 1** Several hot stamped parts in automotive industry



## 2 Materials and Methods

### 2.1 Surface Morphologies at Elevated Temperatures

The quenchable 22MnB5 steel sheets (C: 0.22 %, Si: 0.23 %, Mn: 1.2 %, P: 0.015 %, B: 0.0014 %; in wt%) with thickness of 1.8 mm were employed for this experiment. The influence of temperature on the degree of oxidation of bare 22MnB5 steel sheets without stamping was first evaluated. The specimens were reheated to the austenitizing temperatures 850, 900 and 950 °C, at a rate of 15 °C/s, and austenitized for 5 min followed by cooling down in air for a few minutes.

The surface morphologies of the specimens were examined by digital cameras and scanning electron microscopy (SEM; Quanta 200 FEG). For further estimate the degree of oxidation on sheets, the mean elemental composition of each specimens surface was analyzed with energy dispersive X-ray spectrometer (EDX) incorporated into the SEM using the “area scanning” mode.

### 2.2 Hot Tensile Tests Using the Gleebe 3500 Machine

To investigate the material mechanical behaviour at elevated temperatures, uniaxial tensile tests were performed isothermally by using a Gleebe 3500 thermo-simulation machine. The standardized specimens were machined along the rolling direction with a height of 147.25 mm [12]. The specimens austenitized at 900 °C for 5 min followed by cooling down to the deformation temperatures of 500, 600, 700, 800 and 900 °C, respectively. A constant cooling rate of 35 °C/s for the cooling operation was realized. Strain rates of 0.45, 0.10 and 0.015 s<sup>-1</sup> were selected as the forming process parameters. The specimens were drawn isothermally to failure, and then liquid nitrogen quenched.



**Fig. 2** The experimental apparatus and simplified FE model used for the simulation of hot metal sheet forming

### 2.3 Forming Limit Tests and Simulation

A sheet forming processing was analyzed in 800 °C using the commercially available FE package, ABAQUS/Standard in this study. The modelled blank, die, and punch are corresponding to the experimental setup (see Fig. 2). The mechanical contact between blank and tools is defined using a kinematic contact method. Both of temperature of blank and die was assumed to 800 °C. The friction force is modelled as rate-independent friction model with a static friction coefficient of 0.15. The value of  $R$  is 1.0, meaning the sheet is isotropic. The punch has a velocity of 30 mm/s. The Young's modulus and Poisson's ratios as a function of temperature are taken from the literature [5]. The plastic deformation properties of 22MnB5 steel were obtained from the tensile tests in this study (Sect. 3.2).

For comparison with simulation results, forming limit tests of steel sheets 22MnB5 in the metastable austenitic phase are performed to validate the prediction models for FLD of steel 22MnB5. The tests are regarded as isothermal forming at 600, 700 and 800 °C since temperature variation of specimens was not so pronounced. The testing is carried out on a 2000 kN hydraulic press including a hemispherical punch with diameter of 100 mm. The experimental apparatus is shown in Fig. 2a. The test scheme and procedure are those of the Nakajima test according to ISO 12004, the length of all tested dog-bone specimens is 180 mm, variations of the strain path and the average strain rate are obtained by reducing the width of specimens from 180 to 20 mm. Ground grids with diameter of 2.5 mm were printed onto the surface of specimens by applying photochemical etching method in case of the grids to be illegible after heat treatment.

During the Nakajima tests, the specimens are austenitized at 900 °C for 5 min according to actual hot stamping process firstly, and then the specimens were rapidly transferred into the testing apparatus. When the temperature of specimens reduced to determinate temperatures at 600, 700 and 800 °C, tests were immediately performed with stamping velocity of 30 mm/s and finished in no more than 1.0 s.

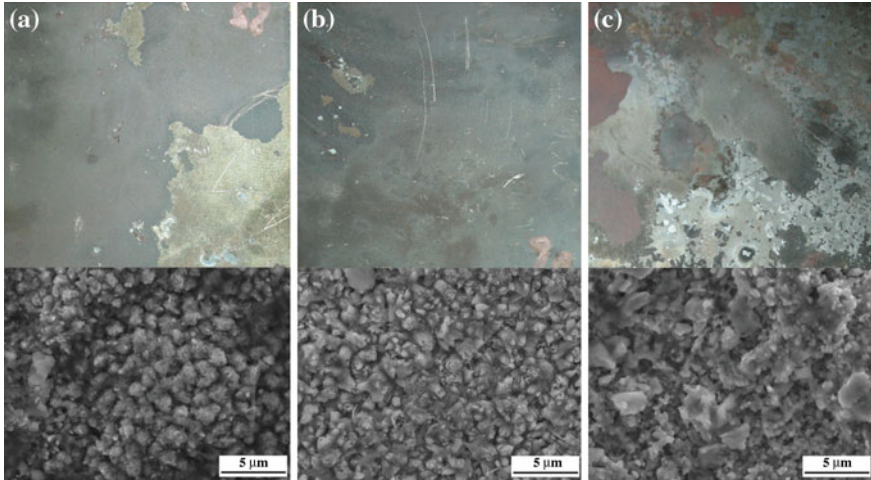


**Fig. 3** Surface morphologies of heated sheets after different heat treatment: **a** 850 °C, **b** 900 °C, **c** 950 °C

### 3 Experimental Results and Discussion

#### 3.1 High Temperature Oxidation Resistance

Surface morphologies of the 22MnB5 steel sheets after heat treatment at 850, 900 and 950 °C are illustrated in Fig. 3. The small exfoliation and severe exfoliation of surface layers were observed by means of macro photographs at 850 and 950 °C, respectively. Whereas the oxide scales just appear and the exfoliation is not observed at 900 °C. The SEM surface morphologies (see underside of Fig. 3) of the sheets heated at 900 °C are uniform and dense and free of cracks, which is better than those of others. As determined by EDX, the oxygen content is 34.42 at.% in the oxidation layer heated at 900 °C, which were considerably higher than those in the layer heated at 850 °C about 41.87 at.% and at 950 °C about 40.19 at.%, thus evidencing thinner oxidation layer on the sheet heated at 900 °C.

Although the bare 22MnB5 steel sheets show the better oxidation resistance performance at 900 °C, but the excessive oxide scale still may hinder the heat conduction properties and alter the tribological properties between the steel and the dies in actual hot stamping processing. In order to avoid scale formation and decarburization, a hot stamping method carried out several surface protection methods: (1) reducing gas atmosphere [13]; (2) using lubricant oils [4]; (3) aluminized coating [14]; (4) Al-Si coating [15]; (5) galvanized coatings [16] and so on.



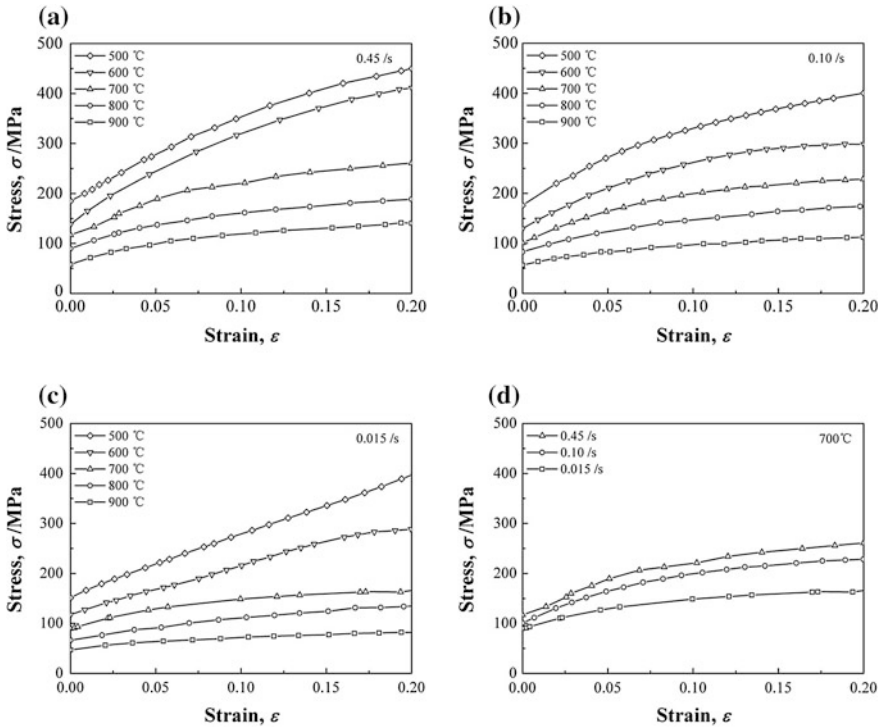


**Fig. 4** The flow curve properties of 22MnB5 to temperature at strain rate equal to  $0.45 \text{ s}^{-1}$  (a),  $0.10 \text{ s}^{-1}$  (b),  $0.015 \text{ s}^{-1}$  (c) and to strain rate at initial testing temperatures of 500, 600, 700, 800 and  $900 \text{ }^\circ\text{C}$  (d)

### 3.2 Flow Behavior of 22MnB5

Figure 4 shows the material sensitivity of 22MnB5 to strain rate and temperature at austenitizing temperature region ( $500\text{--}900 \text{ }^\circ\text{C}$ ): temperature has a strong effect while strain rate seems less influencing the material properties. With increasing deformation temperature, the flow stress of 22MnB5 reduced at the same strain rates (see Fig. 4a, b and c). Especially, when the temperature exceeds  $700 \text{ }^\circ\text{C}$ , the stress reduced significantly. This was mainly because the material yielding shows softening phenomenon at high temperature. Under the same deformation temperature (see Fig. 4d), the flow stress curves increase with the strain rates, the main cause of this kind of phenomenon is that there is not sufficient time to soften at higher strain rates.

Compared with several constitutive equations by many researchers, the stress–strain curves match Inoue Katsuro power exponent during plastic deformation function model as followed:

$$\sigma = K \dot{\epsilon}^n \epsilon^m \quad (2)$$

**Table 1** The parameters of Inoue Katsuro constitutive equation

Temperature (°C)	<i>K</i>	<i>m</i>	<i>n</i>		
			0.015/s	0.1/s	0.45/s
900	233.178	0.196	0.148	0.200	0.218
800	332.112	0.165	0.170	0.204	0.246
700	440.030	0.162	0.187	0.212	0.252
600	678.980	0.144	0.250	0.270	0.295
500	811.188	0.108	0.269	0.278	0.316

where,  $\sigma$  is flow stress;  $K$  is strain hardening coefficient;  $\epsilon$  is strain value;  $\dot{\epsilon}$  is strain rate;  $n$  is strain hardening exponent;  $m$  is strain rate sensitivity.

By logarithmic transformation of analytic solutions express the tress–strain relationship during plastic deformation. The equation  $\ln\sigma = \ln K + n \ln \epsilon + m \ln \dot{\epsilon}$  was fitted using least square fitting method. The fitting results are all  $y = ax + b$ , where  $a$  is strain hardening exponent  $n$ ,  $b$  is  $\ln K + m \ln \dot{\epsilon}$ .

As a result, the values of  $K$ ,  $n$  and  $m$  at different temperatures and different strain rates were shown in Table 1. The date of stress and strain at other temperature and strain rate were further obtained based on the above-mentioned constitutive equations using interpolation method.

The data have been approved for simulation software of hot stamping process, which can save a lot of time and experimentation costs (Table 1).

However,  $K$ ,  $n$  and  $m$  are all function of deformation temperature  $T$ . To assume that standard reference temperature is 500 °C. According to previous experience of other researchers, the constitutive equation with temperature-dependent was derived as follows:

$$\sigma = K(T)\epsilon^{n(T,\dot{\epsilon})}\dot{\epsilon}^{m(T)} \tag{3}$$

$$K(T) = A\exp(\beta/T) \tag{4}$$

$$\sigma = A\exp(\beta/T)\epsilon^{n(T,\dot{\epsilon})}\dot{\epsilon}^{m(T)} \tag{5}$$

where,

$$n(T) = n_0\exp(-C_n(T - T_0)) \tag{6}$$

$$n(\dot{\epsilon}) = (1 + \gamma\dot{\epsilon})n(T) \tag{7}$$

$$n(\dot{\epsilon}, T) = (1 + \gamma\dot{\epsilon})n_0\exp(-C_n(T - T_0)) \tag{8}$$

$$m(T) = m_0\exp(C_m(T - T_0)) \tag{9}$$

$n_0$  is strain hardening exponent during quasci-static strength test at 500 °C;  $m_0$  is strain rate sensitivity at 500 °C;  $A$ ,  $\beta$ ,  $C_n$ ,  $C_m$  and  $\gamma$  are constant.

Where,  $A = 79.2$ ;  $\beta = 1190$ ;  $n_0 = 0.267$ ;  $C_n = 0.00158$ ;  $m_0 = 0.108$ ;  $C_m = 0.00133$ ;  $T_0 = 500$  °C;  $\gamma = 0.126$ . The Eq. 4 is applicable to fit stress-strain properties of 22MnB5 steel sheet approximately.

### 3.3 Forming Limit Diagram

Considering ever-changing temperature of 22MnB5 sheets during hot stamping processing, the criterion of materials failure would be related with material performance at ever-changing temperature. For accurate predicate materials failure mode during non-isothermal forming processing, the isothermal FLD was compared with the forming limit predication model, which is the same with Boron-steel sheet, in order to establish the predication method for hot forming limits in related with deformation temperature. The FLD related with deformation temperature will be obtained using this mentioned model and the flow curve properties at elevated temperature.

Figure 5 shows the strain distribution of the stamped samples with two different widths of 140 and 180 mm at 800 °C.

The simulation values of FLD at different temperatures (800, 700 and 600 °C) are shown in Fig. 7b. On the left hand side of FLD, the forming limit increases with the deformation temperature. On the right hand side, the forming limit increases with the forming temperature at 600–700 °C, but at 800 °C, with the larger minor strain, the forming limits decrease.

The temperature of austenitized specimens reduced to 800, 700 and 600 °C, then isothermal-like bulging immediately, respectively. The stamped samples with different width are shown in Fig. 6a, b and c. As the deformation temperature increases, the dilacerations of specimens are getting narrow. Three kinds of grids on the stamped samples were selected and measured to determine the FLD. They are marginal, critical and cracked grids as shown in Fig. 6d. The critical grid covers the width of necking band. The marginal grid is next to the critical grid and is out of localized necking. The cracked grid is closed to the critical grid but fractured. The major strain  $\varepsilon_1$  is  $\ln(l_1/d)$  and the minor strain  $\varepsilon_2$  is  $\ln(l_2/d)$ .

Figure 7a describes in the form of the formability limits that were obtained at 600, 700 and 800 °C by varying the strain path from equal biaxial stretching to uniaxial stretching. On the left-hand side of FLD, the forming limit curves (FLC) with the minus slope increase as the forming temperature increases from 600 to 800 °C; on the right-hand side of FLD, the tendency of the forming limit curve at 600 and 700 °C is opposite with those of sample stamped at 800 °C: by increasing the minor strain, the major strain is increased at 600 and 700 °C, and the increasing rate of FLC at 600 °C is large than those of FLC at 700 °C, meaning curve slope is shifted up; by increasing the minor strain, the major strain is decreased at 800 °C.

On the both side of FLD, the forming limit cures accord with same linear relationship between minor strain and the major strain at 800 °C, as shown Eq. 10.

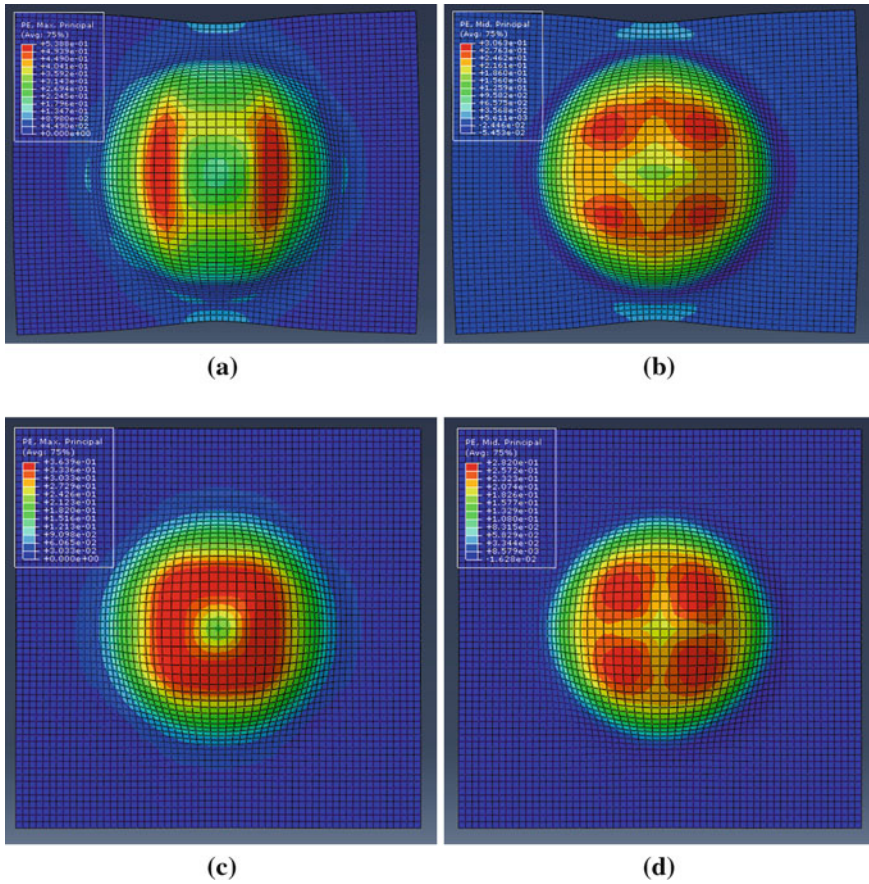


**Fig. 5** Strain distribution of stamped samples with different width: **a** 180 × 140 mm, major strain; **b** 180 × 140 mm, minor strain; **c** 180 × 180 mm, major strain; **d** 180 × 180 mm, minor strain

On the left and right sides, the forming limit curves accord with linear relationship at 600 and 700 °C as shown Eqs. 11 and 12, respectively.

$$\varepsilon_1 = 0.56 - 0.63\varepsilon_2; \text{ at } 800^\circ\text{C} \tag{10}$$

$$\varepsilon_1 = 0.50 - 0.65\varepsilon_2(\varepsilon_2 < 0), 0.50 + 0.43\varepsilon_2(\varepsilon_2 \geq 0); \text{ at } 700^\circ\text{C} \tag{11}$$

$$\varepsilon_1 = 0.48 - 0.69\varepsilon_2(\varepsilon_2 < 0), 0.48 + 0.91\varepsilon_2(\varepsilon_2 \geq 0); \text{ at } 600^\circ\text{C} \tag{12}$$

Numerical results are compared to experimental results to show the acceptable agreement.

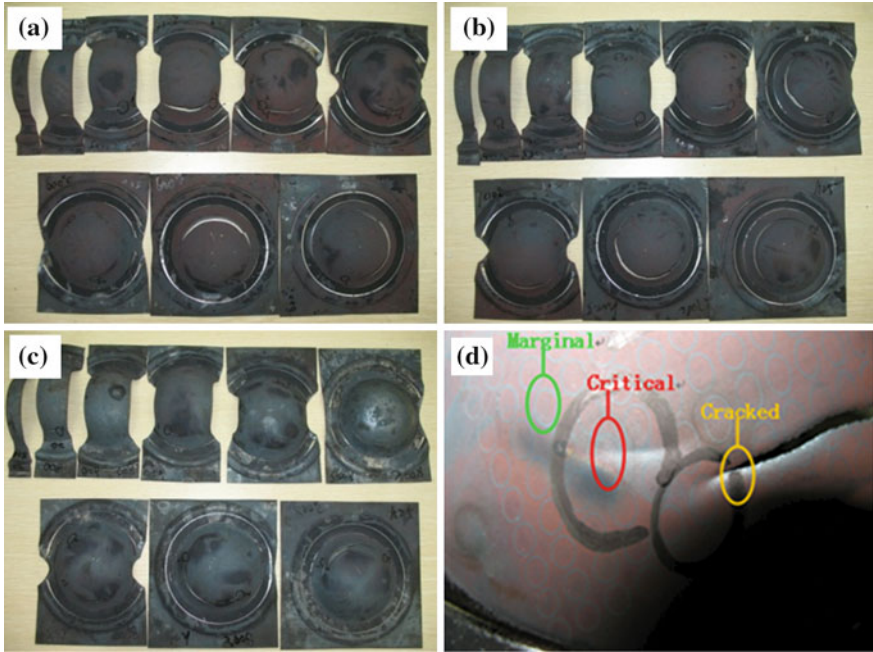


Fig. 6 Stamped samples of 22MnB5 sheets: a 600 °C, b 700 °C, c 800 °C, d illustration of limit strains measuring

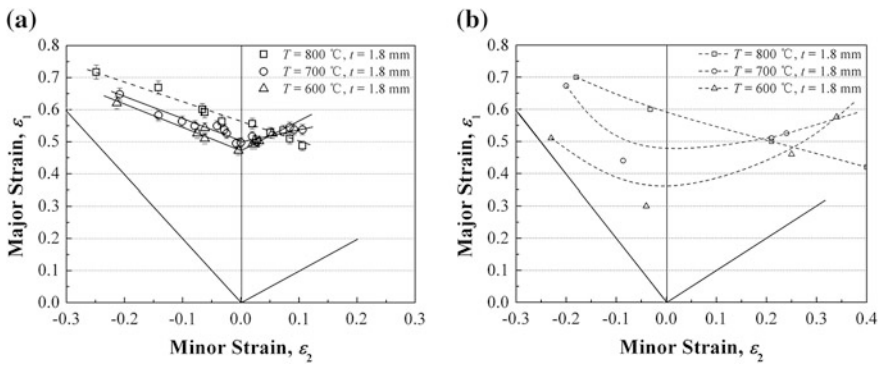


Fig. 7 FLD of 22MnB5 at different temperatures by experiment (a) and simulation date (b)

### 4 Conclusions

High temperature oxidation resistance, flow stress curves and forming limit diagram of the uncoated hot stamping steel 22MnB5 were investigated.

- (1) Compared with the specimens heated at 850 and 950 °C, the specimens austenitized at 900 °C have better surface quality, but oxidation layer without exfoliated still exists.
- (2) In the temperature range of 500–900 °C with the strain rates of 0.45, 0.10 and 0.015 s<sup>-1</sup>, the isothermal flow stress of 22MnB5 with austenite microstructure satisfied the typical Inoue Katsuro constitutive equation:  $\sigma = K\epsilon^n \dot{\epsilon}^m$ . The least squares curve fitting results show that constitutive equation satisfied  $\sigma = K \exp(\beta/T) \epsilon^{m(T,\dot{\epsilon})} \dot{\epsilon}^{m(T)}$  during the nono-isothermal deformation.
- (3) The results of simulation date and tests date about failure mode and FLD of specimen are consistent, so the creditability and rationality of simulation method are verified.

**Acknowledgments** This work was financially supported by the Supporting Program of the “twelfth Five-year Plan” for Sci & Tech Research of China [2011BAG03B00]. The authors would like to thank Benteler for their support regarding the supply with 22MnB5 sheet for free.

## References

1. Karbasian H, Tekkaya AE (2010) A review on hot stamping. *J Mater Process Technol* 210(11):2103–2118
2. Åkerström P (2006) Modeling and simulation of hot stamping. Luleå University of Technology, Sweden
3. Borsetto F, Ghiotti A, Bruschi S (2009) Investigation of the high strength steel Al-Si coating during hot stamping operations. *Key Eng Mater* 410–411:289–296
4. Mori K, Ito D (2009) Prevention of oxidation in hot stamping of quenchable steel sheet by oxidation preventive oil. *CIRP Annals Manuf Tech* 58(1):267–270
5. Naderi M, Durrenberger L, Molinari A, Bleck W (2008) Constitutive relationships for 22MnB5 boron steel deformed isothermally at high temperatures. *Mater Sci Eng A* 478(1–2):130–139
6. Merklein M, Lechler J, Geiger M (2006) Characterisation of the flow properties of the quench enable ultra high strength steel 22MnB5. *Ann CIRP* 55(1):229–232
7. Cui J, Lei C, Xing Z, Li C, Ma S (2012) Predictions of the mechanical properties and microstructure evolution of high strength steel in hot stamping. *J Mater Eng Perform*. doi:10.1007/s11665-012-0180-9
8. Rao KP, Prasad YKD, Hawbolt EB (1996) Hot deformation studies on a low-carbon steel Part 1—flow curves and the constitutive relationship. *J Mater Process Technol* 56(1–4):897–907
9. McQueen HJ, Ryan ND (2002) Constitutive analysis in hot working. *Mater Sci Eng A* 322(1–2):43–63
10. Molinari A, Ravichandran G (2005) Constitutive modeling of high-strain-rate deformation in metals based on the evolution of an effective microstructural length. *Mech Mater* 37(7):737–752
11. Mirzadeh H, Cabrera JM, Najafizadeh A (2011) Constitutive relationships for hot deformation of austenite. *Acta Mater* 59(16):6441–6448
12. Min JY, Lin JP, Min YA, Li FF (2012) On the ferrite and bainite transformation in isothermally deformed 22MnB5 steels. *Mater Sci Eng A* 550:375–387

13. Wiberg S, Laumen C (2009) Verfahren zum Presshärten von Metalle. Patent EP2088213
14. Azushima A, Uda K, Yanagida A (2012) Friction behavior of aluminum-coated 22MnB5 in hot stamping under dry and lubricated conditions. *J Mater Process Technol* 212(5):1014–1021
15. Fan DW, Kim HS, Oh JK, Chin KG, De Cooman BC (2010) Coating degradation in hot stamping. *ISIJ Int* 50(4):561–568
16. Lee CW, Fan DW, Lee SJ, De Cooman BC (2011) 8th International conference on zinc and zinc alloy coated steel sheet, Genova, Italy, 2011, pp 327–334



# Systematic Optimization of Concurrent Design of Product and Locating Strategy by Datum Flow Chain

Shan Jun and Cao Jun

**Abstract** *Research and/or Engineering Questions/Objective.* In the vehicle building, the matching of outer surface, such as front face, is most important and is increasingly concerned by customers. Many companies and researchers commit themselves in the improvement of matching quality of vehicle. Basically, it is revealed that not only product design, but also the locating strategy of fixture design play a significant role in the improvement of matching quality. However, if we want get an optimized product design and locating strategy of fixture, traditionally it's quietly difficult because always the fixture design is carried out after the product design, and consequently is restricted by the fixed product design. It is obviously that if we want get an optimized scheme, many times lead to engineering change. So it is most valuable for us to find a systematic method for concurrent product and locating strategy design in the very early design stage, to achieve the high matching quality. *Methodology.* In this paper, the datum flow chain is introduced as a systematic approach in the development of concurrent design about product and locating strategy of jig fixture in the very early design stage. For instance, the structure and jig fixture design of fender and hood is taken. First, with given key characteristics, the datum flow chain is presented. Then, based on the datum flow chain, proper product and locating strategy design is carried out to bypass the maximum part variation to get a optimized dimension performance. *Results.* By the application of datum flow chain, we can find the preferred locating strategy immediately. To make a validation of application of datum flow chain, finally, a 2D tolerance analysis is carried out for two locating strategy, and it's indicated that datum flow chain can make a optimized locating

---

F2012-H02-008

---

S. Jun (✉) · C. Jun

Saic Motor Passenger Vehicle Co. Ltd., Shanghai, People's Republic of China  
e-mail: caojun@saicmotor.com



strategy design in the early product design stage. *Limitations of this study.* In this paper, the concurrent design of product and locating strategy by datum flow chain is only confined in a qualitative analysis in the very early stage. Further study can be how to carry out a quantitative analysis about the determined product and fixture design by using datum flow chain. *What does the paper offer that is new in the field in comparison to other works of the author.* Tolerance analysis is a powerful method to investigate whether the product and fixture design (locating scheme) meet the quality requirement, such as ADCATS, VisVSA, 3DCS. However, it is always applied in the detailed design stage, with determined structure. Meanwhile, Datum flow chain is a systematic approach about assembly design for optimizing dimensional performance, raised by Whitney, is extensively applied in many fields. However, its application in concurrent product and fixture design is fairly rare. In this paper, it is presented a method about the concurrent product and locating strategy design to get optimized matching quality in the very early design stage. *Conclusion.* By using DFC method, the concurrently structure design (“contacts” design) and locating strategy design can be carried out to by-pass the maximum variation (body variation). Consequently, the optimized product design and process design is realized in the very early stage to avoid time-consuming and expensive engineering change.

**Keywords** Datum flow chain · Matching quality · Locating strategy design · Product design · Concurrent design

## 1 Motivation

In the vehicle build, the matching of outer surface, such as front face, is most important and is increasingly concerned by customers. Many companies and researchers commit themselves in the improvement of matching quality of vehicle. Basically, it is revealed that not only product design and product quality, but also the locating strategy of fixture design play a significant role in the improvement of matching quality. However, if we want get an optimized locating strategy, traditionally it's quietly difficult because always the fixture design is carried out after the product design, and consequently is restricted by the fixed product design. It is obviously that if we want get an optimized scheme, many times lead to engineering change. So it is most valuable for us to find a systematic method for locating strategy design in the very early design stage, to achieve the high matching quality.

Tolerance analysis is a powerful method to investigate whether the fixture design (locating scheme) meet the quality requirement. Many method and software, such as, ADCATS [1] (Direct Linearization Method) developed by Kenneth W. Chase team of Brigham Young University, VisVSA, 3DCS (Monte Carlo method), is widely used in carry out the validation of locating strategy, however, it is always be applied in the detailed design stage, with determined

structure. Meanwhile, Datum flow chain is a systematic approach about assembly design for optimize dimensional performance, firstly raised by Whitney [2], is extensively applied in many fields, such as automotive industry, airplane, and so on. However, its application in fixture design is fairly rare.

In this paper, the datum flow chain is introduced as a systematic approach in the development of concurrent design of product (structure) and process (locating strategy of jig fixture) in the very early design stage. For instance, the jig fixture design of fender and hood is taken. First, two different locating strategy of fender and hood is presented, then the datum flow chain method is utilized to analysis the two different locating strategy, and the liaison graph is present consequently. By the application of datum flow chain, we can find the preferred locating strategy. To make a validation of application of datum flow chain, finally, a 2D tolerance analysis is carried out for two locating strategy, and it's indicated that datum flow chain can make a optimized locating strategy design in the early product design stage.

## 2 Methodology of Datum Flow Chain

In the datum flow chain theory, separated joints between parts are separated into two classes by Whitney [2]:

- “Mates” convey dimensional location and constraint from one part to another.
  - when all of a part’s mates are complete, it should be constrained in all six degrees of freedom unless free motion is part of its function.
- “Contacts” are redundant and provide strength or partial constraint.

By using Datum Flow Chain, instead of liaison diagram, is used to identify the part mates that convey dimensional control and identifies the hierarchy that determines which parts or fixtures define the locations of which other parts.

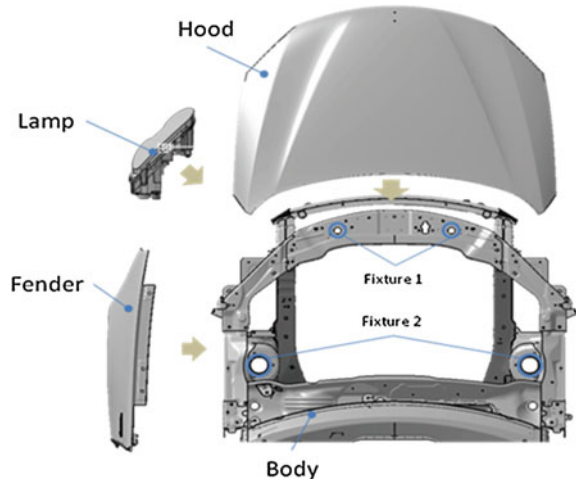
## 3 Systematic Optimization About Structure Design and Locating Strategy Design by Datum Flow Chain

### 3.1 Locating strategy #1

The matching between headlamp and hood is most sensitive to customer, and on another side, it's also difficult due to complicated and 3D dimension chain in the plant. So, it's important for us to make concurrent design of part structure and process (locating strategy of fixture) in the very early stage.

As shown in Fig. 1, it's an example of front face, including body, hood, fender and lamp. Hood is mounted onto body using fixture 1, and fender is mounted onto

**Fig. 1** Locating strategy #1  
(Fixture 1 and Fixture 2  
Using different locating hole)



body using fixture 2. Lamp is connected to fender directly and also mounted onto body.

The gap between lamp and hood is investigated as KC. As we all know, because of variation accumulation, the body consists of several hundreds parts, always has the maximum dimension errors, compared to the single lamp, hood and fender. So, in the very early design stage, we try to reduce the influence of body variation. The joints between lamp and body, hood and body, fender and body are designed to be slip type, and should be “contacts”, and do not convey dimensional control. For the locating strategy #1, corresponding DFC is illustrated in Fig. 2. As shown, in this locating strategy, the joints between lamp and fender, fender and fixture1, fixture 1 and body, body and fixture 2, fixture 2 and hood is “mates”. However, it can be found that, although the “contacts” design between lamp and body, fender and body, hood and body is utilized, the body variation also cannot be by-passed.

### 3.2 Locating Strategy #2

For the Locating strategy #2, as shown in Fig. 3, the fixture for hood and fender mounting is carried out by using common locating hole.

The DFC of locating strategy #2 is illustrated in Fig. 4. As shown, due to the same locating hole is used for fixture 1 and fixture 2, the variation between them is only determined by themselves. As a result, the body variation as the maximum one is by-passed. Consequently, by using the “contacts” structure design and proper locating strategy design, only out-surface part variations and fixture variation are contributed to the final matching quality.

Based on the analysis above on, the locating strategy #2 has more advantage in the achievement of matching quality, so it is chosen as the final product design and

**Fig. 2** Datum flow chain of locating strategy #1

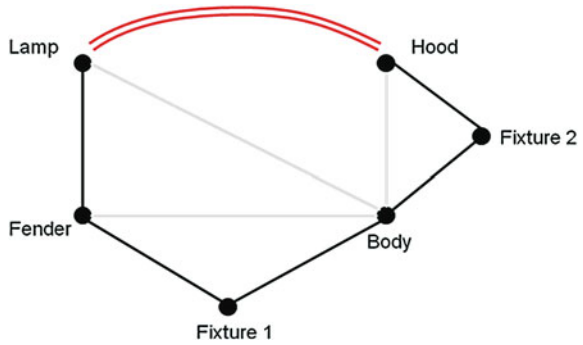


**Fig. 3** Locating strategy #2 (Fixture 1 and Fixture 2 using same locating hole)

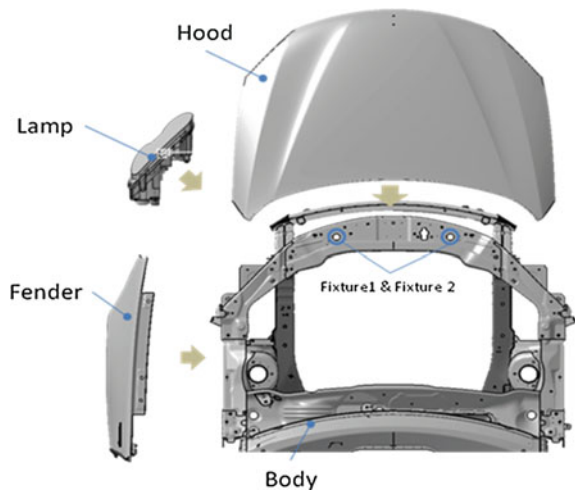
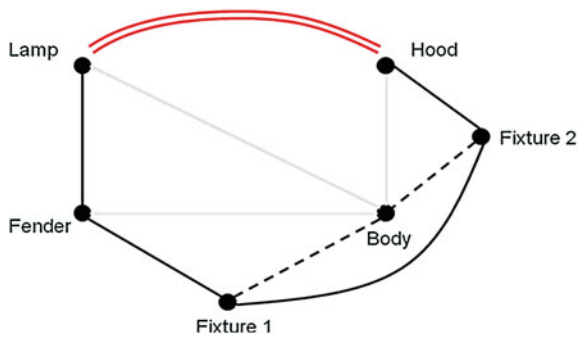


**Fig. 4** Datum flow chain of locating strategy #2



locating strategy. In the following words, one 2-way tolerance analysis is utilized to validate if it is available for the DTS requirement.

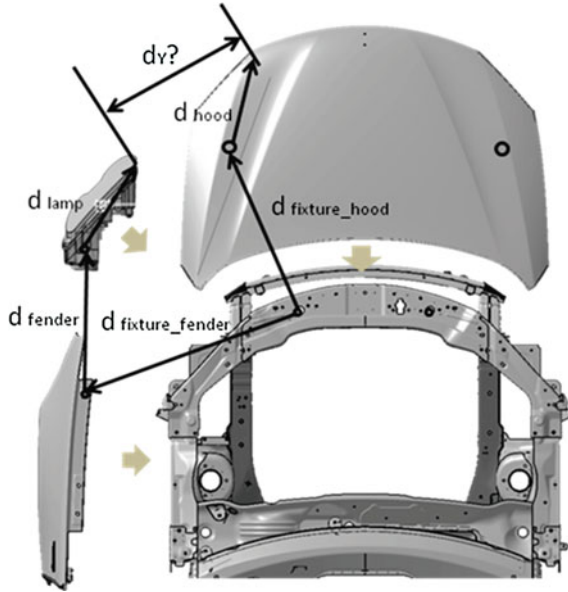


Fig. 5 The dimension chain of front face

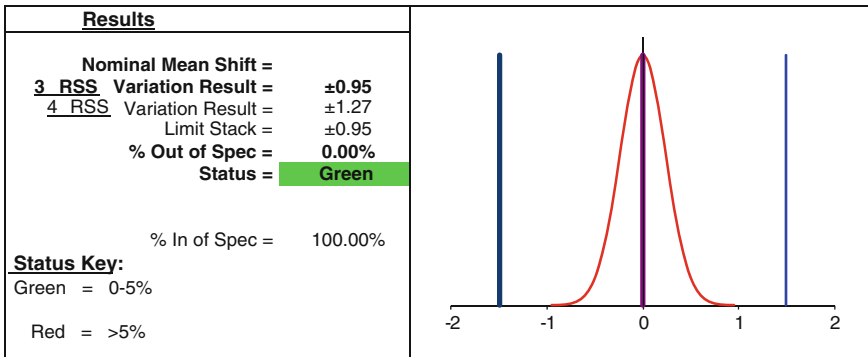


Fig. 6 OOS of locating strategy #2

### 4 2-Way Tolerance Analysis About the Locating Strategy #2

The dimension chain about locating strategy #2 is shown in Fig. 5. The tolerance of fixture locating pin is generally  $\pm 0.2$  mm,  $d_{\text{fixture\_hood}} = d_{\text{fixture\_fender}} = \pm 0.2$  mm, the tolerance of hood assembly  $d_{\text{hood}} = \pm 0.5$  mm, and the fender tolerance  $d_{\text{fender}} = \pm 0.3$  mm, headlamp tolerance  $d_{\text{lamp}} = \pm 0.7$  mm.

By using RSS method, the gap tolerance between hood and headlamp is:

$$\begin{aligned} d_Y &= \pm \sqrt{d_{\text{fixture\_hood}}^2 + d_{\text{fixture\_fender}}^2 + d_{\text{hood}}^2 + d_{\text{fender}}^2 + d_{\text{lamp}}^2} \\ &= \pm \sqrt{0.2^2 + 0.2^2 + 0.5^2 + 0.3^2 + 0.7^2} \\ &= \pm 0.95 \text{ (mm)} \end{aligned}$$

As shown in Fig. 6, DTS requirement is  $\pm 1.0$  mm, the tolerance  $\pm 0.95$  mm, out of spec is 0. So, this design can satisfy the DTS requirement.

## 5 Conclusions

In this paper, it is presented that by using datum flow chain, for the locating strategy design to get optimized matching quality in early product design stage of whole vehicle. For the whole vehicle, the variations of each part are very different. Based on DFC method, the concurrently structure design (“contacts” design) and proper locating strategy design is utilized to bypass the maximum body variation. Consequently, the optimized product design and process design is realized in the very early stage to avoid time-consuming and expensive engineering change.

## References

1. Chase KW (1999) Tolerance allocation methods for designers. University Hill, Provo
2. Mantripragada R, Whitney DE (1998) The datum flow chain: a systematic approach to assembly design and modeling. Res Eng Des 10(3):150–165

**Part III**  
**Welding, Joining and Fastening**

# Laser Remote Process Technology on Automotive Manufacture

Johannes Buehrle, Martin Bea and Ruediger Brockmann

**Abstract** This paper gives an overview on the state-of-the-art in remote laser applications with high power disk lasers. Remote welding and cutting applications unlock significant improvements in cycle time and equipment utilization compared with conventional methods. The main contribution comes from the virtually instantaneous positioning of the laser beam between two geometries. Most current welding application in automotive car body and subassembly are shown. The examples highlight the presented benefits of remote application. An overview is also given about remote cutting; two distinctly different cutting processes are presented and discussed. Examples for combined utilization of remote welding and remote cutting are given.

**Keywords** Solid state laser · PFO · Remote welding · “RobScan” process

Every minute the laser is waiting for parts, the welding system is literally in a holding pattern, which decreases the potential for increased throughput and revenue. To counteract this and maximize the economic justification for a laser welding system, the “beam on part” time should be as close as possible to 100 %. One thing that can be done to maximize “beam on” time is to utilize a process that has become known as remote welding.

While conventional laser welding uses a robot or a Cartesian system to manipulate the beam or work piece, remote welding uses a welding head with scanning mirrors on distance (hence “remote”), to position the focused laser beam

---

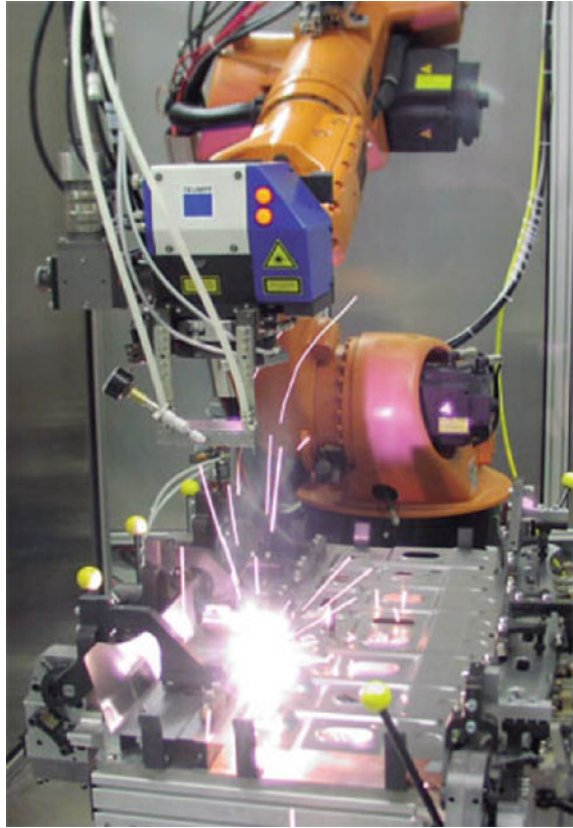
F2012-H04-002

---

J. Buehrle (✉) · M. Bea · R. Brockmann  
TRUMPF Laser- und Systemtechnik GmbH, Ditzingen, Germany  
e-mail: sarah.tang@cn.trumpf.com



**Fig. 1** Remote welding of automotive part



over the work piece. This means, the biggest potential of cycle time improvements, are not in the increase of beam on time, but in the significant off time reduction. The light weight and highly dynamic scanning mirrors enable extremely fast positioning in-between welds, which simply means the laser is spending more time joining parts and much less time waiting to be in position to create the next weld. The results are higher throughput, less stations, and lower costs.

Remote scanner welding is used for many automotive applications, including: seating (recliners, frames, tracks, panels), body in white (trunks, rear panels, doors/hang on parts, side walls, pillars) and interior (IP beams, rear shelf/hat rack); see Fig. 1. Compared to conventional laser welding, remote scanner welding has the following advantages:

- Reduced cycle time (via reduction of index time),
- Programmable weld shapes (ability to customize weld shape to optimize component strength),
- Large stand-off (longer protection glass life), and
- Reduced number of clamping fixtures (via reduced number of stations).

Remote laser welding, or so called “welding on the fly”, combines a robot and scanner optics to position the focused laser beam on the workpiece simultaneously (“on the fly”). It takes only a few seconds to join components like car doors with high integrity laser welds. The robot arm guides the scanner optics along a smooth path about half a meter over the workpiece. Extremely nimble scanning mirrors direct the focal point in fractions of a second from weld seam to weld seam. A fiber-delivered, solid state laser such as the TruDisk disk laser from TRUMPF is the source of the joining power far away from the processing station.

The scanning optic or programmable focusing optic (PFO) at the end of the laser’s fiber optic cable is the central element for precise positioning of the laser’s focus point on the component to be welded. Inside the PFO, two scanner mirrors direct the beam through a “flat field” optic, which focuses the beam onto a common focus plane no matter where it is in the work envelope of the PFO. The PFO is also equipped with a motorized lens that allows the focus plane to be moved up and down in the Z axis. The repositioning of the focused laser beam from one end of the entire work envelope to the other takes a mere 30 ms.

## **1 Remote Welding on the Fly**

There are three basic preconditions for welding on the fly: First, a laser with excellent beam quality and the appropriate power is required. Beam quality is the measure of focusability of a laser, and the long focal lengths required for remote welding necessitate superior beam quality (i.e. 4–8 mm-mrad) in order to achieve the appropriate focused spot size (i.e., about 0.6 mm) at the workpiece. For remote welding in automotive body production, typically about 4–6 kW of laser power is used.

## **2 Second a Precise and Dynamic Multi-Axis Robot or Positioning System**

Third, a precise positioning of the weld seams, which requires axis synchronization between the robot and the scanner control. This allows the weld shape programmed in the scanner control, let’s say a “C” shape, to really be a “C” shape with the robot moving at various speeds over the part to be welded. Some control architectures use “time” synchronization. The problem here is that if the robot speed is changed for any reason, the weld shape will also change because the axes are not synchronized.

**Fig. 2** Remote welding of door panel showing linear stitches and various size “C” or staple shaped welds



### 3 Optimizing the Process

Welding patterns in any selected shape and size can be achieved when welding on the fly with a PFO. Independent of robot speed, precise weld shapes can be used in the joining of components—a task that a rather clumsy and imprecise robot cannot attain.

Though linear welds require significantly less flange width than a resistance spot weld, sometimes other shapes, such as a C or staple-shaped weld, provide the ideal balance between increased strength and reduced weight (Fig. 2). Whether short lines, circles, C-shaped or S-shaped welds, the size, arrangement, and orientation of the laser weld seams allow for optimized weight and strength of the welded assembly.

Besides being able to optimize both strength and weight through strategic employment of weld seam shapes, laser welding’s single-sided access provides another advantage compared to resistance spot welding’s double-sided access. Closed cross sections, such as tubes and profiles used for frames, are much more rigid compared to open sections and formed sheet metal, thereby increasing vehicle strength while reducing weight and cost.

### 4 Maximizing Throughput

Compared to resistance spot welding, on the fly laser scanner welding represents a significantly more efficient alternative for an increasing number of automotive components. The relatively long re-positioning times associated with moving the spot welding gun from one weld location to another are almost completely eliminated with remote scanner welding. The continuous motion of the scanner head in combination with the rapid positioning of the laser focus point by the

scanner mirrors accounts for the dramatic increase in throughput. Not only this, but producing a laser weld with the identical strength of a resistance spot weld requires only a fraction of the time.

These time savings increase the throughput of welded assemblies and the number of seams produced on them. For the body in white shop, where sheet metal thicknesses are typically in the range of 0.6–1.8 mm thick, each weld spot requires about 2 s, whereas a comparable laser weld seam can be generated in less than 0.4 s. Thus, the welding time alone is reduced by a factor of five.

## 5 Paradigm for Series Production

Daimler AG was the first automobile manufacturer to use on the fly remote welding in series production. For this purpose, Daimler developed the “RobScan” process, which it has been using since 2007 at its factory in Germany (Bremen & Sindelfingen) and South Africa (East London) to weld C-class automotive body components. Today, nearly 70 RobScan systems are in use. The RobScan systems are equipped with the PFO 33 scanner and over 30 diode pumped disk lasers with output powers ranging from 3 to 4 kW.

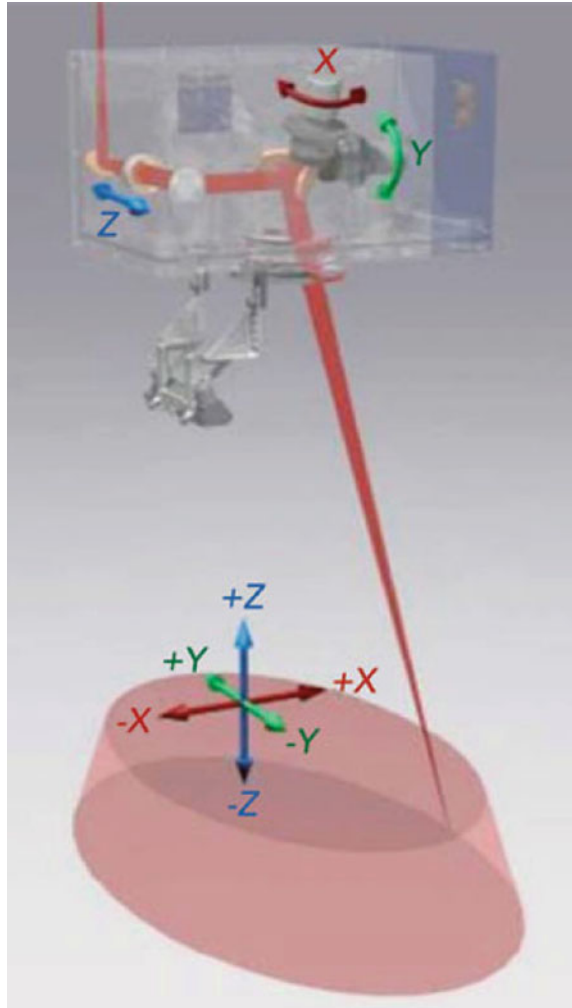
Since January 2009, Daimler has been working with the second generation of RobScan. Further optimized production quality and cost efficiency, due to shortened cycle times and improved utilization of the installed laser power, are among the advantages. These are achieved by means of four innovations: (1) Variable focus position of the laser beam along the Z axis, (2) reduced weld penetration, (3) further development of on-line weld quality control, and (4) off-line simulation in system programming.

The additional Z axis in the PFO 3D makes it possible to weld at different distances from the scanner optics, or up or down an incline, without changing the robot path in the Z axis (Fig. 3). Reducing penetration from full to partial decreases the amount of weld spatter and increases process speed without impacting weld strength.

The robot path can be programmed offline with new CAD simulation tools. The system tests the accessibility of all weld seams, carries out a collision test with the clamping device and optimizes the coordination of robot and scanner movement. This reduces installation and change-over time, improves the cycle times, and helps in the equipment planning of complex installations. Off-line simulation also ensures that the robot path and travel speed have been optimized.

Twenty systems of the new RobScan generation with the PFO 3D scanner have been added for E Class production at Sindelfingen. In the C and E class car bodies, welding on the fly with the new RobScan process has replaced up to 15 % of the resistance weld spots. Seven 6 kW disk lasers are used at Sindelfingen for production of the E class. By using the new scanner optics and the advanced robot path and simulation tools, the company was able to make further reductions in the number of remote systems needed for the E class series production.

**Fig. 3** PFO 3D illustration showing 3D work envelope



## 6 Efficiency Increase

One on the fly laser welding station replaces up to five conventional resistance spot welding stations. At the same time, just one or two clamping stations are enough to join structural components. This allows users to open free spaces in production because different components can be processed, or different processes, such as laser dimpling in addition to the laser welding, can be carried out all in one single laser welding station. In comparison to resistance spot welding, production time has been reduced by up to 80 %.

If just the processing speeds are compared, the welding speed at a laser power of 4 kW is about six times faster; at 6 kW, it's about ten times faster. At high

duty cycle and maximum laser output power, a five-fold higher production capacity is possible.

The advantages are not only quantitative; there are also advantages in quality of parts because remote laser welding decreases production tolerances. On the one hand, it subjects the parts to less heat input and mechanical stress than the usual welding processes. The parts are not distorted as much and their structural geometry is not affected. On the other hand, the lower number of positioning and clamping procedures contributes to an even greater dimensional stability of the welded components as well as the entire car body.

As a result of the advantages in component and vehicle properties, the overall costs of remote laser welding compared to resistance spot welding are favorable in spite of the relatively high cost of the production tool and laser. The savings achieved are associated with significantly greater flexibility because it is possible to weld different car body styles on the same remote welding line. For a long time already, the use of remote processing has not been restricted to doors, sidewalls, or rear center assemblies made of sheet metal. More and more automotive part suppliers use it to produce other subassemblies such as bumpers, rocker rails, wheel wells or instrument panel carriers.

## 7 Design for Laser Welding

Laser welding will continue to take its place in the fabrication of car bodies. How quickly that will happen depends primarily on the designers' increasing awareness of the advantages of this laser process. The greatest advantages in costs and productivity compared to resistance spot welding can be achieved when components are intentionally designed or re-designed to take advantage of the laser joining process. Here are a few considerations:

- Reduce the component weight and cost by reducing or even eliminating flange widths (enabled by single sided, narrow beam access) (Fig. 4)
- Reduce the component weight and cost by reducing gage thickness (enabled by using optimized weld shapes or continuous weld seams in high stress regions of parts normally spot-welded together)
- Reduce the component weight and cost and increase strength by elimination of access holes in structural reinforcements needed for resistance spot back-up electrodes (Fig. 5)
- Reduce the as-welded distortion and thereby reduce or eliminate post process rework or straightening due to the low heat input associated with the laser welding process, or by reducing the number of processing steps and associated fixtures
- Eliminate secondary processes such as grinding and finishing by taking advantage of the high weld seam aesthetics

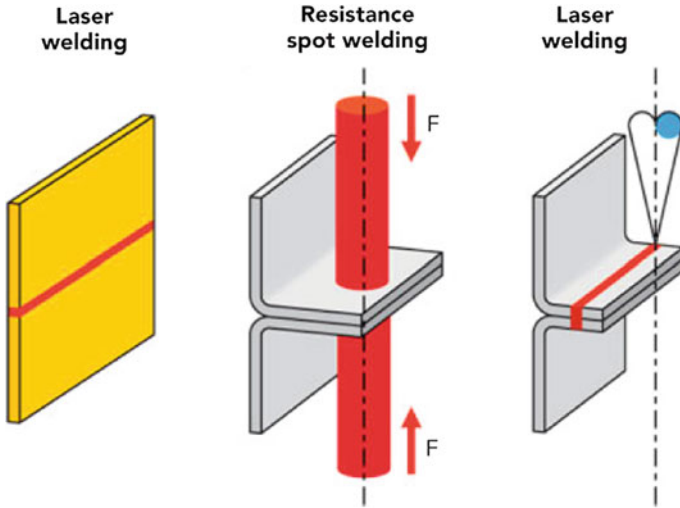
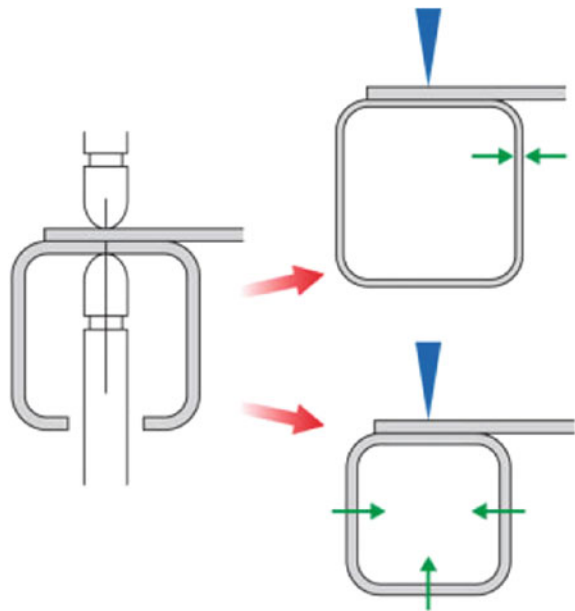


**Fig. 4** Laser welding can either reduce or eliminate flanges compared with resistance spot welding

**Fig. 5** Laser welding's single sided access can reduce weight and increase strength compared to resistance spot welding



- Employ unique styling of components enabled by laser welding and/or laser brazing (e.g., laser brazing of an automotive ditch joint thereby eliminating sealing and the use of plastic molding to “fill-in” the ditch).

Those who thoroughly consider these points are on the right track to benefiting the most from laser welding.

As the world's leading provider of laser manufacturing technology, TRUMPF is the one stop shop for all car manufacturers seeking cost-efficient, high-speed, top quality solutions for their production requirements: starting with laser systems and extending through numerical control, beam sources, beam guidance and optics to all-round after sales support. We are not car manufacturers, but we do have a hand in manufacturing almost every modern day car: The majority of production lines contain lasers and machines built by TRUMPF. They help to speed up workflows and make them more flexible, save costs, improve efficiency, and quite simply enable things to be done that would be impossible using conventional methods.

Our applications specialists are there to help you at any time with their expert knowledge in welding, cutting, marking and many other laser-based manufacturing processes employed in the automotive industry, even if your product idea is still at the development stage. Our Laser Application Centers can provide you with competent advice on process design and help you to work out the most cost-efficient end-to-end solution for your process chain. If required, we can also conduct feasibility studies and cycle time analyses, fabricate prototype parts, and recommend optimized lightweight construction methods using laser-based processes. And you can always rely on the support of our global service network serving the automotive industry and its suppliers—there is sure to be a service center near you.



# Characteristic Analysis of the Gas-Powder Stream for Laser Cladding

Weihong Liu, Binshi Xu, Shiyun Dong and Shixing Yan

**Abstract** The characteristics of the particle solid structure and the particle velocity distribution in the gas-powder (Fe-based alloy) stream for off-axis laser cladding were examined by particle image velocimetry technique, and the effect of feed parameters on them was also investigated. The results show that the solid and the gas in the stream were diverse of structure and velocity, and related to the property of materials and powder feed condition. The lower density is, the more concentrated of powder stream is. The particle velocity is lower than the gas velocity. At the transverse section, the particle velocity distribution can be described by Gaussian law. The particle velocity is enhanced with increasing rate of carrying gas flow, reducing powder feed rate and particle size.

**Keywords** Laser cladding · Gas-powder stream · Particle velocity · Particle solid structure · PIV technique

Laser cladding technology has been widely applied to automotive manufacture for its specific properties (such as high temperature, wear resistance, corrosion resistance and so on) and excellent forming accuracy with a small heat affect zone. Quantitative description of its physical processes is not only to better select and optimize the cladding conditions, but also be of great benefit to closed-loop quality control, which is significant for the science and technology development.

---

F2012-H04-005

---

W. Liu (✉)

Beijing Automotive Technology Center, Beijing, China  
e-mail: liuweihong@beijing-atc.com.cn

B. Xu · S. Dong · S. Yan

Academy of Armored Forces Engineering, Beijing, China

Interaction between the laser and the powder flow is the primary stage of off-axis powder feeding laser cladding, which has influence on the pool formation, the surface quality of the cladding layer, etc. There are two essential questions which are the attenuation of laser beam energy through the powder stream and the temperature of powder particle by the laser beam irradiation [1]. Through analysis in-depth it is not difficult to find that they are closely related to the particle concentration and particle velocity in coupling region of powder stream and laser beam. Because the physical process is very complex and hard to describe, it is very difficult to build an accurate analysis and numerical mode [2–10]. Experimental study is the best method to make up for the deficiency above [11–14]. Therefore, the particle (Fe901) velocity field characteristics in gas-powder stream for off-axis laser cladding was examined through the non-contact velocity measurement technique of particle image velocity (PIV) in this paper. Furthermore, the rate of carrying gas flow, the powder feed rate and the particle size were also investigated.

## 1 Experiment

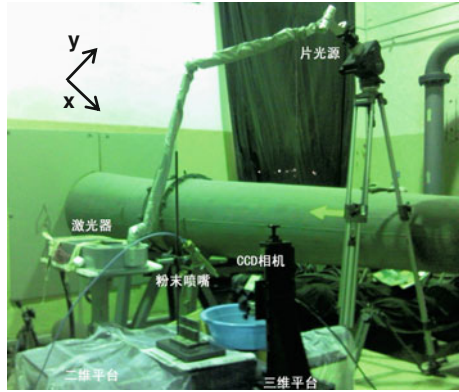
### 1.1 Experimental Equipments

Experimental equipments are used which included the examining system, powder feed system and positioner. A 3D-DM2-4M350 three dimension particle image velocimetry equipment is used which is comprise of sheet light source, image capture, synchronous control, analysis and display systems. A SM-LASER350-10 PIV double-pulse laser with a wave length of 532 nm, energy of 350 mJ, frequency of 10 Hz, pulse width less than 6 ns and least laser beam thickness of 1.0 mm is used to emblaze the taking zone. A SM-CCD4M15 digital image system with double exposure, resolution of  $2048 \times 2048$  pixel, bit depth of 12 bit, frequency of image capture of 15 frame/s, least time interval between two pictures of 200 ns is used to record the real-time information of particle moving. And a SM-Micro-Pulse725 synchronous controller is used to control the touching off and time delay between light source and CCD camera. The precision of time delay is 0.25 ns. A MicroVec V2.0 software is used to display and analyze the real-time experimental image data. For powders, they are transferred in gas through a PFL-2A powder feeder whose working voltage is linear with powder feed rate. And positioner is comprised of several tridimensional coordinate racks and rotating rigs to control position and attitude of the nozzle, light source and CCD camera.

### 1.2 Experimental Materials

The test material is Fe901 alloy which has an excellent fluidity. The size of the particle is between  $-140$  and  $+325$  mesh. Before testing, the powder is griddled to be three types such as  $-150 +200$  mesh,  $-200 +250$  mesh and

**Fig. 1** Photograph of experimental apparatus used for the measurement of the gas-powder stream for laser cladding by PIV technique



–250 + 300 mesh by a Tyler standard sieve. Meanwhile, the spherical SiO<sub>2</sub> powder with a diameter of 2 μm is used to tracing the character of gas field. And the Al powder with particle size of 200 + 300 mesh is used to be a comparison object.

### 1.3 Experimental Procedure

Experimental equipments for PIV analysis are shown as Fig. 1. During the process of powder stream axes-section analysis, the angle between nozzle axes and horizon is 45°. Then the horizontal central line of image is fixed up with the axes of powder stream to benefit for observing and analysis.

The typical powder feed parameter is shown as gas flow rate ( $Q$ ) of 200 L/h (100–250 L/h), powder feed voltage ( $u$ ) of 12 V (8–16 V), inner diameter of nozzle ( $d_0$ ) of 2.0 mm, particle size of –250 + 300 mesh (–150 + 300 mesh). Before experiment, the powder SiO<sub>2</sub> is dried to avoid aggregating.

The sizes of axes and crossing imaging section are 52.3 mm × 52.3 mm and 43.5 mm × 40.9 mm with amplification ratio of 25.548 and 17.462 μm/pixel respectively. The interval of double exposure time is between 20 and 30 μs. The recording frequency is twice per second. 100 images are recorded continuously under every condition. The cross-correlation algorithm with calculating window of 32 × 32 and grid spacing of 32 × 32 is used to analyze images. Moreover, a factor of time-average velocity is adopted to eliminate the error of measuring data caused by waving of powder feed rate. The coordinate system is shown in Fig. 1. Then, time-average velocity  $\bar{v}_t$  means the arithmetical average of particle instantaneous velocity  $v_i$  during the testing time which could be calculated as follow:

$$\bar{v}_t = \frac{\sum_{i=1}^N v_i}{N} \tag{1}$$

In this function,  $v_i$  represents the statistical average displacement  $\Delta S_i$  of a local particle group during the pulse time interval  $\Delta t$  of sheet light source, which could also be calculated as follow:

$$v_i = \frac{\Delta S_i}{\Delta t} \quad (2)$$

Concerning the limit of character of powder stream, the image analysis technique and practical application of engineering, the location for analysis is fixed on the section (c–c) as a distance of 20 mm to the nozzle tip.

## 2 Results

### 2.1 Structure of Powder Stream

Structures of solid field and gas field in gas-powder stream under the typical condition are shown in Figs. 2 and 3. It is found that the structure of the solid field is not equal to the gas field. For Fe901 powder stream, a radial character along the axis direction (x) appears near the nozzle exit; in front of distance to the nozzle tip about 7 mm (b–b), particles accumulate, but behind 7 mm they disperse quickly. For SiO<sub>2</sub> powder stream, its shape does not vary in the zone distance to the nozzle tip (a–a) 10 mm, then turn into coherent structure.

Further study on the effect of gas flow rate, powder feed rate, particle size and type of material on powder stream characters is investigated. Results indicate that material type is the most significant factor. Character of Al powder stream is shown in Fig. 4. It shows that initial length of stream increased and expanding angle descended compared to the Fe powder stream. Moreover, most of particles concentrate in the center of axes which is similar to the gas stream character (Fig. 3). The less of metal powder density is, the more similar to the character of gas field will be.

### 2.2 Particle Velocity Field

The velocity of solid and gas in air-powder stream under the typical condition are shown from Figs. 5 to 6. As shown in Fig. 5, velocity of particles on the center line is high (Fig. 5a), and it moves almost along the center line (Fig. 5b); with the increase of distance to the center line, velocity descend and moving direction diverges gradually. For laser cladding technology, laser beam spot diameter is less than powder stream diameter commonly, which means radial displacement for particles moving in the laser beam could be neglected, and simplified to moving along the nozzle center line. Along powder flow direction (x) (Fig. 5c), particle velocity increases slowly then descend with the increase of distance to nozzle tip,

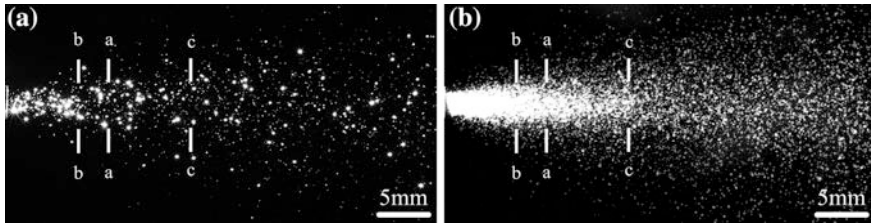


**Fig. 2** Images of the particle Fe901 with  $-250 + 300$  mesh,  $d_0 = 2.0$  mm,  $Q = 200$  L/h and  $u = 12$  V **a** instantaneous image **b** compound of 50 instantaneous images

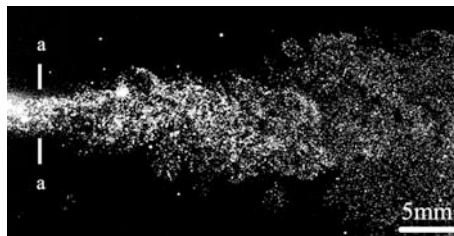


**Fig. 3** Image of the particle  $SO_2$  with  $d_0 = 2.0$  mm and  $Q = 200$  L/h

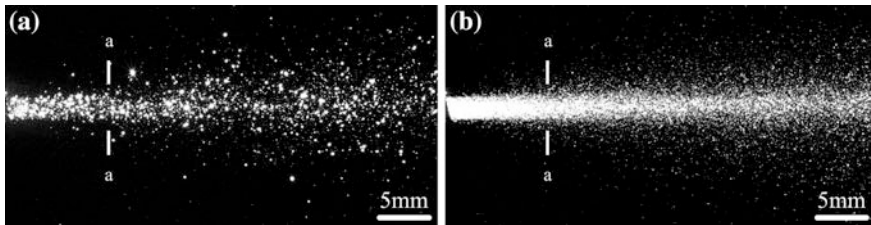


**Fig. 4** Images of the particle Al with  $-250 + 300$  mesh,  $d_0 = 2.0$  mm,  $Q = 200$  L/h and  $u = 12$  V **a** instantaneous image **b** compound of 50 instantaneous images

particle velocity distributing in the analysis zone are between 3.50 and 4.00 m/s. Along the transverse direction, the particle velocity field distribution is wide and fit for Gaussian rule, which means particle velocity  $v_p(y, z)$  at any point  $(y, z)$  could be expressed as Eq. (3):

$$v_p(y, z) = v_{p,m} \exp\left(-\frac{y^2 + z^2}{2R_{p,v}^2}\right) \tag{3}$$

where,  $v_{p,m}$  is the peak particle velocity at the stream centre,  $R_{p,v}$  is the nominal stream radius reaching  $e^{-1/2}$  of the maximum particle velocity. It can be seen in Fig. 6 that particle  $SiO_2$  velocity in the center line are between 4.0 and 7.0 m/s and particle velocity field profile is narrow. From the above we can see that the particle velocity in the gas-powder stream is less significantly than the gas velocity.

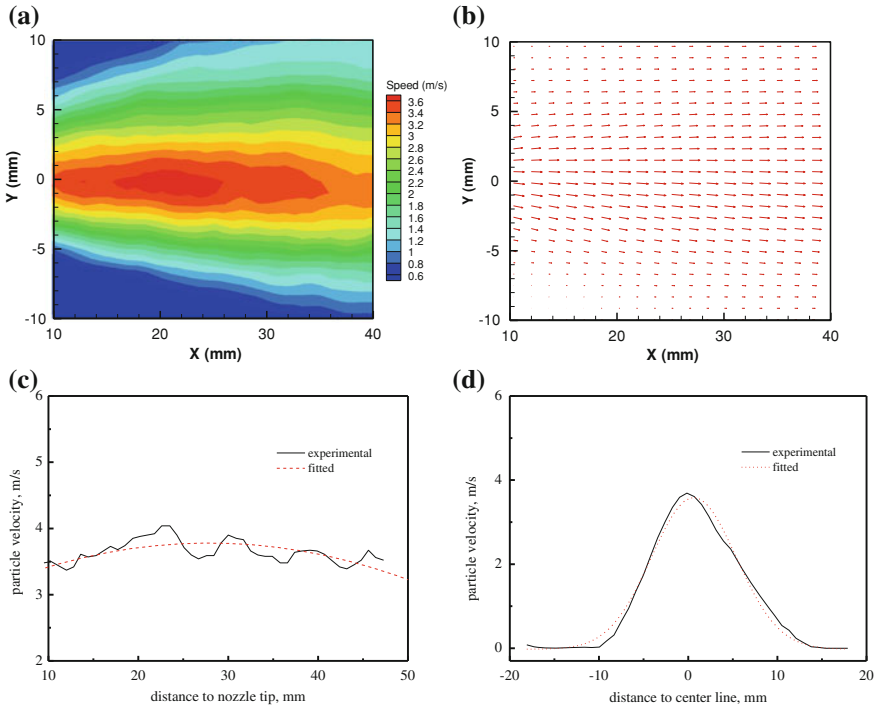


**Fig. 5** The particle time average velocity profile of the powder Fe901 with  $-250 + 300$  mesh,  $d_o = 2.0$  mm,  $Q = 200$  L/h and  $u = 12$  V **a** contour map **b** vector map **c** along center line **d** distance to nozzle tip of 20 mm

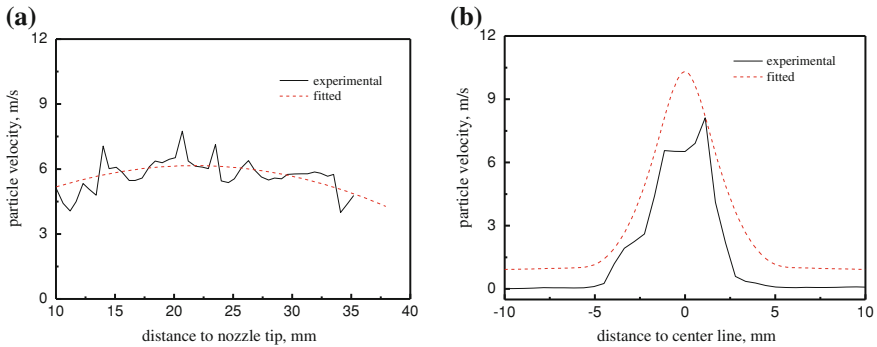


**Fig. 6** The particle time average velocity profile of the powder  $SiO_2$  with  $d_o = 2.0$  mm and  $Q = 200$  L/h **a** along center line **b** distance to nozzle tip of 20 mm

The influence of powder feed parameters such as gas flow rate, powder feed rate, particle size and material density on particle velocity is shown in Fig. 7. It is easy to understand that the maximum particle velocity enhanced from 2.07 to 4.53 m/s

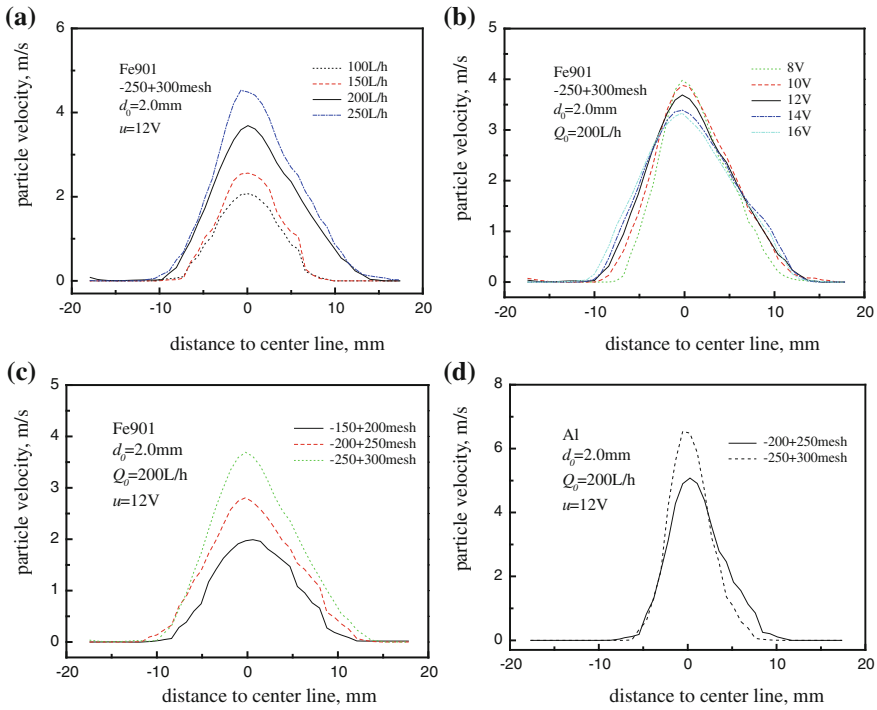


**Fig. 7** Effect of powder feed parameters on the particle velocity profile along 20 mm transverse plane of the gas-powder stream for laser cladding **a** gas flow rate **b** powder feed rate **c** particle size **d** material density

when gas flow rate rises from 100 to 250 L/h (Fig. 7a). However, the maximum particle velocity reduces slowly from 3.98 to 3.33 m/s with the increase of powder feed rate (Fig. 7b), and the maximum particle velocity decreases from 3.69 to 1.99 m/s when particle size increases from  $-250 + 300$  to  $-150 + 200$  mesh (Fig. 7c). In comparison with Fe901 powder, the peak particle velocity of Al powder noticeable increases (Fig. 7d), especially the smaller particle. As an example, the values with particle size  $-200 + 250$  and  $-250 + 300$  mesh are about 6.00 and 8.00 m/s, respectively. In conclusion, particle velocity increase with enhancing of gas flow rate and decreasing of powder feed rate, particle size and material density. It also further verifies that the method of replacing the powder velocity by the gas velocity is very unsatisfactory for quantitative analysis.

### 3 Discussion

When solid stream and gas stream jetting out of the nozzle, weight of gas stream increases due to flowing of surrounding medium induced by continuous exchange of mass and momentum between gas and its surrounding mediums. Further the

**Table 1** Particle velocity (distance to nozzle tip 32 mm) using PIV technique under condition of annular coaxial powder feed [14]

Powder feed rate, g/s	0.67				0.33	0.5	0.83
Gas flow rate, m <sup>3</sup> /h	0.6	0.8	1.2	1.4	1.2		
Average velocity, m/s	1.82	2.16	2.31	2.47	2.00	2.16	2.38

diameter of powder stream increases so that cone-shaped flow field has formed. This character of powder stream is induced by different forces bearing on powders in different zones. In center of powder stream, particle velocity is high as the driving forces of high gas velocity. With the increase of distance to axes, driving capability of gas decreases as well as particle velocity; however, when away from the axes, particles still has certain velocity caused by inertia forces although losing the driving capability of gas. Thus, the structure of powder stream is different and the particle velocity distribution is wide compared to gas stream.

When other powder feed parameters are constant, as gas flow rate increases, velocity and kinetic energy of gas increase as well as the kinetic energy transferred to powders, thus particle velocity increases too. With increasing of powder feed rate, the number of particles per minute increases, and energy dissipation for particles before jetting out of nozzles increases too, which is the main reason for decline of particle velocity. With reducing of powder size decreases, volume of a grain grows. However, the increase of mass of a grain is the significant reason for particle velocity decreasing. The lower material density is, the less mass of a grain is, and the better following capability with gas stream will be. Thus, character of Al powder is more close to gas flowing field that velocity in axes center increases significantly.

Dr Li Huishan in Tianjin Polytechnic University has performed similar work [14]. Compared to the experimental results in this study, they are basically identical except the influence of powder feed rate (see Table 1). Obviously, it shows that the researches on powder velocity field are objective and universality. The construction of nozzle in the literature is annular. Author reported that the rise of particle velocity with increase of powder feed rate resulted from increase of potential energy. Moreover, data processing method has an impact on particle velocity through a further investigation on original data, especially when particle size is small. The average particle velocity comprises of time-average velocity and space-average velocity. Time-average velocity is like that mentioned above. While space-average velocity means the average velocity for all particles during the present time, which is:

$$\bar{v}_s = \frac{\Delta S_{p,e}}{\Delta t} \quad (4)$$

where  $\Delta S_{p,e}$  is the statistical average displacement of a local particle group during the pulse time interval  $\Delta t$  of sheet light source during the present time. Time-average velocity is low, which is just two thirds of space-average velocity as



particle size of  $-150 + 200$  mesh. Moreover, further research is needed to perform in the future.

## 4 Conclusion

- (1) PIV is an effective technique for visual measure of the gas-powder stream during laser cladding process.
- (2) Structure of the powder stream is different from the gas stream, and related to the property of materials. The lower density is, the more concentrated of powder stream is.
- (3) Distribution of particle velocity is fit for Gaussian rule. Particle velocity of Fe-base alloy is lower than of gas whose track is linear.
- (4) The particle velocity increases with the increase of gas flow rate and the decrease of powder feed rate and powder size.

## References

1. Liu Z, Huang W, Wan B (2003) Investigation of basic problems of the numerical model for powder-feed laser cladding. *Chin J Lasers* 30(6):567–570
2. Picasso M, Marsden CF, Wanière JD et al (1994) A simple but realistic model for laser cladding. *Metall Mater Trans B* 25B(4):281–291
3. Fu Yunchang et al (2002) A theoretical model for laser and powder particles interaction during laser cladding. *J Mater Process Technol* 128(3):106–112
4. Liu Z, Qiu X, Yao Y et al (2007) Research on energy redistribution of laser power in process of powder feeding laser cladding. *Laser J* 28(3):75–76
5. Liu Z, Chen J, Huang W et al (2004) Temperature rise model of laser cladding material powder by side-injection with experiment investigation. *Chin J Lasers* 31(7):875–878
6. Dong C, Yao Jianhua, Hu X et al (2010) Three dimensional numerical simulation of coaxial powder feeding flow with carrying gas. *Chin J Lasers* 37(1):261–265
7. Yang N, Yang X (2008) Model of interaction between metal powder particle and laser beam in Laser cladding. *Acta Optica Sinica* 28(9):1745–1750
8. Lin Jehming (1999) Temperature analysis of the powder streams in coaxial laser cladding. *Opt Laser Technol* 31(8):565–570
9. Jin X, Yang X, Feng L et al (2007) Numerical simulation of coaxial powder flow with carrying gas in laser manufacturing. *Chin J Mech Eng* 43(5):161–166
10. Yang Y, Song Y (1998) Interaction of a laser beam and alloy powders in powder feed laser Cladding. *Chin J Lasers* A25(3):280–284
11. Lin Jehming (1999) Concentration mode of the powder stream in coaxial laser cladding [J]. *Opt Laser Technol* 31(3):251–257
12. Pinkerton AJ, Li L (2004) Modelling powder concentration distribution from a coaxial deposition nozzle for laser-based rapid tooling. *J Manuf Sci Eng* 126(1):33–41
13. Yang X, Lei J, Liu Y et al (2006) Experimental measurement of metal powder stream concentration field in laser manufacturing. *Chin J Lasers* 33(7):993–997
14. Li H (2004) Theoretical and experimental study on the interaction of laser and metal powder flow in the laser remanufacturing. Tianjin Polytech Univ, Tianjin

**Part IV**  
**Stamping Technology**

# Hot V-Bend Formability of Galvannealed Boron Steel for Hot Stamping

Masahiro Nakata, Koji Akioka, Masaru Takahashi,  
Hiroshi Takebayashi, Kazuhito Imai, Toru Takayama  
and Nobusato Kojima

**Abstract** The hot stamping process has been widely applied to the production of automotive body parts because the stamped panels with both high strength and good shape-accuracy are easily obtained. For the purpose of omitting the descaling treatment, the galvannealed (GA) boron steel for hot stamping was developed. When the steel is hot formed with the existence of liquid zinc, brittle fracture occurs by the infiltration of liquid zinc into the solid metal. This phenomenon is well known as Liquid Metal Embrittlement (LME). In this study hot V-bend test was carried out to estimate LME behaviour for GA boron steel in terms of suitable conditions of both heating and forming processes. First, LME disappeared with an increase of dwell time in gas furnace. In this heating condition, the dwell time that LME disappeared was 225 s. And the depth of LME crack became small as dwell time, and LME crack of 10 micrometer size was also observed in the dwell time of 210 s just before liquid zinc would be completely depleted from the  $\Gamma$  contents index  $I_{\Gamma}$  based on X-ray diffraction pattern analysis for  $\Gamma$ -phase of V-bent test specimen. In addition, in such condition, LME did not occur when a bending strain was small of 0.05 true strain. The overbend crush test for V-bent test specimen was carried out to investigate the influence of LME crack on the crash performance. Consequently it turned out that LME crack of about 10 micrometer did not have much influence on the crash performance. And this method is supposed to be very simple and valuable as a quality verification test for LME of the hot stamped parts in production.

---

F2012-H06-004

---

M. Nakata (✉) · K. Akioka · M. Takahashi · H. Takebayashi · K. Imai · T. Takayama ·  
N. Kojima  
R&D Division, Sumitomo Metal Industries, LTD, Osaka, Japan  
e-mail: nakata-ms2@sumitomometals.co.jp

**Keywords** Galvannealed boron steel • Liquid metal embrittlement • Dwell time in combustion gas furnace • Bending strain • Crash performance

## 1 Introduction

Recently the hot stamping process has been widely applied to the production of automotive body parts because the pressed panel with both high strength and good shape-accuracy are easily obtained. The feature of hot stamping process is quenching in the forming process, then it is necessary to heat up once above Ac3 for austenization. In this heat treatment the surface of steel sheet is oxidized; iron oxide layer is formed at high temperature. Generally, the de-scaling treatment such as shot blasting is necessary to remove the iron oxide layer to ensure good weldability and paintability [1].

The galvannealed (GA) boron steel that doesn't need the de-scaling treatment for hot stamping was developed [2–4]. And this steel has been in production for about 10 years. It was reported that the GA boron steel after hot stamping had Fe–Zn solid solution layer as a coating substrate and ZnO wavy film that covered Fe–Zn solid solution layer [5]. When the steel is formed in high temperature with the existence of liquid zinc, brittle fracture occurs by the infiltration of liquid zinc into grain boundary of the solid metal. This phenomenon is well known as Liquid Metal Embrittlement (LME). And it is known that if heating time is not enough, LME will occur in GA boron steel for hot stamping [5]. The objective of this study was to investigate the suitable heating and forming conditions not to occur LME of GA boron steel and the morphology of LME crack.

## 2 Hot V-Bend Test Methods

### 2.1 Test Material

GA boron steel of 2.6 mm thickness for hot stamping was used in the experiments. The characteristics of test material are shown in Table 1. Coating weight and Fe content of GA were measured by ICP-MS analysis. And the size of test specimen was rectangle of 60 × 40 mm.

### 2.2 Heat Treatment Condition

Test specimen was heated in a combustion gas furnace. Heating conditions are shown in Table 2. The temperature in gas furnace was set to 900 °C. Dwell time in gas furnace was changed between 150 and 360 s. Forming start temperature was

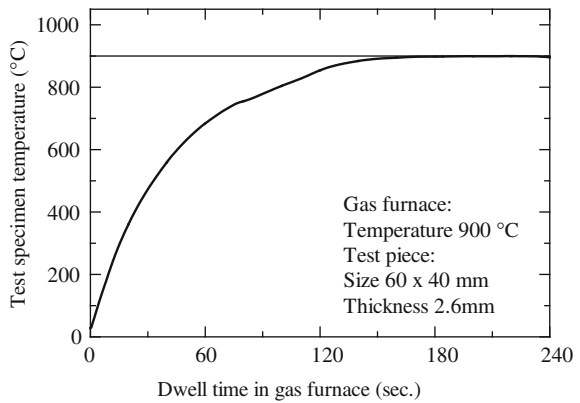
**Table 1** Characteristics of test material

Thickness (mm)	Chemical composition (mass %)				GA coating	
	C	Si	Mn	B	Coating weight (g/m <sup>2</sup> )	Fe content (%)
2.6	0.21	0.24	1.3	0.0018	61.0	12.5

**Table 2** Heating conditions

Items	Test conditions
Air/Fuel ratio	1.1
Temperature in gas furnace (°C)	900
Dwell time in gas furnace (seconds)	150, 180, 195, 210, 225, 240, 270, 360
Forming start temperature (°C)	Above 782

**Fig. 1** Representative temperature history



set above 782 °C to which liquid zinc existed on Fe–Zn equilibrium diagram [6] during measuring the temperature of test specimen by thermo couple. A heating rate would change widely depending on the specification of a combustion gas furnace and the size and the thickness of test specimen. Then Fig. 1 shows the representative temperature history of test specimen in a heating process. When the furnace temperature was 900 °C, the temperature of test specimen reached to 900 °C in about 165 s.

### 2.3 Hot V-Bend Test Methods

Hot V-bend test tools are shown in Fig. 2. These tools were set to the Hydraulic press machine. Test specimen was taken out of gas furnace after heated up to the

**Fig. 2** Schematic illustration of hot V-bend test

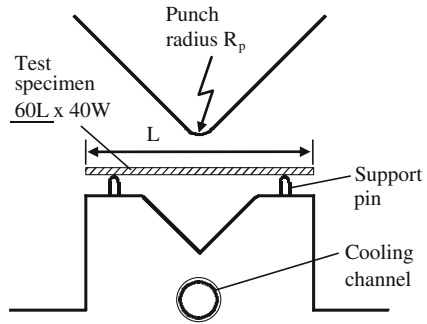
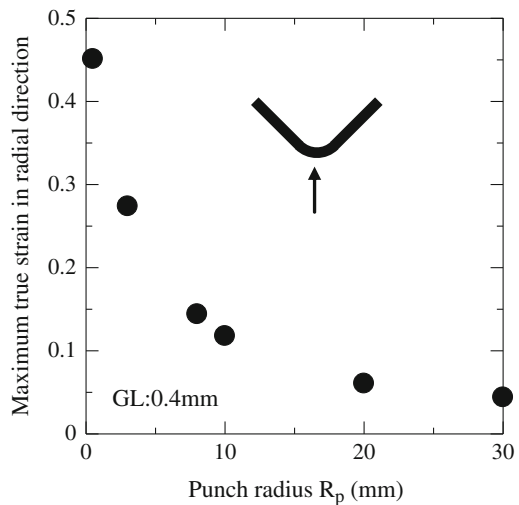


**Table 3** Forming conditions

Items	Test conditions
Forming speed (mm/s)	300
Bottoming load (kN)	40
Hold time in dead bottom (seconds)	30
Punch radius $R_p$ (mm)	0.5, 3, 8, 10, 20, 30

**Fig. 3** Maximum true strain at the apex of bending portion



predetermined dwell time shown in Table 2 and was transferred to the lower tool. Table 3 shows the forming conditions. The punch radius  $R_p$  was widely changed between 0.5 and 30 mm. The maximum true strain in radial direction at the apex of a bending portion was shown in Fig. 3. Quite large true strain of 0.45, which did not exist in actual parts, occurred at the apex when  $R_p$  was 0.5 mm. On the other hand the true strain remained 0.05 when  $R_p$  was 30 mm. Then the strain was measured from the Vickers indentation with a 0.4 mm pitch.

**Table 4** Effect of dwell time in gas furnace on LME ( $R_p0.5$ )

Dwell time in gas furnace (sec.)							
150	180	195	210	225	240	270	360
NG	NG	NG	NG	<b>OK</b>	<b>OK</b>	<b>OK</b>	<b>OK</b>

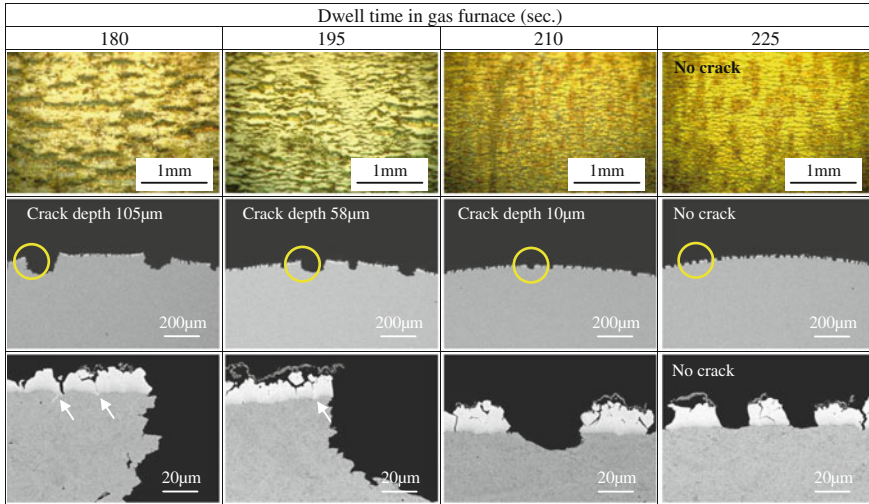


**Fig. 4** Microscope observation and cross-sectional BSE-SEM images ( $R_p0.5$ )

### 3 Experimental Results About Liquid Metal Embrittlement

#### 3.1 Process Window About Heat Treatment Conditions

The effects of dwell time in gas furnace on LME are shown in Table 4. This data was estimated when  $R_p$  was 0.5 mm which derived the true strain of 0.45. When there was a crack which went into base metal in cross-sectional observation of SEM, it judged as LME. LME was easy to generate on the heating conditions that the dwell time was short, and LME disappeared in the dwell time for 225 s or more. This dwell time in which LME disappeared had the hold time at 900 °C for about 60 s after 900 °C attainment. In addition, even if heating time was long such as 360 s, as for the coating layers, such as solid solution layer and ZnO film layer, the problem was not found in a visual observation and a cross-sectional observation of SEM.

The microscope observation and cross-sectional BSE-SEM images at the apex of a bending portion with punch radius of 0.5 mm are shown in Fig. 4. When the dwell times are 180 and 195 s, some cracks can be easily found out also with a visual observation or a microscope observation. And these crack depth are not less than 50 micrometers, and the crack has the morphology with a gently-sloping

**Fig. 5** XRD pattern and estimation

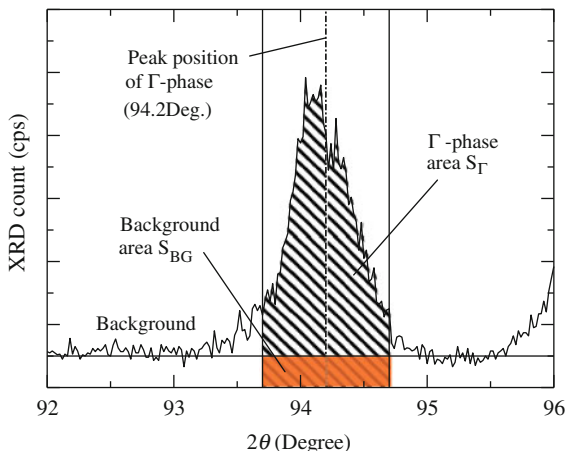
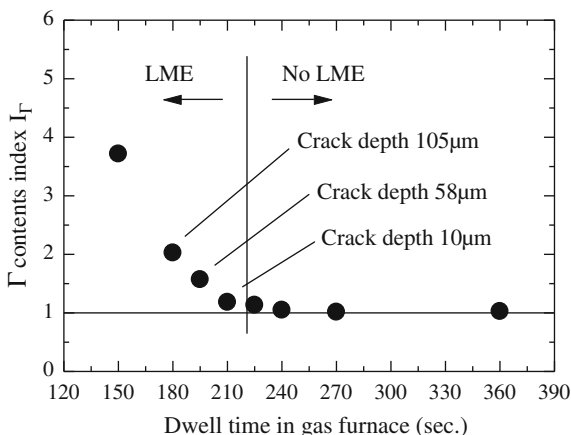


**Fig. 6** Relationship between dwell time in gas furnace and  $\Gamma$  contents index  $I_\Gamma$



bottom. In addition the high brightness region which indicated high zinc density was observed. On the other hand when the dwell time was 210 s, LME crack was indistinguishable from the crack of Fe–Zn solid solution in surface observation not only a visual observation but also a microscope observation. Then this crack depth was only about 10 micrometers.

It is well known that liquid zinc that exists while forming at high temperature derives LME. And liquid zinc is supposed to transform to  $\delta + \Gamma$  phase during die quenching with usual cooling rate. Therefore,  $\Gamma$  intensity was measured by X-ray diffraction with Co  $K\alpha$  radiation source in each heating conditions for V-bent specimens. The estimation method is described below. Figure 5 shows the instance of XRD pattern. The  $\Gamma$ -phase area  $S_\Gamma$  was defined as the integration of a chart of the range of  $94.2 \pm 0.5^\circ$ . Next, the background area  $S_{BG}$  was defined as the integration of the background chart of the range of  $91 \pm 0.5^\circ$ . The  $\Gamma$  contents



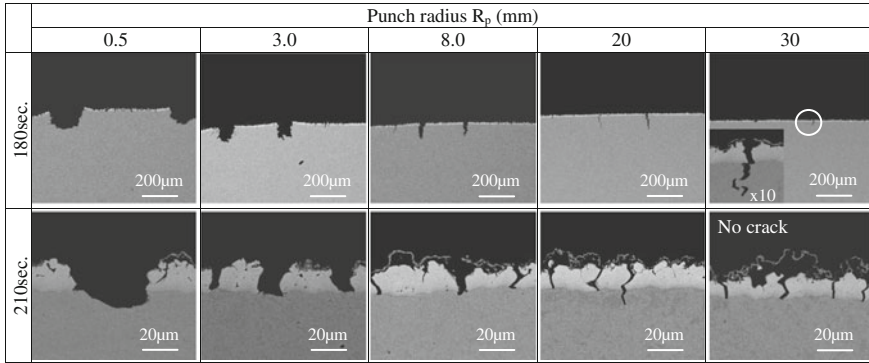


**Fig. 7** Cross sectional BSE-SEM images in case of different punch radius

index  $I_{\Gamma}$  was defined in the following equation. It is thought that liquid zinc existed much so that this index is large.

$$I_{\Gamma} = S_{\Gamma}/S_{BG}$$

Figure 6 shows the relationship between dwell time in gas furnace and  $\Gamma$  contents index  $I_{\Gamma}$ . With an increase of dwell time, this index was reduced to a parabolic. In addition, this index was well agreement also with the size of LME crack. It is considered that liquid zinc has been depleted with an increase of heating time and the quantity which goes into a base metal decreased.

### 3.2 Effects of V-Bend Punch Radius

Figure 7 shows cross sectional BSE-SEM images in case of different punch radius when the dwell times in gas furnace were 180 and 210 s. First, in the dwell time of 180 s, LME crack occurred even in  $R_p30$  of 0.05 true strain. In addition, the crack depth did not change so much with the expansion of the punch radius  $R_p$ . On the other hand, the morphology of LME crack became sharp gradually with an increase of punch radius. From these results, it is considered that in the forming of small  $R_p$ , a sharp crack occurred in early stage of forming and it became open and grew up to be a shape of a gently-sloping bottom. On the other hand, in the dwell time of 210 s, LME crack was small by any  $R_p$ , and LME crack was not observed in  $R_p30$  of about 0.05 true strain. In the state with little liquid zinc just before the complete of Fe-Zn solid solution formation, it turned out that liquid zinc did not go into a base metal in some amounts of hot deformation.

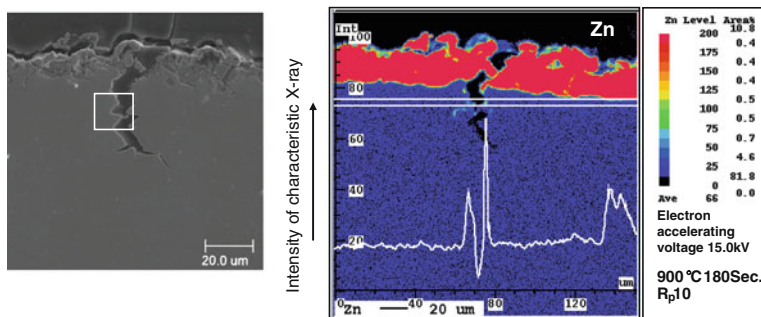


**Fig. 8** FE-SEM image and EPMA mapping image of Zn at LME crack portion

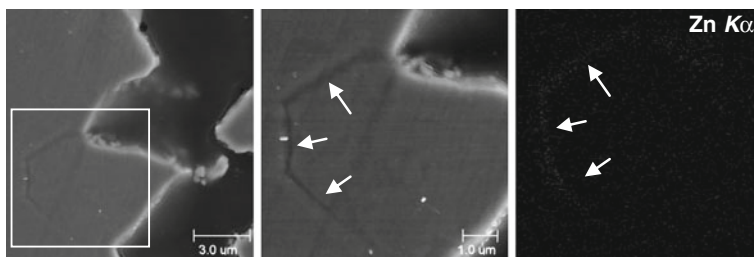


**Fig. 9** FE-SEM images and EDS mapping image near LME crack

### 3.3 Elementary Analysis of LME Crack Portion

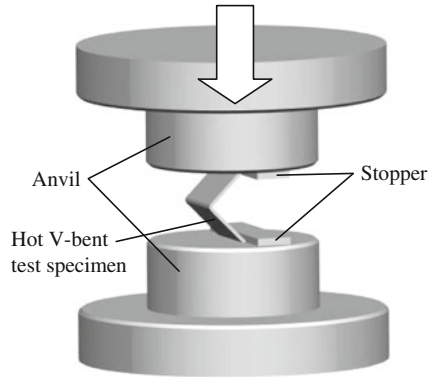
FE-SEM image and EPMA mapping image of zinc at LME crack portion is shown in Fig. 8. Test specimen was heated with 900 °C 180 s and was stamped with the punch radius of  $R_p10$ . Although zinc infiltration into the base metal was not so obvious from EPMA mapping image and it is considered that the amount of zinc was not so much, zinc was detected by WDS line analysis. So this crack was verified to be originated in LME. According to FE-SEM/EDS analysis, Zinc trace was detected at grain boundary near the LME crack as shown in Fig. 9.

## 4 Effects of LME Crack on Crush Property

### 4.1 Idea and Experimental Methods

LME occurs on the tip of bending portion such as punch shoulder of hat shaped channel [5, 7]. LME crack is supposed to affect the crush performance of the hot

**Fig. 10** Overbend crush test for V-bent test specimen



stamped parts, according to LME crack progresses to the thickness direction when the bent portion in hot stamping is additionally overbent in a crash deformation. In other words, it is considered that by performing the test that hot V-bent test specimen having LME crack is overbent, it can be estimated the effects of LME on the crash performance. In this study, the overbend crush test as shown in Fig. 10 was carried out. Test specimen was inserted between the upper and the lower anvils so that the apex of bending portion faced to horizontal direction. The stopper was set on the anvil so that test specimen does not slip between the upper and the lower anvils. Next the anvil went down at a speed of 0.5 mm/s until a predetermined stroke. We investigated the effect of LME crack from the overbending deformation resistance per specimen width and an observation of the fracture at the overbent apex.

## 4.2 Experimental Results

Figure 11 shows the overbend crush load per specimen width in the forming condition of  $R_p0.5$  and  $R_p8.0$  that have different crack morphology when the dwell times are 180, 195, 210 and 225 s. The overbend crush load once increased and it fell gently after it had a peak. Then the peak load only in the dwell time of 180 s with the large crack depth over 100 micrometer as shown in Fig. 4 was slightly smaller than the others. After having peak load, the fall of crush load became earlier with an increase of dwell time. However, the dwell time of 210 s which has a minute LME crack and it of 225 s without LME crack had almost same crush property. Moreover, the above results were almost the same at  $R_p0.5$  and  $R_p8.0$ . Figure 12 shows appearances of overbent apex after overbend tests. The fracture was larger in the conditions that the crush load is smaller in Fig. 11, and it turned out that the decline of crush load was promoted by LME crack. In the dwell time of 210 and 225 s with same crush load, the size of the fracture was also the same. Consequently it turned out that LME crack of about

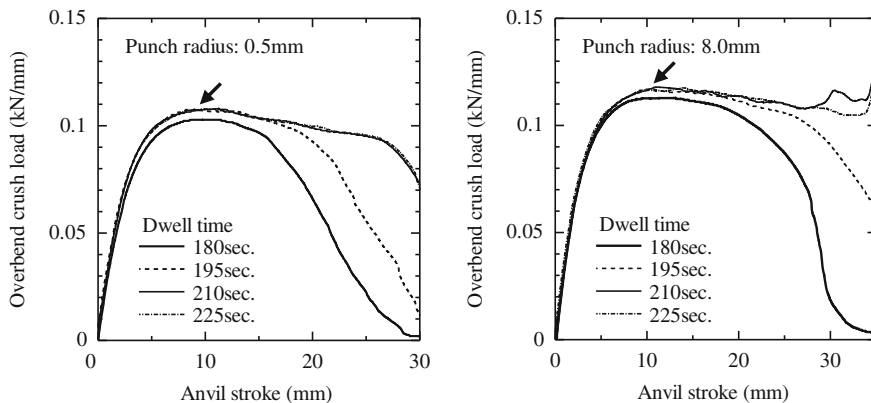


Fig. 11 Overbend crush load per specimen width (Left  $R_p0.5$ , Right  $R_p8.0$ )

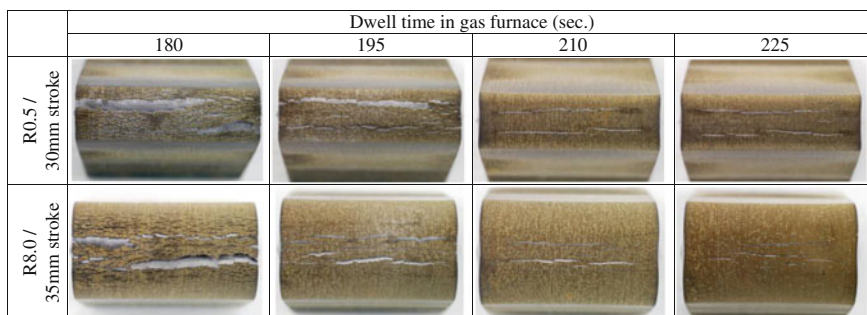


Fig. 12 Appearances of overbent apex after overbend tests

10 micrometer does not have much influence on the crash performance. And this method is very simple and valuable as a quality verification test for LME of the hot stamped parts in production. If a V-shape specimen is cut out from the punch shoulder region of hot stamped parts and the overbend crush load is measured, the existence of LME crack which has much influence on the crash performance can be inspected.

## 5 Conclusion

The hot V-bend test was carried out to estimate LME for GA boron steel in terms of suitable conditions of both heating and forming processes. And the overbend crush test for hot V-bent test specimen having LME crack was carried out to investigate the influence of LME crack on the crash performance. The following results are obtained.

(1) LME disappeared with an increase of dwell time in gas furnace. The dwell time that LME disappeared was 225 s in this experiment. And the depth of LME crack became small as dwell time, and LME crack of 10 micrometer size was also observed in the dwell time of 210 s just before liquid zinc would be completely depleted from the  $\Gamma$  contents index  $I_{\Gamma}$  based on X-ray diffraction pattern analysis for  $\Gamma$ -phase of V-bent test specimen. In addition, LME did not occur when a bending strain was small of 0.05 true strain in the dwell time of 210 s.

(2) Overbend crush load became small with an increase of dwell time in gas furnace. However LME crack of about 10 micrometer did not have much influence on the crash performance from the overbending deformation resistance per specimen width and an observation of the fracture at the overbent apex. This method is supposed to be very simple and valuable as a quality verification test for LME of the hot stamped parts in production.

## References

1. Jonsson M (2008) Press hardening, from innovation to global technology. In: Proceedings of the 1st international conference hot sheet metal forming of high-performance steel, Kassel, Germany, 22–24 Oct 2008, GRIPS media GmbH, p 253
2. Ichikawa M et al (2004) Development of press quenching technology using Zn plated steel sheet. Proc JSAE Annu Congr 83–04:20045684
3. Imai K et al (2005) Properties of hot stamped Galvannealed steel sheet. SEAIQ 34(4):47
4. Imai K et al (2005) Property of press quenched zinc plated steel sheet. CAMP-ISIJ 1(8):557
5. Kojima N et al (2011) Metallurgical behaviour of uncoated and Galvannealed boron steels in hot stamping process. In: Proceedings of the 3rd international conference hot sheet metal forming of high-performance steel, Kassel, Germany, 13–17 June 2011, GRIPS media GmbH p.511
6. Burton BP, Perrot P (1993) Phase diagram of binary iron alloys. In: Okamoto H (ed.) ASM international, Materials Park, Ohio, p 459
7. Drillet P et al (2011) Study of cracks propagation inside the steel on press hardened steel zinc based coating. GALVATECH 2011

# Research on Holding Pressure and Cooling Process During Hot Forming of Ultra-High Strength Steel 22MnB5

Xiaona Wang, Fangwu Ma, Qiang Liu and Fuquan Zhao

**Abstract** During the stage of holding pressure and cooling process in the hot forming process, the control of various parameters is very important to ensure the quality of hot forming parts. With binding reasonable die design and finite element simulation, the paper puts forward optimum technological parameters of holding pressure and cooling process. On the basis of above study, the constitutive equation is established in the paper with experimental data which can reflect the true flow stress under different conditions. Through finite simulation results, it can be seen that there is very important effect of holding time on hot forming temperature field and stress and strain state. Therefore, it is very necessary to design reasonable holding pressure time in order to make the temperature even and stress and strain reasonable.

**Keywords** Ultra-high strength steel · Hot forming · Holding pressure and cooling process · Process parameters · Constitutive relationship model

## 1 Introduction

In the automotive industry, the usage of ultra-high strength steels offers the possibility to reduce the weight of automobiles and maintain the safety requirement. In order to avoid the difficulties such as large forming force, low formability and

---

F2012-H06-005

---

X. Wang (✉) · F. Ma · Q. Liu · F. Zhao  
Zhejiang Geely Automobile Research Institute Co Ltd, Hangzhou, China  
e-mail: wangxiaona78@163.com

occurrence of springback during cold stamping of these materials, hot stamping has been developed which combines forming and quenching in one process step. Research shows that fuel consumption of automobile is closely related to the weight. With reducing 10 % weight of automobiles, the fuel consumption will decrease 6–10 % and emission will decrease 4 %.

Along with the development of automobile industry for light weight car bodies, more and more advanced high strength and ultra-high strength steels have been used to produce automobile parts. Using of the ultra-high strength steels not only reduces the weight of automobiles, but also improves crash safety and decreases gas emissions. In order to avoid the difficulties such as large forming force, low formability and occurrence of springback during cold stamping of these materials, hot stamping has been developed which combines forming and quenching in one process step. Hot stamping is non-isothermal high-temperature forming process, in which complex ultra-high strength parts are produced, with the goal of no springback. In hot stamping process, the blanks are austenitized and subsequently formed and quenched in the die. During quenching, the austenitic microstructure transforms into a martensitic one because of rapid cooling. The martensite evolution during quenching causes an increased tensile strength of up to 1,500 MPa.

## 2 Material Parameters

In the automotive industry for direct and indirect hot stamping the quenchable, ultra-high strength steel 22MnB5 is commonly used. The chemical constituent of 22MnB5 is shown in Table 1. 22MnB5 steel grade is the most commonly used steel grade in hot stamping process. Initially, the material exhibits a ferritic-pearlitic microstructure with a tensile strength of about 600 MPa. After the hot stamping process, the component finally has a martensitic microstructure with a total strength of about 1500 MPa. During hot stamping process, the blank has to be austenitized in a furnace for at least 5 min at 950 °C in order to achieve such a microstructure and hardness transformation. Afterwards, the blank is formed and quenched simultaneously by the water-cooled die for 5–10 s. Due to the contact between the hot blank and the cold tool, the blank is quenched in the closed tool.

Therefore, the relationship between stress and strain of ultra-high strength steel 22MnB5 under high deformation temperature is necessary to be studied. Figure 1 shows the material sensitivity to strain rate. Figure 2 shows the material sensitivity to deformation temperature. With deformation temperature increasing, the deformation resistance of ultra-high strength steel 22MnB5 is decreasing. And with strain rate increasing, the deformation resistance is increasing. Deformation temperature has a strong effect while strain rate seems less influencing the material process window.

**Table 1** Chemical compositions of the studied 22MnB5 (wt %)

C	Mn	Si	P	S	Al	Cr	B	Ti	Mo
0.22	1.25	0.25	0.0025	0.008	0.03	0.2	0.03	0.035	0.1

**Fig. 1** Material sensitivity to strain rate at initial temperature 600 °C

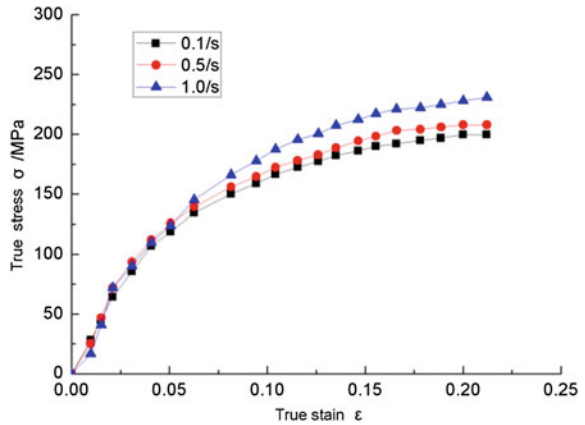
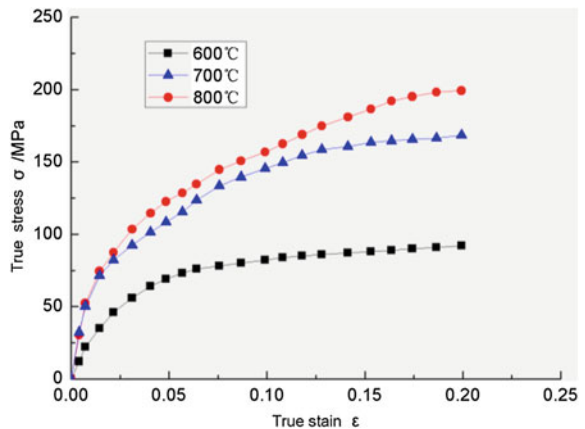


**Fig. 2** Material sensitivity to temperature at strain rate equal to 0.5/s



Hot stamping is a thermo-mechanical forming process with intended phase transformation. Depending on the temperature history and mechanical deformation, different phases and phase mixtures evolve. During the solid-state phase transformations, heat is released, which influences the thermal field. Furthermore, depending on the mixture of micro constituents, both the mechanical and thermal properties vary with temperature and deformation. Consequently, a realistic FE



**Table 2** Fitting results of K and m under at deformation temperature 900 °C

Temperature (°C)	Strain rate $\dot{\varepsilon}$ (/s)	$\ln \dot{\varepsilon}$	$\ln K + m \ln \dot{\varepsilon}$	Fitting result
900	0.015	-4.19971	4.6123	m = 0.196
	0.1	-2.30259	5.0378	K = 233.178
	0.45	-0.79851	5.2745	

model for process simulation must consider interaction between the mechanical, thermal and microstructural fields [1–4].

### 3 Constitutive Equation

According to the curve of strain and stress, the constitutive equation is fit such as:

$$\sigma = K \varepsilon^n \dot{\varepsilon}^m \quad (1)$$

where K is hardening coefficient; n is hardening exponent; m is strain rate sensitivity.

After taking logarithm of the above equation, the following equation is shown as:

$$\ln \sigma = \ln K + n \ln \varepsilon + m \ln \dot{\varepsilon} \quad (2)$$

with adopting the least square linear-fitting method, the linear relation of this formula has been validated. The fitting results are as the following:

$$y = a \bullet x + b \quad (3)$$

The fitting results at deformation temperature 900 °C are shown in the Table 2. According to the above method, all fitting results are shown in the Table 3.

### 4 FE Model

The planform of a commercial vehicle front cross member internal plate is shown in Fig. 3 and side elevation is shown in Fig. 4. The thickness of the blank is 1.8 mm. The length of the part is 1,180 mm and longitudinal deepness is 55 mm. From view of the part and size, it can be seen that curvature of the part is relatively big and the drawing surface is relatively deep.

In order to form easily, the binder surface of front cross member internal plate is done which is shown in Fig. 5. The blank size is 1,270 mm × 230 mm and thickness is 1.8 mm. The die with hyperbatic structure is applied to form (in Fig. 6). The blank shape and size are shown in Fig. 7. The other parameters are following:

**Table 3** Parameters of constitutive equation

Strain rate	Temperature (°C)	0.015/s	0.1/s	0.45/s
900	n	0.148	0.200	0.218
	m	0.196		
	K	233.178		
800	n	0.170	0.204	0.246
	m	0.165		
	K	332.112		
700	n	0.187	0.212	0.252
	m	0.162		
	K	440.030		
600	n	0.250	0.270	0.295
	m	0.144		
	K	678.980		
500	n	0.269	0.278	0.316
	m	0.108		
	K	811.188		



**Fig. 3** Planform of a commercial vehicle front cross member internal plate

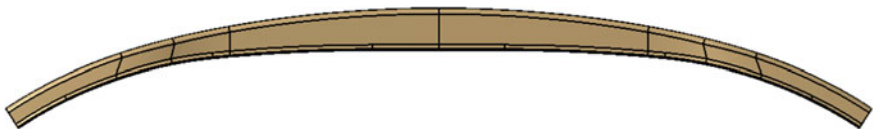


**Fig. 4** Side elevation of a commercial vehicle front cross member internal plate

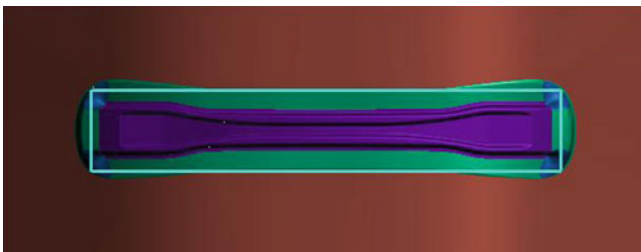
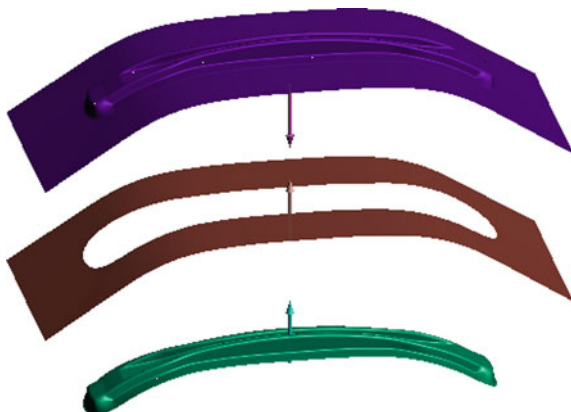


**Fig. 5** Binder surface of die

- (1) The die clearance is  $C = 1.1 t$  ( $t$  is thickness of the blank);
- (2) The initial temperature of die is  $75\text{ }^{\circ}\text{C}$ ;

**Fig. 6** Die with hyperbatic structure



- (3) The ambient temperature is 20 °C;
- (4) The initial temperature of the blank is 850 °C;
- (5) The time of transferring the blank from furnace to die is 6 s.

## 5 Analysis of Hold Pressure and Cooling Process

After forming, the part temperature rapidly decreases and quench is realized during hold pressure and cooling process. So, the ultra-high strength is obtained. In order to meet work efficiency and part properties, the following parameters are necessary to be selected, such as: proper holding pressure time, pressure keeping force. The effect of holding pressure time and pressure keeping time on part temperature and cooling rate must be studied in order to ensure part quality. The pressure force is selected by press. In the paper, the effect of pressure force on part temperature is analyzed in order to obtain reasonable pressure region [4] (Table 4).

The temperatures of parts are relatively compared in the paper. Because of part symmetry, the right side is selected to be analyzed. The certain meaning of number is as the following: (Figs. 8 and 9).

When the die temperature is 25 °C, the part temperature will decrease about 120 °C with holding pressure time increasing 2 s through analyzing the temperature distribution of part. With die temperature increasing, the decreasing degrade of part temperature will decrease with holding pressure time increasing. When die temperature is 75 °C, the whole temperature of part will decrease about 80 °C with increasing 2 s of pressure holding time. If the holding pressure time is longer, the part properties are better because die temperature is low. However, long holding pressure time will have heavy effect on work efficiency. Thus, the holding pressure time is selected as 5 s.

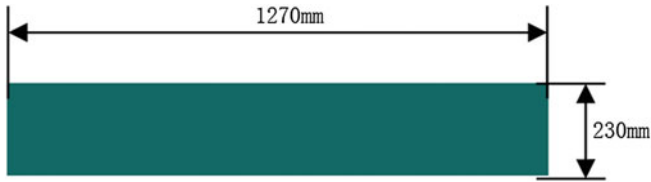
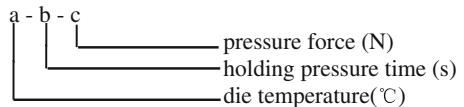


**Fig. 7** Shape and size of blank

**Table 4** Effect of holding pressure time and pressure force on cooling rate

No	Die temperature (°C)	Holding pressure time (s)	Pressure force (N)	Temperature after drawing (°C)	Temperature after holding (°C)		
1	25	3	0	779.529–672.077	691.959–189.866		
2			60		524.790–138.073		
3			120		460.032–138.073		
4		5	0		660.131–88.199		
5			60		416.044–60.350		
6			120		347.850–60.350		
7		75	7		0	779.547–679.893	629.811–49.179
8					60		331.139–36.054
9					120		267.724–36.054
10	3		0	669.662–227.998			
11			60	540.189–180.370			
12			120	492.834–180.370			
13	7	5	0	779.547–679.893	625.188–132.754		
14			60		438.143–107.867		
15			120		383.132–99.831		
16		7	0		586.151–96.196		
17			60		358.230–85.255		
18			120		302.325–81.619		

**Fig. 8** The meanings of serial number



With increasing 60 N of pressure keeping force, the part temperature will decrease 200 °C when pressure keeping force ranges from 0 to 60 N. When pressure keeping force ranges from 60 to 120 N, the part temperature will decrease about 80 °C. For the rapidly decreasing of part temperature, the bigger pressure keeping force is more effective. In actual production process, excessive pressing keeping force will consume too large energy. So, there is certain limited condition for different pressure. With combining the above studies and structure of front cross member internal plate, the following parameters are defined:

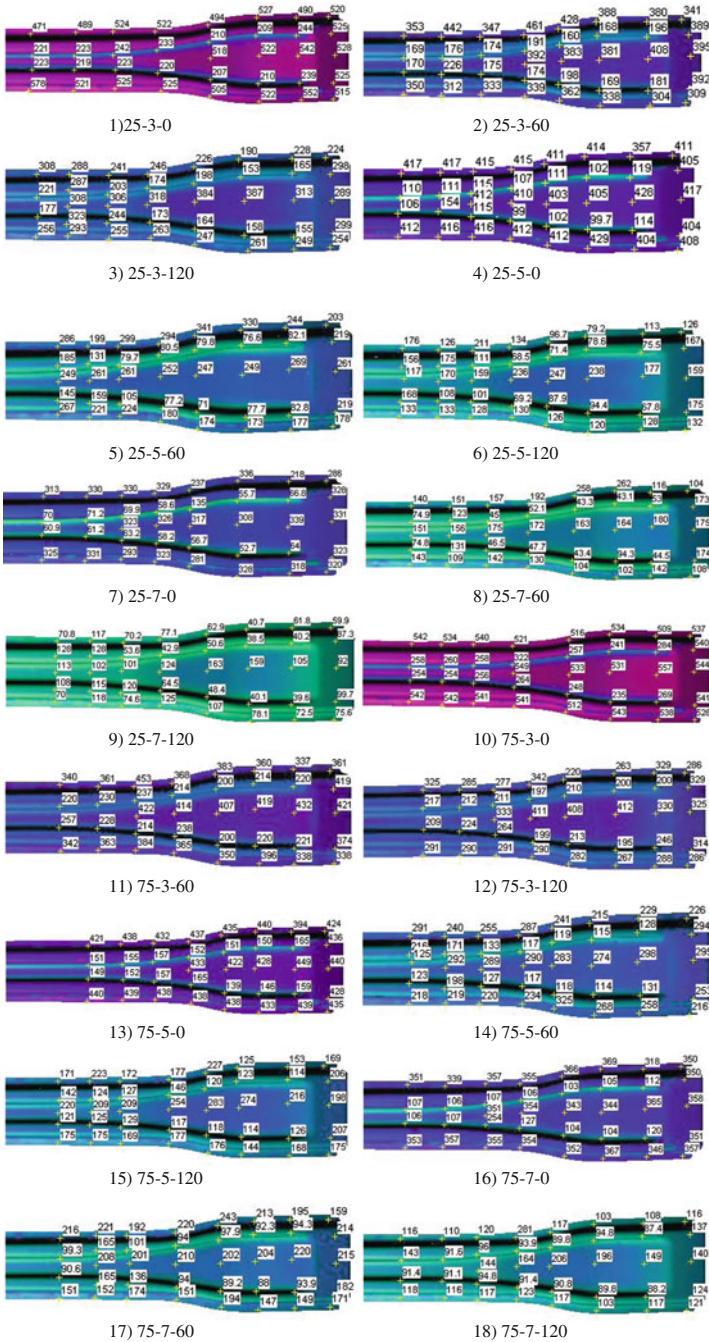


Fig. 9 Temperature distribution of parts after holding pressure

- (1) The holding pressure time is 5 s;
- (2) The press keeping force is 60 N;
- (3) Mould-opening temperature is about 200 °C.

## 6 Conclusion

With adopting fitting method, the constitutive equation is obtained in the paper through studying the strain and stress of ultra-strength steel 22MnB5, which is applied for FE simulation of hot stamping. At the same time, the holding pressure and cooling process of a commercial vehicle front cross member internal plate is analyzed in order to select reasonable parameters.

## References

1. Sun J, Jing Z Vehicle light weight technology and application
2. Karbasian H, Tekkaya AE (2010) A review on hot stamping. *J Mater Process Technol* 210:2103–2118
3. Merklein M, Lechler J (2006) Investigation of the thermo-mechanical properties of hot stamping steels. *J Mater Process Technol* 177:452–455
4. Wang L, Wang Z (2012) Hot stamping parts quality control factors analysis. *Forging and stamping technology* 35(2012):117–120

# Research on Heavy-Duty Truck Axle Housing Hydroforming

Weicheng Zhu, Chenglin Xu, Yucheng Zhang, Zhuang Fu, Shibao Liu, Guansheng Wang, Haiping Li, Wencheng Li, Hanying Li and Baoyang Song

**Abstract** The hydroforming technology for axle housing of heavy-duty trucks was developed as well as the process parameters and controlling relationship between axle feeding with internal pressure and sealing were obtained. Based on the uneven distribution of axle housing material, the heavy-duty truck axle housing hydroforming was simulated by finite element analysis. The major failure mode during hydroforming such as cracking and wrinkling has been resolved. At last, 1:1 axle housing of heavy-duty trucks processing under high pressure source has been finished.

**Keywords** Hydroforming · Heavy-duty truck · Axle housing · FE analysis · Process

## 1 Introduction

The axle housing which supports the truck loading and transfers the movement to wheels, plays an important role in commercial vehicles. To reduce the weight under spring to decrease dynamic load and improve driving comfort, we should reduce axle housing weight under enough strength and stiffness, higher strength and lighter are the trends of axle housing development [1].

---

F2012-H06-008

---

W. Zhu · C. Xu · Y. Zhang · Z. Fu · S. Liu (✉) · G. Wang · H. Li · W. Li · H. Li · B. Song  
China FAW Co., Ltd, Changchun, China  
e-mail: xuchenglin@rdc.faw.com.cn



**Fig. 1** Casting axle housing



**Fig. 2** Stamping-welding axle housing



**Fig. 3** Mechanical expansion axle housing

According to manufacture process, axle housing can be classified into casting axle housing (Fig. 1), stamping-welding axle housing (Fig. 2), mechanical expansion axle housing (Fig. 3) and hydroforming axle housing Table 1.

## 2 The Current Situation of Hydroforming Axle Housing Research

Hydroforming technology is a lightweight structure manufacturing technology which achieves weight reductions of around 30 %, reduction of components and improved part properties are only some of the advantages in comparison with the manufacturing of such components by conventional sheet metal forming processes [3]. The most successful auto parts manufacturing applications is subframe. The section perimeter of subframe is slightly different while has great shape changes, it is appropriate for hydroforming. Automotive rear axle housing is one of the most representative products for the straight hydroforming process. Compared to the traditional manufacturing method, the stamp-welding process, the hydroforming



**Table 1** Comparison of various manufacturing processes for axle housings [2]

	Advantage	Disadvantage	Application	Development prospects
Casting axle housing	Variable thickness distribution, high stiffness and strength	Thick-walled, heavy, poor impact resistance	Middle and heavy duty truck	Mainly in heavy duty truck
Stamping-welding axle housing	Light, high efficiency	Excessive process, simple section, excessive welding, High welding quality requirements	Various application on light duty, middle duty and heavy duty truck	Dominant in a certain period of time
Mechanical expansion axle housing	High material utilization, light, high strength and impact resistance	Low efficiency, special equipment	Light duty, middle duty and heavy duty truck	Gradually expand application
Hydroforming axle housing	Light, high material utilization, less manufacture process, reasonable thickness distribution, high stiffness and strength	Technology immaturity, under development and trial production	Light duty, middle duty and heavy duty truck	New technology, fine market prospects

process can form rear axle housing from just a single tubular blank without welding, which leads to higher structural integrity, and shorter development time [4]. But the housing shape determines the characteristics of the uneven distribution of the material, Therefore, the hydroforming process is very difficult. Currently, related reports about practical application of hydroforming axle housing have not been found both at home and abroad.

The advantages of hydroforming axle housing are obtained housing back cover and triangle portion directly during forming. Omitting back cover and triangle portion fabrication and welding process, eliminating welding effect also improves axle housing strength and stiffness. The leaf springs areas can be thickening during sinking process, and improve the intensity. Processing strengthening effect is obvious after cold sinking.

Hydroforming axle housing is the use of hydroforming technology with both ending sinking and local reshaping to form axle housing. The two main process routes are as follows:

- Route 1: Circular tube hydroforming- sinking -middle region reshaping;
- Route 2: Circular tube sinking - hydroforming -middle region reshaping.

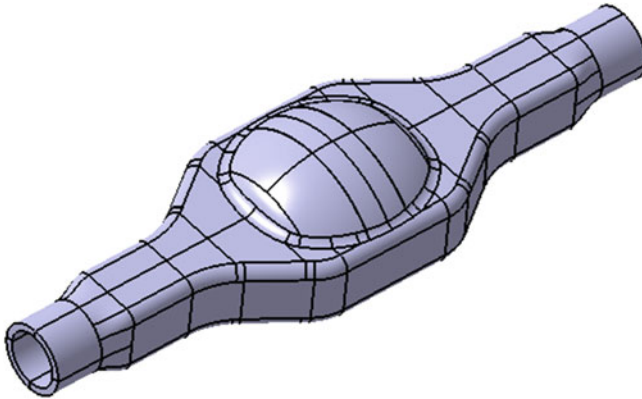


**Fig. 4** Hydroforming wheel deceleration axle housing

Both routes can realize axle housing hydroforming manufacturing process. Considering uneven thickness and material hardening during sinking that affect sealing, we adopt route 1 for our study. The section perimeter ratio for axle housing lute hole and two sides is up to 2–4, the deformation is much larger than subframe. During hydroforming process, we should ensure not only sufficient tube inner pressure, but also good match of inner pressure and material feeding. The main failure during trial process is the back cover regional cracking and wrinkling.

### 3 Hydroforming Axle Housing Process Analysis

A typical hydroforming axle housing process workflow is as below:

Tube cutting-ending turning- Phosphide and saponification (this 3-step process could be done by tube supplier)-Hydroforming process 1 and 2 (depending on Section perimeter ratio)-Ending turning- Local normalizing –Sinking -Annealing-Phosphide and saponification-Forming-Reducer hole cutting- Reshaping (depending on section perimeter ratio).

We carried out the study on the wheel deceleration axle housing, the hydroforming wheel deceleration axle housing is shown in Fig. 4.

During hydroforming process, loading path is a critical factor. Loading path is related to material property, friction and tooling shape, especially for large diameter and thick-walled tube hydroforming process, there is no relevant information, and we can only conclude the proper loading path by finite element analysis and trial. Through tube mechanical properties measurement, finite element analysis and comparing the result to actual process, we concluded the finite element analysis model that can be used to guide the actual process. The reasonable loading path is shown in Fig. 5, which avoids defects such as cracking and wrinkling. We analyze the whole process of axle housing forming, the hydroforming process is shown in Figs. 6 and 7, and the final shape can be seen in Fig. 8.

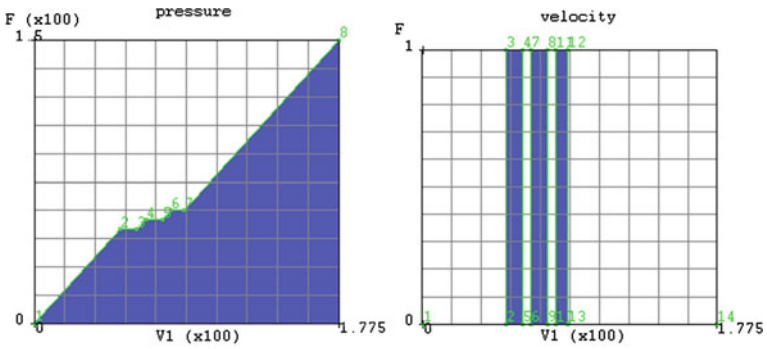


Fig. 5 Loading path

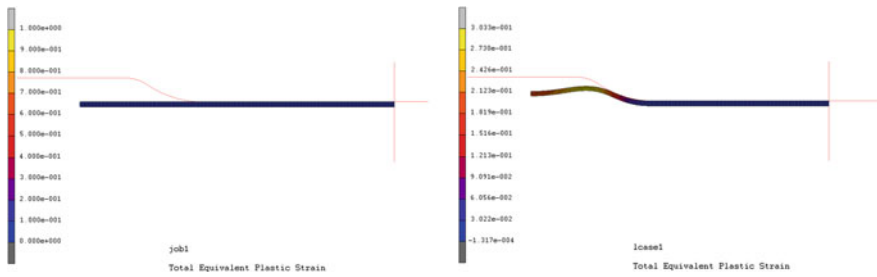


Fig. 6 Hydroforming process

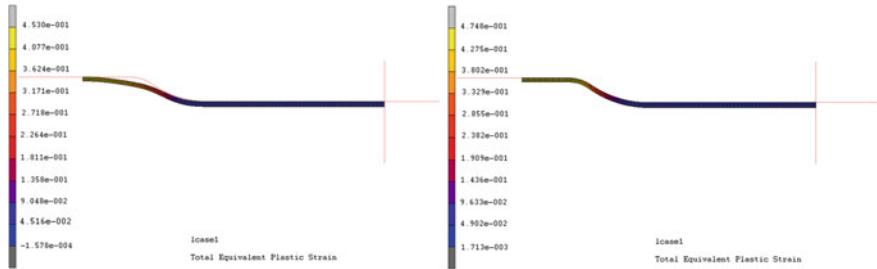
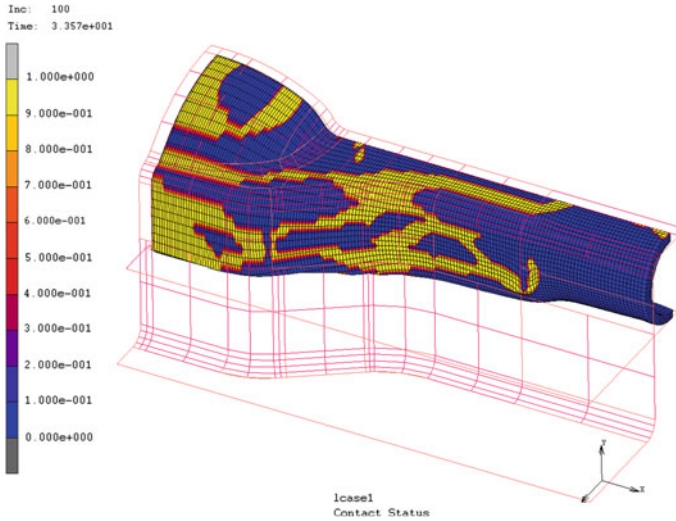


Fig. 7 Hydroforming process

### 4 Trial Process and Problem Analysis

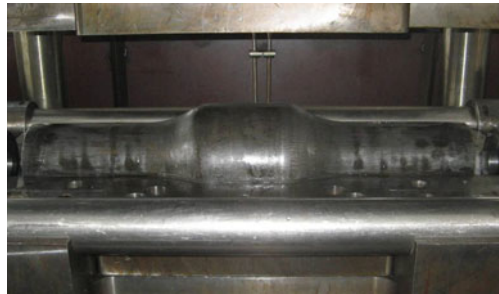
The hydroforming process was carried out on our independent intellectual property patents clamping equipment, the components after hydroforming is shown in Fig. 9.

The four common failure modes during hydroforming are buckling, bursting, wrinkling and folding back [5]. The main failure during trial process is the back cover regional cracking and wrinkling.



**Fig. 8** Hydroforming process

**Fig. 9** Components after hydroforming



Successful hydroforming requires the proper combination of internal pressure and axial feeding. The inner pressure is too high during material initial feeding or the feeding is not sufficient with inner pressure increasing, which will result in extreme thinning of middle part, then the middle part will crack; the initial inner pressure is low or the material feeding is too fast, which will cause wrinkling, as shown in Fig. 10, which can be eliminated by matching inner pressure and material feeding.

We encountered tube surface coursing and end cracking during sinking process, as shown in Figs. 11 and 12. This is caused by tube material severe hardening as repeated sinking, so annealing process needs to be adopted to restore their plasticity, also we can consider hot sinking, which will reduce processes and improve the surface quality.

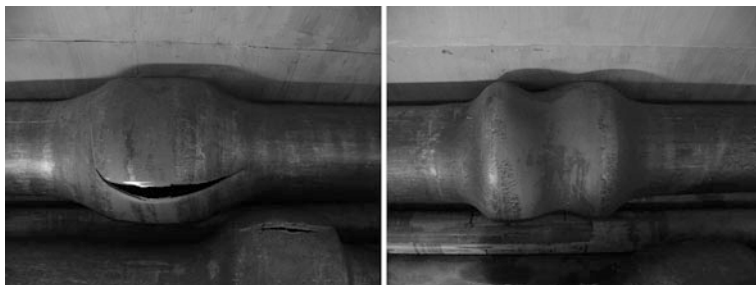


**Fig. 10** Cracking failure and wrinkling failure

**Fig. 11** Surface coursing



**Fig. 12** End cracking





**Fig. 13** Components after hydroforming



**Fig. 14** 1:1 wheel deceleration axle housing

We carried out dozens of axle housing hydroforming process according to the loading path that was confirmed by simulation and experiment, the components after hydroforming is shown in Fig. 13. After sinking and reshaping process, the wheel deceleration axle housing can be obtained as Fig. 14. The hydroforming axle housing wall thickness distributions of different location is shown in Fig. 15 after splitting, it has reasonable thickness distribution as strength requirement different along axle housing.

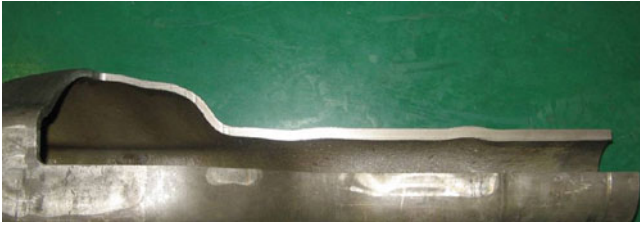


**Fig. 15** Hydroforming axle housing wall thickness distributions

## 5 Achievements and Prospects

The R&D Center of China FAW Co., Ltd carried out study on axle housing hydroforming technology since 2002. 1:5 housing hydroforming process and equipment were developed within a year. The Center emphasized on solving series problem such as high pressure sourcing, feeding institutions synchronization, hydroforming process matching and reshaping process. Subsequently high pressure source and clamping machine with independent intellectual property patents for 1:1 axle housing were developed, which significantly reduced the system pressure of master cylinder and saved equipment cost. We carried out systematic study on 420 axle housing hydroforming process, solving key problem such as fluid adding, pressure increasing, synchronization and process matching. We have developed the entire hydroforming technology of wheel deceleration axle housing.

The study is carried out basically on laboratory condition, which has some difference with mass production. But systemically study of the whole process demonstrated the feasibility of the heavy-duty truck axle housing hydroforming process. And we concluded the key technical solutions of axle housing hydroforming as below:

- (1) The effective FE model of axle housing hydroforming process.
- (2) Axle housing hydroforming process and tooling design guidelines.
- (3) The sealing method of using water as hydroforming media.
- (4) Material feeding and inner pressure matching relation and automatic control technology.
- (5) Reshaping axle housing back cover and fillet.

Compared to the existing manufacturing process of axle housing, hydroforming process has more advantages. The development and application of hydroforming process will lead to a new stage of axle housing manufacture, the hydroforming axle housing will win the market, and have broad prospects.

**Acknowledgments** This paper is achievement of our project team nearly 10 years' work, reflecting the collective wisdom and selflessness of the entire project team. Here, I will express my heartfelt thanks to all the people that participated, helped and concerned the project.

## References

1. Liu W (2004) Vehicle axle design. Tsinghua University Press, Beijing, pp 2–6 (In Chinese)
2. Lei LP, Kim J, Kang BS (2000) Analysis and design of hydroforming process for automobile rear axle housing by FEM. *Int J Mach Tools Manuf* 40:1691–1708
3. Dohmann F, Hartl Ch (1998) Hydroforming components for automotive applications. *Fabricator* 28(2):30–38
4. Lei L-P, Kim J, Kang S-J, Kang B-S (2003) Rigid-plastic finite element analysis of hydroforming process and its applications. *J Mater Process Technol* 139:187–194
5. Dohmann F, Hartl Ch (1997) Tube hydroforming—research and practical application. *J Mater Process Technol* 71:174–186



**Part V**  
**Paints, Polymers and Coatings**

# Weight Reduction and Paint-Less of Plastic Parts of Automobile by Polypropylene/Elastomer Blends

Hiroaki Nagashima and Kayo Kikuchi

**Abstract** Recently the technology on weight reduction such as foam injection molding and thin-wall injection molding has developed to reduce the weight of plastic parts of automobile. Paint-less technology by using pre-colored material has also developed to save the painting cost and the environmental load. This report introduces our study on filler-less polypropylene/elastomer blends that have high mechanical properties and colorability, and low density.

**Keywords** Polypropylene · Elastomer · Polymer blend · Weight reduction · Paint-less

## 1 Introduction

Polypropylene (hereinafter referred to as PP) is widely used with automotive interior/exterior plastic parts including bumpers and/or trim parts for being low cost and excelling also in the material property balance and/or molding formability. The basic concept of the material design is based on ICP (=Impact Copolymer) where ethylene propylene rubber (EPR) is blended within PP via the copolymerization and comprised mainly of ternary systems that complement

---

F2012-H07-002

---

H. Nagashima (✉) · K. Kikuchi  
Research and Development Promotion Department, Suzuki Motor Corporation,  
Hamamatsu, Japan  
e-mail: nagashimah@hhq.suzuki.co.jp

rigidity and impact resistance through the elastomer and the inorganic filler materials such as talc, etc. [1]. Based on the material design, an optimum formulation is determined according to the required performance of each of the parts.

In recent years, along with the demand for reducing the weight of automotive plastic parts, lowering of the density of resin materials is also required. In addition, switching to a paint-less process is being promoted in view of reducing environmentally hazardous substances and for reducing the cost of painting materials, and performance that used to be supplemented by paintings is expected with resin materials, such as high color development and scratch resistance capabilities. Though there are similar needs with PP, those needs are not yet met under the current conditions. As the main factor, the impact of adding talc to apply rigidity and/or heat resistance can be cited. By adding talc, the specific density surges, and this further results in causing issues with the quality of color development to deteriorate by clouding substrates making whitening conspicuous when scratched. Various attempts have been grappled with, up to now, to lower the density and apply transparency such as approaches from additives using crystal nucleating agents, others from inorganic filler materials to replace talc, etc.; however, all of these efforts proved to be insufficient to comprehensively satisfy all the aspects of transparency, rigidity and impact resistance.

In this study, in order to comply with weight reduction and paint-less needs, we aimed to acquire material properties of rigidity and/or impact resistance, etc. similar to the existing ternary PP types through the use of only binary systems of PP/elastomers where there are no inorganic filler materials such as talc, etc. added, which becomes one of the factors that increase density as well as reducing transparency and/or scratch resistance.

As a result of the study, it became evident that the blend of homo-polypropylene (hereinafter referred to as h-PP) and hydrogenation-type styrene, ethylene butylene, and styrene triblock copolymer (hereinafter referred to as SEBS) could be compatible by offering an equivalent rigidity as well as impact resistance similar to the existing ternary PP types and could manifest a high level of transparency. In this manuscript, we hereby report on its manifestation mechanism as well as weight reduction and/or application to automotive plastic parts with the purpose of switching to a paint-less process.

## **2 Direction of New Material Design and Property Test Method**

### ***2.1 Direction of New Material Design***

In terms of material design, it's difficult for the existing ICP to acquire rigidity without blending such inorganic filler materials as talc. In addition, EPR is not

**Table 1** Characteristics of SEBS used in this study

Sample	$M_w^{*1}$	$M_n^{*2}$	Styrene/EB wt %
SEBS-a	$12.0 \times 10^4$	$11.4 \times 10^4$	12/88
SEBS-b	$5.50 \times 10^4$	$5.24 \times 10^4$	18/82
SEBS-c	$5.50 \times 10^4$	$5.24 \times 10^4$	42/58

\*1 Weight average molecular weight

\*2 Number average molecular weight

appropriate for pursuing transparency when considering the visible radiation's wavelength regions (approximately 380–780 nm) due to having a dispersed particle size on the order of more than several  $\mu\text{m}$  within PP. Thus, in this study, we established the basic direction of the material design concept different from the existing method by selecting h-PP as the base PP, which excels in hardness and transparency, and by realizing the rigidity and impact resistance to be complementary by adding elastomers. Based on this direction, as for elastomers, we considered a styrene-type elastomer to be most effective in enhancing the effects of impact resistance [2] and opted for SEBSs, which excel in weatherability and heat resistance in view of their uses on paint-less products.

## 2.2 Samples

In this study, h-PP (Modulus of elasticity in flexure: 2100 MPa, Charpy impact strength (23 °C): 1.0 kJ/m<sup>2</sup>, Rockwell's hardness: HRR 111, MFR: 40 g/10 min) and three types of SEBS-a to c (Table 1) with differing styrene amounts were used as samples.

For comparing density, color development as well as scratch resistance, a ternary PP type with a talc additive amount of 15 wt % (as lubricant, oleamide 0.3 wt (100 : 0.3) additive, density: 1.01 g/cm<sup>3</sup>, bending modulus: 1530 MPa, Charpy impact strength (23 °C): 36 kJ/m<sup>2</sup>, Rockwell's hardness: HRR 37, MFR; 41 g/10 min) were used.

## 2.3 Sample Preparation

The material process was conducted using the twin screw extruder KTX-30 (made by Kobe Steel Ltd., screw diameter 32 mm, L/D = 44). A pellet was produced by setting the fusion zone's cylinder temperature at 200 °C and mixing with a rotation rate of 180 rpm and discharge of 15 kg/h.

## 2.4 Measurement

### (1) Mechanical property

Modulus of elasticity in flexure: Measured in accordance with ISO 178, 1993.

Charpy impact strength: Measured in accordance with ISO 179, 1993.

Rockwell's hardness: Measured in accordance with ISO 2039/2-87.

Density: Measured in accordance with ISO 1183-87.

Molding shrinkage: Measured in accordance with ASTM D 955-89.

\* Test piece size:  $80 \times 70 \times t$  3.0 mm

Coefficient of linear expansion (TMA method): Measured in accordance with JIS K 7197.

### (2) Transparency

A mirror plate with a thickness of  $t = 2$  mm was injection-molded, and transparency was measured with Haze values using a Haze computer (HZ-2 of Suga Test Instruments Co., Ltd.).

### (3) Morphology observation

The injection-molded strips of test pieces were cut in the direction of resin flow (MD) as well as the vertical direction (TD) of resin flow, and after forming into ultra-thin pieces consisting of 100 nm in thickness using a freezing microtome, they were dyed with ruthenium tetroxide. Morphology was observed by using a transmission electron microscope (H-8100 made by Hitachi High-Technologies).

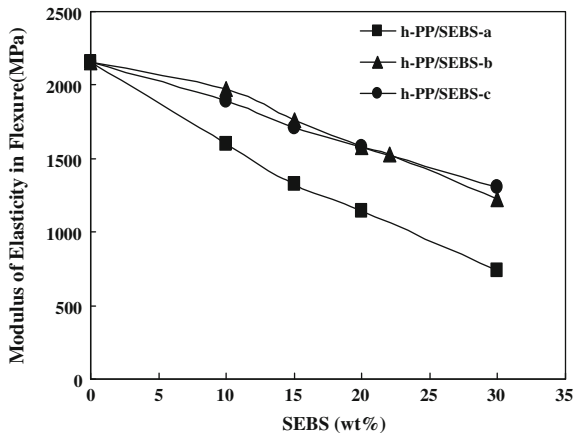
### (4) Color development

The two colors, silver metallic, which is vulnerable to the transparency of the materials, and black were evaluated. With regard to the silver metallic color, aluminum flakes comprised of an average particle diameter of 20  $\mu\text{m}$  were added one part by weight to the pellet produced for coloring, and for the black color, carbon black comprised of an average particle diameter of 20  $\mu\text{m}$  at one part by weight was added for coloring. The glossy feel of the silver metallic color was evaluated based on flip-flop values (hereinafter referred to as FF value), and for the black color, it was evaluated based on luminosity ( $L^*$  value). Flip-flop as well as  $L^*$  values were measured using a spectrophotometer (CM-508d made by Konica Minolta).

### (5) Scratch resistance

With regard to the material for evaluating scratch resistance, the erucamide blended with a 0.2 part per weight used as a lubricant at the time of manufacturing the pellets was applied. For the evaluation, an automatic cross-cut tester (No. 551 made by Yasuda Seiki Co., Ltd.) specified in JIS K5400 was used. A cross-cut scratch test was conducted with the test conditions using a needle made of sapphire with a tip of R0.3 and a load of 4.41 N, and after making scratches of  $11 \times 11$

**Fig. 1** Plots of modulus of elasticity in flexure against SEBS Content



cuts, the depths of the scratches where the scratches were applied were measured using a surface roughness tester (50SMC2 N-K made by Taylor-Hobson).

### 3 Results and Discussions

Shown in Figs. 1, 2 and 3 are the results of modulus of elasticity in flexure, Rockwell’s hardness, and Charpy impact strength (23 °C) for each of the SEBS additive amounts. The modulus of elasticity in flexure as well as the Rockwell’s hardness deteriorated along with the increased SEBS amounts in either of the types. Among these, the h-PP/SEBS-a blend type indicated the most significant degradation. On the other hand, Charpy impact strength (23 °C) sharply increased with h-PP/SEBS-a blends as well as h-PP/SEBS-b blend types when the SEBS additive amount was set at 15–30 wt % levels. As for the h-PP/SEBS-c blend types, they gradually increased when the SEBS additive amount exceeded a 20 wt % level.

The measurement results of the Haze values are shown for each SEBS additive amount in Fig. 4. Here, the Haze values are the values that indicate the degree of cloudiness of the resins and can be shown in the Formula (1). The Haze value is the value where a diffuse transmittance (Td) is divided by the total transmittance (Tt). And it is shown to indicate its transparency to be higher, the smaller its value.

$$\text{Haze (\%)} = \frac{\text{Diffuse Transmission}}{\text{Total Transmission}} \times 100 \tag{1}$$

With regard to h-PP/SEBS-a blend types, the Haze value was smaller than the h-PP type measured as a single unit, and furthermore, it showed behaviors of trending toward reduction along with an increased SEBS-a additive amount. On the other hand, the Haze value of h-PP/SEBS-b as well as h-PP/SEBS-c blend types increased more than the h-PP type when it was measured as a single unit.

**Fig. 2** Plots of Rockwell's hardness against SEBS content

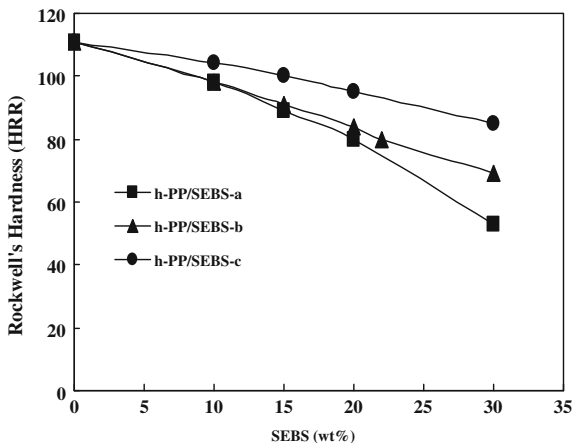


**Fig. 3** Plots of Charpy impact strength (23 °C) against SEBS content

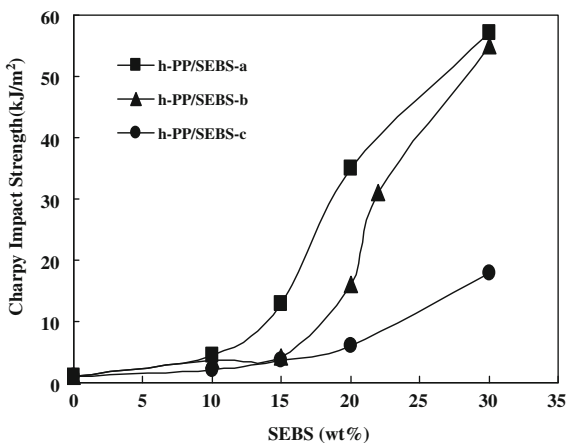
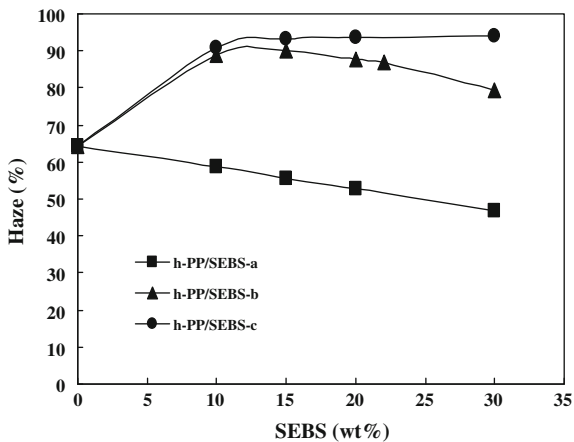


**Fig. 4** Plots of Haze against the SEBS content



In addition, while h-PP/SEBS-b blend types exhibited behaviors to reduce Haze values at the point where the SEBS additive amount exceeded 15 wt %, h-PP/SEBS-c blend types, on the contrary, remained nearly constant as far as Haze values were concerned with no bearing on whether the SEBS additive amounts were increased or not.

Typically, a dispersed particle size can be cited as a factor for manifesting impact resistance with regard to elastomer blend types. In terms of polymer blend types, elastomers, in melted states while being blended and mold-processed, repeat integrations through divisions and collisions from shearing, and according to Taylor, a minimum particle size of a dispersed particle with regard to polymer blends is shown in Formula 2 [3].

$$d = (c \cdot \gamma / \eta_0) (dV_x / d_y) f (\eta_0 / \eta_m) \quad (2)$$

Shown here are the ratios of  $d$  minimum particle size,  $\gamma$  interfacial tension,  $dV_x/d_y$  shear speed,  $\eta_0/\eta_m$ , matrix viscosity ( $\eta_0$ ) as well as dispersed phase viscosity ( $\eta_m$ ). Taylor theorizes that interfacial tension has a significant influence on the dispersed particle size and that the smaller the interfacial tension, the smaller the dispersed particle size. In other words, this signifies that the dispersed particle size becomes smaller, the higher its compatibility. Additionally, with regard to types like PP/elastomer blends where micro-deformation patterns indicate shearing deformations, it is known that the manifestation effects of impact resistance are more evident the smaller the diffused particle size of the elastomers [4]. Based on these findings, it can be estimated that out of the h-PP/SEBS blend types, SEBS-a indicated high compatibility with PP, thereby acquiring the highest manifestation effects against impact resistance, and on the other hand, it was more challenging for SEBS-c to acquire manifestation effects against a impact resistance that is low in its compatibility with PP.

As for transparency, the Haze value for each of the blend types indicated differing behaviors, and with regard to these also, it can be assumed that the variances of compatibility with SEBS versus PP must have played a role. Haze values did not increase compared with the h-PP type as a single unit by adding SEBS to h-PP/SEBS-a blend types. This can be implied as having SEBS dispersed at a particle size of less than approximately 380–780 nm as the visible light wavelength for SEBS-a with a high compatibility with PP. Furthermore, due to the fact that Haze values decreased as the additive amounts of SEBS increased, it can be surmised that the dispersion of visible light was reduced due to the effects of hindering crystallization and refining spherulites working on h-PP [5]. It can be suggested that, due to the fact that Haze values increased by adding SEBS, most SEBS with a particle size exceeding the visible light's wavelength regions must have dispersed on h-PP/SEBS-b as well as h-PP/SEBS-c blend types.

Morphology observation results through TEM of the h-PP/SEBS-b blend types are shown in Fig. 5. When the SEBS additive amount is set at 10 wt %, there exist many SEBSs where their particle size is longer than visible light's wavelengths for both MD (A) as well as TC (C). On the other hand, it is evident that many SEBSs



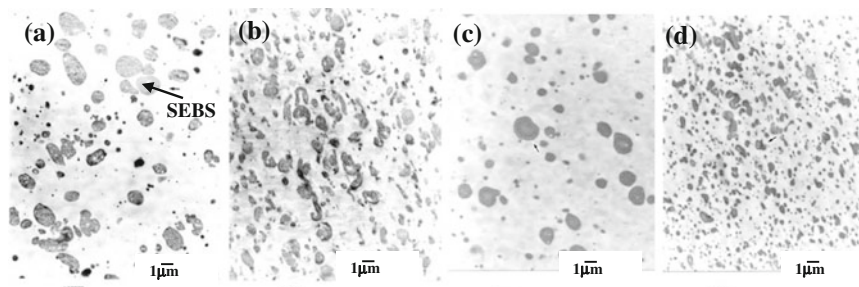


**Fig. 5** TEM micrographs of h-PP/SEBS-b blends. **a** h-PP/SEBS-b = 90/10 wt %, MD; **b** h-PP/SEBS-b = 78/22 wt %, MD; **c** h-PP/SEBS-b = 90/10 wt %, TD; **d** h-PP/SEBS-b = 78/22 wt %, TD

exist whose particle size is less than the visible light's wavelength regions when the SEBS additive amount is set at 22 wt % under either MD (B) or TD (D). In other words, it can be assumed that Haze values decreased due to an increase in the ratios of SEBS where dispersion occurs with a particle size of less than the visible light's wavelength regions bordering around the SEBS additive amount of 15 wt % with h-PP/SEBS-b blend types.

As stated above, it's evident that impacts on mechanical properties and/or transparency greatly differ with h-PP/SEBS types depending on SEBS types and additive amounts. With regard to material design, the key is how well an optimum formulation can be achieved which complements both target physical properties and transparency for these characteristics.

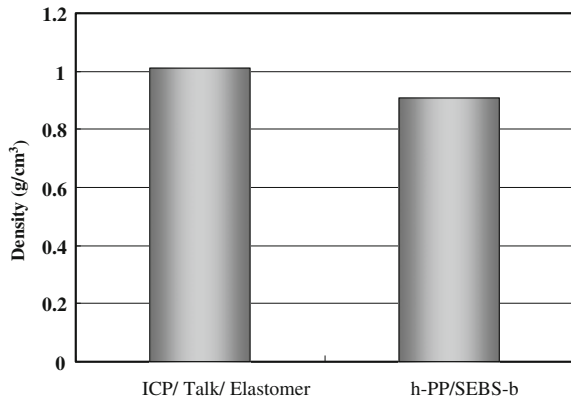
## 4 Application for Automotive Plastic Parts

### 4.1 Application for Reducing Weight of Plastic Parts

The direction of the material design in this study rests with the notion of balancing mechanical properties such as rigidity and/or impact resistance required with materials for bumpers and trim parts without resorting to any inorganic filler materials like talc. We have focused this time on bumper materials where rigidity as well as impact resistance are required by setting our targets for a modulus of elasticity in flexure of more than 1500 MPa and a Charpy impact strength (23 °C) of more than 30 kJ/m<sup>2</sup>.

Based on the results of the modulus of elasticity in flexure, charpy impact strength and haze values as shown in Figs. 1, 3 and 4, it's crucial to select SEBSs that are able to efficiently acquire a balance of rigidity, impact resistance and transparency. Though SEBS-a shows a good compatibility with PP and is conducive in acquiring impact resistance and/or transparency, it exhibits a reduced

**Fig. 6** Density of ICP/talc/elastomer blends and h-PP/SEBS-b blends (78/22 wt %)



rigidity. On the other hand, though SEBS-c tends to indicate rigidity with a greater ratio of hard layers comprised of styrene chains, it's not appropriate for obtaining impact resistance and/or transparency. Among these, SEBS-b being a blend with h-PP excels in the balance between rigidity and impact resistance by indicating an equivalent reduction of modulus of elasticity in flexure versus h-PP/SEBS-c blend types and at the same time showing a similar behavior as h-PP/SEBS-a blend types with the Charpy impact strength. When considering the current target physical properties, SEBS-b is suitable where its SEBS additive amount was optimized with h-PP blend types. As a result, the target physical properties were met through h-PP/SEBS-b = 78/22 wt %. Results of density with a ternary PP type (hereinafter referred to as existing material) as well as the developed h-PP/SEBS-b = 78/22 wt % (hereinafter referred to as developed material) are shown in Fig. 6. The developed material can achieve a 10 % weight reduction versus existing material with the premise of having the same thickness.

## 4.2 Application for Paint-Less Resin Parts

### (1) Color development

Photographs of mirror molded product ( $t = 2$  mm) for existing material (a) as well as developed material (b) are shown in Fig. 7. Compared to the existing material exhibiting a clouding condition due to the impact of talc and/or elastomer, the developed material acquired transparency. The developed material can realize a high level of color development that cannot be achieved with the existing material for obtaining this transparency. With regard to silver metallic color and/or black, etc. which are greatly influenced by the transparency of substrates, it was challenging to acquire a glossy feel and/or the pitch-darkness of the black color with the existing material, but due to the color development quality of the developed material, a high quality feel can be attained that is unprecedented in the past by eradicating a plastic feel.

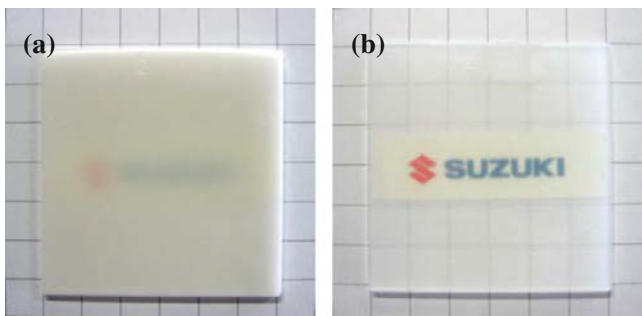
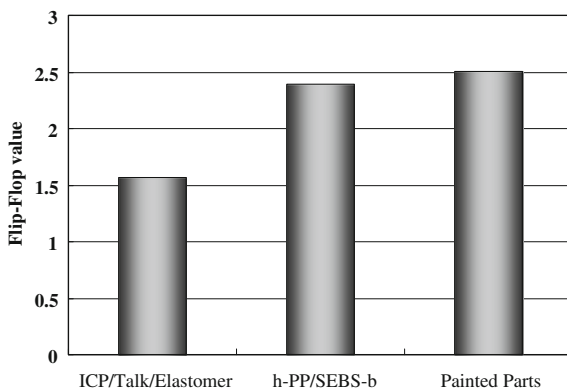


**Fig. 7** Visually observed optical transparency of **a** ICP/talc/elastomer blends and **b** h-PP/SEBS-b blends (78/22 wt %)

**Fig. 8** Flip-flop values of pre-colored silver metallic ICP/talc/elastomer blends and h-PP/SEBS-b blends (78/22 wt %), and silver metallic painted parts

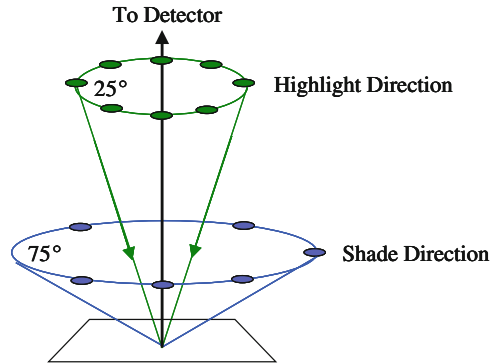


Measurement results of flip-flop values of the silver metallic colored product and silver metallic painted product on the existing as well as developed materials are shown in Fig. 8. As shown in Fig. 9, the FF value here is the value derived by dividing the highlighted luminosity by the shaded luminosity and is indicated through the Formula (3). The higher this FF value is, the higher the gloss. The developed material indicated the same FF value as the silver metallic coated color and attained a color tone with a high level of gloss.

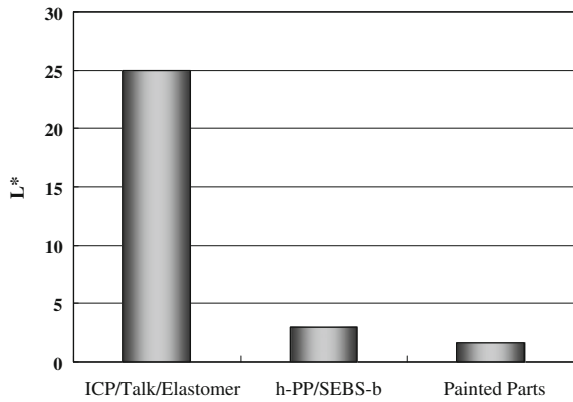
Shown in Fig. 10 are the measurement results of luminosity ( $L^*$  value) with regard to black colored product and pitch-dark painted product of the existing material, as well as of developed material. Here, the lower the  $L^*$  value, the higher the blackness of the color is indicated. A color tone that is high in blackness for the developed material was achieved by indicating an  $L^*$  value equivalent to the pitch-dark coated one.

$$\text{Flip-Flop} = \frac{\text{Lightness when highlighted}}{\text{Lightness when shaded}} \quad (3)$$

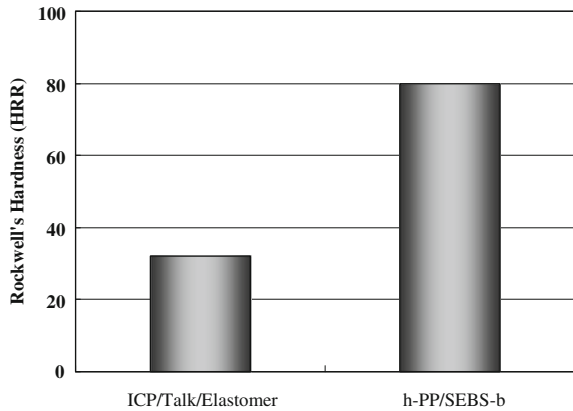
**Fig. 9** Measurement of flip-flop value



**Fig. 10** L\* values of pre-colored black ICP/talc/elastomer blends and h-PP/SEBS-b blends (78/22 wt %), and jet-black painted parts



**Fig. 11** Rockwell's hardness of ICP/talc/elastomer blends and h-PP/SEBS-b blends (78/22 wt %)



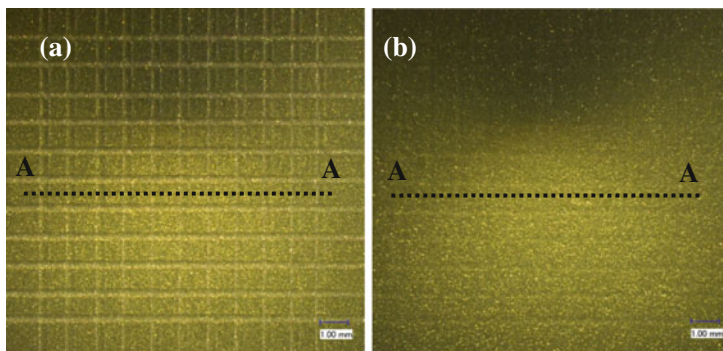


**Fig. 12** Scratch testing results of **a** ICP/talc/elastomer blends and **b** h-PP/SEBS-b blends (78/22 wt %)

## (2) Scratch resistance

Rockwell's hardness of the existing material (a) and developed material (b) and scratch resistance test results of mirror molded product ( $t = 2$  mm) in the cross-cut scratch test are shown in Figs. 11 and 12. It's evident that the Rockwell hardness of the developed material is enhanced and harder by approximately 2.5 times the existing material. As shown in Fig. 11, by enhancing the Rockwell hardness, it was discovered that the scratch marks were hardly discernible on the developed material while the marks were clearly visible on the existing material through the cross-cut scratch test. An A–A cross section drawing indicating depths of the scratches from Fig. 12 is shown in Fig. 13. The depth of scratches of the developed material were reduced by approximately 37.5 % versus the existing material, and the enhancement of scratch resistant performance was confirmed.

## 4.3 Size Stability

### (3) Molding shrinkage factors

Table 2 indicates the measurement results of molding shrinkage factors on the existing material (a) and developed material (b). As the developed material has no fillers added, molding shrinkage factors of MD and TD are greater versus the existing material. For that reason, it's necessary to develop a new mold because no existing mold currently used can be substituted.

### (4) Coefficient of linear expansion

Table 3 shows measurement results of the coefficient of linear expansion of the existing material (a) as well as the developed material (b). Similar to the results of the molding shrinkage factors, due to the fact that the developed material has no fillers added, it has a greater coefficient of linear expansion on MD and TD than

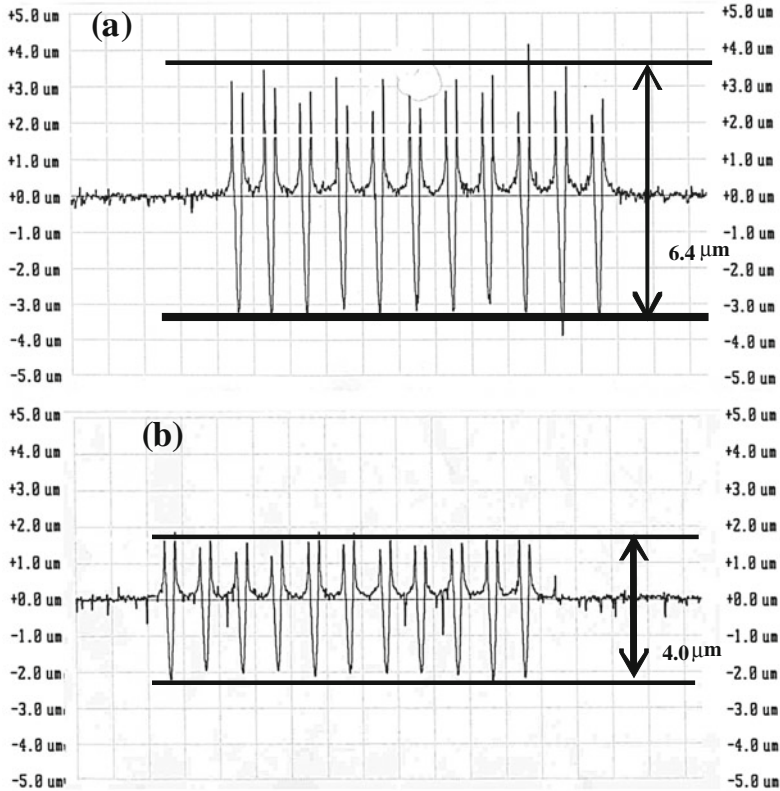


**Fig. 13** Scratch depth of **a** ICP/talc/elastomer blends and **b** h-PP/SEBS-b blends (78/22 wt %)

**Table 2** Molding shrinkage of **a** ICP/talc/elastomer blends and **b** h-PP/SEBS-b blends (78/22 wt %)

Direction	Unit	(a)	(b)
MD	%	1.0	1.2
TD	%	0.5	1.3

**Table 3** Coefficient of linear expansion of **a** ICP/talc/elastomer blends and **b** h-PP/SEBS-b blends (78/22 wt %)

Direction	Unit	(a)	(b)
MD	1/K	$7.6 \times 10^{-5}$	$11 \times 10^{-5}$
TD	1/K	$8.2 \times 10^{-5}$	$14 \times 10^{-5}$

the existing material, which indicates a poor size stability. In recent years, enhancement of quality regarding gaps with exterior parts such as bumpers, etc. is required, and so reducing the coefficient of linear expansion is one of the issues to tackle as we move forward.

## 5 Conclusion

With the mounting demand for fuel economy, environment and cost, it can be predicted that the requests for “weight reduction” and “paint-less process” are to be increased even more in terms of automotive plastic parts as well. These developed materials are resin materials that are created based on the new material design concept in order to respond to these demands. Now that the issues with switching to low density and high color development, which have been challenging to realize with the existing material design, and scratch resistance are further improved, we can expect to launch the new material design concept onto automotive plastic parts as we move forward.

## References

1. Fujita Y (2005) Development status of automotive polypropylene (PP), the Society of Automotive Engineers of Japan, Inc. Spring conference materials forum text, pp 36–39
2. Polymer materials/technology commissioner (inc.) (2004) Service center for Industrial Technology, p 701
3. Taylor GI (1934) *Prod Royal Soc (A)* 146–501
4. Ide F (2001) Polymer materials’ functional characteristics and high-performance technology. Institute for plastic industry, pp 15–36
5. Ahmad Z, Kumar D, Saroop M (2010) *Polymer engineering and science*. pp 331–341

# Physical Properties of TPO Airbag Cover Using DFSS (Design for Six Sigma) Concept

Woojeong Oh, Hyeondon Kim, Yong Chun, Eungsoo Kim, Jeongmoo Lee and Kidae Choi

**Abstract** Airbag modules are necessary items for passive safety systems in automobile. Airbag covers are usually used for covering modules and must be torn easily by airbag cushion deployment in various environmental conditions because airbag covers have to work very low and high temperature. In order to meet the performance of TPO for airbag cover, optimized compositions were made with mixture design and Taguchi method by DOE of DFSS. Optimized compositions of TPO by DFSS could satisfy material properties and airbag deployment test in heat aging, temperature cycle and thermal shock conditions.

**Keywords** TPO (Thermoplastic polyolefin) · Airbag cover · DAB (Driver airbag) · Deployment · DFSS (Design for six sigma)

## 1 Introduction

Nowadays, automobile is really necessary items for our life and we cannot imagine living without automobile. Therefore, airbag modules are necessary items for passive safety systems in automobile. Frequently, we are exposed to the danger of traffic accident in driving. If airbag module doesn't work in crash, how we can imagine that situation? So, airbag module must have good reliability to be

---

F2012-H07-004

---

W. Oh (✉) · H. Kim · Y. Chun  
Hyundai Mobis, Seoul, South Korea  
e-mail: friend@mobis.co.kr

E. Kim · J. Lee · K. Choi  
LG Chemical, Seoul, South Korea



**Fig. 1** Structure of driver airbag

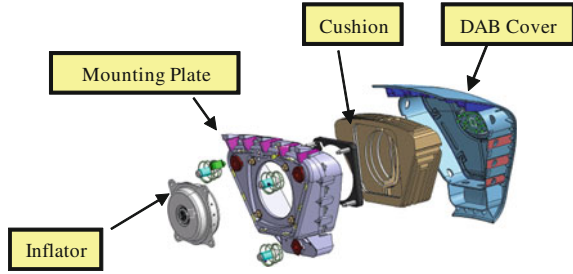
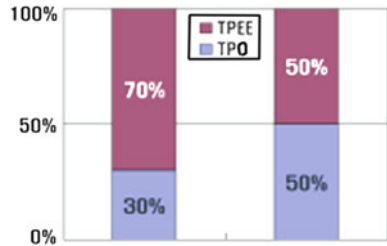


**Fig. 2** Portion of airbag cover material (2006, 2010)



deployed properly and timely to protect passengers with safe. Airbag is one of most important items to satisfy both reliability and quality [1]. Airbag module consists of airbag cover, cushion, retaining part, inflator and so on. General structure of airbag module is shown in Fig. 1. Airbag covers are usually used for covering modules such as DAB (driver airbag), PAB (passenger airbag), and KAB (knee airbag). Airbag cover is located on the top of module and especially DAB cover is frequently pressed for blowing horn. So it has to be rigid enough to hold initial shape and contain airbag cushion during lifetime of vehicle. On the other hand, airbag cover must be torn easily by airbag cushion deployment and have a good touch feeling due to contact of passenger. So it has to be soft enough to deploy airbag module and make a good feeling. It is difficult to make DAB cover materials for airbag cover to meet these two opposed properties.

In the respect of DAB cover materials, TPEE (Thermoplastic polyester elastomer) was mainly used because of its elastic and rigid properties in low and high temperature. But for some day past, airbag is obligatory adopted for satisfying severe safety regulations and competition of airbag market was intensified. So TPO (thermoplastic polyolefin) was spotlighted for airbag cover and production of TPO increased rapidly. Portion of TPO and TPEE for airbag cover is shown in Fig. 2. In this paper, we optimized formulations of TPO materials to meet the required performance of airbag cover by using DFSS concept and verified in the point of mechanical and engineering aspects [2, 3].

**Table 1** Main components of TPO materials

Type	Maker	PP	Rubber			
			Styrene rubber	EPR	EBR	EOR
TPO	A	○	○	○	○	○
	B	○	○	○	X	○
	C	○	○	○	○	X
TPEE	D	PBT, PTMG				
	E	PBT, PTMG				

*PBT* Poly Buthylene Terephthalate  
*EPR* Ethylene Propylene Rubber  
*EBR* Ethylene Butene Rubber  
*PTMG* Poly Tetra Methylene Glycol  
*EOR* Ethylene Octene Rubber



**Fig. 3** Rubber and PP pellets

## 2 Experimental

TPO materials generally consist of rubbers, PP (polypropylene) and additives. PP is mainly used for sustain the shape of products and maintain mechanical properties. Rubber is used for absorbing impact from outside and preventing the broken fragment of materials during deployment. The general components of conventional TPO for airbag cover are listed in Table 1 and their shapes showed in Fig. 3.

Conventional TPO for bumper and electronic parts cannot satisfy the performance of airbag deployment because airbag cover has to work in very low and high temperature such as  $-35$  and  $80$  °C. Formulations of TPO for airbag cover are quite different from them (Fig. 4).

Generally, rubbers are used not only one component but also above three components to meet the requirements. For example, Styrene rubber is very effective impact modifier with low glass transition temperature but price is very high. On the other hand, ethylene rubbers have advantage in price but effect of absorbing impacts is not better than styrene rubber.

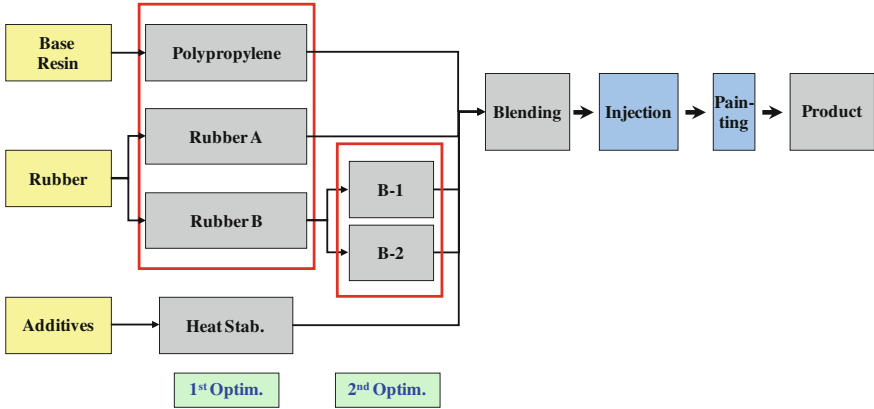


**Fig. 4** Diagrams of components in TPO resin

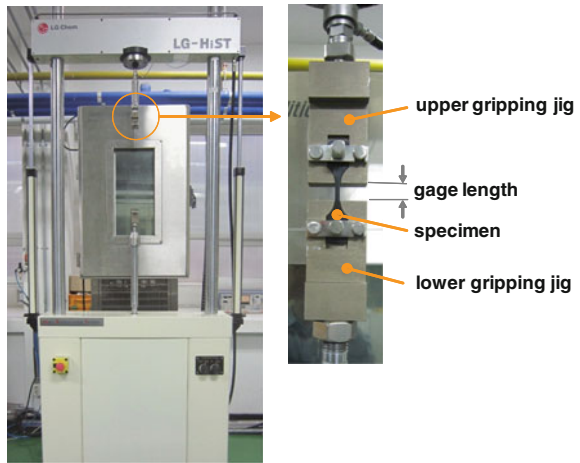
To find optimum composition in finding solution for airbag cover, the approach by DFSS concept was used and we could find optimized mechanical properties of materials. In order to meet the performance of TPO for airbag cover, optimized compositions of PP, rubber and additives must be decided precisely. In this study, mixture design and Taguchi method by DOE of DFSS were used for optimizations. For optimization of composition, key factors such as flexural modulus, IZOD impact strength and hardness were tested in mixture compositions. After optimizations of composition, materials properties and airbag deployment test were fulfilled. In air bag deployment test, airbag cushion have to protect the passenger in 50 ms from outer environments, so airbag cover must be opened completely within 30 ms. But general mechanical properties such as tensile strength with 50 mm/min speed cannot explain the behaviour of airbag cover completely. Therefore, in addition to general mechanical properties, high strain rate test was performed. LG-HIST which was used for high strain rate tester and the test specimens are shown in Figs. 5 and 6 (Table 2).

### 3 Results

In making TPO for airbag cover, cover must have high impact strength for absorbing energy, high flexural modulus and desired hardness about Shore 40D. We chose these factors for output. As mentioned earlier, TPO consists of PP and rubber with low T<sub>g</sub> (glass transition temperature) and high T<sub>g</sub>. So we chose these factors for input. Robust engineering concept is used with based on these input and output components, P-diagrams was expressed in Fig. 7. In the optimizing compositions of PP and rubber, if contents of PP rise up to 60 %, hardness and horn effort performance can be satisfied, but deployment could be able to be passed by

**Fig. 5** High strain rate tester

**High strain rate tester (LG-HIST)**



- Max. Test Speed: 4m/sec

**Fig. 6** Test specimen of high strain rate tester

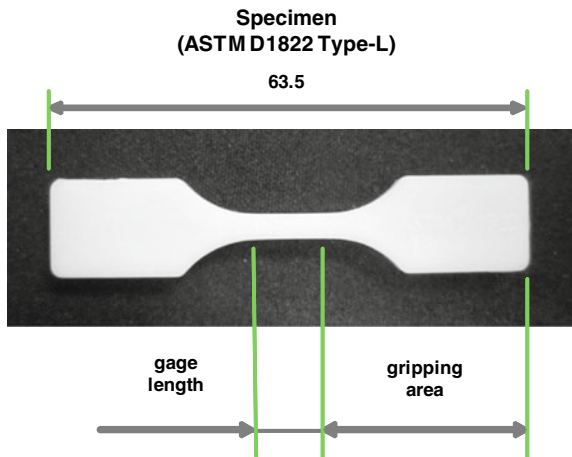


**Table 2** Input factors of P-diagram

No	Factor	Contents (%)	Remark
1	PP	40-60	Injection/mech. prop.
2	Rubber A	20-30	Low temp.
3	Rubber B	10-40	-
4	Additives (Heat stab.)	0.5-1.5	1 (Fix)

Fig. 7 Parameters of P-diagrams

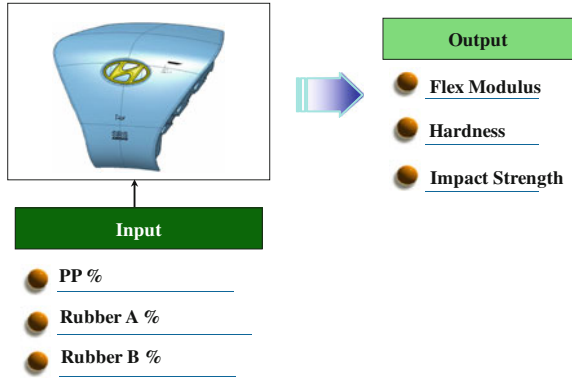
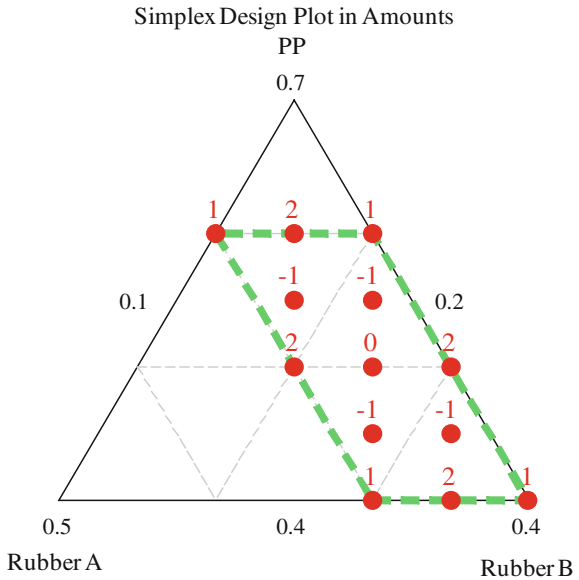


Fig. 8 Mixture design of extreme vertices



brittleness of cover in low temperature. On the other hand, rubber contents cannot be excesses up to 70 % because cover cannot be rigid enough to sustain pressing forces of horn and it can be taken off easily due to too much softness in high temperature. At first optimization of PP and rubbers, mixture design of extreme vertices was constructed in Fig. 8 and mechanical properties test of 13 specimens were performed in Table 3. For satisfying the performance of airbag deployment, airbag cover material must have high impact energy and flexural modulus (Smaller-the-Better) and optimal hardness (Nominal-the-Best). With these properties and test results, optimized compositions of PP/rubber A/rubber B are calculated by MINITAB shown in Fig. 9. Optimum formulations of PP/rubber A/rubber B were 43/25/32 % and it is shown in Fig. 10. At second step, rubber B with two different

**Table 3** Mechanical properties of 13 test matrix

No.	Contents (%)			Results					
	PP A	Rubber B	Rubber B	Flex modulus (kgf/cm <sup>2</sup> )	Hardness (Shore D)	Flex strength (kgf/cm <sup>2</sup> )	Tensile strength (kgf/cm <sup>2</sup> )	Elon- gation (%)	IZOD (kgf.cm/ cm)
1	55	27.5	17.5	5,195	49	130	152	528	NB
2	60	20	20	5,633	52	143	151	546	NB
3	60	25	15	5,685	51	147	151	544	NB
4	40	20	40	3,205	38	74	141	560	NB
5	60	30	10	5,708	50	145	150	532	NB
6	55	22.5	22.5	5,324	47	128	148	507	NB
7	40	25	35	3,132	39	74	146	553	NB
8	40	30	30	2,965	38	72	134	541	NB
9	50	30	20	4,402	43	103	154	550	NB
10	50	20	30	4,564	45	108	170	571	NB
11	45	27.5	27.5	3,791	41	88	148	545	NB
12	45	22.5	32.5	4,159	42	94	157	588	NB
13	50	25	25	4,477	45	109	167	597	NB

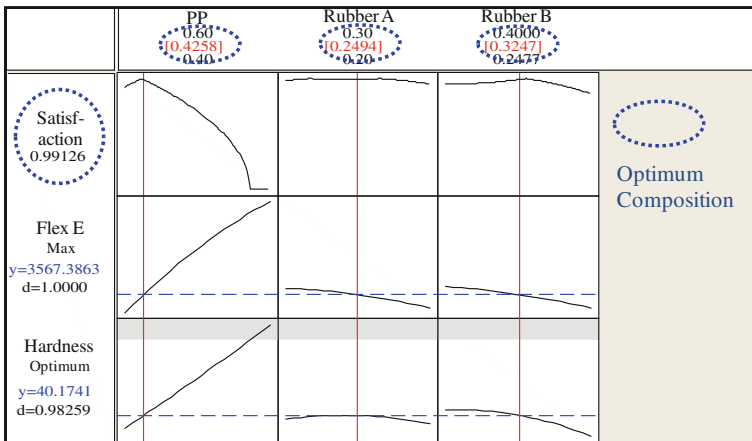
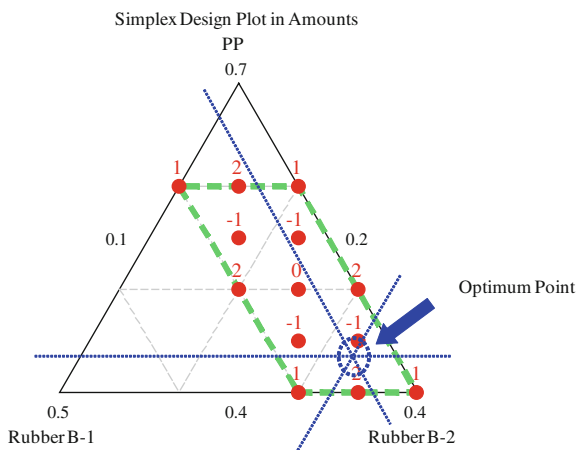


**Fig. 9** Optimization graph of PP/rubber A/rubber B

rubber B-1 and B-2 were designed by orthogonal arrays and five kinds of samples were tested. Also calculating with MINITAB, we could get optimized compositions of TPO with PP/rubber A/rubber B-1/rubber B-2. To analyze and confirm the reliability of this optimized TPO composition, five kinds of Compounds with same composition were made and tested. According to test data, standard deviations and tolerance were calculated. According to Cp value, hardness was sensitive to process capability and it is required to control the compounding process precisely not to produce defective goods (Figs. 11, 12 and 13).

**Fig. 10** Mixture design of extreme vertices



From getting optimized compositions of TPO, we observed SEM (Scanning Electron Microscope) and it showed in Fig. 14. It is clearly observed that rubber domains with spherical shape are dispersed homogeneously in PP matrix.

For applying TPO by DFSS to airbag cover, highly strain rate test was performed to measure strain, stress and toughness energy. The speed of crosshead is 3 m/min and test graph show in Fig. 15. The test results were compared with the other material which is commercially available in airbag cover. Tensile behaviour of these two materials showed very closely. We measured tensile toughness between two materials. Tensile toughness is the area of S–S curve mathematically, and it means the energy that material can absorb from outer impacts. The absorbing energy were very close to each other with 6.27, 6.35 J, In low and high atmospheric temperature, TPO by DFSS also showed good mechanical properties. This fact is very important because airbag should work in low and high temperature condition due to exposure of automobile from outside. So it was supposed that TPO by DFSS can be applied in airbag cover materials (Tables 4, 5 and 6).

In these results, airbag covers with TPO by DFSS were made, and airbag module were assembled to perform airbag deployment testing. The test was performed in three environmental conditions, and the test results were shown in Table 7. Generally, airbag cover can be torn and broken at unexpected spot in low temperature, and can be taken off from module in high temperature. Moreover, airbag cover can be degraded in heat aging and temperature shock due to chain scission of polymer. In test result, airbag module made from TPO cover with DFSS concept showed very clear shapes of tear line in cover and good airbag deployment performance.

In conclusion, optimized compositions of TPO by DFSS could satisfy material properties and airbag deployment test in heat aging, temperature cycle and thermal shock conditions (Fig. 16).

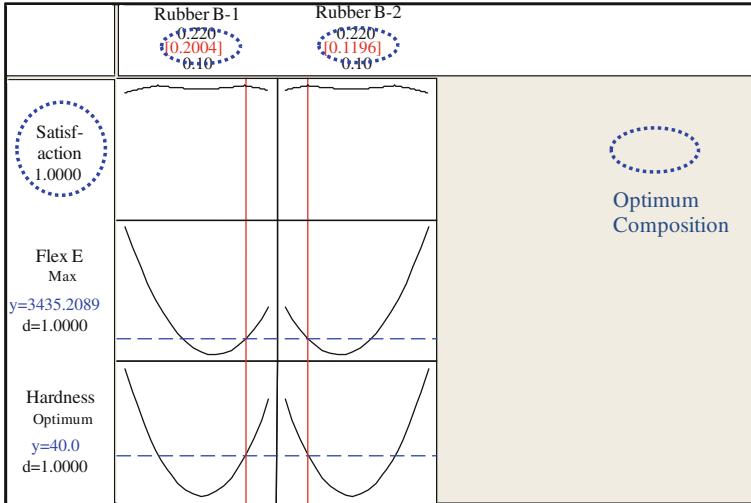


Fig. 11 Optimization graph of PP/rubber B-1/rubber B-2

Fig. 12 Histogram of flex modulus

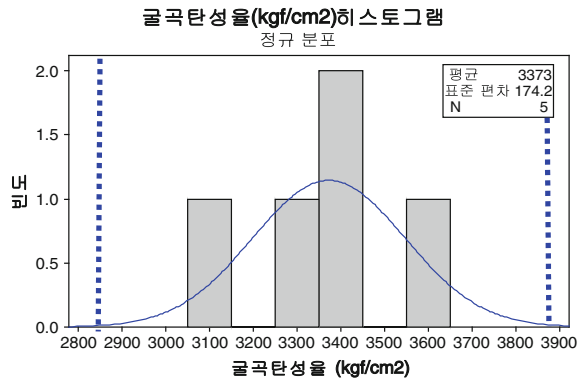
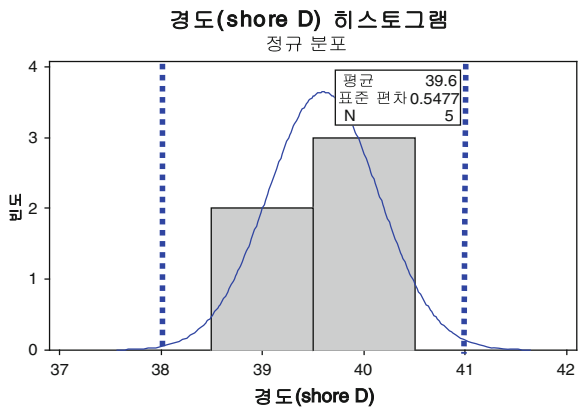


Fig. 13 Histogram of hardness





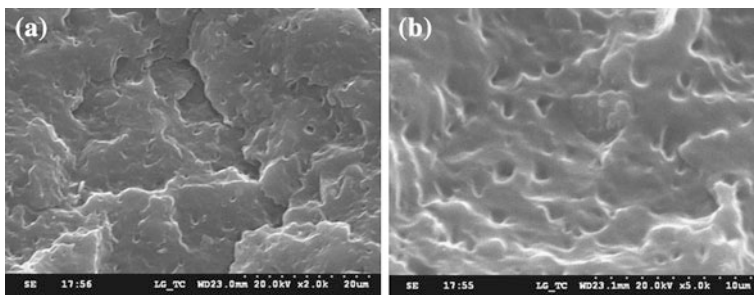


Fig. 14 SEM Image of TPO materials. a 2000x, b 5000x

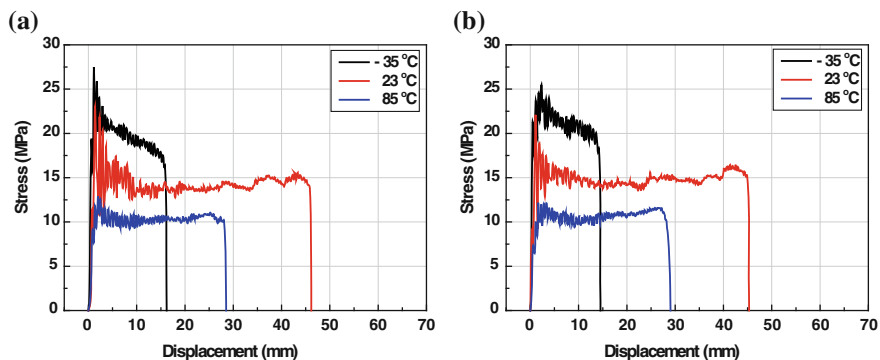


Fig. 15 S-S curve of high strain rate test a TPO by DFSS b Commercial TPO material

Table 4 Mechanical properties of five test matrix

No.	Contents (%)		Results						
	PP	Rubber	Rubber	Flexural modulus (kgf/cm <sup>2</sup> )	Hardness (Shore D)	Flexural strength (kgf/cm <sup>2</sup> )	Tensile strength (kgf/cm <sup>2</sup> )	Elongation (%)	IZOD (kgf.cm/cm)
	A	B	B-1 B-2 32						
Control	43	25	32	3,860	42	87	161	608	NB
1			13	3,520	40	80	153	605	NB
2			16	3,524	41	77	148	620	NB
3			22	3,443	40	71	141	625	NB
4			10	3,352	39	76	146	613	NB
5			19	3,632	41	73	145	621	NB

Table 5 Test results of five compounded samples

	Average	Std. Dev.	Tolerance	Spec. of products	Cp
Flex modulus (kgf/cm <sup>2</sup> )	3,373	174.2	522	2,851–3,895 (±15.6 %)	1.01
Hardness (Shore D)	39.6	0.548	1.6	38–41 (±4.0 %)	0.97

**Table 6** Tensile toughness energy of 2 TPO materials

	Low temp		Ambient		High temp		Remark
	(a)	(b)	(a)	(b)	(a)	(b)	
Energy	2.95	3.03	6.27	6.35	2.88	2.99	Unit: J

**Table 7** Test results of airbag deployment test

	Baseline		Heat aging		Thermal shock		Remark
	Low temp	High temp	Low temp	High temp	Low temp	High temp	
Results	○	○	○	○	○	○	Pass

*Baseline* Airbag deployment test w/o aging

*Heat aging* Airbag deployment test with high temperature aging

*Temperature Shock* Airbag deployment test with low & high temperature cycle

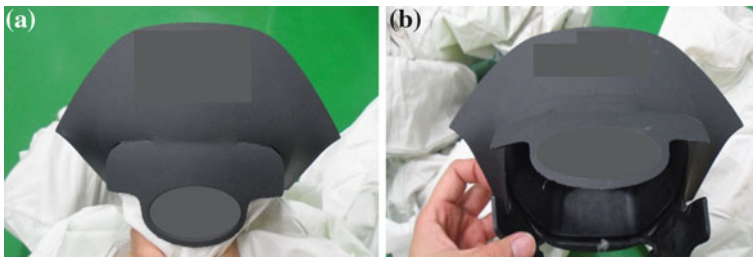


**Fig. 16** Airbag module tested by airbag deployment of **a** Low temperature **b** High temperature

### 4 Conclusions

We could verify that optimized composition of airbag covers by DFSS can satisfy airbag performance and DFSS can be a powerful tool for finding solutions. We could set guide lines of mechanical properties for airbag cover in Mobis products. And we are convinced of applications of DFSS tool in various products of automobile.

### References

1. James Harrington H, Leslie C (1999) Anderson, reliability simplified: going beyond quality to keep customers for life. McGraw-Hill, New York
2. Pyzdeks T (2001) The six sigma handbook. McGraw-Hill, New York
3. Taguchi G et al (2004) Taguchi’s quality engineering handbook. Wiley & Sons Inc, Hoboken

# Building Analysis Methodology of an Integrally Female Vacuum Forming and Injection Compression Moulding

Jo Hyunkwon, Yang Heeseung, Lee Hyunchul, Jang Ickgeun,  
Park Eunjung and Lee Siwook

**Abstract** In recent times the automotive interior industry has tended to focused on low cost, comfortable, eco-friendly products. However, the vast majority of automotive interior products (door trims, instrument panels, pillars etc.) have been made using hard and uncomfortable materials; mostly plastic. To create a softer texture, the products have often been covered with a skin sheet of some kind, like leather or artificial leather (TPO, PVC sheet). This creates problems however, as the adhesives required to attach the skin sheet to the plastic contain several toxic substances that are prohibited in Europe, Australia and many other countries. Furthermore, the common alternative—water-borne—is very expensive. In this paper, to overcome these problems, we introduce the Integrally Female Vacuum Forming and Injection Compression Moulding (ICM), and report the analysis methodology used to access it.

**Keywords** Female vacuum forming · ICM (Injection compression moulding) · Door trim · Eco-friendly · Interior product

---

F2012-H07-005

---

J. Hyunkwon (✉) · Y. Heeseung · L. Hyunchul · J. Ickgeun · P. Eunjung  
Hanil E-Wha Co., Ltd, Seoul, South Korea  
e-mail: johk@hanileh.com

L. Siwook  
CAEpro Co., Ltd, Seoul, South Korea

## 1 Introduction

Current trends in the automotive market have seen both an increase in sales of compact cars and a decrease in the market share of mid and full-sized car. This is largely due to a combination of changes in environmental regulation, increasing oil prices and a general downturn in the global economy. However, customer's demand their compact cars have same level of luxury as the mid or full-sized cars [1]. To meet this expectation, many car companies have tried to develop comfortable and eco-friendly products at low cost. However, almost all of automotive interior products have been made using plastic, which result in a somewhat "hard" and uncomfortable driving experience. To overcome this, automotive interior manufactures cover products with a skin sheet of some kind, like leather, artificial leather, or different kinds of adhesives. Unfortunately, these methods require the use of several toxic substances that are prohibited in many countries, and the alternatives increase the product price significantly.

In a bid to in-part solve this problem, our company has developed a new method: An Integrally Female Vacuum Forming and ICM. Importantly, this method doesn't use harmful substances, minimize the production cost, and has already been patented.

In this paper, we briefly describe the method suggested by our company and introduce a new injection moulding analysis methodology. Given that there is no commercial software available to analyse the method, we devised a program to solve some unforeseen product development problems.

## 2 An Integrally Female Vacuum Forming and ICM

This method foundation has been provided by Injection Compression Moulding (below ICM). ICM has been used to overcome the high pressure generated inside the moulding cavity [2]. In the automotive industry, it has been often used to make the lens of a head lamp. In this case, when the melted resin is injected into the moulding cavity, the mould isn't closed perfectly and is left open a little. This causes the melted resin to flow more easily into the extremities of the cavity so it is under relatively lower pressure and stress. After the resin is forced into the unfilled portions of the cavity, the upper cavity (or movement cavity) closes to mould the product. This produces a more uniform packing pressure across the cavity. This also results in more homogeneous physical product and less moulded-in stresses compared to conventional injection moulding (see Fig. 1).

Based on this process, where the ICM allowed for lower pressure in the cavity, our company developed a method that attached the artificial leather sheet (PVC, TPO) to the product in the upper cavity. The foam of the artificial sheet was created by melting the resin at a high temperature, before adhering it to the cooled plastic. This method called the HPM method, and has been used by our company for more than 15 years. Furthermore, the low covering price has great benefits.

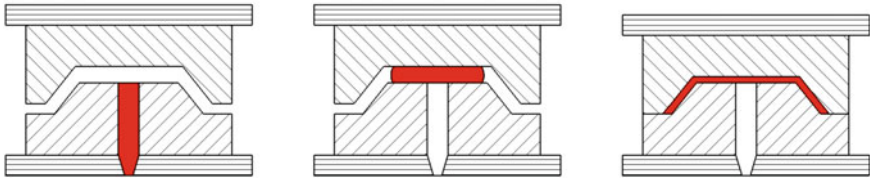


Fig. 1 The process of an injection compression moulding

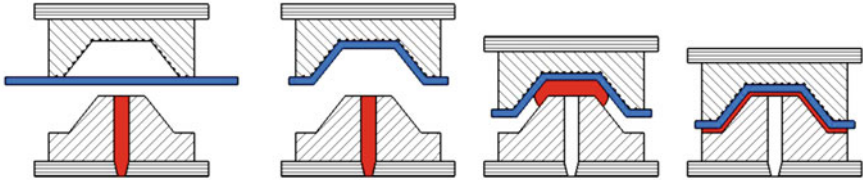


Fig. 2 The process of an integrally female vacuum forming and ICM

However, the current variety of complex interior designs makes using it almost impossible because of the poor quality, so this it's use has decreased.

However, further investigation into this method was suggested, because it doesn't require the use of adhesive substances to attach sheet to plastic. So our company has tried to overcome the various, complex design issues, and tested an Integrally Female Vacuum Forming and ICM (see Fig. 2). The leather or artificial sheet consists of a skin (leather, PVC, TPO) and foam (PP, PU) and made so that the end product can "breathe" (see Fig. 3). The sheet is moved on the head and is then pulled into the correct shape and pattern similar to products produced using the Female Vacuum Forming. The melted plastic resin is then injected into the lower cavity with the upper cavity closing and moulding the product like ICM. Simultaneously the sheet is attached to the plastic like HPM.

We applied this to an Instrument Panel sub-product (see Fig. 4). An unexpected problem occurred however in the development stage. The skin of the product was partly dented. It was apparent upon cutting the product and checking the cross-section that the foam of the dented sheet was thinner than the other areas, making the appearance a problem. Given there was no commercial analysis program for this method, it wasn't initially obvious why the foam was thinner in certain areas. Therefore we built an analysis methodology for it.

### 3 Building Analysis Methodology

Given there are many commercial programs for flow analysis of injection moulding, and that almost all of the programs provide analysis of the module of ICM but not this method, we needed to find the a way to connect the ICM and another analysis module that supply the relationship between multi materials.

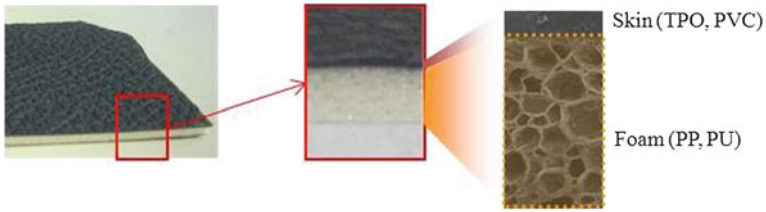


**Fig. 3** The construction section of a original sheet

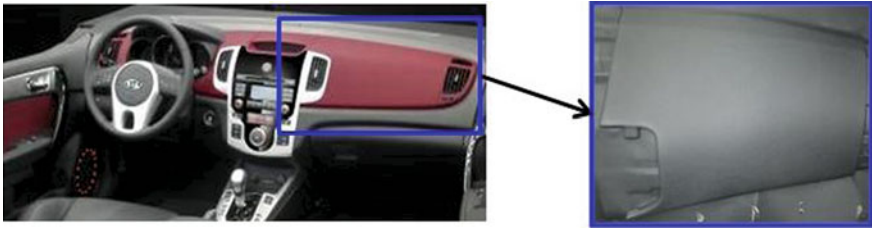


**Fig. 4** An instrument panel and sub-product

In building this methodology, we used a commercial 3D-TIMON program designed by TORAY in Japan, which supports API (Application Program Interface) for the user to handle more easily the results. Basically, we used two modules: (1) ICM and (2) Multi-mould. A Multi-mould analysis module deals with the process—one melted plastic resin is injected, cooled, and hardened [3]. Now that the plastic resin has set, other melted plastic resin is injected. This allows the second resin to spread evenly across the set plastic and adhere to the product. First, 3D solid product design data should be transferred to the mesh model for flow analysis. The mesh model (see Fig. 5) is separated into the sheet part and the core part, and filled with melted plastic resin. Using the core part mesh model, we can analyze the process of the melted resin being injected and the flow in cavity with the ICM module. In this process, we check out the filling of the melted resin and the balance of the flow, and then extract the result of pressure and temperature per mesh, and the different time units that affect the sheet. The sheet mesh elements are applied to specific materials such as TPO or PP, and the extracted result is corresponded with each mesh element using the Multi-mould analysis module. In addition the core part mesh model must have two layers (see Fig. 6). If it does not have two layer, the analysis process fails. Through this process, we were able to analyse the sheet properties, including the pressure and temperature (see Fig. 7).

After examining the result, it became apparent that there was a high temperature in the area where we had the dent (see Table 1). According to the results, each of the three points is located different location and the temperature changes in each of those three point per unit time are evaluated. When observing the temperature changes of a Point 1, you can see that the highest temperature is over the melting temperature. Furthermore, both points 2 and 3's temperatures aren't exceeding it.

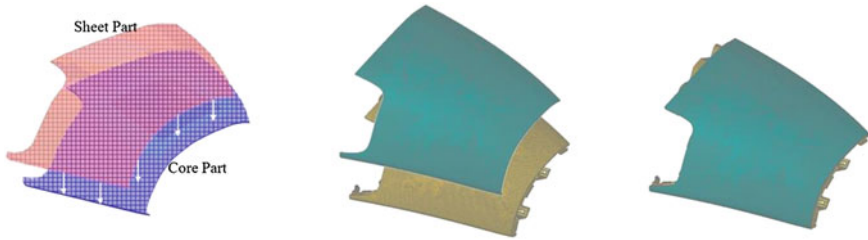


Fig. 5 The structure of a separated mesh model

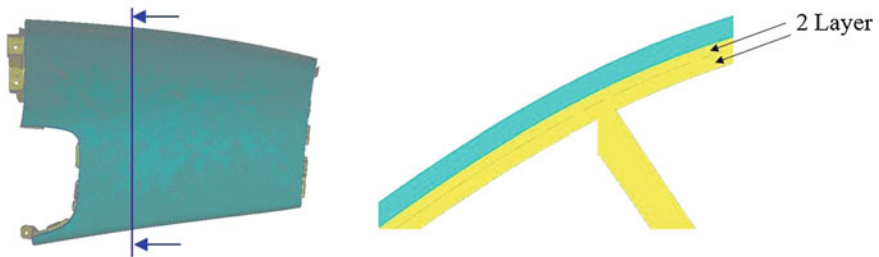


Fig. 6 The section of mesh model and 2 layer core mesh

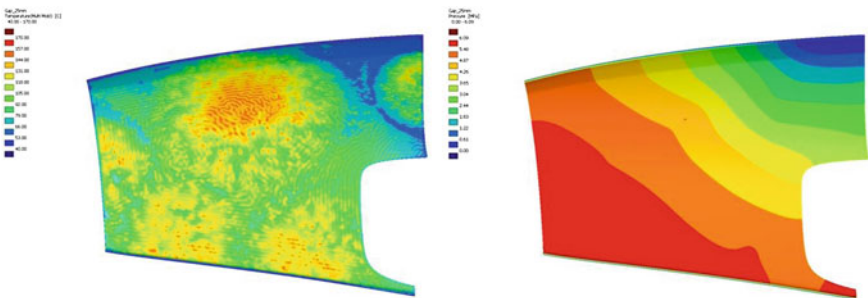
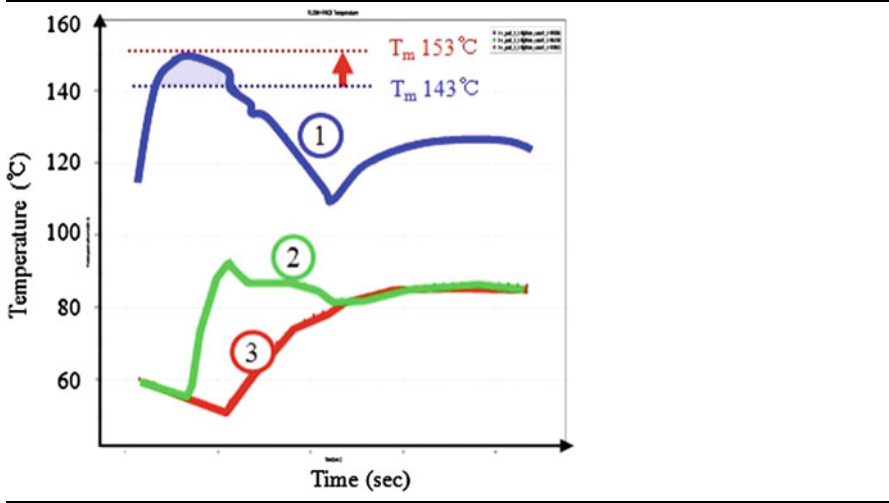


Fig. 7 The result of the sheet backside—temperature and pressure

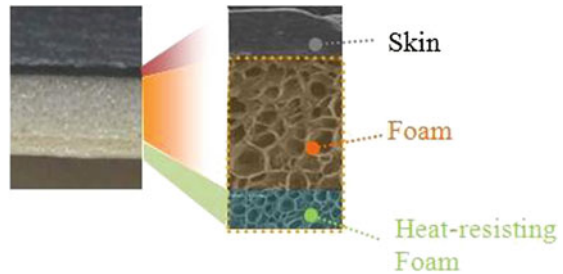
Therefore it was hypothesised that the foam at point 1 had been exposed to the heat for too long and thus the thickness reduced and the dent created.

To prevent the foam from being over exposed, we tested two solutions. The first solution required putting several new and additional cooling channels. The other method requires adding the heat-resisting foam to the original foam (see Fig. 8).

**Table 1** The temperature changes of each points



**Fig. 8** The construction section of a improved sheet



#### 4 Application of an Integrally Female Vacuum Forming and ICM

A centre trim, sub product of a door trim (see Fig. 9) is the one of the interior products that the customer often comes into physical contact with. In compact cars, there is a character line without a centre trim or a plastic product, because this extra cost is seen as too expensive. Furthermore, this requires toxic substances as a covering or paint. But the suggested method enables us to cover the plastic at a lower cost, avoids the use of harmful substances. So our company pre-developed a centre trim using this method (see Fig. 10). The analysis methodology was built after the centre trim moulding. We could not pre-validate, and therefore the centre trim sheet repeatedly had the afore mentioned dent problem. Therefore, we implemented the heat analysis. Figure 11 is a mesh model, and Fig. 12 is the results. The result of temperature analysis showed that some areas had higher than





Fig. 9 The door trim and centre trim—hyundai accent. a Automobile interior, b Door trim

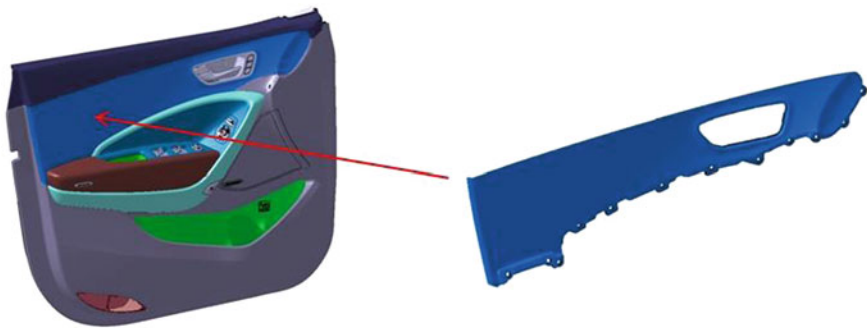


Fig. 10 The door trim and centre trim 3D data of developing product

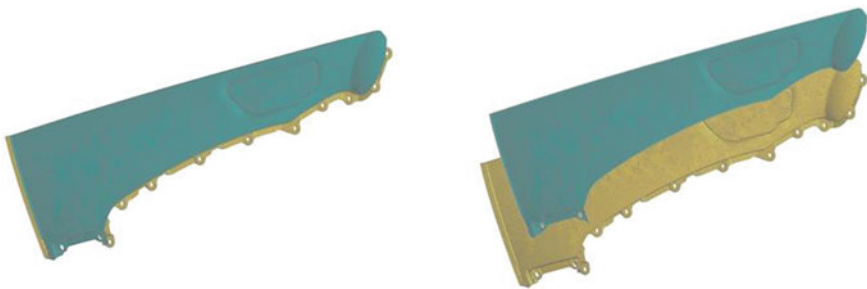
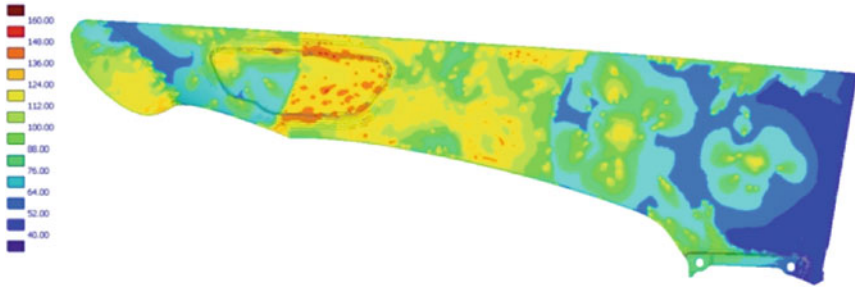


Fig. 11 Mesh model data for analysis

the optimal foam melting temperature exposure, with this correlating with the dented areas. Eventually the heat-resisting foam was adhered to the sheet by putting a few additional cooling channels and improving the sheet surface quality.



**Fig. 12** The result of analysis—temperature distribution

## 5 Conclusion

This paper introduces the injection-moulding method that satisfies the desire for a comfortable, eco-friendly product made at low cost. Above all, we have developed and demonstrated the analysis methodology of this new method, which now allows us to pre validate the quality. Through this methodology we can anticipate the problems before making a product mould, and develop the product with minimal trouble-shooting issues.

Until now this method has been limited to products with a corner radius of less than 2 mm. To overcome this restriction, we will develop a new methodology connecting injection moulding analysis and structure analysis.

## References

1. Kong B, Bae J, Cho Y (2011) Development of the overmolding crash-pad. In: KSAE 2011 annual conference, KSAE11-A0358, pp 1941–1947
2. Kennedy P (1995) Flow analysis of injectino molds. Hanser Publishers, Cincinnati
3. Shin N, Oh H, Kang S (2010) The optimization of injection molding process by CAE. Daekwangseolim, Seoul

# Effect of Artificial Environment Test on Performance of Automotive Coating

Naxin Wang, Tao Wu, Dazheng Liao, Shu Zhang and Ran Zhao

**Abstract** This paper focuses on the attenuation of the mechanical properties of body coating when it is subject to medium, temperature, humidity, climate, sunshine and other environmental factors. Regular means, i.e., the detection of coating stone-chip resistance and cross cut test, are used to evaluate the attenuation. The article has drawn the conclusion that the second mechanical property is necessary for controlling body coating. In the technological conditions of the coating material and coating standards of exterior body painted parts, there must have project and control indexes of related coating second mechanical property.

**Keywords** Artificial environment test · Stone-chip resistance · Cross cut test · Coating

## 1 Introduction

During use, automobile coating is often subject to the destructions by environmental factors such as temperature, humidity, sunshine, moisture, medium and alternation between temperature and humidity. The old coating demonstrates decrease in the overall mechanical properties of the coating. The most common

---

F2012-H07-009

---

N. Wang (✉) · D. Liao · S. Zhang · R. Zhao  
FAW Group Corporation R&D Center, Changchun, China  
e-mail: wangnaxin@rdc.faw.com.cn

T. Wu  
FAW Group Corporation, Department of Manufacturing Technology, Changchun, China

**Table 1** Plate making process and performance

No.	Color of metallic finish	Manufacturers	Simple process	Film thickness ( $\mu\text{m}$ )	Stone-chip resistance (Grade and depth code)	Adhesion (Grade)
1-1-1	Gold	1	ED-BC-CC	82-86	2, C	0
1-1-2	Gold	1	ED-BC-CC	88-92	2-3, C	0
2-1-1	Gold	2	ED-BC-CC	82-88	2, C	0
2-1-2	Gold	2	ED-BC-CC	84-90	2, C	0
1-2-1	Red	1	ED-BC-CC	90-94	3, A	1
1-2-2	Red	1	ED-BC-CC	90-92	3, A	1
2-2-1	Red	2	ED-BC-CC	94-96	2-3, B	0
2-2-2	Red	2	ED-BC-CC	90-96	3, B	0
1-3-1	Blue	1	ED-BC-CC	86-88	2, B	0
1-3-2	Blue	1	ED-BC-CC	84-88	2, B	1
2-3-1	Blue	2	ED-BC-CC	96-104	3, B	0
2-3-2	Blue	2	ED-BC-CC	94-98	3, B	0

test projects for evaluation of coating mechanical properties are the stone-chip resistance and cross cut tests. The two tests reflect from different aspects the comprehensive properties of coating in terms of flexibility, bond strength and matching between layers, etc.

However, in order to simulate the damage on car body coating during use, domestic and international car companies have adopted a variety of artificial simulation environment test methods. Normal artificial simulation environment test methods include salt spray test, humidity test, artificial aging test, corrosion alternating test, climate alternating test and temperature change tests. Among them, the former three tests have corresponding national standards in China, while the latter three tests generally follow the car company's own corporate standards. European and American automotive companies have already defined the requirements for secondary stone-chip resistance and cross cut tests in their corporate standards after climate alternating test, temperature change test and moisture resistance tests.

Therefore, it is quite necessary to discuss the necessity of detection of coating secondary mechanical properties and determine the combined test method for secondary properties after optimal artificial environment test. The experiments and conclusions are available for reference.

**Table 2** Test conditions of a variety of accelerated environmental testing

No.	Environmental testing	Test conditions	Accumulated time (h)
1	Salt spray fog test	Salt spray fog test according to GB/T1771	240
2	Humidity test	Humidity-continuous condensation test according to GB/T13893	240
3	Artificial weathering test	Artificial weathering (Xenon radiation) test according to GB/T1865	1,500
4	Alternative corrosion test	① 4 h salt spray fog test according to GB/T1771 ② 4 h aging in the standard climate (including cooling-off phase) ③ 16 h humid aging at elevated temperature, climate according to GB/T13893 (40 ± 3) °C, 100 % humidity *①-③ is a cycle, a total of 10 cycles	240
5	Alternative climate test	Testing of resistance to environmental cycle test (+80/-40) °C ① With 1 h from room temperature to 80 °C ② Maintain 4 h in 80 °C and control the humidity of 80 % ③ With 2 h from 80 °C down to -40 °C ④ Maintain 4 h in -40 °C ⑤ Warming to 23 °C in 1 h *①-⑤ is one cycle, a total of 20 cycles	240
6	Alternative temperature test	① The 90 °C for 240 h ② Cooling to -40 °C for 24 h *①-② is a cycle, one cycle	264
7	Salt spray fog test/artificial weathering test	① Salt spray fog test according to GB/T1771 for 240 h ② Artificial weathering test for 120 h *①-② is a cycle, one cycle	360
8	Humidity test/artificial weathering test	① Humidity test: 240 h (38 ± 2) °C, the surface of the test panels continue to produce condensed water ② Artificial aging test for 120 h *①-② is a cycle, one cycle	360
9	Alternative corrosion/ alternative climate/ artificial weathering	① Corrosion alternating 10 cycles ② Climate alternating 20 cycles ③ Artificial aging test for 120 h *①-③ is a cycle, one cycle	600
10	Alternative climate/ alternative corrosion/ artificial weathering	① Climate alternating 20 cycles ② Corrosion alternating 10 cycles ③ Artificial aging test for 120 h *①-③ is a cycle, one cycle	600

**Table 3** Stone-chip resistance and cross cut test results of gold metallic paint

Environmental testing category	Secondary stone-chip resistance (grade, depth code)					Secondary cross cut (grade)				
	1-1-1	1-1-2	2-1-1	2-1-2	2-1-2	1-1-1	1-1-1	1-1-2	2-1-1	2-1-2
	Original value (Ori)	2, C	2-3, C	2, C	2, C	2, C	0	0	0	0
Salt spray test (SS)	2-3, C	2-3, C	2-3, C	2-3, C	3, B	1	1	1	1	1
Moisture resistance test (MR)	3-4, C	4, C	3, C	3-4, C	3-4, C	1	0	1	1	1
Artificial aging test (AA)	3, C	3, C	2-3, C	2-3, C	2-3, C	2	2	2	1	1
Corrosion alternating test (CoA)	3, C	3, C	3, B	3, B	3, B	0	0	1	1	1
Climate alternating test (CIA)	5, B	5, B	6-7, B paint layer cracks	6-7, B paint layer cracks	6-7, B paint layer cracks	2	2	2	3	3
Temperature change test (TC)	3, C	3-4, C	2, C	3, C	3, C	2	2	2	2	2
Salt spray test/artificial aging test (SS/AA)	3, C	3-4, C	3-4, C	3-4, C	3-4, C	1	1	2	2	1
Moisture resistance test/artificial aging test (MR/AA)	3-4, C	3-4, C	3, C	3-4, C	3-4, C	1	1	1	1	1
Corrosion alternating/climate alternating/artificial aging test (CoA/CIA/AA)	3, C	4, C	3, B	3, B	3, B	2	2	2	3	3
Climate alternating/corrosion alternating/artificial aging test (CIA/CoA/AA)	3-4, C	3-4, B	3, B paint layer cracks	3, B paint layer cracks	3, B paint layer cracks	2	2	2	2	2

**Table 4** Stone-chip resistance and cross cut test results of red metallic paint

Environmental testing category	Secondary stone-chip resistance (grade, depth code)						Secondary cross cut (grade)									
	1-2-1		1-2-2		2-2-1		2-2-2		1-2-1		1-2-2		2-2-1		2-2-2	
Original value (Ori)	3, A	3, A	2-3, B	2-3, B	3, B	3, B	1	1	1	0	0					
Salt spray test (SS)	4, A	4-5, A	2-3, B	2-3, B	3, B	3, B	2	2	2	1	1					
Moisture resistance test (MR)	4-5, A	4-5, A	4, B	4, B	4, B	4, B	1	2	2	1	1					
Artificial aging test (AA)	3-4, B	3-4, B	3, B	3, B	3, B	3, B	2	2	2	1	1					
Corrosion alternating test (CoA)	3, A	3, A	3, B	3, B	3, B	3, B	2	2	2	1	1					
Climate alternating test (CIA)	5, B	5, B	6, B paint layer cracks	6, B paint layer cracks	6, B paint layer cracks	6, B paint layer cracks	3	4	4	2	2					
Temperature change test (TC)	4-5, B	5, B	2, B	2, B	3, B	3, B	3	3	3	1	1					
Salt spray test/artificial aging test (SS/AA)	4, B	4, B	2-3, B	2-3, B	3, B	3, B	2	2	2	1	1					
Moisture resistance test/artificial aging test (MR/AA)	4-5, B	4-5, B	4-5, B	4-5, B	4, B	4, B	3	3	3	1	1					
Corrosion alternating/artificial aging test (CoA/CIA/AA)	6-7, B	6-7, B	6, B paint layer cracks	6, B paint layer cracks	6, B	6, B	4	4	4	3	3					
Climate of alternating/corrosion alternating/artificial aging test (CIA/CoA/AA)	6-7, B	6-7, B	6-7, B paint layer cracks	6-7, B paint layer cracks	6-7, B paint layer cracks	6-7, B paint layer cracks	4	4	4	4	4					

**Table 5** Stone-chip resistance and cross cut test results of blue metallic paint

Environmental testing category	Secondary stone-chip resistance (grade, depth code)						Secondary cross cut (grade)					
	1-3-1		1-3-2		2-3-1		2-3-2		1-3-1	1-3-2	2-3-1	2-3-2
	1-3-1	1-3-2	2-3-1	2-3-2	2-3-1	2-3-2	2-3-1	2-3-2	1-3-1	1-3-2	2-3-1	2-3-2
Original value (Ori)	2, B	2, B	3, B	3, B			3, B		0	1	0	0
Salt spray test (SS)	2-3, B	2-3, B	2, B				3-4, B		1	1	1	1
Moisture resistance test (MR)	3-4, B	3-4, B	3-4, B				4, B		1	1	1	1
Artificial aging test (AA)	3-4, B	4-5, B	3-4, B				4, B		1	1	1	1
Corrosion alternating test (CoA)	2-3, B	3, B	3-4, B				3-4, B		1	1	1	1
Climate alternating test (CIA)	5, B	5, B	6, B	6, B	6, B	6, B	6, B	6, B	3	4	3	3
Temperature change test (TC)	5, B	5, B	3, B				4-5, B		2	2	1	1
Salt spray test/artificial aging test (SS/AA)	3, B	4, B	4, B				4-5, B		1	2	1	1
Moisture resistance test/artificial aging test (MR/AA)	2, B	2, B	4, B				4, B		1	1	1	1
Corrosion alternating/climate alternating/artificial aging test (CoA/CIA/AA)	6, B	6-7, B	6-7, B	6, B	6, B	6, B	6, B	6, B	3	3	4	4
Climate alternating/corrosion alternating/artificial aging test (CIA/CoA/AA)	6, B	6-7, B	6, B	6, B	6, B	6, B	6-7, B	6, B	4	4	3	3



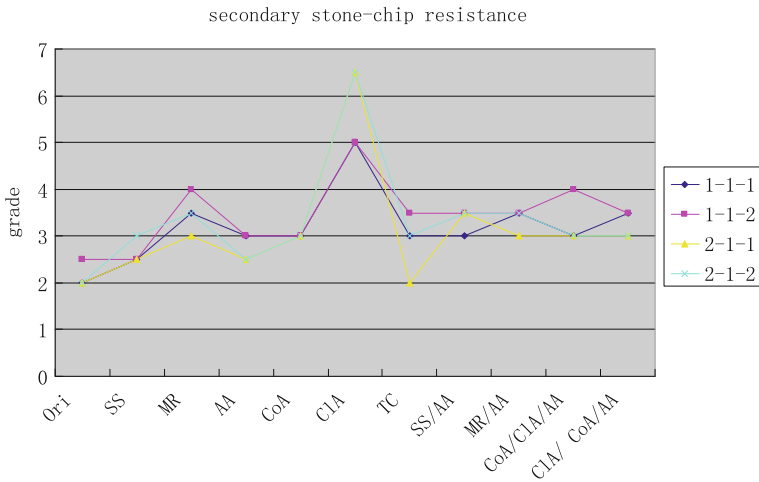


Fig. 1 Secondary stone-chip resistance of gold metal paint characteristics curve

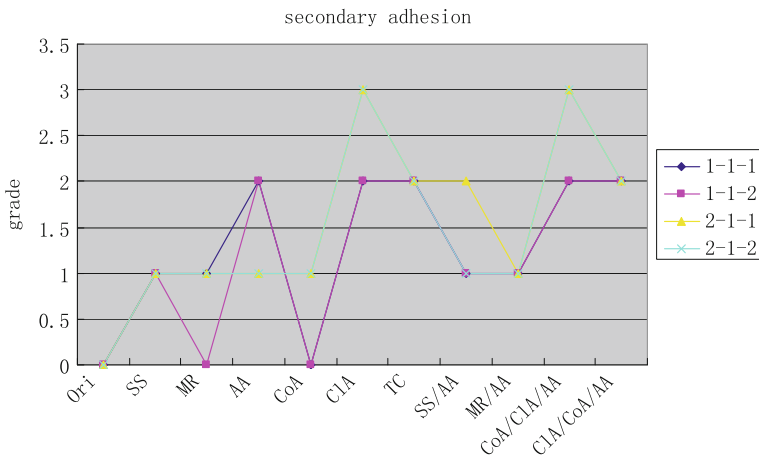


Fig. 2 Secondary adhesion of gold metal paint characteristics curve

## 2 Test Section

### 2.1 Preparation of Test Samples

Metallic paint of three colors by two manufacturers has been used in the preparation of sample plates. Plate making process and performance are shown in Table 1.

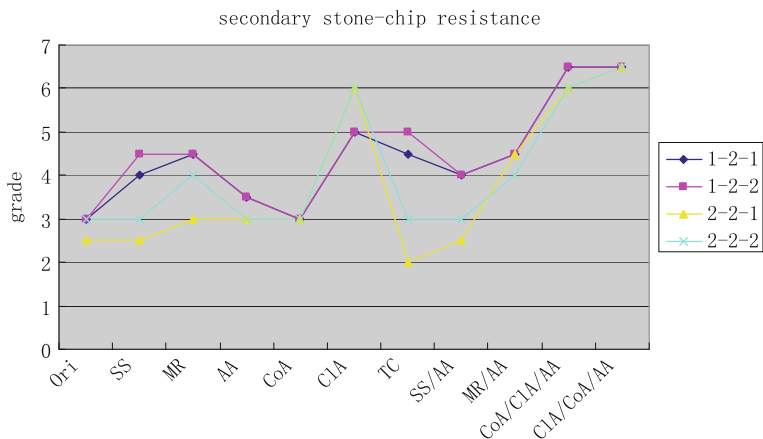


Fig. 3 Secondary stone-clip resistance of red metal paint characteristics curve

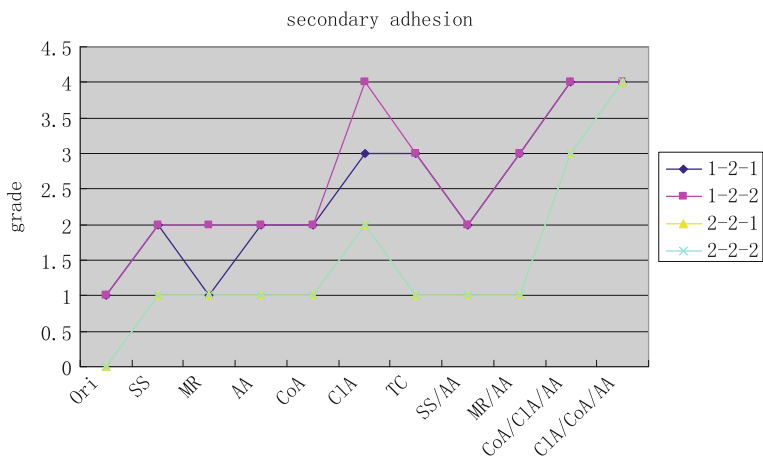


Fig. 4 Secondary adhesion of red metal paint characteristics curve

### 2.2 Test Conditions

The stone-chip resistance test method of test samples is in accordance with the ISO 20567-1 “Paints and varnishes—Coating of resistance stoning of contents Part 1: Repeated impact test”; equipment type is VDA Model 508; environmental conditions ( $23 \pm 2$ ) °C and relative humidity ( $50 \pm 5$ ) %; air pressure 100 kPa; the samples are hit twice.

Cross cut test method is in accordance with GB/T 9286-1988 “Paints and varnishes—cut test”.

Test conditions of a variety of accelerated environmental testing are shown in Table 2.

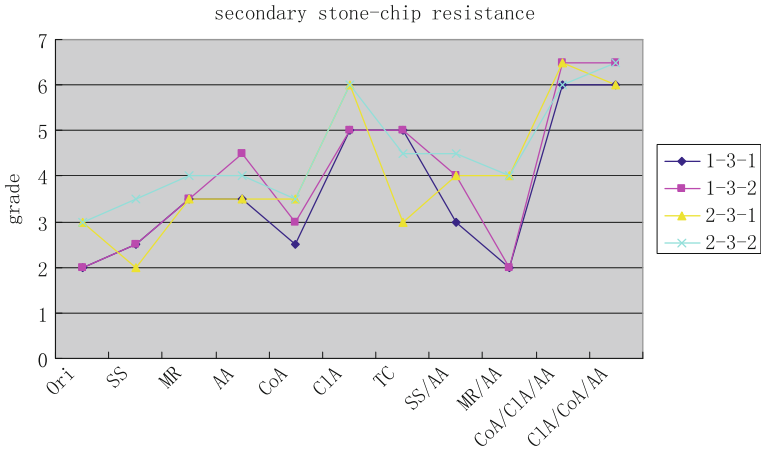


Fig. 5 Secondary stone-clip resistance of blue metal paint characteristics curve

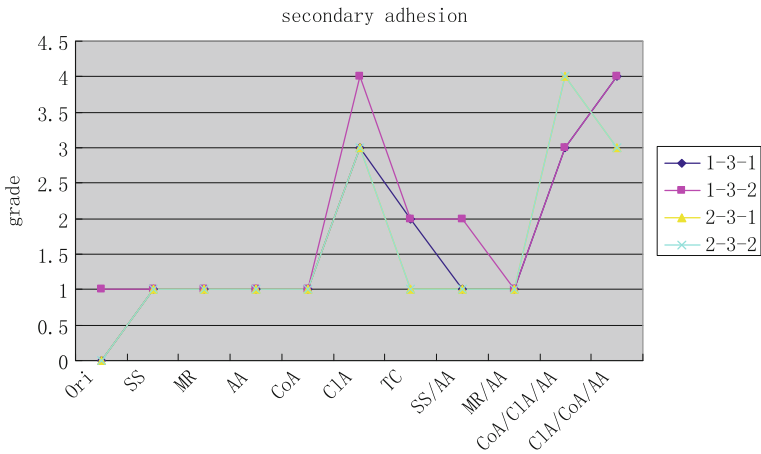


Fig. 6 Secondary adhesion of blue metal paint characteristics curve

### 2.3 Test Results and Analysis

Results of secondary stone-chip resistance and cross cut tests after different simulation environment tests are shown in Tables 3, 4 and 5. The relation curve of environmental testing and secondary stone-chip resistance level is shown in Figs. 1, 2, 3, 4, 5 and 6.

From Tables 3–5 and Figs. 1–6, both the secondary stone-chip resistance of coating and the cross cut test after all kinds of artificial environment tests have varying degrees of decline; Among various environment tests with accumulated time of less than 300 h, climate alternating tests have caused the severest

attenuation of the secondary stone-chip resistance of coating and the cross cut test, followed by temperature changing tests, the attenuation after which is quite obvious. While among those environment tests with accumulated time of over 300 h, the secondary stone-chip resistance of coating and the cross cut test have suffered from the severest attenuation after two tests corrosion alternating/climate alternating/artificial aging and climate alternating/corrosion alternating/artificial aging tests.

### **3 Conclusions**

Due to a variety of environmental erosion and continuous blow from sand to the car body coating during the vehicles' using life cycle, control of the secondary mechanical property of body coating is necessary. For the technological conditions of the coating material and coating standards of body exterior painted parts, there must have project and control indexes of related coating secondary mechanical property.

Due to the great impact of climate alternating test with a relatively short cycle on the secondary stone-chip resistance of coating and cross cut test, it can be applied to the quadratic performance testing free to primer coating. Since different coating systems are designed for automotive products, it is recommended that on the basis of this article, appropriate quadratic performance test method standards shall be established for the quality control of body layer in accordance with the actual situation (corresponding experimental verification shall be carried out on different coating structures).

**Part VI**  
**Exterior Body Panels**

# A Prediction Approach for Oil Canning of Sheet Metal Forming Based on Strain Gradient

Kangkang Yan, Xinyu Wang, Zhongxiao Wang, Yu Zhang  
and Ping Hu

**Abstract** From test studying, it indicates that the lower strain magnitude and non-homogeneous strain distribution are the causes of oil canning in large flat/sweep areas of stamping product. In order to eliminate oil canning defect, the minimum equivalent strain in deformation zone should be greater than 2 % and the strain gradient be as small as possible. The prediction approach was proposed for oil canning problem based on strain gradient and equivalent strain magnitude, and the approach was integrated into KMAS-UFT software aiming at predicting oil canning problem by CAE analysis. The paper takes hood outer panel as an example and carries out CAE analysis. It is confirmed that the prediction approach is both accurate and effective.

**Keywords** Prediction approach · Oil canning · Strain gradient · Sheet metal forming · Auto body panel

## 1 Introduction

Sheet metal forming is the main way of auto body panel manufacture, the quality of body panel is very important for automobile market performance [1]. Oil canning is one of auto body panel defects which is common and difficult to be

---

F2012-H08-003

---

K. Yan (✉) · X. Wang · Z. Wang · Y. Zhang  
Body Department, China FAW Group Corporation R&D Center, Changchun, China  
e-mail: yankangkang@rdc.faw.com.cn

P. Hu  
School of Automotive Engineering, Dalian University of Technology, Dalian, China

**Fig. 1** Oil canning defect of truck roof



solved in sheet metal forming. What's more, such a defect is always detected after the die is put into operation. The damping structural adhesive was filled into the gap between inner and outer panel to solve this problem because the automobile styling has been frozen [2, 3]. This solution increases the weight and cost greatly [4, 5].

The objective of this research is to investigate a CAE analysis approach that could predict and solve oil canning before vehicle trial production. Using this approach, the oil canning defect could be diagnosed and solved during the stage of automobile body panel design.

## 2 Generation Mechanism of Oil Canning

From the viewpoint of performance of auto body panel, a stamped part needs to bear a certain level of static, normal load on a large, unsupported, flat/sweep area without elastic instability. If the elastic instability occurs, there are two or more equilibrium positions in the area, and the equilibrium state changes randomly with a light disturbance. Geometrically, the elastic instability results in a buckle, which is referred to as oil canning [6], as shown in Fig. 1. Oil canning often occurs in large, thin stamped parts, such as automotive exterior panels, appliance shells, structural panels, and even metal sheets from sheet manufacturers.

From the test research, it can be found that if the deformation in the large flat area of stamping is not homogeneous, the first type of residual stress remains in the area after unloading, causing the probability of oil canning arising increased sharply and the reduction of oil canning load. In addition, the more severe the inhomogeneous deformation, the larger the first type of residual stress. Therefore, it is very important to prevent the first type of residual stress during the automotive stamping processes. What is more, the oil canning becomes severe when the deformation is low, and the strain distribution is not uniform in the area. Therefore, we can draw a conclusion that the global inhomogeneous deformation and low strain magnitude are the reasons of stamping oil canning.

### 3 Prediction Approach for Oil Canning

#### 3.1 Evaluation Index of Oil Canning

In order to eliminate oil canning, the deformation magnitude and distribution in the large, unsupported, flat/sweep area of stamping must meet certain requirements. So, two types of evaluation index were proposed for quantifying the strain magnitude and distribution evenness indirectly. In the paper, use the equivalent strain  $\varepsilon_e$  as a reference to quantify the deformation magnitude, thus the global strain deformation of stamping was quantified. In addition, the strain gradient  $grad(\varepsilon)$  on a quasi contour line (QCL) network are applied for indirectly quantifying the degree of first type of residual stress in large flat/sweep areas of stamping, the degrees of deformation distribution evenness can be quantified.

The equivalent strain  $\varepsilon_e$  is used as the first evaluation index for deformation magnitude, equivalent strain  $\varepsilon_e$  can be determined by using Eq. (1).

$$\varepsilon_e = \frac{\sqrt{1+R}}{1+2R} \sqrt{R(\varepsilon_1 - \varepsilon_2)^2 + (\varepsilon_2 - R\varepsilon_3)^2 + (R\varepsilon_3 - \varepsilon_1)^2} \quad (1)$$

Where R is plastic strain ratios,  $\varepsilon_1$ ,  $\varepsilon_2$  and  $\varepsilon_3$  respectively represent 1st, 2nd and 3rd principal strains of deformation area.

In order to accurately evaluate the degrees of deformation distribution evenness of auto body panel, and be easy to calculate strain gradient, a contour line needed to be established is a reference to key feature of stamping, the line is termed as quasi contour line (QCL) in the paper, along which the strain gradients can be calculated. When strains are measured on the circle grids ellipses, the first group QCL is generated by approximately following the major and minor strain direction. According to the boundary contour or key feature line of auto body panel, the other groups QCL were generated by expanding first group QCL along with the major and minor strain direction. So, the QCL network can be constructed for evaluating the degrees of deformation distribution evenness. According to the characteristics of auto body panel, the QCL network have slightly different shape layout. Take applications of the door outer panel as an example, the QCL network template were given for build the door outer panel QCL network, as shown in Fig. 2. Based on QCL network template, the QCL network and strain distribution of door outer panel as shown in Fig. 3.

The strain gradients are applied for evaluating degrees of deformation distribution evenness in oil canning analysis. Strain gradients are directly obtained through forming processing strains that are accurately calculated with finite element analysis or measured with circle grid analysis. Strain gradients along the QCL are generated by calculating strain distributions using major and minor surface principal strains in formed workpiece, and can be calculated by using Eq. (2), calculation model as shown in Fig. 4. If the surface principal strains is measured through circle grid analysis,  $grad^{(i)}(\varepsilon_{1qcl})$  and  $grad^{(i)}(\varepsilon_{2qcl})$  are defined



**Fig. 2** QCL network template for door outer panel

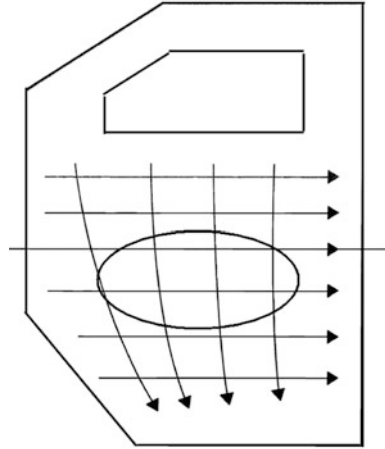
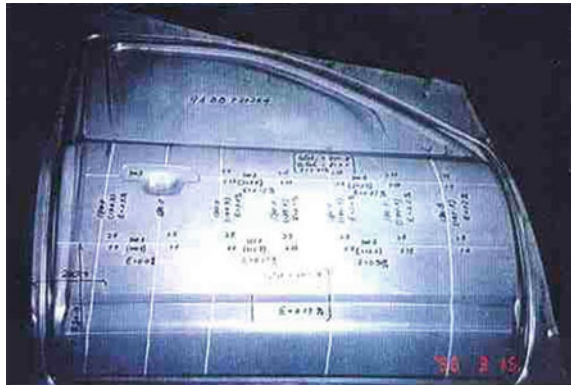


**Fig. 3** Strain distribution along with QCL network



as the major and minor strain gradients of the No.i circle grids center along with QCL, for the FEA method, these defined as the major and minor strain gradients of No.i node respectively.

$$\begin{cases} grad^{(i)}(\varepsilon_{1qcl}) = \frac{(\varepsilon_1^{(i)} - \varepsilon_1^{(i+1)})}{\Delta l^{(i)}} \\ grad^{(i)}(\varepsilon_{2qcl}) = \frac{(\varepsilon_2^{(i)} - \varepsilon_2^{(i+1)})}{\Delta l^{(i)}} \end{cases} \quad (2)$$

Where  $\varepsilon_1^{(i)}$  and  $\varepsilon_2^{(i)}$  respectively represent major and minor surface principal strains of the No.i circle grids center, by analogy,  $\varepsilon_1^{(i+1)}$  and  $\varepsilon_2^{(i+1)}$  represent the next one.  $\Delta l^{(i)}$  is defined as the intervals between the No. i circle grids center and the next one of formed workpiece.

The interval  $\Delta l^{(i)}$  between each two adjacent grid centers is too small to be measured. Therefore, the interval between each of two adjacent, deformed circle

**Fig. 4** Model of strain gradients calculation

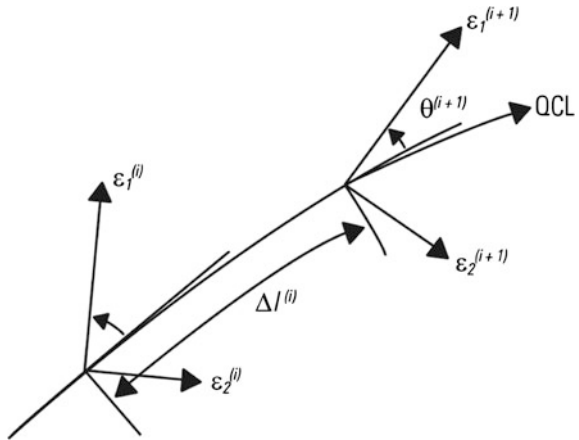
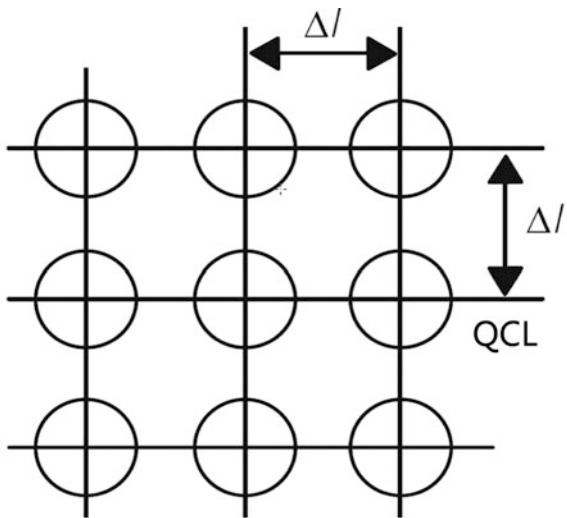


**Fig. 5** Original circle grids

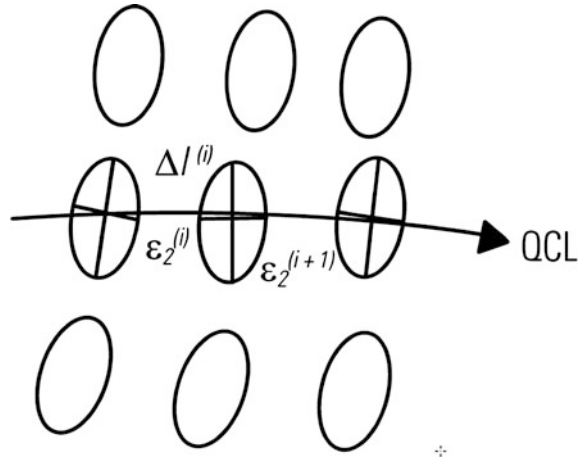


grid centers  $\Delta l^{(i)}$  is equal to the original interval plus its length change, which is described by Eq. (3).

$$\Delta l^{(i)} = \Delta l \left( 1 + \frac{\varepsilon_2^{(i)} + \varepsilon_2^{(i+1)}}{2} \right) \tag{3}$$

Where  $\Delta l$  is the original interval of circle grid, as shown in Fig. 5. And  $\frac{\varepsilon_2^{(i)} + \varepsilon_2^{(i+1)}}{2}$  is the average minor strain between the two deformed ellipses approximately direction, deformed circle grid as shown in Fig. 6.

Fig. 6 Deformed circle grids



### 3.2 Prediction Approach for Oil Canning

When diagnosing and solving an oil canning problem in manufacturing production, the first thing is to establish the oil canning criterion. Then, the oil canning is identified, and its severity can be measured. Finally, differences of strain magnitude and gradients between the criterion and the current situation are determined, and the problem is to be solved by adjusting metal flows.

Oil canning is related to both strain magnitude and strain distribution. It should be noted that inhomogeneous deformation and low strain magnitude are twins for the oil canning, they often occur simultaneously. During the diagnosis process for oil canning, the low stretch must be checked first, then to evaluate the degrees of deformation distribution evenness.

As a rule of thumb, 2 % equivalent strain is used as the threshold of strain magnitude for avoiding oil canning defect occurrence. If the minimum equivalent strain in the large flat/sweep area of the formed workpiece is lower than the threshold strain (2 %), the formability state is unsafe, the minimum equivalent strain needs to be enhanced until it becomes larger than 2 %.

Furthermore, the severity of strain distribution evenness is calculated by using Eq. (2). If the strain gradients along the QCL are not consistent, as shown in Fig. 7, the stamped part fails to pass the standard oil canning formability. The metal flow in the area is then to be adjusted to improve the strain distribution evenness, that is to say, to reduce the strain gradient magnitudes. In fact, the perfect strain gradients for a stamping to be oil canning free are zero. That is to say, the deformation in the large flat/sweep area of a formed workpiece is homogeneous. However, this is unrealistic. The ideal situation is that the deformation in the area belongs to the same strain magnitude level.

**Fig. 7** Strain gradients are not consistent

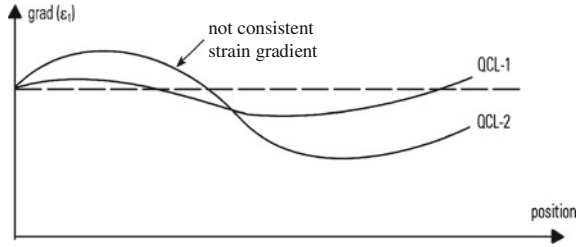
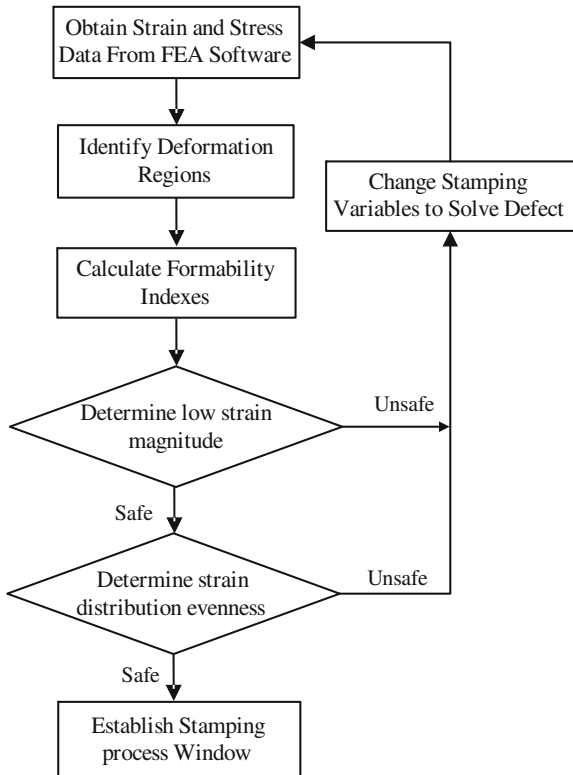


**Fig. 8** CAE analysis procedure for oil canning



## 4 CAE Analysis on Oil Canning

### 4.1 CAE Analysis Procedure

In order to solve oil canning defect in stamping part design process, a CAE analysis procedure for oil canning diagnosis and problem solving is explained. There are six steps included in the flow CAE analysis on oil canning as follows, as shown in Fig. 8.

- Step 1: After FEM simulation, generate stress, strain and displacement of element and node from formed workpiece, then input obtained data into the CAE analysis system.
- Step 2: Define oil canning analysis region, constructing QCL network to calculate strain gradient.
- Step 3: Calculate formability index. The minimum equivalent strain  $\varepsilon_e$  are calculated as the strain magnitude indexes by using Eq. (1), and the strain gradients  $grad(\varepsilon)$  are calculated as the strain distribution evenness indexes by using Eq. (2).
- Step 4: Determine low strain magnitude. Comparing the minimum equivalent strain in the large flat area of the formed workpiece with corresponding failure criteria, a formability state of the forming process is identified. If  $\varepsilon_e > 2\%$ , the formability state is safe, further determine strain distribution evenness. Otherwise, it is unsafe, calculate ranges of metal flow adjustments for solving low stretch problem, and then, repeating the step1–step4 until the formability state is safe.
- Step 5: Determine strain distribution evenness. If the distribution of strain gradients along QCL is consistent, the formability state is safe. Establish stamping process windows. If not consistent, it is unsafe. The ranges of metal flow adjustments is calculated
- Step 6: Establish stamping process window. If formability state is safe, the robust ranges of formability, material, and tooling are established, this robust range is referred to as the stamping process window for production stability control.

## 4.2 CAE Analysis Software

Using Components Object Model technology, integrated the prediction approach for oil canning of sheet metal forming based on strain gradient, research and develop the special CAE analysis software KMAS-UFT [7], which is used for analyzing on the oil canning much accurately, as shown in Fig. 9.

## 4.3 Case Verification

Using an automotive hood outer as an example of the oil canning diagnosis and analyzing procedure is illustrated below. Carry out FEM simulation on drawing process of hood outer with the special stamping CAE software KMAS-UFT, as shown in Fig. 10. Adopt H180BD + Z with the thickness 0.75 mm as the hood

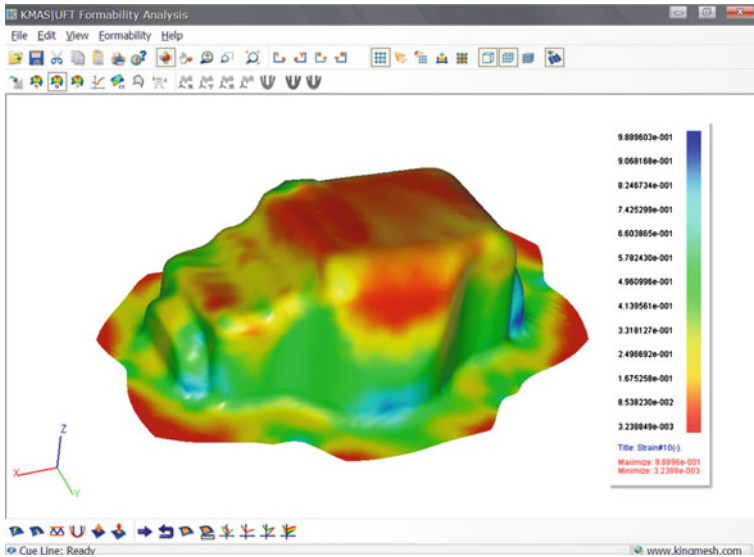
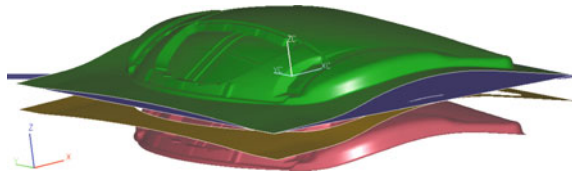


Fig. 9 KMAS-UFT user interface

Fig. 10 Hood outer FEM model



outer material, which is bake hardenable sheet metal [8]. Sheet mechanics performance parameters are given in Table 1.

Since the oil canning problem often occurs in power dome area of automotive hood outer, selected the power dome area as the deformation region. The deformation state of low strain magnitude is determined firstly. By circulative search, the minimum equivalent strain element in the deformation region is No. 44947 element, of which the minimum equivalent strain being 3.08 %, which is far in excess of 2 % of the low stretch threshold. The deformation state of low strain is passed, as shown in Fig. 11.

According to the hood outer features in deformation zone, the QCL network is established to calculate the strain gradient. The major and minor strain gradients along the group of QCL can be obtained by KMAS-UFT software, as shown in Fig. 12. It can be seen from the figure that the strain gradients along with QCL are not consistent, the strain difference of adjacent element is more than 40 %. The deformation distribution of stamping part is not homogeneous, resulting in oil canning defect of sheet metal forming. The deformation state of strain distribution evenness determination is unsafe, as shown in Fig. 13. Compare the Load versus

**Table 1** Bake hardenable sheet metal mechanical properties

Symbol	Property	Quantity
$\sigma_s$	Yield stress	185.2 MPa
$E$	Young's modulus	210 GPa
$\mu$	Poisson's ratio	0.3
$n$	Hardening exponent	0.21
$K$	Strength coefficient	587.2 MPa
$r$	Normal anisotropic coefficient	1.66

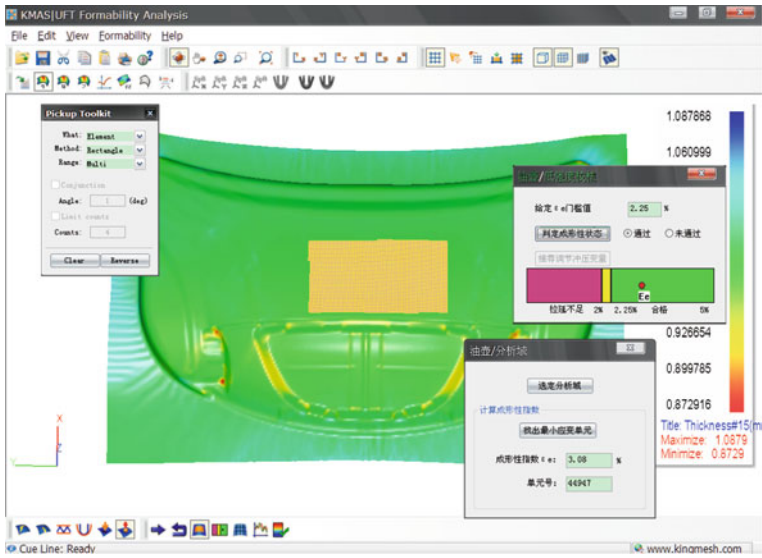


**Fig. 11** Deformation state of low strain magnitude

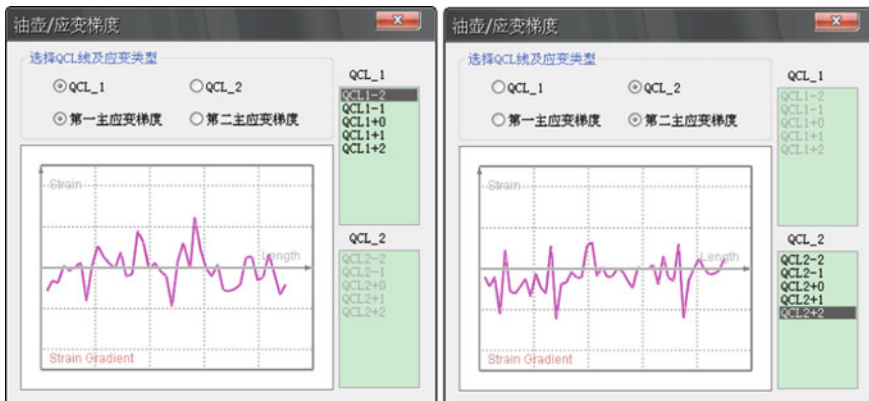


**Fig. 12** Major and minor strain gradients along QCL

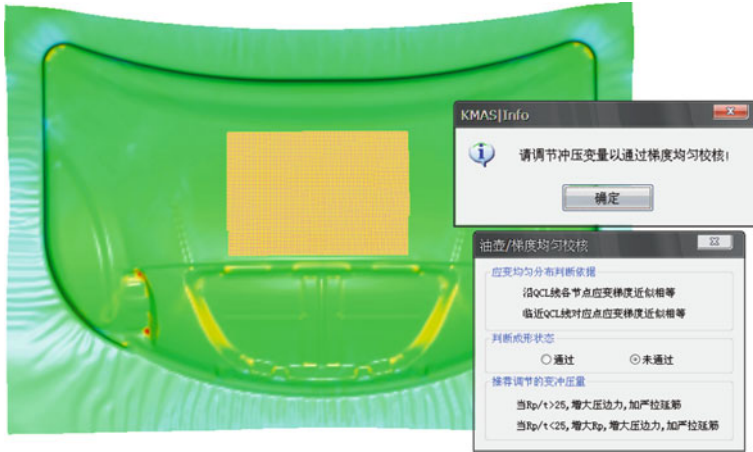


Fig. 13 Deformation state of strain distribution evenness

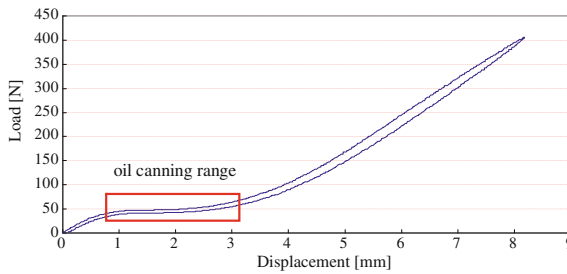


Fig. 14 Load versus displacement of oil canning test

Displacement curve of hood outer panel oil canning test, as shown in Fig. 14. It is confirmed that the oil canning defect predicted by KMAS-UFT is well consistent with that of the test result from formed workpiece. In view of oil canning, it can be eliminated by adjusting punch radius, drawbead and blank holder force, further by changing forming depth.

## 5 Conclusion

The test studying indicated that when the strain magnitude is small and non-homogeneous strain distribution in large flat area of stamping product, the first type of residual stress remains in the area after unloading, resulting in the probability of oil canning occurrence increased rapidly. Therefore, we can draw a conclusion that the inhomogeneous deformation and low strain magnitude are the



causes of stamping oil canning. In order to avoid oil canning, the minimum equivalent strain of deformation region should be greater than 2 % and the strain gradient be as small as possible.

Based on strain gradient and equivalent strain magnitude in stamping part, an approach was proposed for predicting oil canning defect. And the approach was integrated into KMAS-UFT software aiming at predicting oil canning problem by CAE analysis. Take hood outer panel as an example and make the CAE analysis for oil canning. It has been confirmed that the approach proposed in this paper is feasible, effective, and accurate.

## References

1. Jeswiet J, Geiger M, Engel U et al (2008) Metal forming progress since 2000. *CIRP J Manuf Sci Technol* 1(1):2–17
2. Mohan Iyengar R, Chang T, Laxman S et al (2004) Grade and gage sensitivities to oil canning loads of a door assembly considering forming effects. SAE 2004-01-0164
3. Guo M, Hu Y, Sanghera R (2009) Finite element analyses and correlations on oil canning of a door outer panels. SAE 2009-01-0818
4. Liu SD, Xiao X, Zhang L et al (2007) Stamping effect on oil canning and dent resistance performances of an automotive roof panel generality. SAE 2007-01-1696
5. Mohan Lyengar R, Chang T, Zhao Y et al (2003) Validation of non-linear load-controlled CAE analysis of oil-canning test of hood and door assemble. SAE technical paper no 2003-01-0603
6. Xu Y (2006) Modern formability: measurement, analysis and applications. Hanser Gardner Publications, Cincinnati
7. Yan K, Ping Hu, Xu Y (2009) CAE analysis numerical analysis approach for stamping edge split of high strength steel considering sheared burr effect. *J Jilin Univ (Eng Technol Edn)* 39(s2):301–305
8. Pradhan R (1991) Dent-resistant bake-hardening steels for automotive outer-body application. SAE 910290

**Part VII**  
**Advanced Process Management**

# A New Connection Solution for Hybrid Vehicle

**Julian Zhou**

**Abstract** The trend for passenger vehicle development is to incorporate more and more communication, safety and entertainment features to meet customer's desires. At the same time, improving vehicle performance and enhancing driver and passenger's comfort are becoming equally important. All of these have imposed higher and higher pressure on car makers to use smaller connection systems hiding inside a vehicle. For hybrid vehicles, because of the high current and voltage requirements, the requirement of smaller-size connection systems becomes even more challenging as the systems need to meet stricter shielding and sealing needs. This research focuses on the design and the manufacturing process of a connection system for hybrid application. The innovation results in a more flexible design which allows for a streamlined wiring connection system with large-sized cable. The system can work under 300 A, 1000 V electrical conditions with sealing, shielding and pluggable functions which in turn have solved a common problem encountered in hybrid vehicle design. The connection solution combines an inlet connector and a 90° pluggable adaptor with a unique design to reach shielding function. The related technologies include low pressure over molding process, ferrule crimping and round spring contact.

**Keywords** Strict requirements · Customer satisfaction · Innovative design  
New process technology · Good test result

Usually the conventional connector is regarded as too big by customer because the available space inside vehicle is always limited. In one of our development project

---

F2012-H09-002

---

J. Zhou (✉)  
Delphi Packard Electric System Co., Ltd, Shanghai, China  
e-mail: julian.zhou@delphi.com

Fig. 1 (Image 1)

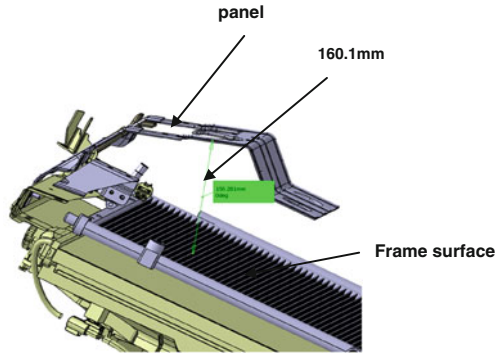
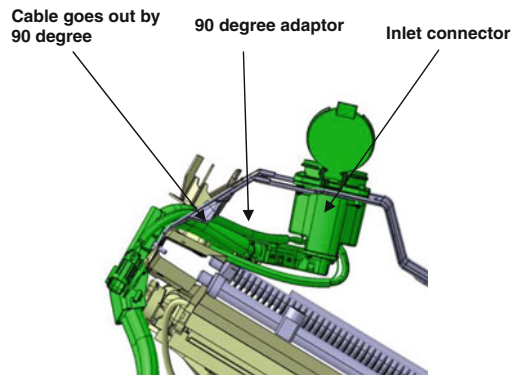


Fig. 2 (Image 2)



named Charger Inlet Connection System, The distance between panel and frame surface is only 160.1 mm (see Fig. 1). The Inlet connector is mounted on the panel. After the cable comes out of inlet connector, it should turn 90° immediately. Because the cable is as thick as 50 mm<sup>2</sup>, it is too tough and impossible to be bent in 90° with a small radius in such a small space. So we have to design a 90° adaptor assembled with inlet connector as a wiring solution to meet this requirement (see Fig. 2).

The challenge is that this wiring solution should meet three critical function requirements. They are shielding, sealing and pluggable between adaptor and inlet connector.

To reach shielding function, the cable braid should be connected in a proper way with outside shielding shell through plastic housing which is for holding the cable and terminal. Let's take a look at adaptor (see Fig. 3). We are using inner ferrule to crimp the cable braid, and outer ferrule to crimp the inner ferrule and a transfer wire between them. The transfer wire is connected with outer shielding shell by soldering. To hold all of them, we are using low pressure over molding material as normal plastic housing, and at same time to reach sealing function between housing and outer shielding shell, and between housing and transfer wire, because normal plastic housing has no sealing function. The advantage of low

Fig. 3 (Image 3)

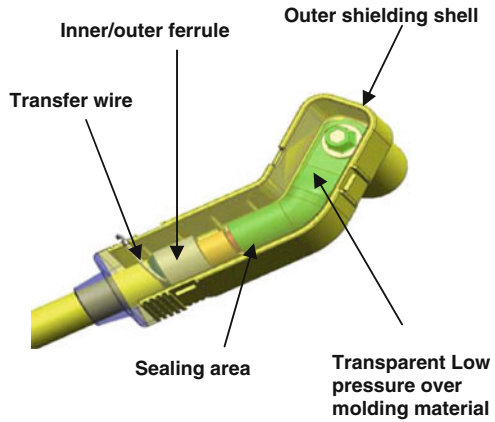


Table 1

Sample	Crimp resistance (mΩ)	Crimp to shell (mΩ)	Cable length (cm)	Overall resistance (mΩ)
1	0.33	2.38	6	2.71
2	0.35	2.4	6	2.75
3	0.32	1.46	3.5	1.78
4	0.27	2.08	6	2.35
5	0.35	2.31	6	2.66
6	0.28	2.25	6	2.53
7	0.29	1.83	5	2.12
8	0.35	2.5	6	2.85
9	0.28	2.13	6	2.85
10	0.35	2.25	6	2.6

pressure over molding process is that it can make a good sealing performance between cable and over molding material. That means over molding material has a good bonding property with cable material. The key to this technology is that we have to select correct material and use a right low pressure over molding process parameter and correct tool design.

During the over molding process, the overall connection resistance from cable shielding braid and outer shielding hell should be lower enough to meet GB/T20234 request 5 mΩ. The test data shows the overall highest resistance is 2.85 mΩ (see Table 1).

The pluggable between inlet connector and adaptor is another big challenge since we should also reach high performance/cost rate. The requirement of mating cycle is 10,000. The temperature should not reach 120 °C while it carries 250 A current. Meaning that we should make sure the contact spring normal force should not be too high and over stress after 10,000 mating cycle. But at same time, the contact normal force should not be too low in order to keep good contact and low

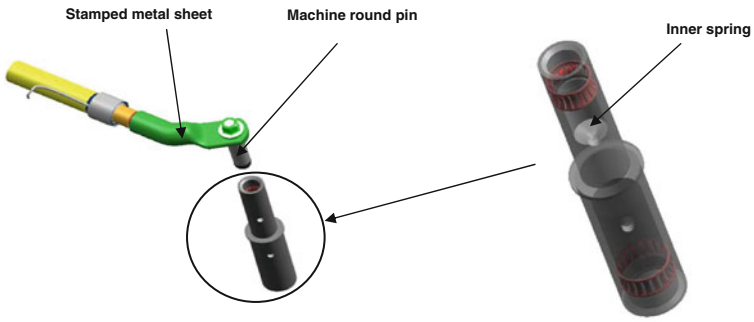


Fig. 4 (Image 4)

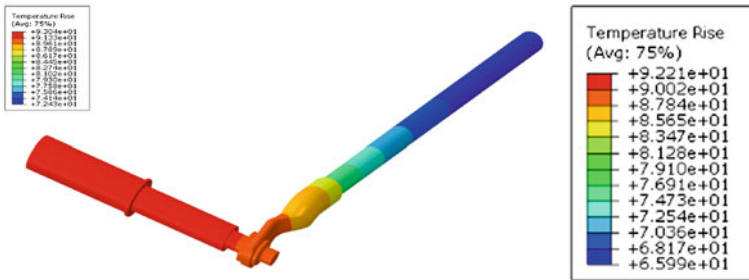


Fig. 5 (Image 5)

Table 2

Sample no.	Engage force (N)
1	45.6
2	50.4
3	88.7
4	51.2
5	33.5
6	32.5
7	50.9
8	56.3
9	85.3
10	88.1
Max	88.7
Min	32.5
Ave	58.3

**Table 3**

Current = 250 A, box temperature = 21.6 °C	
Sample No.	Temperature rise
1	84.8
2	86.9
3	85.5
4	82.6
5	83.4
6	84.5
7	86.5
8	85.2
9	87.5
10	85.7
Ave	85.26
Min	82.6
Max	86.9

contact resistance so that the temperature rise can be controlled under lower range. The design concept is to combine a machined round pin with a stamped metal sheet as a terminal to mate a round socket inside the socket, there is an inner spring which is specially designed to reach low stress relief and therefore to reach highest mating cycle performance (see Fig. 4). The simulation result of our design shows the overall temperature rise is controlled under 120° (see Fig. 5).

The test data of engage force and temperature rise shows the design is under good control and meet GB/T standard (see Tables 2 and 3).

**Part VIII**  
**Other**



# Development of UTS 980 MPa Grade Steel Tube with Excellent Formability for Automotive Body Parts

Masatoshi Aratani, Yasuhide Ishiguro, Yuji Hashimoto,  
Shunsuke Toyoda, Hideto Kimura, Osamu Sonobe  
and Makio Gunji

**Abstract** The enhanced performance of an ultra-high strength steel (UHSS) tube with tensile strength of 980 MPa grade is reported. Recently, strong consideration has been given to the use of steel tubes for automotive components because of the associated weight saving, which leads eventually to a reduction of carbon dioxide emissions. Furthermore, the application of steel tubes offers the advantages of increased stiffness and reduced welding processes due to their closed cross-sectional structure. The newly-developed UHSS tubes have an excellent combination of high strength and ductility (ultimate tensile strength: 1016 MPa, elongation to fracture: 14 %) and show remarkable formability such as rotary-bending workability and hydro formability. The key technologies to obtain these superior properties are the application of a cold rolled sheet steel with a DP (Dual Phase) microstructure having an optimized ferrite/martensite ratio and a CBR (Chance-free Bulge Roll) tube forming mill, which minimizes additional strain in the tube making process. The developed UTS 980 MPa grade steel tube has been applied to an actual automotive body part and contributed to not only weight saving but also improved safety.

**Keywords** Automotive body parts · Electric resistance welded steel tube · High strength · Formability · Hydroforming

---

F2012-H10-003

---

M. Aratani (✉) · Y. Ishiguro · Y. Hashimoto ·  
S. Toyoda · H. Kimura · O. Sonobe  
Steel Research Laboratory, JFE Steel Corporation, Tokyo, Japan  
e-mail: ma-aratani@jfe-steel.co.jp

M. Gunji  
Chita Works, JFE Steel Corporation, Tokyo, Japan

## 1 Introduction

Application of high strength steel tubes to automotive body parts is an effective means of simultaneously satisfying the requirements of weight reduction and improved crashworthiness. As a replacement for welded parts of pressed sheet steels, application of steel tubes with a closed cross-sectional structure offers a large advantage for achieving weight saving while maintaining sufficient stiffness. The use of steel tubes in automotive parts has increased in association with the worldwide spread of the tube hydroforming (THF) technique since the late 1990s [1–4]. Figure 1 shows a schematic illustration of the THF process [4]. THF is often used to manufacture automotive parts, making it possible to form tubes into complex sectional shapes and reduce the weight/number of parts. However, the application of high strength steel tubes to automotive parts manufactured by THF is limited due to deterioration of ductility in the forming process. Especially in the case of ultra-high strength steel tubes of over UTS 980 MPa grade, no examples of application to automotive body parts manufactured by THF have yet been reported. Responding to this situation, a new UTS 980 MPa grade ultra-high strength ERW steel tube with excellent formability was developed by applying a cold rolled sheet steel with excellent formability and a Chance-free Bulge Roll (CBR) tube forming mill. In this paper, the enhanced performance of the developed UTS 980 MPa grade steel tube is reported.

## 2 Advantages of Steel Tubes in Automotive Body Parts

One of the advantages of applying steel tubes to automotive parts instead of welded parts consisting of pressed steel sheets is high impact strength. Improvement of impact strength is particularly important in automotive body parts. In order to compare the impact strength of a tube hydroformed part and welded part of pressed steel sheets, an FEM simulation of axial collapse to a rigid wall at a speed of 50 km/h was conducted. Figure 2 shows the analysis model used in the numerical calculation.

The steel tube used in the calculation is a UTS 780 MPa grade high strength steel tube with an outer diameter of 82.6 mm and wall thickness of 1.8 or 2.0 mm. The steel tube is formed into a rectangular shape with a corner radius of 12 mm by THF. The sheet steel used in the calculation is also a UTS 780 MPa grade high strength sheet steel with a thickness of 2 mm in the hat-shaped pressed part and 0.7 mm in the bottom sheet. The hat-shaped pressed part and bottom part are joined by spot welding at 30 mm intervals, and the welds are assumed to be unbreakable. Figure 3 shows a comparison of the absorbed energy of the hydroformed parts and the welded part by FEM simulation. The hydroformed parts display higher absorbed energy in comparison with the welded part, while also reducing the weight of the part. As seen in these results, application of steel tubes

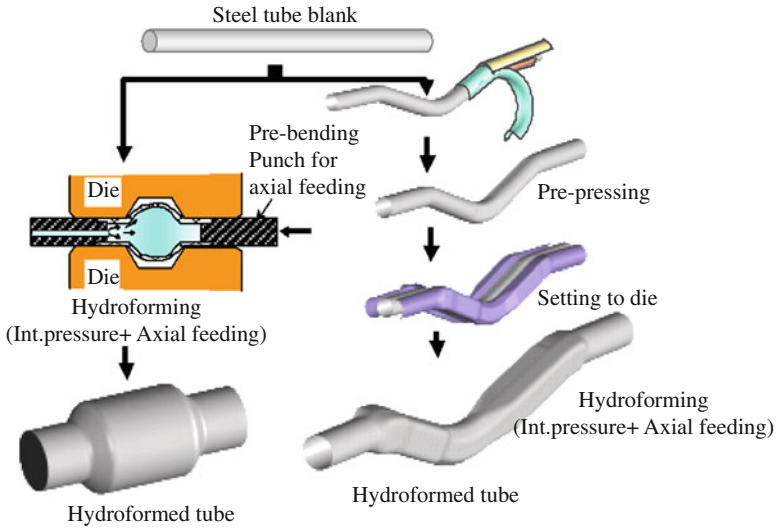


Fig. 1 Schematic illustration of tube hydroforming process [4]

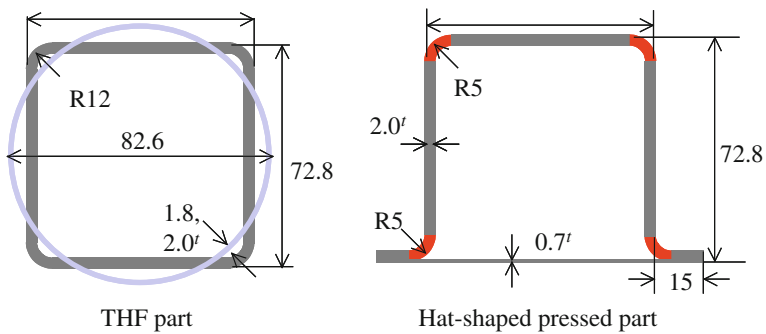
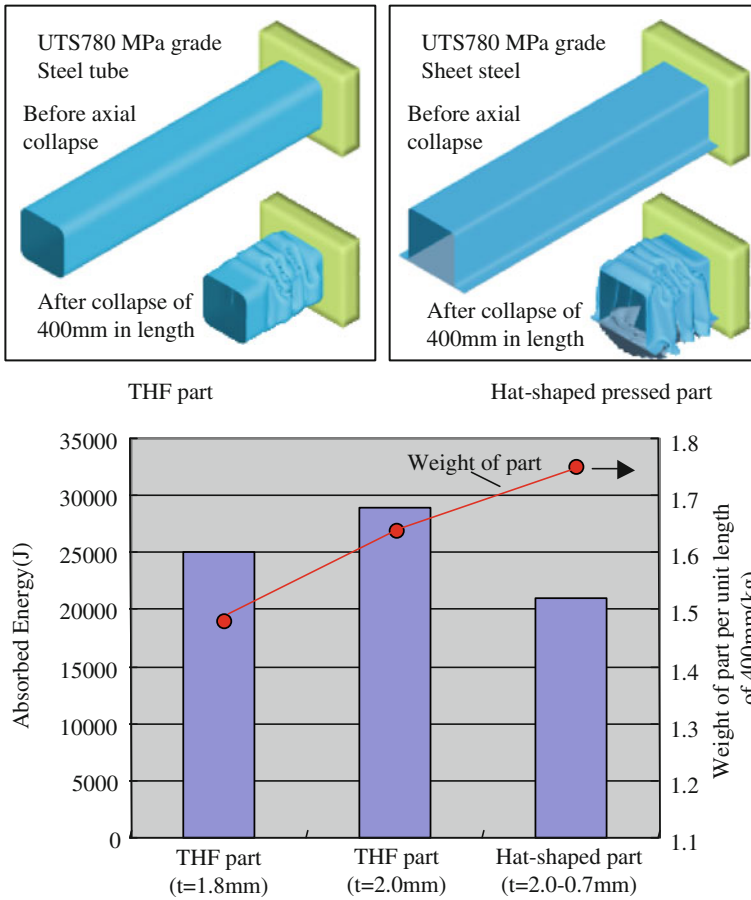


Fig. 2 Analysis models for numerical calculation

to automotive parts is effective for simultaneous achievement of weight saving and crashworthiness.

### 3 UTS 980 MPa Grade Cold Rolled Sheet Steel with Excellent Formability

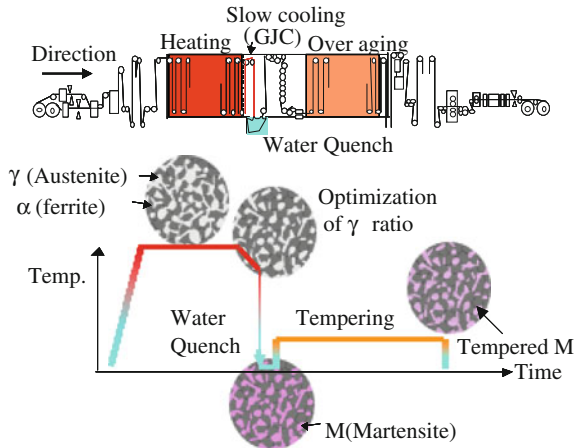
Improvement of the ductility of sheet steels for use in steel tubes is also indispensable for expanding the application of high strength steel tubes. JFE Steel has developed ultra-high strength sheet steels of UTS 780–1470 MPa grades with



**Fig. 3** Comparison of absorbed energy between hydroformed part and hat-shaped pressed sheet steel by FEM simulation

various features, e.g. high elongation, hole expansion formability and a combination of both, applying the originally developed Water-Quench type Continuous Annealing (WQ-CAL) process, which has a high cooling capacity [5, 6]. Figure 4 shows schematic illustrations of the WQ-CAL and the heat cycle of the annealing process [5, 6]. Figure 5 shows the relationship between the elongation (EL) and hole expansion ratio ( $\lambda$ ) of the UTS 980 MPa grade cold rolled sheet steel with a Dual Phase (DP) microstructure manufactured by WQ-CAL [5]. It is possible to manufacture various types of UTS 980 MPa grade sheet steels depending on the intended application by optimizing the ferrite/martensite ratio by adjusting the annealing conditions such the heating temperature, rapid cooling conditions and tempering conditions. Because steel tubes are often subjected to bending and THF, an EL- $\lambda$  balanced type DP sheet steel was selected for the UTS 980 MPa grade steel tube. Table 1 shows the mechanical properties of the UTS 980 MPa grade

**Fig. 4** Schematic illustration of outline of WQ-CAL and heat cycle of annealing process [5, 6]



sheet steel for steel tubes. Figure 6 shows an SEM micrograph of the UTS 980 MPa grade sheet steel [7]. The developed UTS 980 MPa grade sheet steel shows higher elongation compared with a conventional sheet with same level of UTS [8].

#### 4 Chance-Free Bulge Roll Tube Forming Mill

Deterioration of ductility due to additional processing strain in the tube forming process is unavoidable. Therefore, reduction of processing strain during tube making is very important for maintaining the superior ductility of the UTS 980 MPa grade sheet steel as much as possible. To respond to this problem, the CBR (Chance-free Bulge Roll) forming mill originally developed by JFE Steel was used [9]. Figure 7 shows a comparison of the tube making processes using the CBR mill and conventional mill [6, 7, 9]. One feature of CBR tube forming is low additional strain in the tube making process compared with the conventional forming process, resulting in reduced deterioration of the ductility of the sheet steel. Figure 8a shows the appearance of the strip sheet in the cage roll forming zone of the CBR forming mill. In this picture, the upper centre bending roll assembly is taken out for photography. Figure 8b shows a comparison of the appearance of the formed strip in the upper forming process by the CBR mill and conventional mill [6, 7, 9]. In the conventional forming mill, the shape at the edge part of the strip is discontinuous because of the large spacing between the rolls, resulting in an increase of additional strain. In contrast, the edge part formed by the CBR mill is much smoother than that with the conventional mill because the strip edge is sustained by cage rolls which are set at a small interval, and as a result,

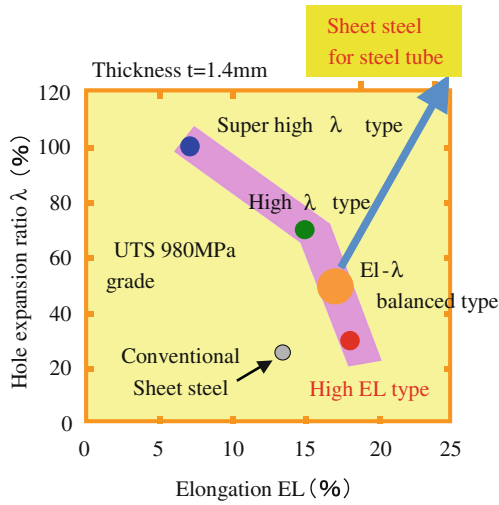


**Fig. 5** Relationship between hole expansion ratio  $\lambda$  and elongation of various types of UTS 980 MPa grade cold rolled sheet steel [5]

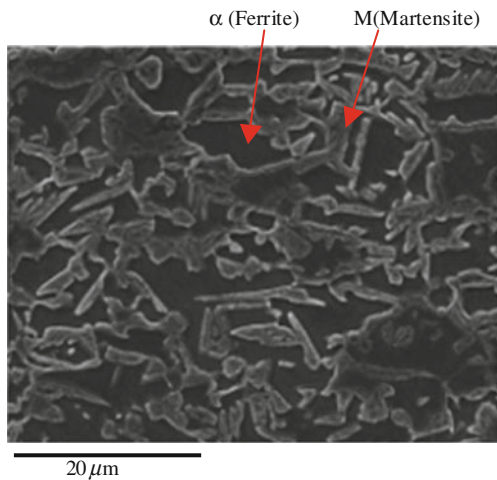
**Table 1** Comparison of tensile properties between developed UTS 980 MPa grade sheet steel and conventional one [8]

Sheet steel	Thickness (mm)	YS <sup>a</sup> (MPa)	TS (MPa)	EL (%)
Developed sheet steel	2.0	695	990	18
Conventional sheet steel [8]	1.2	608	1040	14

Test specimen JIS No.5

<sup>a</sup> YS 0.2 % yield strength

**Fig. 6** SEM micrograph of UTS 980 MPa grade sheet steel for steel tube [7]



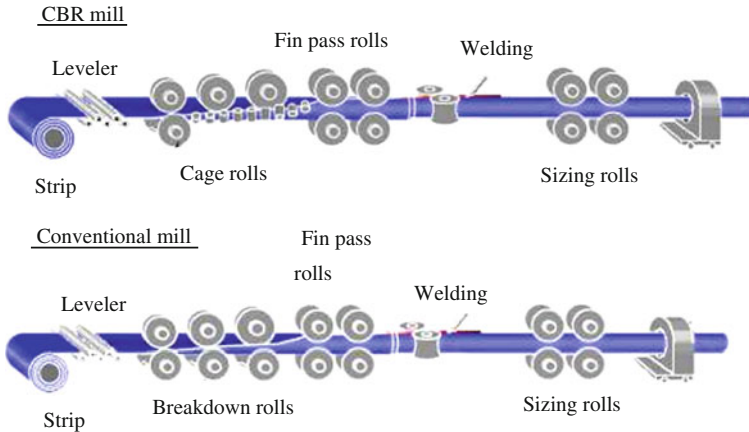


Fig. 7 Schematic illustrations of outline of CBR mill and conventional mill [6, 7, 9]

additional strain during tube forming is reduced. Figure 9 shows a comparison of the uniform elongation of stainless steel tubes with various wall thickness-outer diameter ratios manufactured by the CBR mill and conventional mill [9, 10]. In the steel tubes manufactured by the conventional mill, uniform elongation significantly decreased due to additional strain in the tube forming process. Conversely, the steel tube manufactured by the CBR mill shows higher uniform elongation for all tube sizes in comparison with those of the steel tubes manufactured by the conventional mill. The CBR forming mill can therefore be considered an effective tube forming process, especially for ultra high strength steel tubes.

## 5 Performance of UTS 980 MPa Grade Steel Tube

### 5.1 Tensile Properties

Table 2 shows a comparison of the tensile properties of the UTS 980 MPa grade sheet steel, a steel tube manufactured by the CBR mill and a steel tube manufactured by the conventional mill [6]. The steel tube manufactured by the CBR mill shows 4 % higher elongation in comparison with that of the steel tube manufactured by the conventional mill. This difference in elongation is large in this level of ultra-high strength steel tube. The developed steel tubes with the mechanical properties shown in Table 2 were used in the forming tests described below.

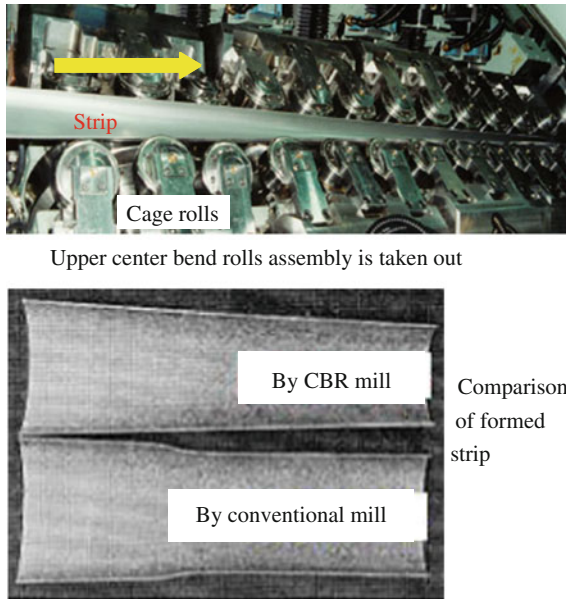


Fig. 8 Appearance of formed strip in the cage roll section [6, 7, 9]

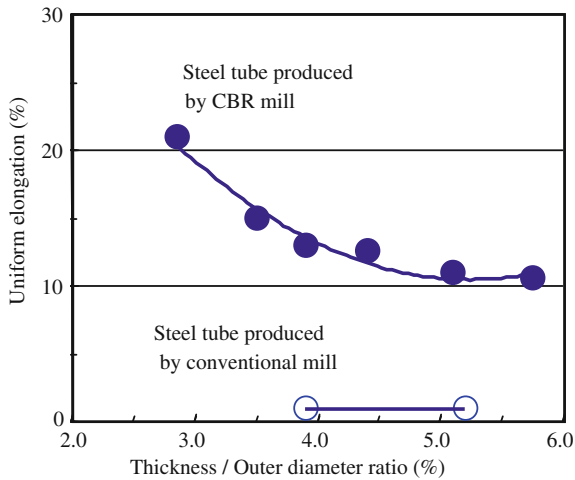


Fig. 9 Comparison of uniform elongation of steel tube produced by CBR mill and conventional one [9, 10]

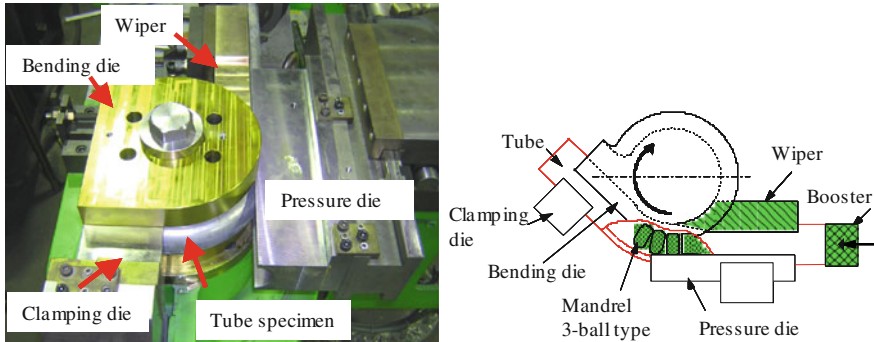


**Table 2** Tensile properties of UTS 980 MPa grade sheet steel and steel tube produced by CBR mill and conventional mill [6]

Sheet/tube	YS (MPa)	TS (MPa)	EL (%)
Sheet steel	695	990	18
Steel tube (by CBR mill)	886	1017	14
Steel tube (by conventional mill)	919	1123	11

*Tube* outer diameter 48.6 mm, thickness 2.0 mm

*Tensile specimen* JIS1No.12A for tube, JIS No.5 for sheet

**Fig. 10** Appearance of stretch bending apparatus [6, 11]

## 5.2 Bendability

Because steel tubes are frequently subjected to bending in actual applications to automotive parts, bending formability is one of the most important properties for steel tubes. Figure 10 shows the appearance and a schematic illustration of a stretch bending apparatus [6, 11]. The bending test was conducted using a three-ball type mandrel and a booster.

In order to evaluate the bending formability of steel tubes, a bending test was conducted with various bending radii. Figure 11 shows the typical appearances of the bent steel tubes [6, 7]. The developed steel tube could be bent to a minimum bending radius of 90 mm (Bending radius/Outer diameter (R/D) ratio = 1.85) without wrinkling or breaking, which is significantly higher formability compared with conventional steel tubes of the same strength grade. Figure 12 shows a comparison of the bending formability of steel tubes manufactured by the CBR mill and conventional mill using the same UTS 980 MPa grade sheet steel. With the steel tube manufactured by the conventional mill, breaking occurred due to deterioration of ductility by additional strain in the tube making process. In contrast, with the steel tube manufactured by the CBR mill, bending was completed without breaking or wrinkling.

**Fig. 11** Appearance of UTS 980 MPa grade steel tubes after stretch bending [6, 7]

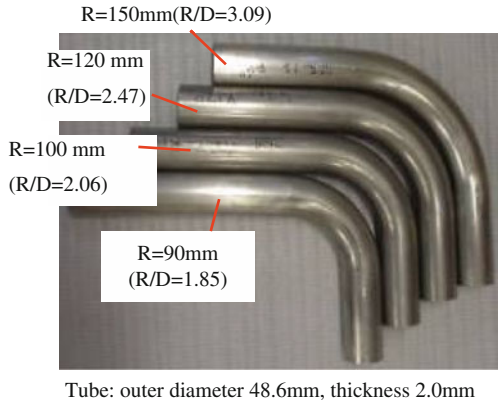
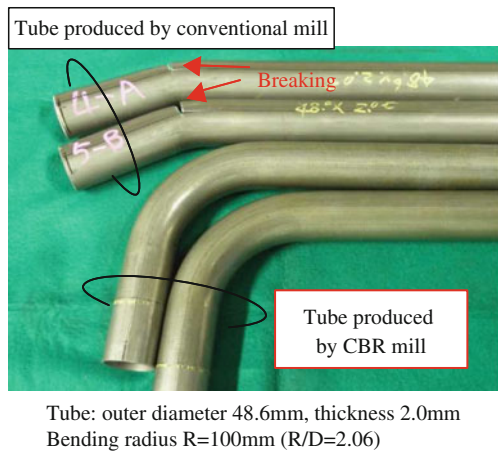


**Fig. 12** Comparison of bendability of UTS 980 MPa grade steel tubes produced by CBR mill and conventional mill



### 5.3 Tube Hydroformability

As mentioned above, THF is an effective forming process that makes it possible to form steel tubes to complicated sectional shapes and is essential for expanding the application of steel tubes as automotive parts. In the actual forming process for automotive parts, THF is often conducted following pre-bending or pre-pressing. Therefore, higher formability is required in steel tubes due to the decrease of the bending radius in pre-bending or the increase of the expansion ratio in THF. In order to evaluate the hydroformability of the developed steel tube, a THF test by forming of a rectangular shape, which simulates the shape of actual automotive body parts, was conducted using a 1000 ton THF machine [7]. Figure 13 shows the THF shape used here [7]. The steel tube blank was 48.6 mm in outer diameter and 280 mm in length. The formed cross-sectional shape was a  $51.8 \times 41.62$  mm rectangle, and the bulge length was 97.2 mm. The corner radius was  $R = 12$  mm and the bulging ratio was 8 %. This is a comparatively difficult shape to form with

**Fig. 13** Dimensions of hydroformed rectangular tube [7]

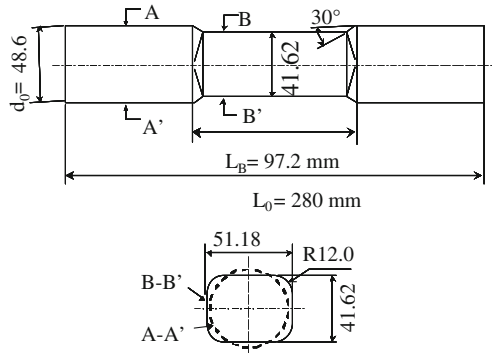
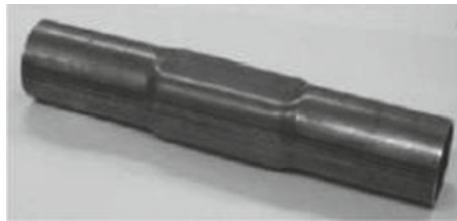
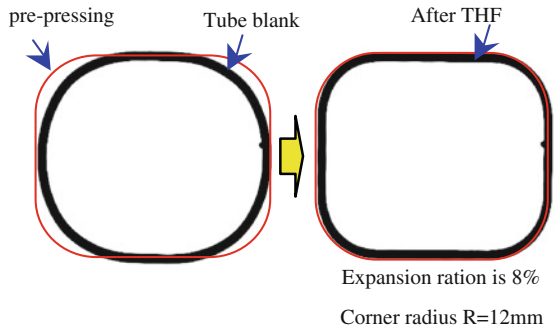


**Fig. 14** Appearance of hydroformed tube [6, 7]

Tube blank : diameter 48.6mm,  
thickness 2.0mm (t/D=4.1%)



After



this level of ultra-high strength steel tube. In this test, pre-pressing was conducted in advance of applying internal pressure. Hydro formability was evaluated by the THF test by applying a maximum internal pressure up to 190 MPa without axial feeding. The test tube samples were set so that the weld portion was positioned at the centre of width of the plane. A lubricant with a frictional coefficient  $\mu = 0.12$  was used. Figure 14 shows the appearance of a hydro formed steel tube [6, 7]. THF was completed without wrinkling or bursting. Based on this result, expansion of the applications of the developed UTS 980 MPa grade steel tubes to automotive

body parts, in which the applicable UTS grade has been 780 MPa or pressed sheet steels have been used conventionally, is expected.

## 6 Conclusion

A new UTS 980 MPa grade steel tube with excellent formability was developed by applying a cold rolled sheet steel with a DP microstructure manufactured by the WQ-CAL and CBR tube forming mill, which minimizes additional strain in the tube making process. The developed steel tube was evaluated as a suitable UHSS tube for THF and applied to an actual automotive body part, contributing to not only weight saving but also improved safety [12]. Based on these results, further expansion of the applications of UHSS tubes to automotive parts is expected to offer many advantages.

## References

1. Manabe K (2003) Perspectives of tube hydroforming of automotive components with light weight and high rigidity. *CAMP-ISIJ* 16:1158
2. Toyoda S, Kawabata Y, Suzuki K (2005) High performance steel tubes for automotive parts. JFE technical report, No. 9, pp 30–35
3. Yoshitake A, Ono M (2004) Application technologies for weight reduction, improving crashworthiness and shortening of development period for automobiles. JFE technical report, No. 4, pp 1–7
4. Sekita T, Kaneto S, Hasuno S, Sato A, Ogawa T, Ogura K (2003) Materials and technologies for automotive use. JFE technical report, No. 2, pp 1–16
5. Matsuoka S, Hasegawa K, Tanaka Y (2007) Newly-developed ultra-high tensile strength steels with excellent formability and weldability. JFE technical report, No. 16, pp 16–20
6. Aratani M, Ishiguro Y, Sonobe O, Gunji M, Sato A (2010) TS 980 MPa grade steel tube with excellent formability for automotive body parts. *Mater Jpn Inst Metal* 49(3):110–112
7. Aratani M, Ishiguro Y, Sonobe O, Hashimoto Y, Gunji M, Sato A (2010) High strength steel tube with excellent formability for automotive body parts. In: *Proceedings of automotive engineering exposition*, No. 157–10, presentation no.292
8. Naemura H (1983) Continuous annealing technology for cold rolled sheet steel and products”, 88th and 89th Nishiyama Kinen Gijyutu Koza, ISIJ, 283–326
9. Toyooka T, Hashimoto Y, Gunji M (2000) High-formability thin walled erw pipe for automobile, produced by CBR forming mill. *Kaswasaki Steel technical report*, vol 32, No. 1, pp 49–53
10. Toyooka T, Hashimoto Y, Kobayashi K, Itatani S, Ide T, Nishida Y (1990) Development of chance-free bulge roll (CBR) forming process for manufacturing ERW pipe. *Kawasaki Steel technical report*, vol 22, No.4, 236–244
11. Suzuki K, Toyoda S, Sato A, Ueno Y, Okada M (2007) Development of a new bending method “PRB” for high strength steel tube and application of high strength steel tubes for automotive parts I” JFE technical report No. 17, pp 52–58
12. Hasegawa Y, Fujita H, Endo T, Fujimoto M, Tanabe J, Yoshida M (2008) Development of front pillar for visibility enhancement. *Honda R&D Tech Rev* 20(2):106–113

# Research on Solutions of Cloud Manufacturing in Automotive Industry

Zhongxiao Jin

**Abstract** Cloud computing will be the next wave of information, and is an industrial revolution. This paper puts forward a solution of cloud manufacturing on the automotive industry. This solution includes two parts, one is the business solutions, in business solutions, this paper puts forward contents of the automotive industry manufacturing clouds to create is: unified product data management platform, unified for total life cycle of the BOM platform, unified manufacturing resources management platform, unified manufacturing execution platform and unified manufacturing quality management platform, and another part is technical solutions, in the technical solutions, this paper puts forward the cloud manufacturing technology solutions based on SOA and the Java EE technology, including distributed computing technology, distributed scheduling technology, distributed transaction processing technology, enterprise service bus technology, cloud computing safety technology and cloud computing cache technology, etc. This paper based on the automotive industry, especially in the China's own brand automotive enterprises, puts forward the solution of applying the cloud computing technology to automotive manufacturing. This solution make manufacturing resources and manufacturing capacity associated with automotive manufacturing virtualization, Servicisation, and through concentrate and intelligent management and operation to realize intelligent, multi-win-win situation, pervasive, and efficient sharing and collaborative; Through the network it can provide safe and reliable, high quality cheap service for the whole life cycle of automotive manufacturing process according to the needs of the automotive at any time. This solution help to speed up China's automotive industry structure adjustment and the

---

F2012-H10-004

---

Z. Jin (✉)  
SAIC Motor Corporation Limited, Shanghai, China  
e-mail: jinzhongxiao@saicmotor.com

transformation of development mode, and improve the China's own brand automotive enterprises core competitiveness, and also help to shorten the gap between the China's own brand automotive enterprises and the world automotive giant.

**Keywords** Own-brand automotive · Cloud computing · Cloud manufacturing · Business architecture · Technology architecture

## 1 Requirement Analysis

### 1. China manufacturing is to the mark of the transformation and upgrading

After 30 years of rapid development, China's manufacturing industry relies on the end of the era of low cost and cheap labour. Whether the debt crisis and the developed countries in Europe to return to the manufacturing of the external pressure, or the inherent law of China's economic development, have determined that the Chinese manufacturing industry must find a new growth mode.

Central strategic plan and the objective requirements of the national industry and information technology development, we should adhere to the new road to industrialization of Chinese characteristics, in accordance with the essence of building a modern industrial system requirements around key elements of transformation and upgrading, speed up the transformation of the mode of development of the manufacturing industry, creating China's manufacturing industry, a new round of growth. This is China's manufacturing industry must be a strategic choice.

### 2. The development needs of China's own-brand automotive

Of its inception, the automotive industry no money, no technology start is particularly difficult. With the reform and opening up, China's automotive industry embarked on cooperation with foreign auto companies, the introduction of the digestion of the path of development of advanced technology from abroad, domestic independent brand car is gradually mature, and become the mainstay of China's automotive industry. But foreign auto companies, after all, just to profit from the huge Chinese market, "market for technology can help our auto companies to be developed, but will also stifle the development of China's national automotive industry, losing its own brand, China's auto companies only the assembly plants of foreign auto companies in China. Thus, China's auto enterprises of independent innovation and self-development, master of their own automotive key, core, cutting-edge technology with a truly independent brands in order to make China's auto industry development and growth.

Establish an independent brand is a necessary condition to enhance self-development capacity of China's automotive products. The joint venture policies of China's automotive industry over 20 years to increase the employment, training and technical personnel, transportation management experience, and dissemination

of marketing concept and made a great contribution. However, in a large number of joint venture, we not only failed to grasp the foreign advanced technology to significantly improve the self-development capacity of China's automotive industry, but lost the original brand and R&D capabilities, Chinese independent brand car business attaches great importance to the value of the product and role, most manufacturers are still advertising promotions, channel building, product promotion-oriented, also failed to attract enough attention for the construction of the brand, and advertising appeals are similar, and can not spread the brand personality. The end result of the stay at the product level with the domestic auto market competition, price competition and a simple promotional tool is not only a reduction in market share and profit decline in more serious is the loss of its own brand value. The carrier of its own brand, not so much automotive products, it is more the automotive's own brand and own brand solution is the right to exist, therefore, its own brand to improve the capacity of independent development is an indispensable prerequisite to establish own brand is to raise the necessary conditions for China's automotive self-development capacity.

### 3. Cloud computing is the golden opportunity of China's auto industry

Cloud computing will become the wave of the next information is the industrial revolution, history has entrusted to the opportunities of the IT industry, foreign auto giants will use cloud computing technology to transform traditional auto industry, which is entrusted by history to a great development of our own brand automotive opportunity, if we seize, we can shorten the gap and foreign auto giants.

## 2 Business Solutions

The business solution is as flow (Fig. 1).

The core of the application architecture is "unified, unified reflects the Group collaborative group strength, which is exhibited in the following aspects.

### 2.1 *Unified Data Management Platform*

Product Data Management (PDM) is the general term of the product life cycle data and processes for effective management methods and techniques. PDM includes the related concepts of engineering data management, file management, configuration management, product information management, product structure management, and so on.

In the auto companies, the use of PDM system can help automotive designers to constantly monitor the quality of vehicle design, control engineering changes, enhance the efficiency of vehicle development, reduce vehicle development cost and enhance the quality of vehicle design.

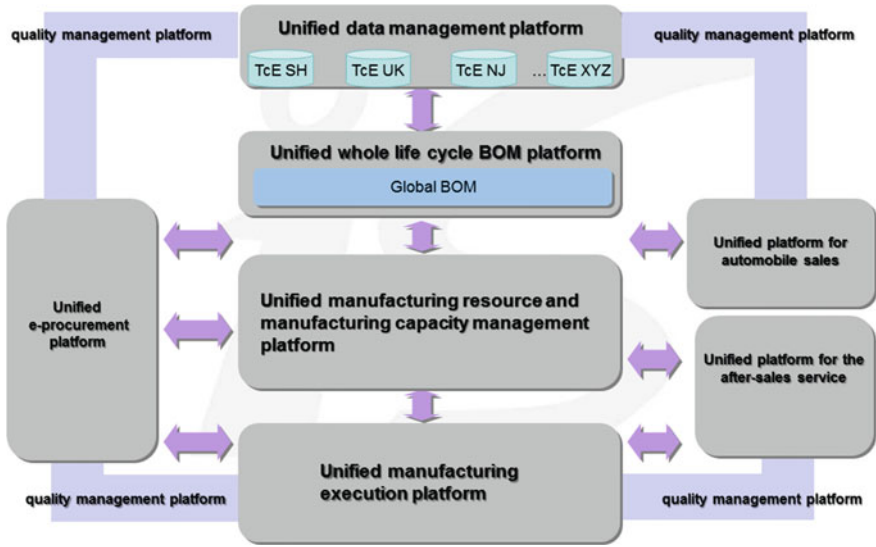


Fig. 1 Business architecture of cloud manufacturing

1. Enhance the efficiency of product development:

The face of the development process and needs to call a large number of electronic data, and establish a comprehensive, unified data management system to system, between platforms, departments, and between upstream and downstream co-design and concurrent engineering; the system effectively manage the data in the form of orderly accumulation of data, strengthen the reuse of reliability and convenience, better support for the increase of the product platform and effectively shorten the development cycle.

2. Enhance the business value chain efficiency:

Effective management and delivery of the engineering CAD data in the system can greatly shorten the cycle from design to physical (Lead Time); seamless connection to a unified platform, information and data delivery, improve the response speed of the entire value chain.

3. R & D capabilities enhance the experience and knowledge accumulation

Given the characteristics of the information system itself, PDM system curing the enterprise's own business processes and management practices, the establishment of the system is Shanghai Automotive independently developed the process of combing, management practices established R & D capacity building process and needs.

4. Cross-regional product development and manufacturing

In order to integrate the global advantage resources, its own brand in the UK, Nanjing technology centre, synchronous development of new products and technical



centre in Shanghai. British engineers, such as: conceptual design, Chinese engineers completed the conceptual design refinement; this model requires the data in the system to maintain a high degree of synchronization. Daily between Britain and pass large amounts of data to ensure that, the British engineer is able to see the results of each other's work.

## ***2.2 Unified Whole Life Cycle BOM Platform***

Auto manufacturers' most of the business are to carry out the around the automotive products, including product R & D (the R & D.), manufacturing processes, production management, procurement, product quality, market sales (S-& M-), financial accounting, etc., is the product BOM data those business units are closely linked. BOM is the core basis of the manufacturing information system data, BOM throughout the design, technology, manufacturing, planning, purchasing, sales, finance almost all departments, and is a bridge and link between the contact the engineering department and production management department.

BOM is an important part of the PDM and ERP systems, the core data of the manufacturing enterprises, the intersection of two major information platforms of the PDM and ERP systems. In the PDM system, BOM is the end result, commonly known as the design BOM, product design perspective, and the product platform for the tree structure of the unit. For ERP system, BOM is the source, usually called the plan BOM.

### **2.2.1 The Value of Unified BOM**

Change orders throughout the multi-plant production and after-sales business through a unified product, to ensure the timely response of the downstream business and multi-plant BOM data synchronization update; BOM data through a unified system platform maintenance and release management to ensure the accuracy of the data and multi-system consistency of the data; by a unified view of the product BOM, the BOM view of the production, sale and cross-cutting development, to ensure that all departments share the same core information.

## ***2.3 Unified Manufacturing Resource and Manufacturing Capacity Management Platform***

Unified manufacturing resource and manufacturing capacity management platform human, financial, material, information, time and space resources owned enterprises, overall balance and optimize the management, coordination of enterprise management department, around the market-oriented business activities, improve the core competitiveness of enterprises, to obtain the best value for money.

## ***2.4 Unified Manufacturing Execution Platform***

Automotive manufacturing execution system is directly related to automotive manufacturing, its business coverage and throughout the common vehicle manufacturing five major manufacturing process, i.e.: stamping manufacturing process, body manufacturing process, the coating manufacturing process, powertrain manufacturing process and assembly manufacturing process and its main function:

Production control: including order management, vehicle tracking and routing control, data acquisition, PMC, and so on.

Materials Management: including medium-and long-term forecast released material pull, material receiving, and warehouse management, and so on.

Quality management: includes on-site quality information defects input and query management, site vehicle quality information defects input and query, auditing, vehicle testing and defect management and tracking system, vehicle flow card management system, quality dark light system, and so on.

To establish a unified manufacturing execution platform to help:

- (1) Accurate knowledge of the production sequence and time: including through online production control, storage area management, a variety of information broadcasting, and a variety of statements to achieve flexible production control, material supply and line quality data collection.
- (2) Vehicles with stamping, engine synchronization: the sequence of vehicle production and self-made parts, subassemblies, synchronization and internal logistics management optimization, and parts traceability and on-line quality control.
- (3) Production and parts supply synchronization: the production of parts and components supplier synchronized, collaborative supplier management process, vendor management, extension, and quality process control, quality of the exchange processing and quality analyse.
- (4) Finished car storage, marketing and transportation synchronization: collaborative production planning and sales plans, sales and shipping simultaneously, process visualization of the logistics supply, quality problems retrospectively.
- (5) The production and marketing synchronization: a single plant by the local factory, global manufacturing and development, to achieve a true sense of the order-driven integrated production, supply chain can be adjusted with the change of business model.

## ***2.5 The Unified Quality Management of the Entire Lifecycle Platform***

Unified quality management platform is for full life cycle coverage model from design to the car service car full life cycle and quality-related functions, including

the quality plan, quality data collection, quality, traceability and control, quality analysis, quality problem prevention of core functionality.

## ***2.6 Advantage of the Solution***

To sum up, it has five advantages:

- (1) Put forward the model of cloud manufacturing for the Automotive Group combined cloud computing and automotive industries.
- (2) Put forward the automotive group's core content of cloud manufacturing.
- (3) Put forward that the automotive group cloud manufacturing platform is for the group's synergies' private cloud.
- (4) Put forward that cloud manufacturing a platform for sharing of the Group's manufacturing capacity and optimization.
- (5) Put forward that cloud manufacturing is to help speed up the transformation of China's auto industrial restructuring and development of the way.

## **3 Technology Solutions**

Technology solutions, including IaaS, PaaS, and SaaS cloud computing model.

### ***3.1 Infrastructure as a Service (IaaS)***

The IaaS solution is based on Cisco's cloud computing data center solutions, as shown below (Fig. 2).

#### **3.1.1 Cisco Cloud Data Center Building Blocks**

Cisco brings an important set of technology building blocks at the foundation of the cloud architectures. They are described as follows.

- 10 Gigabit Ethernet
- Unified Fabric
- Unified Computing.

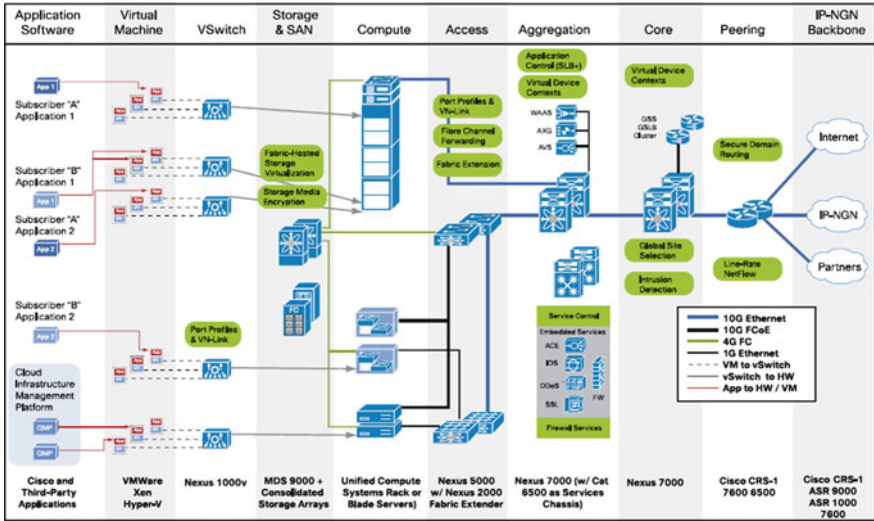


Fig. 2 Cisco cloud computing data center architecture

### 3.2 Platform as a Service (PaaS)

Platform as a Service(PaaS) is using IBM cloud solutions, as follows (Fig. 3). IBM Websphere Virtual Enterprise can:

- Dynamic workload management offers better hardware utilization with lower over-provisioning requirement:
- Allows the amount of physical compute resource allocated to an application to vary as the demand for that application varies.
- Allows administrators to avoid provisioning hardware in siloes for peak utilization by each application. Instead, administrators can allocate for average utilization, with a smaller buffer of extra hardware shared by all applications as they peak.

### 3.3 Software as a Service (SaaS)

Cloud manufacturing’s core content is the application, that is, of SaaS.

The application technology architecture is as flowing (Fig. 4).

1. It is based on Java EE technology

Why do I use Java EE in cloud manufacturing? Because I think Java EE is the most appropriate technology and the reasons are as following:

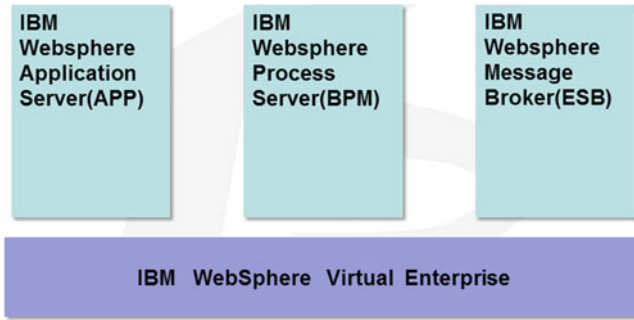


Fig. 3 IBM PaaS solution architecture

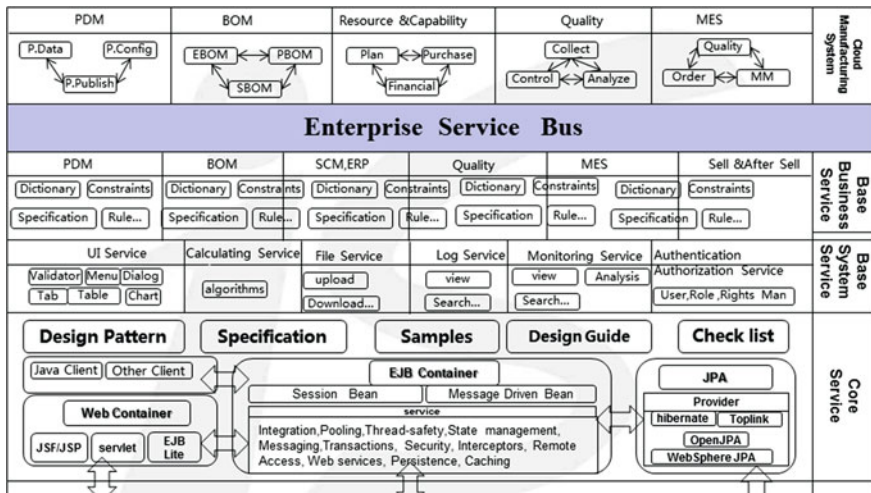


Fig. 4 SaaS solution of cloud manufacturing in automotive industry

- Java EE was designed to be deployed to a distributed environment. Cluster management and extensive monitoring and management capabilities are supported by major application servers.
- The EJB 3 programming model encourages stateless, idempotent, and atomic or transactional design. It is interesting to note that the programming restrictions are very similar to the Google App Engine. In both cases, thread management, file access, changes to the underlying JVM—especially class loading, system properties, and security managers are not allowed.
- Furthermore, both Java EE 5 and Java EE 6 come with standardized packaging—the Enterprise Archive (EAR), which makes the provisioning of cloud apps relatively easy. And EAR solves some cloud-interoperability issues: It’s a lot easier to move an app from one cloud to another. Java EE 5 and 6 are portable, so applications can be easily moved from one application server to

another, regardless of whether they run in a cloud or not. They both will run on JDK 5 or higher.

- The JVM itself comes with fantastic remote debugging, profiling, and monitoring capabilities. This already greatly simplifies the development of distributed apps and should also simplify cloud-enabled apps.

## 2. SaaS is divided into four layers

In order to improve flexibility of cloud manufacturing, we divided the cloud manufacturing platform into four layers.

Layer one: is the core service. It depends on the Java EE application server and uses the technology as above, especially use EJB technology.

Layer two: is the system server layer and it is the common service for all.

Layer three: is the business service and it is the base unit of cloud manufacturing and can be reused for the corresponding cloud manufacturing system module.

Layer four: is the cloud manufacturing sub system.

## 4 Conclusions

Cloud manufacturing platform will be all kinds of automotive manufacturing-related manufacturing resources and manufacturing capabilities, virtualization, service-oriented, and focus on the intelligent management and operation, intelligent, win-win situation, pervasive and efficient sharing and collaborative full life cycle; through the network the services of automotive manufacturing process can be obtained at any time, on-demand use, safe and reliable, high-quality affordable [1]. This solution will help accelerate the changes in China's auto industrial restructuring and development of the way, help to improve the core competitiveness of Chinese own-brand automotive enterprise, but also help Chinese own-brand automotive enterprise to shorten the gap between the world auto giants.

## Reference

1. Li B, Zhang L, Wang S et al (2010) Cloud manufacturing: a new service-oriented networked manufacturing model. *Comput Integr Manuf Syst* 16(1):17, 16

# Manufacturing Technology of Passenger Car Rear Axle Drive

Dongni Li, Zhaodan Yuan, Zhiyong Gao, Guorui Zhao,  
Yongshun Jiang, Hongbiao Gao and Tao Li

**Abstract** The vibration and noise performance of passenger car rear axle drive which be used to meet user comfort requirement depends on the product design and production process control. The objective of this study was to determine methods and specifications for Hypoid Gear Optimization, production control and assembly quality improvement. Based on major gear design parameters determined, the gear noise performance optimization can be achieved by improving gear meshing contact ratio, and reducing motion transmission error. The gear durability optimization can be achieved by selecting manufacture method, reasonable cutter radius, cutter edge radius and strength balance, doing tooth contact analysis and adjustment, surface topography ease-off and stress calculations in GLEASON software. High-precision gear production can be achieved by stabilizing material specification, improving gear blanks accuracy, developing work hold equipment structure and optimizing cutting process. The axle drive noise performance can be improved by controlling the assembly for keeping correct hypoid gear positions. Bearing pre-load and variation control will be used for best load capacity and quietness.

**Keywords** Hypoid gear optimization · Manufacture and assembly control · Axle noise

---

F2012-H10-006

---

D. Li (✉) · Z. Yuan · Z. Gao · G. Zhao · Y. Jiang · H. Gao · T. Li  
China Faw Co., Ltd R&D Center, No.1063, Chuangye Street, Changchun, China  
e-mail: lidongni@rdc.faw.com.cn

## 1 Introduction

The process development which ensure product performance is an important part of rear axle design. The specifications obtained from this study will contribute to product quality control and performance improvement. Driver has been annoyed by transmission/axles noise for many decades, and this noise is closely related with transmission gear pairs design, development, manufacturing and assembly. Hypoid gear pairs of axle are normally complex and very sensitive to any change in design, development or manufacturing. Based on major gear design parameters determined, the gear noise performance optimization can be achieved by improving gear meshing contact ratio, and reducing motion transmission error. The gear durability optimization can be achieved by selecting manufacture method, cutter radius, cutter edge radius, strength balance, doing tooth contact analysis and adjustment, surface topography ease-off and stress calculations in GLEASON software. High-precision gear production can be achieved by stabilizing material specification, improving gear blanks accuracy, developing work hold equipment structure and optimizing cutting process. The axle drive noise performance can be improved by controlling the assembly for keeping correct hypoid gear positions. Bearing pre-load and variation control will be used for best load capacity and quietness.

## 2 Optimize the Gear Micro-Geometry to Obtain a Target Contact Pattern and Minimize the Transmission Error

### 2.1 Basic Calculation

Figure 1 shows the input values for the analysis done in software to reproduce the pinion and gear dimension sheet after design drawing. The values are chosen regarding contact pattern and contact path for good NVH behavior and durability.

Figure 2 shows the radius of curvature at I.B and O.B for the gear have been set to get height crowning at the drive side and coast side. The factor of contact pattern length ensures lengthwise crowning and influences the stability of contact pattern which allow the contact pattern to extend at moderate loads so that no overstress at one specific position at flank may occur.

### 2.2 Contact Area Analysis and Load Distribution

The contact pattern for drive side at different loads is shown in Fig. 3. The graph shows that the contact area increases and the entire tooth is used at higher torques.

Figure 4 shows a maximum value of 55 % of load at one tooth and the total contact ratio is 2.642 which is a good result.



Fig. 1 Basic parameters input

Fig. 2 Tooth face optimization

### 2.3 Motion Error Analysis

For good NVH behavior, the motion graphs are analyzed for different torques according to Fig. 5. The transmission error is 30  $\mu$ rads for bench contact and 81.4  $\mu$ rads for full load.

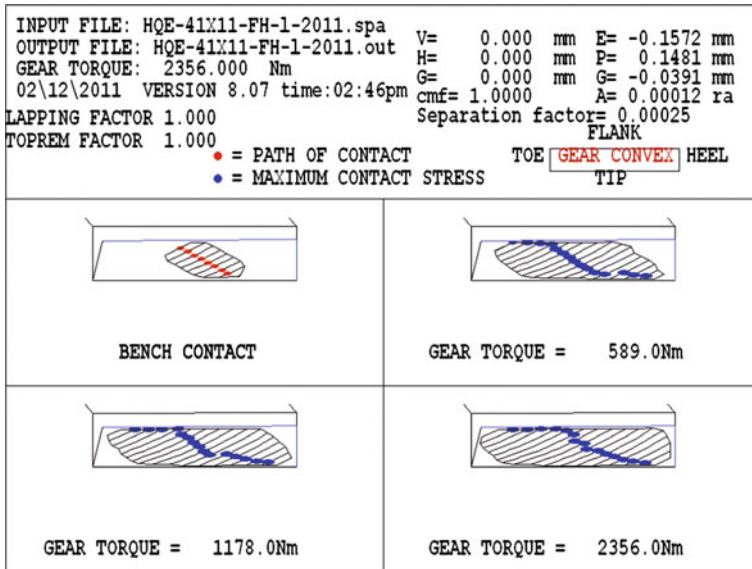


Fig. 3 Contact area expanded

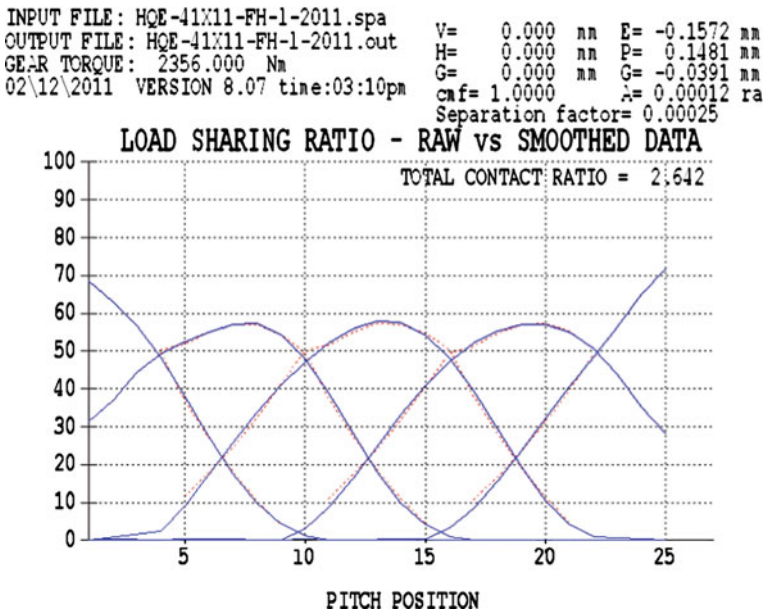


Fig. 4 Load distribution

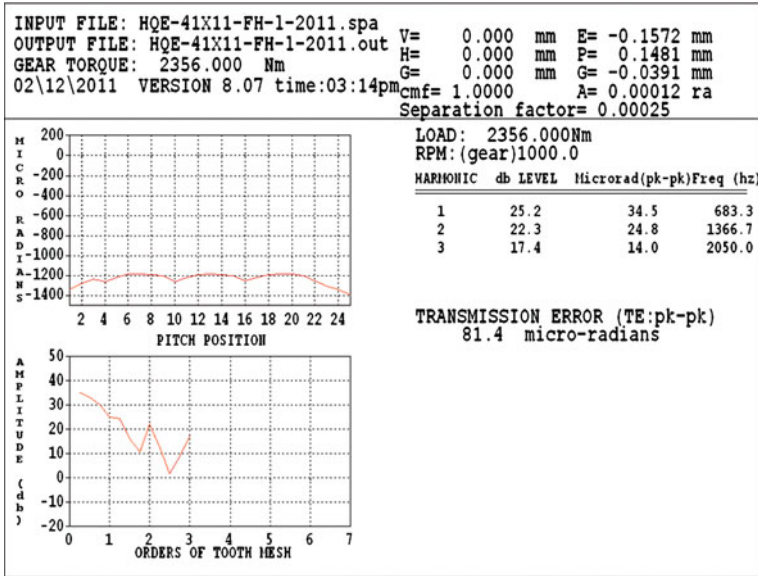


Fig. 5 Motion error analysis

### 2.4 Stress Check

Figures 6, 7 show the calculation result of contact stress and bending stress. With the modification of flank, there are lower contact pressures and a lower risk for pitting. The maximum contact stress at durability torque is about 1516 MPa (safety factor >1).

The maximum root fillet stress distribution along the tooth has a smooth curvature. The bending stress for the gear is higher than for the pinion. At the higher torques the equivalent bending stress at the gear is 544.4 MPa and at the pinion about 426 MPa. The safety factor will be above the limit of 1 and this safety factor will increase further with the applied shot peening.

## 3 Process Optimization for High-Precision Gear Production

### 3.1 Gear Accuracy Control Before Heat Treatment

#### 3.1.1 Fixture Structure

Figures 8, 9.

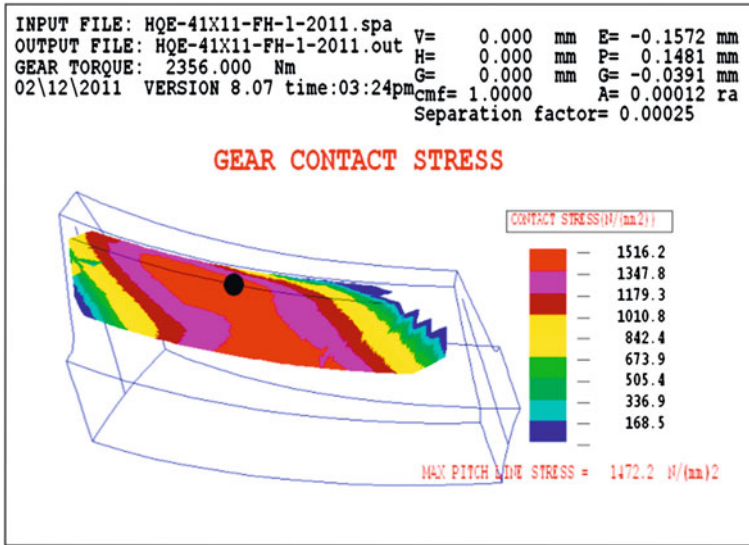


Fig. 6 Contact stress analysis

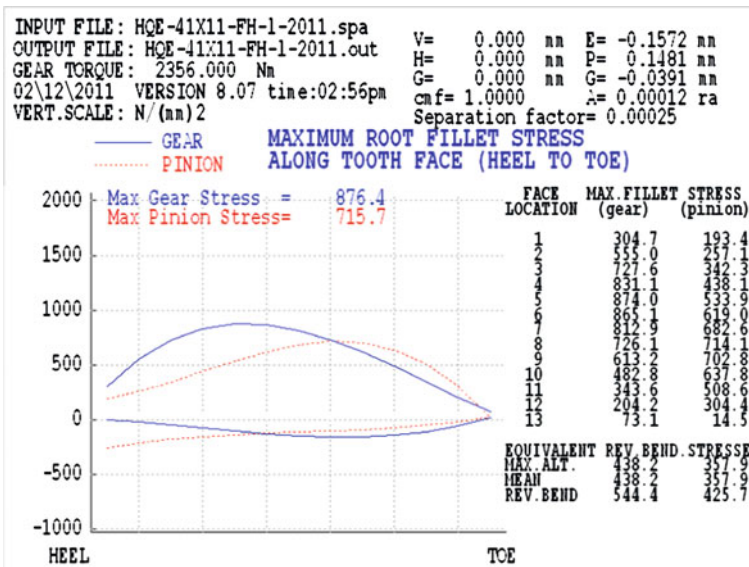


Fig. 7 Root fillet bending stress distribution

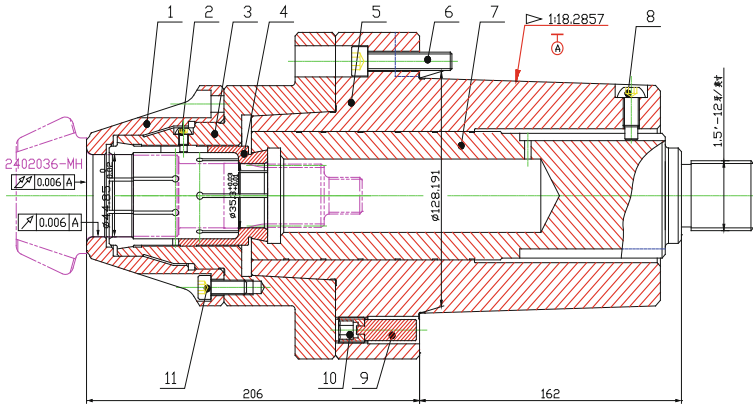


Fig. 8 Workholding equipment for pinion

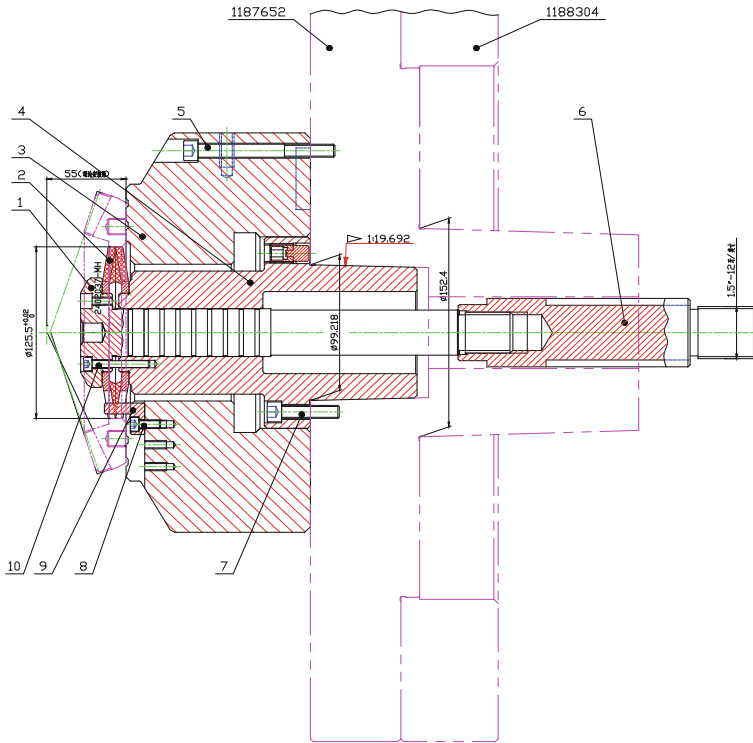
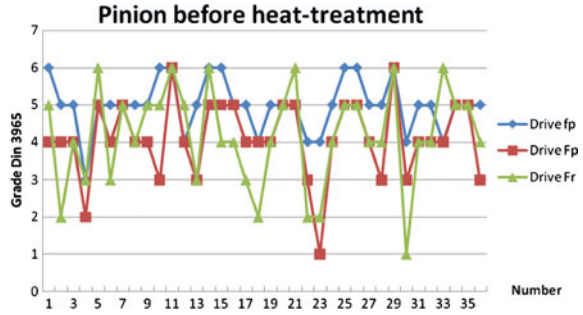
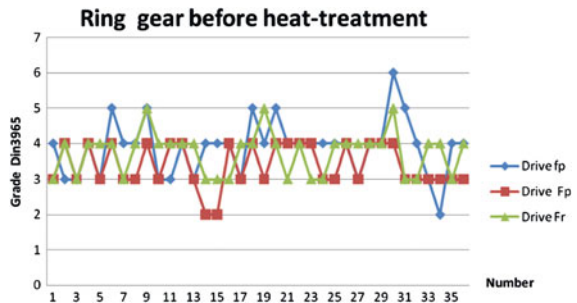


Fig. 9 Workholding equipment for gear

**Fig. 10** Pinion (according to manufacture sequence)



**Fig. 11** Ring gear (according to manufacture sequence)



### 3.1.2 Accuracy Before Heat-Treatment

Figures 10, 11 show manufacture accuracy before heat-treatment. Because the measurement is based on center hole but not mounting surface, the pinion accuracy before heat-treatment is usually 5 grade Din 3965, and this also show the quality of center hole which will be used to position pinion for grinding mounting surface after heat-treatment. The driven gear accuracy before heat-treatment is usually 4 grade Din 3965.

## 3.2 Heat Treatment Accuracy Control

### 3.2.1 Pinion

According to the Figs. 12, 13, the runout of both journals can be almost kept within 0.05 mm. But only as the journal run-out was controlled within 0.025 mm, the most pinion accuracy item can reach grade 6 Din 3965. When the journal runout was controlled within 0.025–0.045 mm, most pinion accuracy will go down to grade 7 Din3965, and several accuracy in grade 8. When the runout is more than 0.045 mm, the teeth accuracy will be difficult to control. With the increase of pinion deformation after heat-treatment, the precision grades loss will be more obvious.

**Fig. 12** The positioning surface runout of the pinion [after heat treatment (according to value growth sequence of journal A)]

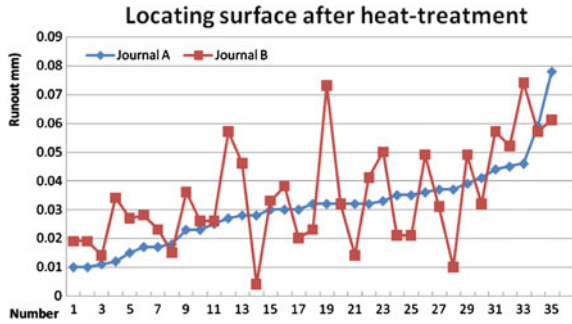
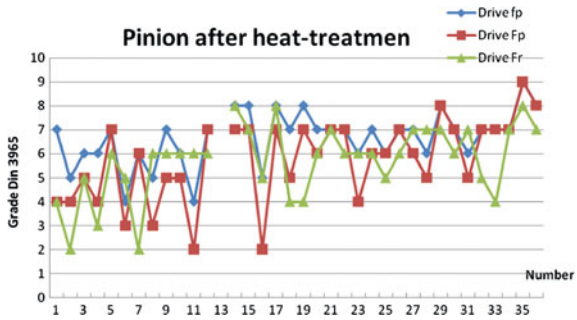


**Fig. 13** The accuracy of the pinion [after heat treatment (according to value growth sequence of journal A)]



**3.2.2 Driven Gear**

According to the Figs. 12, 13, after heat-treatment, the bore roundness is generally controlled within 0.02 mm, and the runout of mounting surface is about 0.02 mm to 0.08 mm. The adjacent pitch and cumulative pitch of the driven gear can be mostly kept at grade 6 Din3965, but the pitch line runout falls down from grade 4 to grade 7 or worse after heat-treatment (Figs. 14, 15).

The ring gear pitch line runout which is closely related with mounting surface quality get worse obviously after heat-treatment. If the runout of mounting surface can be controlled within 0.04 mm, 90 % of ring gear can be controlled at grade 6 after heat-treatment.

**3.2.3 Summary**

According to those mentioned above, in order to control the accuracy of gear pairs after heat-treatment, the pinion’s journal run-out should be controlled within 0.025 mm after heat-treatment, the bore roundness of the driven gear within 0.02 mm, and the mounting surface runout of the driven gear within 0.04 mm.



**Fig. 14** The positioning surface runout of the driven gear [after heat treatment (according to runout growth sequence of mounting surface)]

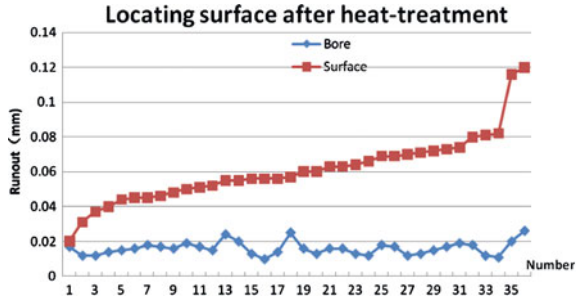


**Fig. 15** Driven gear accuracy [after heat treatment (according to runout growth sequence of mounting surface)]

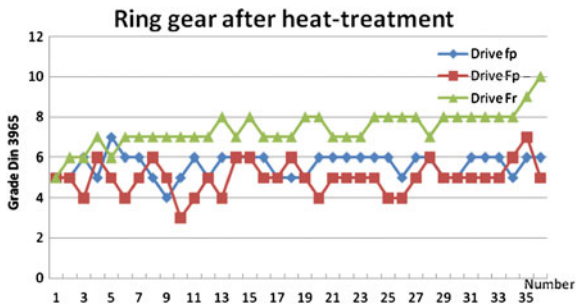
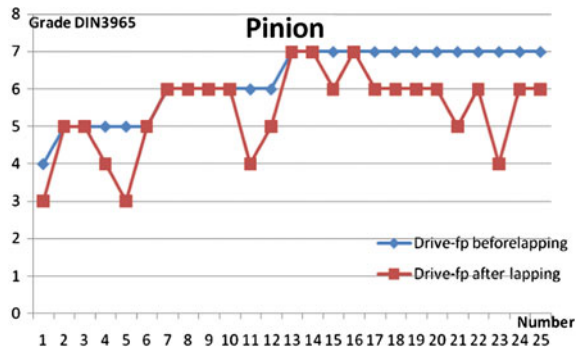


**Fig. 16** Pitch adjacent error change after lapping



### 3.3 Lapping After Heat-Treatment

#### 3.3.1 Accuracy of the Pinion Before and After Lapping

Figures 16, 17, 18 show that lapping process is mostly important for pinion accuracy improvement. After lapping, 90 % pinion accuracy can meet the design requirement of grade 6 Din3965.



**Fig. 17** The pitch cumulative error change after lapping

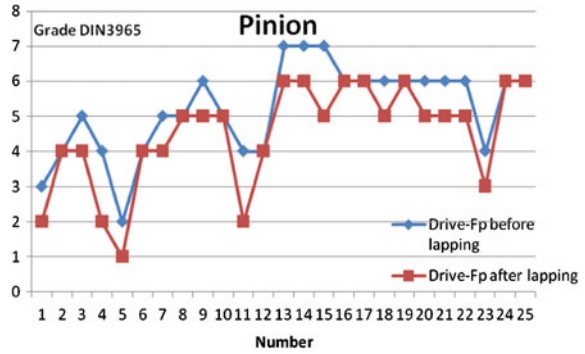


**Fig. 18** Gear ring radical run-out change after lapping

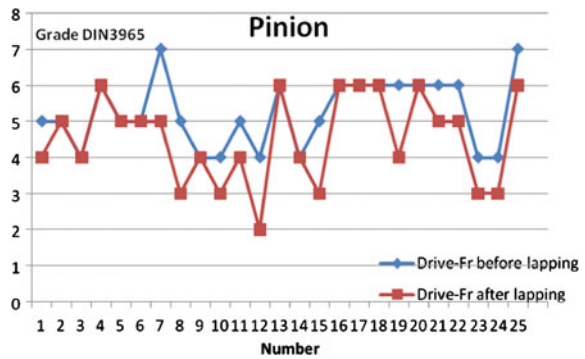
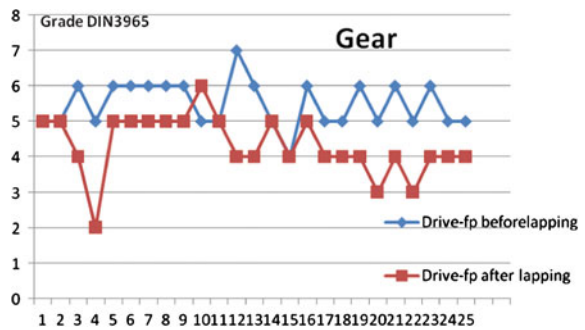


**Fig. 19** Pitch adjacent error change after lapping



**3.3.2 Accuracy of the Driven Gear After Lapping**

According Figs. 19, 20, 21, lapping can decrease obviously pitch adjacent error of gear, but almost has no effect on accuracy improvement about pitch cumulative and runout.

**Fig. 20** Pitch cumulative error change after lapping

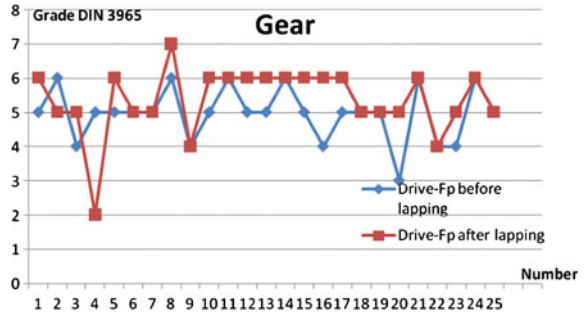


**Fig. 21** Radical run-out change after lapping

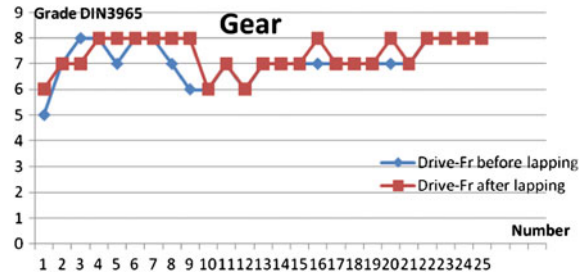
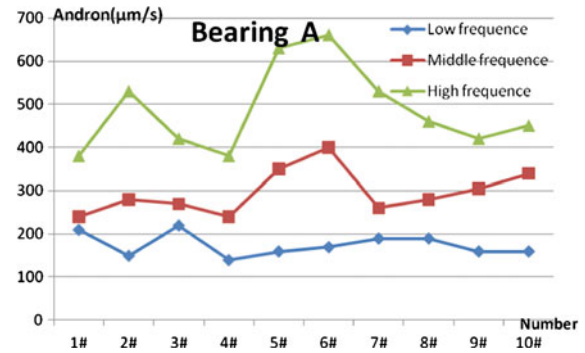


**Fig. 22** Velocity characteristic of bearing A



## 4 Assembly

### 4.1 Assembly Control to Obtain Ideal Work Position

During assembly, pinion must to be adjusted to ideal work position for keeping correct bench contact mark and extension under full-load. Ring gear must to be adjusted to ideal work position for keeping suitable backlash which will meet lubrication requirement when gear pairs mesh during high temperature and different torques condition. Bearing pre-load and variation must be adjusted for improving supporting capacity and reducing misalignment under high load within reasonable bearing life.

**Fig. 23** Velocity characteristic of bearing B

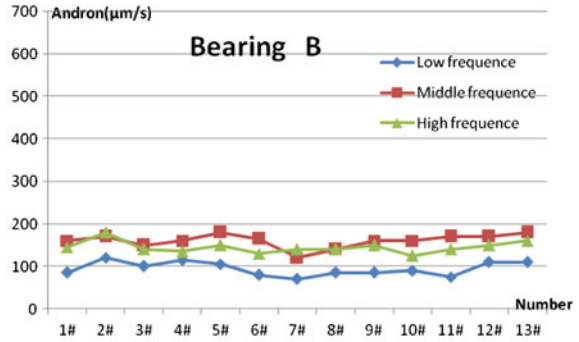
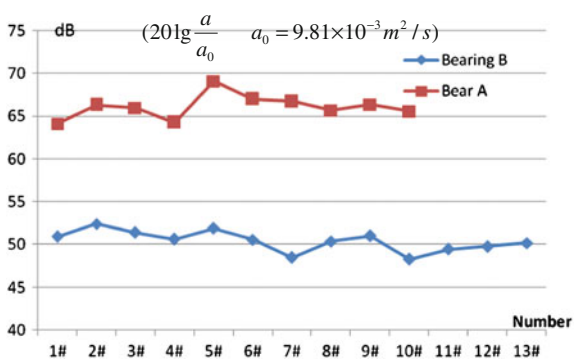


**Fig. 24** Acceleration characteristic of bearing A and B



## 4.2 Bearing Performance

Due to the manufacturing process, assembly and other reasons, bearing performances are different and these also affect axle performance of vibration and noise. We use speed characteristics and acceleration characteristic to compare bearing A and B. Figures 22, 23, 24 show the results.

## 5 Experiment

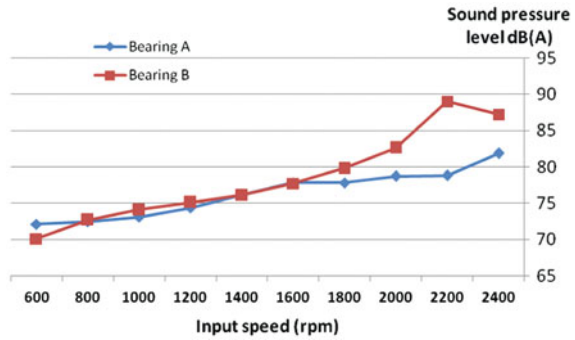
### 5.1 Noise Comparative Experiment of Bearings

Figure 25.

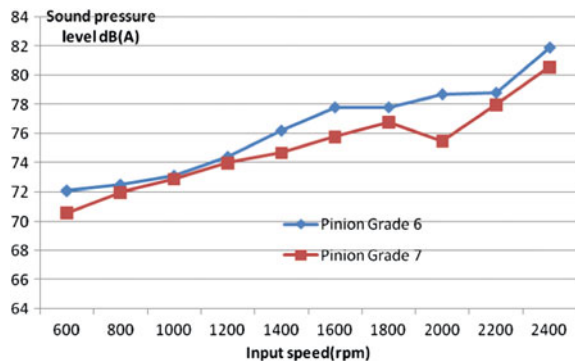
### 5.2 The Effect of Pinion Accuracy on Axle Noise Behavior

Figure 26.

**Fig. 25** Axle noise with different bearing



**Fig. 26** The relation between pinion quality and axle noise level



### 5.3 The Effect of Driven Gear Accuracy on Axle Noise Behavior

Figure 27.

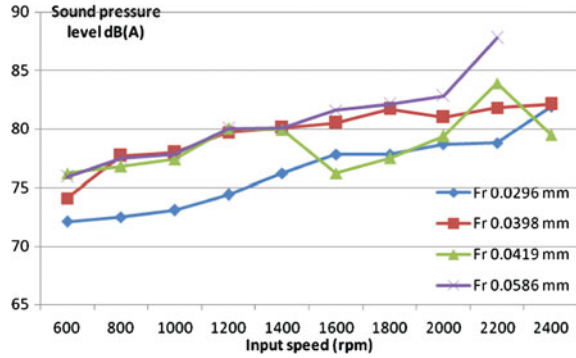
### 5.4 Summary

The pitch line run out of driven gear has great influence to axle noise. When ring gear accuracy is in grade 7 level, the axle noise performance become unstable, although the axle noise result is acceptable at the input speed of 2400 r/min. There is a growth trend of noise along with the speed increase. Thus, gear ring radial run-out shall be controlled within 0.040 mm.

When ring gear accuracy is in grade 7 level, the axle noise experienced a significant increase, especially in high speed. The maximum change is about 6 dB.

For the same gear pairs, bearing performance have great influence to axle noise. The variation of axle noise is about 4–10 dB in high speed conditions for experimental bearing.

**Fig. 27** The relation between ring gear quality and axle noise level



## 6 Conclusion

The study found that (1) The performance of the final product largely depends on process development which obtains the details of the gear parameters after design of the rear axle. (2) The difficulty of gear precision control is how to reduce precision loss of ring gear runout due to heat treatment deformation. The experimental data has been found meeting requirements of the noise. (3) The reasonable lapping is helpful for gear motion error decreasing which have major impact on the gear noise performance. (4) There is relativity between bearing performance, assembling quality and axle noise.

Limitations of this study is the high speed noise performance have not been fully verified.